TUM School of Natural Sciences
Technical University of Munich

Theory of temperature-dependent electronic structure and bulk properties of semiconductors

Stefan A. Seidl

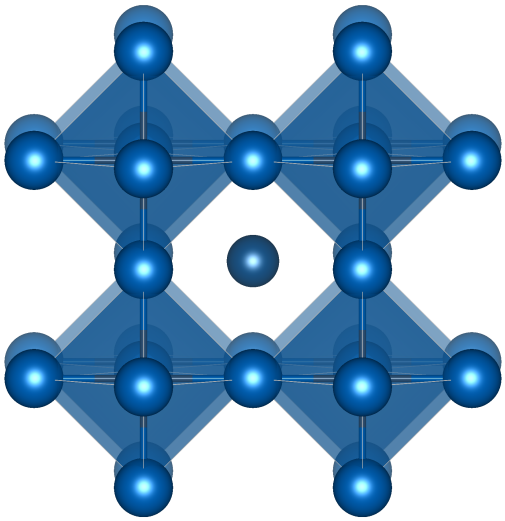

TUM School of Natural Sciences
Technische Universität München

Theory of temperature-dependent electronic structure and bulk properties of semiconductors

Stefan A. Seidl

Vollständiger Abdruck der von der TUM School of Natural Sciences der Technischen Universität München zur Erlangung des akademischen Grades eines

Doktors der Naturwissenschaften (Dr. rer. nat.)

genehmigten Dissertation.

Vorsitz:
Prof. Dr. Christian Back

Prüfer der Dissertation:
1. Prof. Dr. David Egger
2. Prof. Dr. Alessio Gagliardi

Die Dissertation wurde am 23.09.2024 bei der Technischen Universität München eingereicht und durch die TUM School of Natural Sciences am 30.10.2024 angenommen.

Abstract

Energy materials form the basis of photovoltaics (PV) and are usually common inorganic semiconductors or, more recently, also halide perovskites (HaPs). For example, these two types of materials differ in the softness of the lattice, with HaPs having a soft lattice. Characteristics such as the crystal structure and the electronic band gap must be optimized and are key for the development of PV. Therefore the structure-band-gap relationship, i.e. how dynamic-structure fluctuations impact the band gap, has to be rationalized. Specifically, the remarkable optoelectronic properties of HaPs, dominated by vibrational anharmonicity, are not yet understood to full extent. The necessity of an accurate modeling of the structural and electronic properties, also under the influence of temperature, and the understanding of it, is the task of the present work.

Density functional theory is probably the most common approach to access static and dynamic properties of energy materials using exchange-correlation functionals. For example, the calculation of the band-gap value depends strongly on the choice of the exchange energy term in a functional, be it semilocal or exact exchange. Screened hybrid functionals, which contain a mixture of both types of exchange energy, are known to accurately predict electronic structure as well as lattice dynamics. A recently developed functional, SRSH, which belongs to screened range-separated hybrid functionals, has the advantage that it describes optical and electronic properties of semiconductors accurately at the same time. However, it has not yet been clarified whether SRSH can capture the structural and vibrational properties of common inorganic semiconductors accurately. In this work, the accuracy of the SRSH functional is investigated by means of the equilibrium lattice constants and phonon dispersion relations of seven prototypical semiconductors and compared to the accuracy of commonly used exchange-correlation functionals, i.e. the semilocal and hybrid functionals. The SRSH approach demonstrates equal accuracy in the computation of bulk properties for semiconductors compared to the well-established PBE and HSE functionals. In addition, as with the HSE functional, SRSH provides phonon dispersion relations for semiconductors which are more accurate than those obtained with PBE. Therefore, the SRSH functional can be counted among those functionals which represent a uniform accurate framework for the calculation of semiconductor bulk properties.

In the second part of this work, HaPs are investigated, which typically exhibit different average structures in the individual phases, that cannot explain the electronic properties. First-principles molecular dynamics (MD) and stochastic Monte-Carlo (MC) calculations are applied to the prototypical HaP $CsPbBr_3$ to highlight the impact of dynamic-structure fluctuations on the electronic properties at finite tem-

perature. Thermal samples from MD and MC generally lead to larger band-gap values at finite temperature compared to the band-gap value calculated from the static average structure. Especially the mildly changing band gap across phase transitions, as experimentally observed, can only be revealed when the computational method accounts for anharmonic lattice dynamics, as is the case with MD. Contrary to these findings, an average crystal structure perturbed by thermal-activated harmonic phonons, as is the case in MC, leads to a large jump of 450 meV in the band gap at the phase transition of $CsPbBr_3$. Consequently, the decoupled harmonic-phonon picture, neglecting for example phonon-phonon interactions and anharmonic atomic motions, cannot explain the band-gap contributions stemming from vibrational anharmonicity, which is a key in the profound understanding of HaPs.
In summary, this work provides profound insights into the accurate modeling of structural and vibrational properties and their connection to electronic properties of bulk semiconductors. These findings can aid the future development of energy materials on the basis of computational modeling.

Zusammenfassung

Die Grundlage der Photovoltaik bilden Energiematerialien, welche in der Regel aus herkömmlichen anorganischen Halbleitern oder neuerdings auch aus Halogenid-Perowskiten (HaPs) bestehen. Diese beiden Halbleitertypen unterscheiden sich zum Beispiel in der Weichheit des Gitters, wobei HaPs ein weiches Gitter aufweisen. Charakteristische Eigenschaften wie die Kristallstruktur oder die elektronische Bandlücke spielen eine entscheidende Rolle bei der Entwicklung der Photovoltaik und müssen dafür optimiert werden. Hierbei ist ein umfassendes Verständnis wie die Gitterstruktur und vor allem die dynamischen Gitterschwankungen die elektronische Bandlücke beeinflussen unabdingbar. Besonders die herausragenden optoelektronischen Eigenschaften von HaPs stehen in Zusammenhang mit Schwingungsanharmonizität, welche noch nicht gänzlich verstanden ist. Deshalb ist eine akkurate computerbasierte Modellierung der strukturellen Eigenschaften und der elektronischen Eigenschaften, auch unter dem Einfluss der Temperatur, hilfreich und stellt die Hauptaufgabe dieser Dissertation dar.
Die Dichtefunktionaltheorie, welche Austausch-Korrelations-Funktionale verwendet, ist wahrscheinlich die gängigste Theorie um statische und dynamische Eigenschaften von Energiematerialien zu beschreiben. So hängt zum Beispiel der berechnete Wert der Bandlücke stark von der Wahl des Austauschenergieterms des Funktionals ab, welcher ein semilokaler oder ein exakter Austauschenergieterm sein kann. Speziell abschirmende Hybrid-Funktionale, die eine Mischung aus beiden Arten des Austauschenergieterm enthalten, sind dafür bekannt, dass sie sowohl die elektronische Struktur als auch die Gitterdynamik akkurat bestimmen können. Darüber hinaus hat ein kürzlich neu entwickeltes Funktional mit der Bezeichnung SRSH, welches zu den abschirmenden und bereichstrennenden Hybrid-Funktionalen gehört, den Vorteil, dass es gleichzeitig optische und elektronische Eigenschaften von Halbleitern genau beschreiben kann. Allerdings ist noch nicht geklärt, ob das SRSH Funktional auch strukturelle Eigenschaften und Schwingungseigenschaften gängiger anorganischer Halbleiter genau berechnen kann. Deshalb wird in dieser Dissertation die Genauigkeit des SRSH Funktionals anhand der Berechnung der Gitterkonstanten und der Dispersionsrelationen für Phononen von sieben prototypischen Halbleitern untersucht und mit der Genauigkeit von üblich verwendeten Funktionalen verglichen. Diese sind semilokale und hybride Austausch-Korrelations-Funktionale. Als Ergebnis liefert der SRSH-Ansatz eine ähnliche Genauigkeit bei der Berechnung der Bulk-Eigenschaften von Halbleitern wie die etablierten PBE und HSE Funktionale. Zusätzlich lässt sich sagen, dass das SRHS Funktional, wie auch das HSE Funktional, Dispersionsrelationen für Phononen von Halbleitern berechnet, die genauer sind als die, die mit Hilfe von PBE berechnet wurden. Daher bildet der SRSH-Ansatz einen

konsistenten Rahmen für die Berechnung von Bulk-Eigenschaften von Halbleitern.

Im zweiten Teil dieser Dissertation werden HaPs untersucht, die typischerweise unterschiedliche mittlere Strukturen in den einzelnen Phasen aufweisen, welche die elektronischen Eigenschaften nicht erklären können. Mit Hilfe von First-Principles Molekulardynamik (MD) und stochastischer Monte-Carlo (MC) werden Berechnungen für den prototypischen HaP $CsPbBr_3$ durchgeführt, um bei endlicher Temperatur den Einfluss von dynamischen Gitterschwankungen auf die elektronischen Eigenschaften zu untersuchen. Die von MD und MC resultierenden thermischen Samples liefern im Allgemeinen eine größere Bandlücke als die Bandlücke, welche von der statischen mittleren Struktur berechnet wurde. Die experimentell gemessene Bandlücke verändert sich nur geringfügig über die Phasenübergänge hinweg, was sich nur erklären lässt, wenn die Berechnungsmethode auch die anharmonische Gitterdynamik berücksichtigt, wie es in MD der Fall ist. Im Gegensatz zu diesem Ergebnis führt eine mittlere Kristallstruktur, welche von thermisch-aktivierten harmonischen Phononen ausgelenkt ist, wie es in MC der Fall ist, zu einem großen Sprung von 450 meV in der Bandlücke beim Phasenübergang von $CsPbBr_3$. Folglich kann ein entkoppeltes harmonisches Phononen-Modell, das beispielsweise die Phonon-Phonon-Wechselwirkung und anharmonische atomare Bewegungen vernachlässigt, nicht die Beiträge zur Bandlücke erklären, welche sich aus der Schwingungsanharmonizität ergeben. Deshalb stellt die Schwingungsanharmonizität einen fundamentalen Baustein zum tiefgreifenden Verständnis von HaPs dar.
Zusammenfassend lässt sich sagen, dass diese Dissertation fundierte Einblicke in die akkurate Modellierung von strukturellen Eigenschaften und Schwingungseigenschaften bietet und deren Zusammenhang mit den elektronischen Eigenschaften von Halbleitern erklärt. Diese Erkenntnisse können bei der künftigen Entwicklung von Energiematerialien auf Grundlage von Computermodellen hilfreich sein.

List of publications

[1] S. A. Seidl, B. Kretz, C. Gehrmann, and D. A. Egger, "Assessing the accuracy of screened range-separated hybrids for bulk properties of semiconductors", Physical Review Materials, vol. 5, p. 034602, 2021.

[2] S. A. Seidl*, X. Zhu*, G. Reuveni, S. Aharon, C. Gehrmann, S. Caicedo-Dávila, O. Yaffe, and D. A. Egger, "Anharmonic fluctuations govern the band gap of halide perovskites", Physical Review Materials, vol. 7, p. L092401, 2023. *Equal contributions

Acknowledgments

First of all, I would like to thank Prof. David A. Egger for giving me the opportunity to do research in the TheoFEM group at the Technical University of Munich and to write my dissertation including our scientific data. This research would not have been possible without David's guidance and alignment of the scientific way in the right direction. In particular, I would like to mention that I am very grateful to have had the opportunity to present our research findings at the MRS conference at the Hynes Convention Center in Boston.
Special thanks go to Dr. Bernhard Kretz, who acted as my mentor and supported me greatly in writing our paper "Assessing the accuracy of screened range-separated hybrids for bulk properties of semiconductors". Bernhard also helped me with the installation of various electronic-structure codes on supercomputers such as Juwels or Athene and with launching of various Python scripts for extracting the temperature-dependent band gap. Next, I would like to thank Dr. Christian Gehrmann for instructive discussions on Monte-Carlo or molecular dynamics calculations of the temperature-dependent band gap of $CsPbBr_3$, when we often drove back to Regensburg together by car.
Furthermore, I would like to thank Xiangzhou Zhu and Sebastián Caicedo-Dávila for their scientific contributions to our paper "Anharmonic fluctuations govern the band gap of halide perovskites". At this point, many thanks also to all our experimental collaborators Guy Reuveni, Sigalit Aharon and Omer Yaffe from the Weizmann Institute of Science in Rehovot, who shared their knowledge with us and provided experimental data of reflectance measurements for $CsPbBr_3$ single crystals, which can be seen in chapter 4.
Beyond that, I would like to thank all the members of the TheoFEM group for providing a friendly and nice social environment at the physics department. Whether it was a hike in the alps, a trip to the Schliersee or a visit to the Weizmann Institute of Science in Israel - all group activities will remain unforgettable.
Next, I would like to thank Ashwin Ramasubramaniam from the University of Massachusetts at Amherst for providing the implementation of the SRSH functional in the VASP code.
Last but not least, I would like to thank Randy Rückner for instructions on how to use the supercomputer Athene in Regensburg and Dr. Frank Braun for helping me to install the HDF5 library as well as some other computer codes locally on my laptop. Both people belong to the computer center of the University of Regensburg.
Finally, I further acknowledge the Gauss Centre for Supercomputing e.V. for funding this project by providing computing time through the John von Neumann Institute for Computing on the GCS Supercomputer JUWELS at Jülich Supercomputing Centre.

Contents

1. Introduction

Today's world population is confronted with two important facts, namely a constantly growing population and a constantly growing energy consumption per capita. Both facts lead to an increase in total energy consumption, which in principle would not be a problem if the earth's resources were infinite. As this is definitely not the case and fossil fuels in particular are running out in the long term, renewable energies are playing an increasingly important role. This is also supported by the fact that with other energy sources such as nuclear energy, there is the problem of how to store radioactive waste safely in the long term. In addition, the burning of fossil fuels such as oil, coal and gas is causing the problem of climate change, which is reflected in global warming. The latter aspect leads to an acceleration of the transition away from fossil fuels towards renewable energies [3].
In the field of renewable energies, one focus is on solar materials in connection with photovoltaics (PV). The question of whether a material is suitable to be a good solar material depends on the size of its band gap, which is characteristic for semiconductors. The basic concept of PV is to convert the energy of sunlight into electricity. As sunlight is available practically free of charge, PV is a potential technology for covering an increasing proportion of energy requirements. For this purpose, semiconductors are required for utilizing the photovoltaic effect. The device that contains semiconductors for energy conversion is called a solar cell. In general, the larger the solar cell, i.e. the larger the illuminated area, the higher the gained electricity. This correlation motivates to maximize the gained electricity while maintaining the same surface area in order to save space. An important parameter of a solar cell is its efficiency, which, in simple terms, is the ratio between the gained electricity and the radiative energy of the sunlight, or the ratio of output energy to input energy.
In principle, electricity is generated when electrons can overcome a potential barrier with the help of an excitation. The potential barrier is defined as the band gap and is the energy difference between the valence band and the conduction band or between occupied and unoccupied electronic states. The excitation is caused by electromagnetic radiation, such as sunlight, and occurs in portions of photons, i.e. energy bundles of $h\nu$. If the energy of the photon is larger than the band gap, the material can absorb the photon and an excited electron is generated. This creates an electron-hole pair as a quasi-particle, whereby the excited electron is now in the conduction band and the hole remains in the valence band. When the electron-hole pair splits, the resulting free charge carriers move to the corresponding electrodes, which are oppositely charged[1]. Consequently, electricity is generated.
In addition, the charge carrier dynamics are material-dependent and influence the

[1] In simplified terms, this is the process in a solar cell with a p-n junction.

energy conversion efficiency of the solar cell. For instance, the common inorganic semiconductor silicon (Si) achieves an efficiency of 26% in conventional crystalline solar cells [4] and recently an efficiency of 36% in silicon-based multi-junction solar cells [5]. The frequent use of Si solar cells is due to their low-cost production and the abundance of Si on earth. In contrast, the inorganic semiconductor gallium arsenide (GaAs) has a higher energy conversion efficiency as Si, but the production costs of GaAs-based solar cells are considerably higher.
In addition to the class of group III-V semiconductors, such as the composite material GaAs, or the semiconductors of group IV, such as Si, there is the class of halide perovskites (HaPs). Note that HaPs are referred to as energy materials in the new nomenclature. This relatively new class of energy materials is based on the typical perovskite structure of oxides, which was first discovered in the 19th century. However, HaPs attracted great attention in the semiconductor research during the last decade, because of their fast rising energy conversion efficiency in the development of HaP solar cells. For example, emerging PV using HaP solar cells have achieved an efficiency of 26.1% in only 10 years of research [4], making HaPs a promising material for future solar cell applications. Specifically, HaPs can occur in two variants, namely as completely inorganic semiconductors such as $CsPbBr_3$ or in a hybrid variant that also contains organic cations, e.g. an organic molecule as in $MAPbI_3$. While the halogen atom can vary, most HaPs contain lead, which is problematic for the use in solar cells due to its toxicity. Additionally, one characteristic of HaPs is short-term stability, which also has to be overcome, if HaPs should be commercially used in solar cells. Consequently, toxicity and stability continue to pose major challenges. Furthermore, HaPs exhibit structural softness, which results in low-frequency vibrations [6] in comparison to high-frequency vibrations, for example, from stiff diamond. In principle, the structural softness can be associated with HaP characteristics such as vibrational anharmonicity, unusual lattice dynamics, phase transitions, charge carrier dynamics and others.
Comparing HaPs with common inorganic semiconductors on the microscopic level reveals clear differences beyond the chemical composition. While common inorganic semiconductors exhibit a well-defined reference crystal structure, HaPs only refer to this structure as a time average, while undergoing instantaneous structures showing temporal octahedral tiltings [7, 8, 9, 10]. This phenomenon can be explained by the anharmonic atomic motions or thermal disorder characterizing HaPs [11, 12, 13] in conjunction with symmetry breaking of the potential energy surface [8, 14]. Therefore, the description of structural dynamics in the harmonic approximation, in which the potential energy of the nuclei is expanded around equilibrium up to second order in the atomic displacements, is insufficient for HaPs, while being quite successful for common inorganic semiconductors.
With respect to the most important quantity in semiconductor research, the fundamental band gap, the thermal evolution of the band gap shows a very different behavior between HaPs and common inorganic semiconductors. While for common inorganic semiconductors the "Varshni effect" predicts a decreasing band gap with increasing temperature [15], the HaP band gap increases with increasing temper-

ature [16]. Additionally, HaPs exhibit temperature-induced phase transitions that are accompanied by significant changes in the reference crystal structure [6], while the corresponding experimental band-gap only mildly changes over the relevant temperature range [17]. Note that the ambient temperature is not necessarily the temperature to which the solar material is exposed, i.e. in practice the working temperature can be some tens of degrees higher than the ambient temperature. Apart from these differences, solar cells based on HaPs [18] and common inorganic semiconductors [19] have in common that the energy conversion efficiency decreases with increasing temperature. This is due to the fact that higher temperatures lead to a lower electrical conductivity in the solar material.

One key in understanding the thermal motions of atoms is lattice dynamics or atomic vibrations. In the concept of quasi-particles, the lattice vibrations are referred to as phonons, which have quantized energies. In principle, the influence of thermal effects or temperature is basically associated with two phenomena: Electron-phonon coupling and thermal expansion of the lattice. While the electron-phonon coupling has a strong effect on the optical and electronic properties, such as a renormalization of the electronic band structure, the thermal expansion has a rather small influence. For common inorganic semiconductors, the lattice dynamics can be accurately described in the harmonic approximation, i.e. with decoupled harmonic oscillators, but for HaPs a description beyond the harmonic approximation is essential. Therefore, a valid description of HaPs has to incorporate vibrational anharmonicity or anharmonic phonons associated with octahedral tilting as a characteristic of HaP dynamics. In addition, anharmonicity also takes into account phonon-phonon coupling, which, in conjunction with large atomic displacements and structural distortions, leads to short phonon lifetimes for HaPs [20].

However, in addition to experimental research, computer simulations have also contributed significantly to the investigation of solar materials. For instance, a solid-state material can be described by a many-particle Hamilton operator, which can be solved numerically but not analytically. There are several electronic structure codes that are primarily based on plane waves and exploit the fact that crystals are characterized by their periodic structures. Consequently, the modeling of solids as perfect crystals on an atomic scale is achieved by applying a unit-cell. A very successful theory, which calculates the ground state density of a system, is the density functional theory (DFT). The fundamental equation on which DFT is based is a Schrödinger-like equation, namely the Kohn-Sham equation, which is an effective one-particle equation as used in mean-field theories. The ingenious idea in DFT is the use of exchange-correlation functionals, V_{XC}, which allows DFT to be exact if V_{XC} is exact. Specifically, V_{XC} covers all quantum-mechanical interaction as well as corrections to the kinetic energy of a non-interacting system.

The task of finding the best approximation for V_{XC} or optimizing existing functionals is an endless challenge. For example, a very simple approximation of V_{XC} is the local density approximation (LDA), which calculates the exchange-correlation-energy solely from the local charge density. More complex functionals go beyond that local character and also consider density gradients, such as PBE [21], or contain fractions

of exact-exchange, such as the hybrid functional HSE [22, 23]. However, not every functional is appropriate for every system or material. For instance, the B3LYP functional [24, 25] is suitable for molecules, but fails for metals, which can be seen by the fact that it predicts a semiconductor instead [26]. A recently developed functional, the screened range-separated hybrid (SRSH) functional, is characterized by the ability to tune its parameters. In principle, any functional containing parameters can be tuned, but the empirical tuning approach in SRSH additionally ensures that the dielectric constant of the material correctly describes the asymptotic decay of the screened exchange interaction in the long range. Furthermore, individual parameters of the SRSH functional, which determine for example the amount of exact-exchange over the distance or others, can be adjusted to accurately predict a specific quantity. Consequently, the possibility of tuning SRSH raises the question, whether tuning the functional to be accurate in one specific quantity comes at the expense of the accuracy of other quantities. It is known, for example, that electronic and optical properties of common inorganic semiconductors can be accurately described if SRSH is tuned to reproduce band gaps [27, 28]. So far, the performance of SRSH in this case has not been tested for the prediction of bulk properties of common inorganic semiconductors, such as lattice constants, bulk moduli, atomization energies and phonon dispersion relations. This task is covered in chapter 3.
Apart from the well-established use of DFT in semiconductor research, DFT provides only a static description and therefore lacks in the inclusion of thermal effects. Since solar devices are exposed to high working temperatures and thermal effects have a strong impact on the electronic band gap of energy materials, a profound understanding of thermal effects is essential. For this purpose, thermal effects can be investigated, for example, with the help of first-principles molecular dynamics (MD) simulations or stochastic Monte-Carlo (MC) calculations. Both approaches are based on DFT and determine lattice dynamics or the temperature-dependent band gap as a statistical mean value from distorted structures.
A variant of the MC method, as a stochastic sampling approach, calculates phonon-distorted structures and refers thereby to the harmonic approximation. These distorted structures or samples contain the thermal motions of the atoms. The MC method has two advantages, namely the consideration of zero-point energies and the correct prediction of the temperature-dependent trend of the band gap.
In contrast to the limitation of MC to the harmonic approximation, MD accounts for all types of structural fluctuations, i.e. both harmonic and anharmonic fluctuations. This is due to the different ansatz of MD, which solves the classical Newton's equations of motion to describe the system. Atomic forces are calculated and used to update the atomic positions at each MD time step, resulting in a trajectory that describes the atomic configuration in time. The essential advantage of MD is the inclusion of vibrational anharmonicity, which is particularly relevant for very anharmonic materials. For instance, for anharmonic HaPs, MD captures large atomic displacements as well as octahedral tiltings, both typical for HaP dynamics. This leads to an accurate prediction of the thermal evolution of the band gap, also in absolute values.

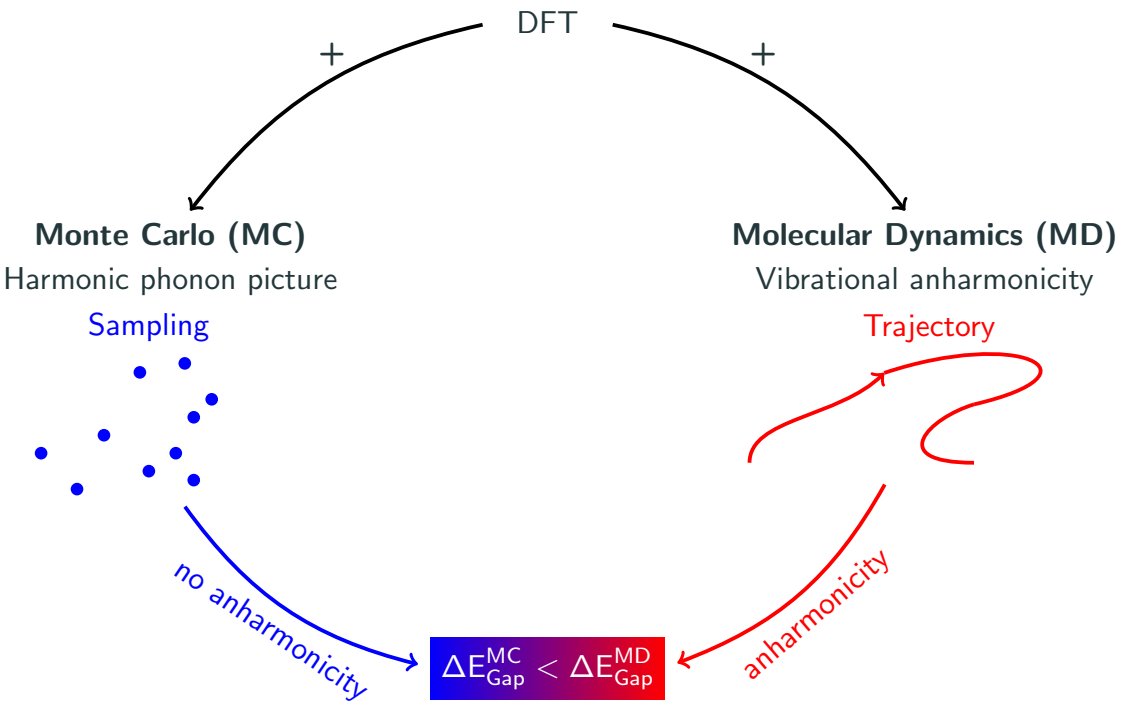

Figure 1.1. Schematic representation of the statistical approaches MC (blue) and MD (red) to illustrate the effects of different thermal motions on the electronic band gap ΔE_{Gap} for anharmonic HaPs. While the stochastic MC method provides samples of distorted structures using phonons calculated in the harmonic approximation, first-principles MD simulations solve the classical Newton's equations of motion to obtain a trajectory containing the positions of the atoms. Consequently, due to the different ansatz of the two methods, MD inherently accounts for anharmonicity, while MC excludes anharmonicity.

To quantify the contribution of vibrational anharmonicity, the equality of MD and MC is first demonstrated for a harmonic material, and then the difference between MC and MD is worked out for a prototypical anharmonic HaP. This task and a microscopic insight into anharmonic fluctuations affecting the HaP band gap are discussed in chapter 4. A schematic comparison of MD and MC with regard to the different methodology and the effect on the temperature-dependent band gap for anharmonic materials is shown in Fig. 1.1. In addition, the temperature-dependent band gap is also calculated for HaPs in chapter 4 using a perturbative method such as the Allen-Heine-Cardona (AHC) theory. This is particularly interesting when comparing the results of AHC and MC, since the AHC theory only contains terms up to the second order of perturbation theory, while MC contains all orders.

2. Theory

2.1. Electronic structure and lattice dynamics

2.1.1. Many-particle Hamilton operator

Following notation for vectors is used ($i, n \in \mathbb{N}$):

$$\begin{aligned} \mathbf{r} &= (\mathbf{r}_1, \ \dots \ , \mathbf{r}_n), \\ \mathbf{r}_i &= (x_i, y_i, z_i)^T. \end{aligned} \tag{2.1}$$

The most general form of the Hamilton operator, not taking into account relativistic effects and assuming one type of atoms, describing a solid state material can be written as following [29]:

$$\hat{H} = \hat{T}_\mathrm{e} + \hat{T}_\mathrm{n} + \hat{V}_\mathrm{e\text{-}e} + \hat{V}_\mathrm{n\text{-}n} + \hat{V}_\mathrm{e\text{-}n} \tag{2.2}$$

with e labelling the electrons and n the nuclei. The first two terms describe the kinetic energy of the electrons and nuclei, with m labelling the electron mass and M the nuclei mass. They read [29]:

$$\begin{aligned} \hat{T}_\mathrm{e} &= -\sum_{i=1}^{N_\mathrm{e}} \frac{\hbar^2}{2m} \nabla_i^2, \\ \hat{T}_\mathrm{n} &= -\sum_{j=1}^{N_\mathrm{n}} \frac{\hbar^2}{2M} \nabla_j^2. \end{aligned} \tag{2.3}$$

Here, N_e is the number of electrons and N_n the number of nuclei. The last three terms of the Hamilton operator in the general form of equation (2.2) denote the interaction between electrons, between nuclei and between electrons and nuclei. Here, $\mathbf{r}_i$ and $\mathbf{r}_j$ denote the electron positions and $\mathbf{R}_i$ and $\mathbf{R}_j$ the nuclei positions, respectively. Z_e and Z_n denote the elementary charge e and the charge of the nuclei, which is a multiple of the elementary charge e. The interaction potentials in (2.2) are described by the Coulomb interaction and can be written as [29]:

$$\begin{aligned} \hat{V}_\mathrm{e\text{-}e} &= \frac{1}{2} \sum_{i=1}^{N_\mathrm{e}} \sum_{j=1, j\neq i}^{N_\mathrm{e}} \frac{Z_\mathrm{e}^2}{|\mathbf{r}_i - \mathbf{r}_j|}, \\ \hat{V}_\mathrm{n\text{-}n} &= \frac{1}{2} \sum_{i=1}^{N_\mathrm{n}} \sum_{j=1, j\neq i}^{N_\mathrm{n}} \frac{Z_\mathrm{n}^2}{|\mathbf{R}_i - \mathbf{R}_j|}, \\ \hat{V}_\mathrm{e\text{-}n} &= \sum_{i=1}^{N_\mathrm{e}} \sum_{j=1}^{N_\mathrm{n}} \frac{Z_\mathrm{e} Z_\mathrm{n}}{|\mathbf{r}_i - \mathbf{R}_j|}. \end{aligned} \tag{2.4}$$

The dynamics of the system is given by the time-dependent Schrödinger equation and can be written with the Hamilton operator from equation (2.2) as [29]

$$i\hbar\frac{\partial}{\partial t}\Psi(\mathbf{r}_1, ..., \mathbf{r}_{N_\mathrm{e}}, \mathbf{R}_1, ..., \mathbf{R}_{N_\mathrm{n}}, t) = \hat{H}\ \Psi(\mathbf{r}_1, ..., \mathbf{r}_{N_\mathrm{e}}, \mathbf{R}_1, ..., \mathbf{R}_{N_\mathrm{n}}, t), \tag{2.5}$$

with Ψ being the many particle wave function depending on the time, t, and the positions of the electrons, $\mathbf{r}_i$, and nuclei, $\mathbf{R}_i$. If the material of interest would not be a solid crystal but a single hydrogen atom, equation (2.5) could be solved analytically by performing a coordinate transformation into centre of gravity coordinates. However, an analytical solution of equation (2.5) for a solid containing thousands of atoms is not possible. Note that solids can often be modeled as periodic crystals with few atoms in a unit-cell, so that the equation (2.5) can be solved numerically. For heavier elements than the hydrogen atom, such as the next element in the periodic table, helium, as well as for more complex systems such as crystals, the large mass difference between the nuclei and the electrons is used to decouple equation (2.5). This leads into two separate equations, one for the nuclei and one for the electrons, and is called Adiabatic or Born-Oppenheimer approximation.

2.1.2. Born-Oppenheimer approximation

The difference between electron and nucleus mass is synonymous with the fact that the movements of electrons and nuclei usually take place on different time scales. Figuratively speaking, the valence electrons stick to the movement of the ions, which consist of nuclei together with inner core electrons[1]. In the following, the total wave function Ψ, depending on the set of valence electrons and ions at positions $\mathbf{r}$ and $\mathbf{R}$ respectively, is a solution of the time-independent Schrödinger equation,

$$E\ \Psi(\mathbf{r}, \mathbf{R}) = \hat{H}\ \Psi(\mathbf{r}, \mathbf{R}). \tag{2.6}$$

In order to decouple equation (2.6), a small parameter χ is introduced, which behaves as follows [30]:

$$\chi \longrightarrow 0 \quad \text{for} \quad M \longrightarrow \infty. \tag{2.7}$$

With the help of χ, the small motions of nuclei away from their equilibrium positions $\mathbf{R}_i^0$ can be expressed as

$$\mathbf{R}_i = \mathbf{R}_i^0 + \chi\mathbf{u}_i, \tag{2.8}$$

where $\mathbf{u}_i$ denotes a displacement vector. Anticipating that the potential is quadratically expanded with respect to the small displacements, one can argue that the kinetic energies of the nuclei should be of the same order of magnitude as the potential. With that argument one can derive following relation for χ

$$\chi = \left(\frac{m}{M}\right)^{\frac{1}{4}}. \tag{2.9}$$

[1] In the following, the terms "ions" and "nuclei" are used synonymously.

Except for hydrogen and helium, the parameter χ is smaller than 0.1. This justifies an expansion of the Hamilton operator and the total wave function with respect to the small parameter χ. When expanding the wave function and truncating after first order, the total wave function Ψ is a product of $\phi(\mathbf{R})$ and $\psi(\mathbf{r}, \mathbf{R})$:

$$\Psi(\mathbf{r}, \mathbf{R}) = \phi(\mathbf{R})\psi(\mathbf{r}, \mathbf{R}). \tag{2.10}$$

Note that the wave function for the electrons $\psi(\mathbf{r}, \mathbf{R})$ depends on the nuclear coordinates $\mathbf{R}$ only as a parameter[2]. Therefore, the electrons obey the following equation

$$\left(\hat{T}_\mathrm{e} + \hat{V}_\mathrm{e\text{-}e} + \hat{V}_\mathrm{e\text{-}n}(\mathbf{R})\right)\psi_n(\mathbf{r}, \mathbf{R}) = E_n(\mathbf{R})\psi_n(\mathbf{r}, \mathbf{R}), \tag{2.11}$$

where the subscript n in $E_n(\mathbf{R})$ and $\psi_n(\mathbf{r}, \mathbf{R})$ denotes the n-th state of the electronic system. Furthermore, the $\mathbf{R}$ dependence is only present in the interaction term $\hat{V}_\mathrm{e\text{-}n}$. The wave function for the nuclei $\phi(\mathbf{R})$ follows the decoupled equation

$$\left(\hat{T}_\mathrm{n} + \hat{V}_\mathrm{n\text{-}n} + E_n(\mathbf{R})\right)\phi(\mathbf{R}) = \epsilon\phi(\mathbf{R}). \tag{2.12}$$

Note that the equation for the nuclei only depends on the electronic eigenenergies $E_n(\mathbf{R})$ of the n-th eigenstate. In principle, it is valid to refer to the ground state energy by disregarding n, since typical excited states that occur at finite temperature do not deviate greatly on the scale, which is important for the ion movement [30]. Physically, $E_n(\mathbf{R})$ can be interpreted as damping of the nuclear motion by the valence electrons. In addition, the extent of the damping effect is independent of whether the electronic system is in the ground or in an excited state, which is true for typically excited states.
This means that the Born-Oppenheimer approximation does not consider the excitation of electrons by nuclei motion or vice versa. Specifically, the approximation does not include derivatives of the electronic wave functions with respect to the nuclear displacements. To formulate this statement in the common terminology, electron-phonon coupling is not taken into account in the Born-Oppenheimer approximation. Going beyond this approximation requires the inclusion of higher order terms in the expansion with respect to the parameter χ.

[2]Normally, parameters are noted as superscript indices. For the sake of simplicity, the notation is left as it is here.

2.1.3. Formal description of electron-phonon interaction

In order to recognize the missing interaction, which is not captured by the Born-Oppenheimer approximation, it is supportive to express the Hamilton operator for a coupled electron-phonon system in second quantization [15]:

$$\begin{aligned}\hat{H} = &\sum_{\mathbf{q}\nu} \hbar\omega_{\mathbf{q}\nu}(\hat{a}^{\dagger}_{\mathbf{q}\nu}\hat{a}_{\mathbf{q}\nu} + \frac{1}{2}) \; + \; \sum_{n\mathbf{k}} \epsilon_{n\mathbf{k}}\hat{c}^{\dagger}_{n\mathbf{k}}\hat{c}_{n\mathbf{k}} \\ &+ \; N_{\mathrm{p}}^{-1/2} \sum_{\mathbf{k},\mathbf{q},m,n,\nu} g_{m,n,\nu}(\mathbf{k},\mathbf{q})\hat{c}^{\dagger}_{m\mathbf{k}+\mathbf{q}}\hat{c}_{n\mathbf{k}}(\hat{a}_{\mathbf{q}\nu} + \hat{a}^{\dagger}_{-\mathbf{q}\nu}) \\ &+ \; N_{\mathrm{p}}^{-1} \sum_{\mathbf{k},\mathbf{q},\mathbf{q}',m,n,\nu,\nu'} g^{\mathrm{DW}}_{m,n,\nu,\nu'}(\mathbf{k},\mathbf{q},\mathbf{q}')\hat{c}^{\dagger}_{m\mathbf{k}+\mathbf{q}+\mathbf{q}'}\hat{c}_{n\mathbf{k}} \\ &\quad \times (\hat{a}_{\mathbf{q}\nu} + \hat{a}^{\dagger}_{-\mathbf{q}\nu})(\hat{a}_{\mathbf{q}'\nu'} + \hat{a}^{\dagger}_{-\mathbf{q}'\nu'}).\end{aligned} \tag{2.13}$$

This form of the Hamilton operator takes into account the interaction of electrons and phonons. An explanation of the individual symbols is given in the following list:

- $\hat{c}^{\dagger}_{n\mathbf{k}}$ and $\hat{c}_{n\mathbf{k}}$: fermionic creation and anihilation operators of electrons
- n: electronic band index
- $\hat{a}^{\dagger}_{\mathbf{q}\nu}$ and $\hat{a}_{\mathbf{q}\nu}$: bosonic creation and anihilation operators of nuclei
- ν: phonon branch index
- $\omega_{\mathbf{q}\nu}$: frequency of the ν-th lattice vibration at the $\mathbf{q}$-point
- $\epsilon_{n\mathbf{k}}$: single-particle electronic eigenvalue at the $\mathbf{k}$-point
- N_{p}: number of unit-cells
- $g_{m,n,\nu}(\mathbf{k},\mathbf{q})$: matrix element including the first-order derivative of the Kohn-Sham potential (see chapter 2.2.1) with respect to the atomic displacement
- $g^{\mathrm{DW}}_{m,n,\nu,\nu'}(\mathbf{k},\mathbf{q},\mathbf{q}')$: Debye-Waller (DW) matrix element including the self-energy

The first term in the first line of equation (2.13) describes the decoupled phonon system and the second term describes the decoupled electron system. The second line determines the interaction between electrons and phonons in first-order nuclear displacements, i.e., mixed terms of the form $\hat{c}^{\dagger}_{n\mathbf{k}} \cdot \hat{c}_{n\mathbf{k}} \cdot \hat{a}_{\mathbf{q}\nu}$ appear. The last term, called Debye-Waller term, which extends over lines three and four of equation (2.13), describes the second-order electron-phonon coupling in the nuclear displacements. In particular, the Debye-Waller term, which describes the electronic self-energy, is important for the calculation of the temperature-dependent electronic band structure. Therefore, it cannot be excluded in the expansion of the nuclear displacements, i.e., the second order is necessary [31]. Note that, the matrix elements g and g^{DW} have the unit of energy and can be interpreted as a measure of the coupling strength

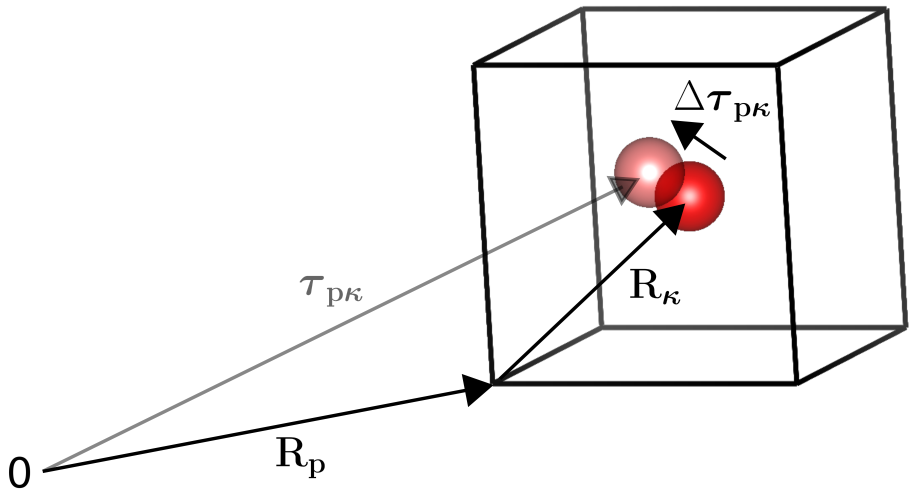

Figure 2.1. Schematic representation of a unit-cell showing the vector-notation of a nucleus exposed to lattice vibrations. In the harmonic approximation lattice vibrations are assumed to be small. The current position of the vibrating nucleus (light red) is given by the vector $\tau_{p\kappa}$, which is the sum of the small displacement vector $\Delta\tau_{p\kappa}$ and the equilibrium position $\tau^0_{p\kappa}$ of the nucleus (red). The static lattice for $\Delta\tau_{p\kappa} = 0$ is described by the vector sum $R_p + R_\kappa$, where R_p points to the p-th unit cell and R_κ points to the κ-th nucleus of the unit-cell (see equation (2.15)).

between electrons and phonons.
However, the expression of the Hamilton operator in equation (2.13) does not include terms such as the phonon self-energy. In general, this expression of the Hamilton operator must be treated with caution, as the terms describing the phonons are only valid in the harmonic (see next chapter 2.1.4) and Born-Oppenheimer approximation. Furthermore, the Hamilton operator in (2.13) is rather a model for the inclusion of the electron-phonon coupling than a helpful guide for the explicit calculation of the occurring parameters.

2.1.4. Harmonic approximation providing phonons

The harmonic approximation starts with the assumption that the electrons are in their ground state when entering the total potential energy in equation (2.12). In addition, the nuclei are located at their lattice positions like classical particles. The equilibrium position of a nucleus can be written as (see Fig. 2.1):

$$\tau^0_{p\kappa} = \mathbf{R}_p + \mathbf{R}_\kappa, \tag{2.14}$$

and the current position including lattice vibrations can be described as follows:

$$\tau_{p\kappa} = \mathbf{R}_p + \mathbf{R}_\kappa + \Delta\tau_{p\kappa}. \tag{2.15}$$

Here, $\mathbf{R}_p$ is the vector pointing to the p-th unit-cell of the crystal, $\mathbf{R}_\kappa$ is the vector pointing to the κ-th nucleus of the unit-cell at equilibrium position, and $\Delta\tau_{p\kappa}$ is a small displacement away from the equilibrium position.

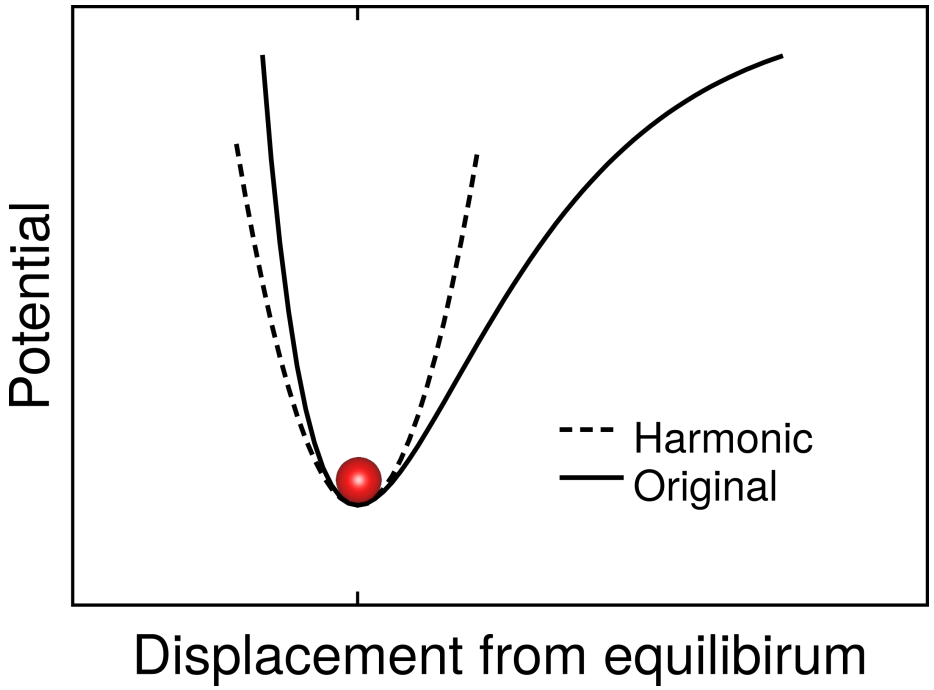

Figure 2.2. Schematic representation of the harmonic approximation, in which the real potential of the nucleus (black solid line showing an arbitrary potential shape) is replaced by a potential of parabolic form (black dashed line). The approximation is only valid for small displacements of the nucleus (red) from its equilibrium position.

To calculate dynamical properties, such as a phonon dispersion relation, from a vibrating lattice one has to start with the harmonic approximation. In this approximation, the total potential energy of the lattice is expanded up to the second-order in the nuclear displacements around their equilibrium positions. Note that the approximation is called harmonic because the real potential of the nuclei is approximated by a potential of parabolic form (see Fig. 2.2).
The first-order term of the potential vanishes because of expanding around the equilibrium position $\boldsymbol{\tau}^0_{p\kappa}$:

$$\left.\frac{\partial U}{\partial \boldsymbol{\tau}_{p\kappa}}\right|_{\boldsymbol{\tau}^0_{p\kappa}} = 0. \tag{2.16}$$

Aborting the expansion after the second-order leads to following expression [15]:

$$U = U_0 + \frac{1}{2}\sum_{p\kappa\alpha}\sum_{p'\kappa'\alpha'}\frac{\partial^2 U}{\partial\tau_{p\kappa\alpha}\partial\tau_{p'\kappa'\alpha'}}\Delta\tau_{p\kappa\alpha}\Delta\tau_{p'\kappa'\alpha'}. \tag{2.17}$$

Here, the summation over α contains the Cartesian coordinates and U_0 is the total potential energy of the nuclei in equilibrium position. The second term is a Hesse matrix, containing the second-order derivatives of the total potential energy with respect to the displacement, and is called the interatomic force constants:

$$C_{p\kappa\alpha,p'\kappa'\alpha'} = \frac{\partial^2 U}{\partial\tau_{p\kappa\alpha}\partial\tau_{p'\kappa'\alpha'}}. \tag{2.18}$$

In order to obtain the eigenvalue equation of the form $A\mathbf{v} = \lambda\mathbf{v}$ one must first perform a Fourier transformation of the interatomic force constant matrix. This leads to the Dynamical matrix:

$$D_{\kappa\alpha,\kappa'\alpha'}(\mathbf{q}) = \frac{1}{\sqrt{M_\kappa M_{\kappa'}}} \sum_{p'} C_{0\kappa\alpha,p'\kappa'\alpha'} \exp(i\mathbf{q}\cdot\mathbf{R}_{p'}). \tag{2.19}$$

With the help of the Dynamical matrix one can formulate the eigenvalue equation:

$$\sum_{\kappa'\alpha'} D_{\kappa\alpha,\kappa'\alpha'}(\mathbf{q}) e_{\kappa'\alpha',\nu}(\mathbf{q}) = \lambda e_{\kappa\alpha,\nu}(\mathbf{q}) \tag{2.20}$$

with $e_{\kappa\alpha,\nu}(\mathbf{q})$ being an eigenvector or phonon mode at a specific q-point. The eigenvalue λ can be identified as the phonon frequency squared, which is q-point dependent:

$$\sum_{\kappa'\alpha'} D_{\kappa\alpha,\kappa'\alpha'}(\mathbf{q}) e_{\kappa'\alpha',\nu}(\mathbf{q}) = \omega^2_{\mathbf{q}\nu} e_{\kappa\alpha,\nu}(\mathbf{q}). \tag{2.21}$$

Since a hermitian matrix has real eigenvalues and the Dynamical matrix is hermitian, the phonon frequencies squared have to be real:

$$\omega^2_{\mathbf{q}\nu} \in \mathbb{R}. \tag{2.22}$$

In addition, due to the Hermitian property of the Dynamical matrix, the eigenvectors $e_{\kappa\alpha,\nu}(\mathbf{q})$ are orthonormal for each $\mathbf{q}$:

$$\begin{aligned} \sum_{\nu} e^*_{\kappa'\alpha',\nu}(\mathbf{q}) e_{\kappa\alpha,\nu}(\mathbf{q}) &= \delta_{\kappa\kappa'}\delta_{\alpha\alpha'} \\ \sum_{\kappa\alpha} e^*_{\kappa\alpha,\nu}(\mathbf{q}) e_{\kappa\alpha,\nu'}(\mathbf{q}) &= \delta_{\nu\nu'} \end{aligned} \tag{2.23}$$

Using the matrix of the interatomic force constants, the Hamilton operator of the nuclei can be expressed as

$$\hat{H}_{\text{nucleus}} = -\sum_{p\kappa\alpha} \frac{\hbar^2}{2M_\kappa} \frac{\partial^2}{\partial\tau^2_{p\kappa\alpha}} + \frac{1}{2} \sum_{p\kappa\alpha} \sum_{p'\kappa'\alpha'} C_{p\kappa\alpha,p'\kappa'\alpha'} \Delta\tau_{p\kappa\alpha} \Delta\tau_{p'\kappa'\alpha'}, \tag{2.24}$$

where the constant term of the 0-th order, U_0, is neglected. Note that this expression of the Hamilton operator for the nuclei first considers the Born-Oppenheimer approximation and second the harmonic approximation. In addition, the Born-Oppenheimer approximation is used to calculate the interatomic force constants via the electronic energy, whereas any kind of excitation is skipped and only the ground state is considered.

However, the important quantities such as the phonon eigenmodes and phonon frequencies are only dependent on the q-point vector of the first Brillouin zone (BZ). For a system containing N atoms in the unit-cell, the calculation of the eigenvalue equation of the Dynamical matrix results in 3N phonon branches: 3 acoustic branches,

i.e. frequencies that go linearly to zero for q in the long-wavelength limit, and 3N-3 optical branches that, in comparison, do not disappear in the long-wavelength limit [32]. In principle, the eigenmodes of the three acoustic branches can be interpreted as the three translation modes in which the ions move together. For the eigenmodes of the 3N-3 optical branches the ions move out of phase. In the result section 3, phonon dispersion relations are calculated along a specific path through the BZ, which show acoustic as well as optical branches.

2.2. Density functional theory

Since the solution of a many-particle Hamilton operator for large periodic systems is still an unsolvable task in terms of computational effort, the problem has to be reduced to an effective one-particle equation[3]. This can be achieved by using a mean-field approach which, apart from kinetic energy, combines all types of interaction in one effective potential or field $V_{eff}(\mathbf{r})$. The effective potential $V_{eff}(\mathbf{r})$ only acts on a single particle. Therefore, an effective one-particle equation for the valence electrons can be derived

$$\left[-\frac{\hbar^2}{2m}\nabla^2 + V_{eff}(\mathbf{r}) \right] \psi(\mathbf{r}) = E\psi(\mathbf{r}), \tag{2.25}$$

which is formally a Schrödinger-like equation. Note that this equation is equivalent to the equation (2.11) including the nucleus- and electron-electron interaction, whereby the nuclei only appear as parameters according to the Born-Oppenheimer approximation.
An example of the approximation of the electron-electron interaction of a system to an effective potential or single-particle potential is the Hartree-Fock (HF) theory. The HF equation is written as [33]:

$$\left[-\frac{\hbar^2}{2m}\nabla^2 + V_n + \sum_{j=1}^{N} \int d\mathbf{r}' \frac{e^2}{|\mathbf{r}-\mathbf{r}'|} \left(|\phi_j(\mathbf{r}')|^2 - \frac{\phi_j^*(\mathbf{r}')\phi_i(\mathbf{r}')\phi_j(\mathbf{r})}{\phi_i(\mathbf{r})} \right) \right] \phi_i(\mathbf{r}) = \epsilon_i \phi_i(\mathbf{r}) \tag{2.26}$$

Here, $\phi_i(\mathbf{r})$ denotes a single particle wave function, forming a basis set, with corresponding single particle energies ϵ_i. Note that the index i runs from 1 to the number of fermions N. The external grid potential is given by V_n. In HF, a single Slater determinant of a non-interacting system is used to describe the full wave function in terms of the orthogonal $\phi_i(\mathbf{r})$.
The HF equation (2.26) is derived from a variational principle and is able to describe the initial interactive electron system by a single particle potential. Since the HF potential, the last term in brackets on the left-hand side of the equation (2.26), is itself dependent on the wave function $\phi_i(\mathbf{r})$, the HF equation can only be solved

[3] Note that methods such as the coupled-cluster method, many-body perturbation theory or the GW approximation can solve a Hamilton operator for small molecules and even small periodic systems.

iteratively. The first term of the HF potential, the so-called Hartree term, takes into account the classical Coulomb repulsion, while the second term takes into account the quantum mechanical exchange and is referred to as the Fock term V_{Fock}. Note that the Fock term is non-local due to the $\mathbf{r}$ and $\mathbf{r}'$ dependence of ϕ occurring in the Fock term. However, the disadvantage of the HF theory is that the calculated energy would never be exact even in the case of a not-truncated, i.e. infinite, basis set of ϕ's. This results from the fact that the exact electron correlation, i.e. the exact electron-electron interaction, cannot be described by the HF potential.
A very powerful method that has been successfully developed in recent decades and follows the mean-field approach is the so-called density functional theory (DFT). In principle, DFT is an extension of the HF theory in order to achieve a more precise description of the effective one-particle potential. This results in a more accurate calculation of the total or ground state energy. On the one hand, the Hartree term V_{Hartree} remains the same in DFT as in HF. On the other hand, the Fock term in the HF theory is replaced in DFT by an exchange-correlation term V_{XC}. Note that V_{XC} or later E_{XC} in the Kohn-Sham approach is mathematically a functional that depends on the electron density n. In particular, V_{XC} accounts for all quantum mechanical interaction. Furthermore, V_{XC} contains also interaction contributions to the kinetic energy, since the expression for the kinetic energy in equation (2.26) is the expression for a non-interacting system.

2.2.1. Kohn-Sham equation

The origin of DFT is based on two important theorems by Pierre Hohenberg and Walter Kohn. The first theorem is as follows[4]:

Hohenberg-Kohn Theorem (HK1):
On the one hand, the external potential V_{ext} is determined as a unique functional, apart from a constant, by the electron density $n(\mathbf{r})$. On the other hand, V_{ext} determines the Hamilton operator $\hat{H}$, which provides the wave function of the ground state. Consequently, the ground-state wave function $\psi_0(\mathbf{r})$ is a unique functional of the ground state density $n_0(\mathbf{r})$ via $\hat{H}$ [34].

The first Hohenberg-Kohn theorem is illustrated in Fig. 2.3. If the ground state electron density $n_0(\mathbf{r})$ is known, the external potential V_{ext} is uniquely determined by it. With the help of the Kohn-Sham equation (see equation below (2.31)), the ground state wave function can be calculated.
The second theorem is as follows:

[4]The original quotation, which contains the first theorem, reads "Thus v(r) is (to within a constant) a unique functional of n(r); since, in turn, v(r) fixes H we see that the full many-particle ground state is a unique functional of n(r)" [34].

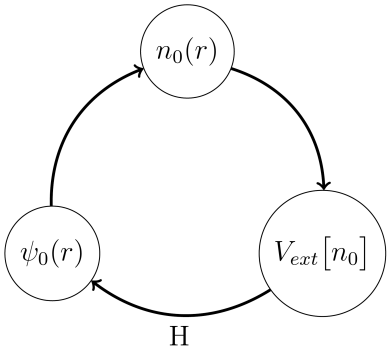

Figure 2.3. Illustration of the first Hohenberg-Kohn theorem, which states that the ground state electron density $n_0(\mathbf{r})$ uniquely determines the external potential V_{ext}. Note that V_{ext} is a functional of the $n_0(\mathbf{r})$. The Kohn-Sham Hamilton operator in turn depends on the external potential V_{ext} and provides the ground state wave function as a solution. The electron density $n_0(\mathbf{r})$ itself is given by the product of the ground state wave function (see equation (2.27)).

Hohenberg-Kohn Theorem (HK2):
The functional that provides the true ground state energy of the system only provides the lowest energy if the input density is the true ground state density [34]. This means that the ground state density of the non-interacting system corresponds to the true ground state density.

Note that the second theorem is directly related to the variation principle. The two theorems HK1 and HK2 form the basis for the derivation of DFT.
The idea of Hohenberg and Kohn was to combine the dependence of the ground state density n_0 on the ground state wave function ψ_0 and the dependence of the ground state energy E_0 on the ground state wave function ψ_0 in order to derive a dependence of the ground state energy E_0 on the ground state density n_0:

$$\left.\begin{array}{ll} n_0(\mathbf{r}) & = n_0[\psi_0] \\ E_0 & = E_0[\psi_0] \end{array}\right\} \quad E_0 = E_0[n_0(\mathbf{r})].$$

This combination has the advantage that the knowledge of all 3N spatial coordinates of the electrons, which enter the wave function $\psi_i(\mathbf{r}_1, ..., \mathbf{r}_N)$, can be replaced by only the knowledge of the spatial coordinates of the charge density $n(\mathbf{r})$. In general, the charge density is a scalar function and has following form:

$$n(\mathbf{r}) = \sum_{i=1}^{N} |\psi_i(\mathbf{r})|^2, \tag{2.27}$$

where $\psi_i(\mathbf{r})$ is the many-body wave function of a non-interacting system, which is exactly described by one Slater determinant. The next step in the derivation of DFT is to formulate the energy density functional

$$E[n(\mathbf{r})] = T[n(\mathbf{r})] + V_n[n(\mathbf{r})] + E_{\text{Hartree}}[n(\mathbf{r})] + E_{\text{XC}}[n(\mathbf{r})], \tag{2.28}$$

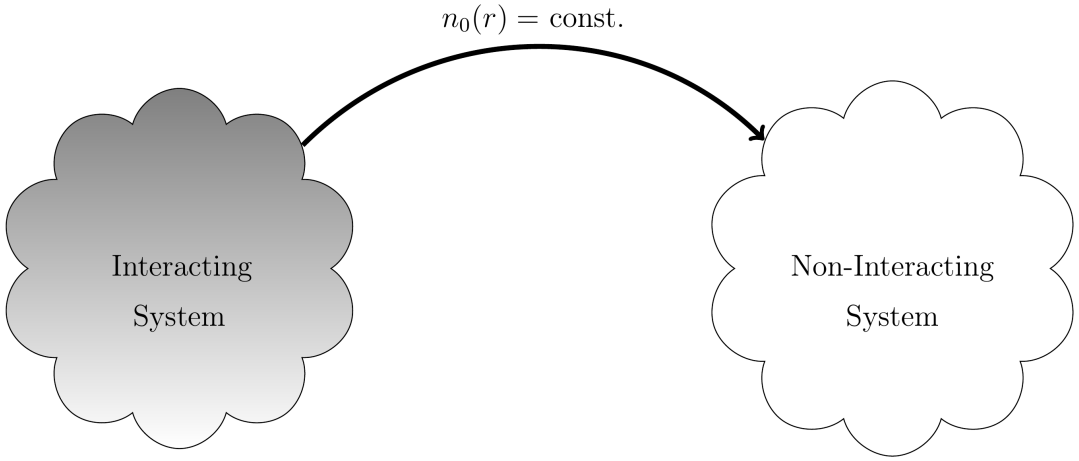

Figure 2.4. Illustration of the Kohn-Sham mapping [35], which states the mapping from an interacting to a non-interacting system by keeping the ground state density constant.

which consists of functionals of the kinetic energy T, the grid potential V_n, the classical electron-electron interaction E_{Hartree} (E_{H}) and the exchange-correlation energy E_{XC}. Note that each single term is a functional of the density. The exchange-correlation energy E_{XC} will be explained in more detail in the next section 2.2.2. The expressions for E_{H} as well as for V_n are already known from the HF theory. In order to obtain an expression for the kinetic energy functional, which is in principle an expression of an interacting system, the expression for the kinetic energy of a non-interacting system is used. This approach leads to the necessity of the Kohn-Sham mapping [35], which is illustrated in Fig. 2.4.
The Kohn-Sham mapping aims to map the interacting system onto a non-interacting system by keeping the ground state charge density constant. It follows that the same expression can be used for the kinetic energy of a non-interacting system as for the kinetic energy of an interacting system:

$$T[n_{0,\text{interacting}}(\mathbf{r})] = T[n_{0,\text{non-interacting}}(\mathbf{r})]. \tag{2.29}$$

In Kohn-Sham DFT, the interaction contributions of the kinetic energy, which also originate from the electron-electron interaction, are not included in the energy functional $T[n_0(\mathbf{r})]$, but in the exchange-correlation functional E_{XC} [29].
Consequently, DFT is a formally exact theory. However, the exact exchange-correlation is not known. Based on the Kohn-Sham mapping, the total wave function can be described with a single Slater determinant as for a non-interacting system. Note that, in comparison, the HF theory approximates a linear combination of Slater determinants for a interacting system by only one Slater determinant.
Since the specific form of E_{XC} is unknown, the challenge in DFT is to construct an accurate description of E_{XC}. Next, E_{XC} is divided into the exchange energy E_{X} and the correlation energy E_{C}. The former, the exchange, which contains all quantum-mechanical interactions as well as corrections to the kinetic energy, is dominated by the Pauli principle. The latter, the correlation is primarily caused by the interaction

of non-local charge densities. For example, two atoms, i and j, are correlated by a charge density that is described by a function $f(\mathbf{r}_i, \mathbf{r}_j)$. Often, the correlation functional is approximated by the GGA correlation (see chapter 2.2.3), which does not take non-local correlation into account. Note that there are also functionals, which consider non-local correlation, such as functionals including Van der Waals interaction.
From the Hohenberg-Kohn theorems and the Kohn-Sham mapping one can derive the Kohn-Sham equation by varying the energy density functional $E[n(\mathbf{r})]$ in equation (2.28). The variation principle is applied for the corresponding one-particle wave function ψ_i to be optimised and using the normalisation of the wave function:

$$\delta_{\psi_i^*}\left\{E[n(\mathbf{r})] - \sum_{j=1}^{N}\epsilon_j\left(\int d^3r|\psi_j(\mathbf{r})|^2 - 1\right)\right\} = 0. \tag{2.30}$$

Applying the variational principle provides the Kohn-Sham equation, which is the fundamental equation of DFT:

$$\left[-\frac{\hbar^2}{2m}\nabla^2 + V_n(\mathbf{r}) + e^2\int d^3r\frac{n(\mathbf{r}')}{|\mathbf{r}-\mathbf{r}'|} + \frac{\delta E_{\mathrm{XC}}\left[n(\mathbf{r})\right]}{\delta n(\mathbf{r})}\right]\psi_i(\mathbf{r}) = \epsilon_i\psi_i(\mathbf{r}). \tag{2.31}$$

Since the solution of the wave function is determined by the density-dependent potential and the density in turn depends on the wave function, the Kohn-Sham equation must be solved self-consistently.
The algorithm for the iterative solution of the Kohn-Sham equation is shown in Fig. 2.5. First, the use of a pseudo-potential replaces the functional of the grid potential V_n, which covers all ions including the inner core electrons. The pseudo-potential approach, which is explained in more detail in chapter 2.2.6, does not replace the valence electrons. To determine an initial or input charge density, the input wave function is given as a trial superposition of atomic orbitals. Next, the functionals E_{H} and E_{XC} are calculated with the help of the initial charge density. All three functionals form V_{eff} and the Kohn-Sham equation can be solved for the first time. The solution, i.e. the new wave functions, are in turn used to calculate the new charge density or output charge density.
If the energy difference resulting from the energies calculated with the input and output charge density is below a specific energy convergence threshold, the ground state density is found. As soon as the ground state density and thus also the ground state energy is found, post-processing can begin.
However, if the energy difference resulting from the corresponding input and output charge densities is larger than the convergence threshold, the iteration process must be restarted. For this purpose, the output charge density is mixed with the input charge density in specific fractions and the algorithm is restarted with the calculation of the potentials. In principle, the iteration procedure must be continued by mixing the old and new densities until they are equal, i.e. $n_{\mathrm{in}} = n_{\mathrm{out}}$, or at least below a

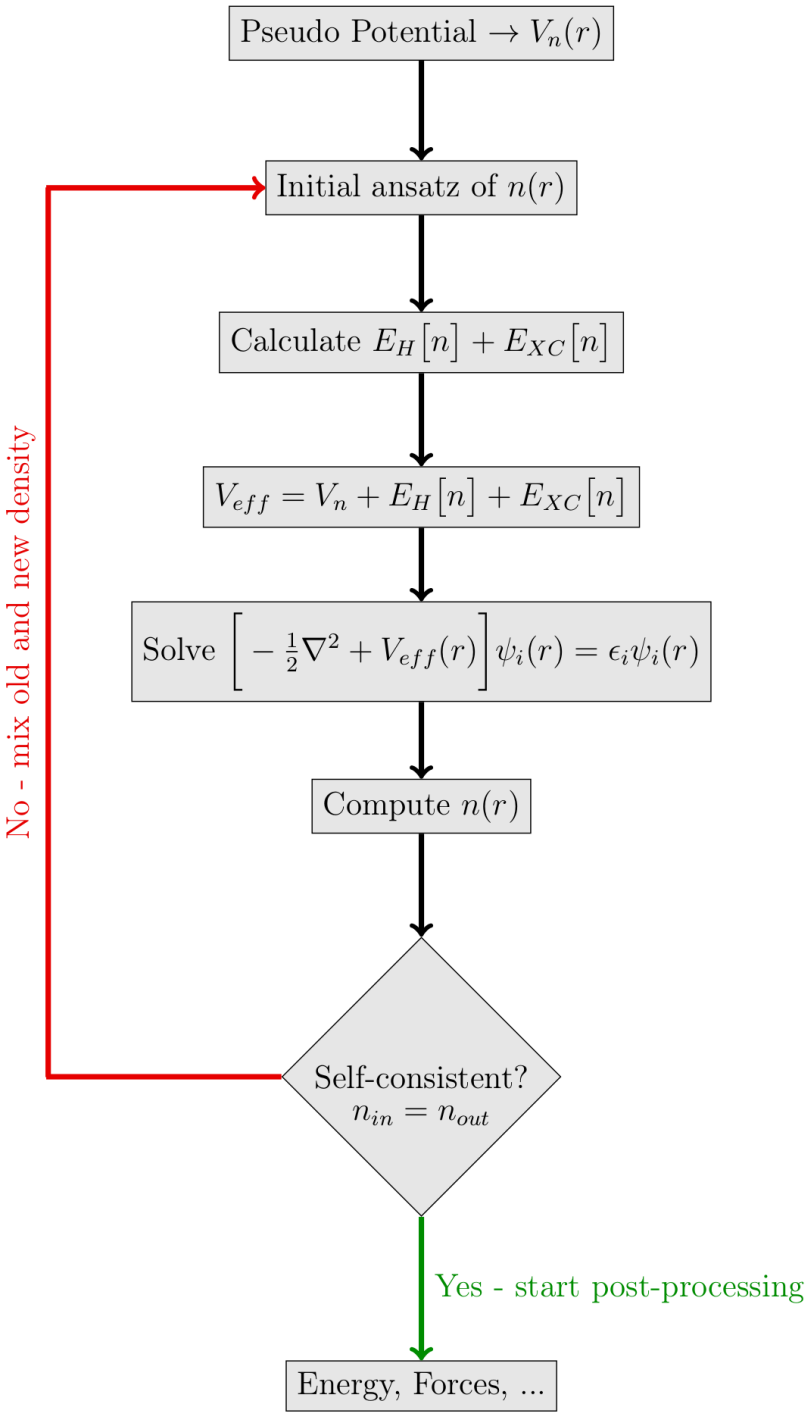

Figure 2.5. Illustration of the DFT algorithm for the self-consistent calculation of the ground state density of a system by updating V_{eff}.

threshold value, i.e. $n_{\text{out}} - n_{\text{in}} \leq \delta$ [5]. As soon as the last iteration step is completed, self-consistency is achieved.
The energy solutions $\epsilon_i(\mathbf{k})$ of the Kohn-Sham equation (2.31) are interpreted as eigenenergies that are k-point-dependent on k-points of the 1st BZ, if the system is periodic. The set of eigenenergies along a specific path through the BZ refers to the electronic band structure interpretation of DFT eigenvalues. The Fermi level can be understood as the boundary energy that distinguishes occupied from unoccupied electronic states. For 0 K, the occupation of the electronic states is a sharp step function. The eigenenergy belonging to the highest occupied band with the highest value is referred to as the valence band maximum (VBM). Accordingly, the eigenenergy belonging to the lowest unoccupied band with the lowest energy value is referred to as the conduction band minimum (CBM). In DFT, the electronic band gap or Kohn-Sham gap is defined as the difference between the VBM and CBM. The exact electronic band gap is the fundamental band gap, which coincides with the Kohn-Sham gap by adding the derivative discontinuity (DD) [37]:

$$E_{\text{Fundamental Gap}} = E_{\text{Kohn-Sham Gap}} + \text{DD}. \tag{2.32}$$

Basically, the DD is a kink in the shape of the exchange-correlation energy when the electron number changes [37]. Note that adding or removing of an electron from the system causes an integer change in the total number of electrons. In principle, the DD can be traced back to the fact that the chemical potential is discontinuous when the number of electrons is changed, which means that the energy for adding or removing an electron is not the same [38]. In contrast to E_{XC}, V_n and E_{H} do not exhibit a DD.
However, solving the Kohn-Sham equation provides the wave function ψ_i and energies ϵ_i, which are only fictitious quantities of a fictitious system. In the usual nomenclature, these quantities approximated by Kohn-Sham DFT are often referred to the fundamental band gap and real wave function. The question of the accuracy of the Kohn-Sham approximation leads to the DFT band gap problem, which means that the band gap is drastically underestimated by conventional DFT. On the one hand, band gaps calculated with standard DFT functionals such as the LDA or PBE functionals suffer greatly from the underestimation of the band gap. On the other hand, band gaps from HF are greatly overestimated. Thus it is therefore somewhat intuitive to start mixing HF theory into DFT. This leads to the class of so-called hybrid functionals that also contain a fraction of the Fock exchange in addition to the PBE exchange.
Note that the Kohn-Sham equation 2.31 is the basis of Kohn-Sham DFT, in which the E_{XC} functional is only dependent on a local or semilocal density. The extension of Kohn-Sham DFT is the generalized Kohn-Sham formalism [39], which involves non-local functionals that are explicitly orbital-dependent, such as the Fock exchange.

[5] The question of how close the two electron densities, n_{in} and n_{out}, must be to each other for them to be considered identical is answered in chapter "7.4 Achieving self-consistency" of [36]. In principle, one could only use n_{out} as new input density, but mixing n_{out} with n_{in} usually leads to improved convergence behavior, i.e. fewer iteration steps are required.

However, the development of exchange-correlation functionals is an ongoing task, as described next.

2.2.2. Exchange-correlation functionals

In general the analytical form of the exchange-correlation functional E_{XC} is unknown. In principle, DFT would be exact if E_{XC} includes all quantum mechanical interaction as well as corrections to the kinetic energy of a non-interacting system, which are not covered by the terms V_{n}, E_{H} and T of the Kohn-Sham equation (2.31).

One first attempt to find an explicit expression for E_{XC} is the local density approximation (LDA) [40]. In this approximation, the density is approximated by a function that only has a local dependency, i.e., is only dependent on $\mathbf{r}$. Here, only an expression for the exchange energy E_{X} can be derived exactly without taking the spin into account. The relation between the exchange functional and the exchange energy $\epsilon_{\mathrm{X}}^{\mathrm{unif}}$, where $\epsilon_{\mathrm{X}}^{\mathrm{unif}}$ is the exchange energy per electron of a homogeneous or uniform electron gas with the density $n(\mathbf{r})$, is as follows [33]:

$$E_{\mathrm{X}}^{\mathrm{LDA}}[n(\mathbf{r})] = \int d^3r\ \epsilon_{\mathrm{X}}^{\mathrm{unif}}(n(\mathbf{r}))n(\mathbf{r}). \tag{2.33}$$

For the ground state charge density the following relation holds:

$$n = \frac{N}{V} = \frac{k_{\mathrm{F}}^3}{3\pi^2} \tag{2.34}$$

with the volume V, the number of electrons N and the Fermi wave vector k_{F}. From the homogeneous electron gas as in the Hartree-Fock approximation it is known:

$$E_{\mathrm{X}} = -\frac{3e^2}{4\pi}Nk_{\mathrm{F}} = -\frac{3e^2}{4\pi}N(3\pi^2 n)^{\frac{1}{3}}. \tag{2.35}$$

For the exchange energy per electron $\epsilon_{\mathrm{X}}^{\mathrm{unif}}$ the following relation holds:

$$\epsilon_{\mathrm{X}}^{\mathrm{unif}} = \frac{E_{\mathrm{X}}}{N} = -\frac{3e^2}{4\pi}(3\pi^2 n)^{\frac{1}{3}}. \tag{2.36}$$

Inserting this expression into (2.33), provides the following expression for the LDA exchange energy

$$E_{\mathrm{X}}^{\mathrm{LDA}}[n(\mathbf{r})] = -\frac{3e^2}{4\pi}(3\pi^2)^{\frac{1}{3}}\int d^3r\ n(\mathbf{r})^{\frac{4}{3}}. \tag{2.37}$$

Taking the variation of the LDA exchange energy with respect to the density $n(\mathbf{r})$ results in the following expression:

$$\frac{\delta E_{\mathrm{X}}^{\mathrm{LDA}}[n(\mathbf{r})]}{\delta n(\mathbf{r})} = -2e^2\left(\frac{3}{8\pi}n(\mathbf{r})\right)^{\frac{1}{3}}. \tag{2.38}$$

Note that this expression is only the LDA exchange energy resulting from a charge density, which is approximated by the charge density of the homogeneous electron gas. In addition, no expression for the correlation energy is given here. In order to derive an expression for the correlation energy, it is not possible to refer to the HF theory, which does not contain any correlation by default.
However, the performance of DFT with LDA leads to an underestimation of the electronic band gap [41]. Since LDA only calculates a locally dependent charge density $n(\mathbf{r})$, which only depends on the position $\mathbf{r}$, the calculation is also less computationally demanding than for other functionals, such as hybrid functionals. To circumvent the limitation of LDA by using the density of the homogeneous electron gas, one must in principle overcome the locality of the LDA approximation. In other words, the functional must take into account the inhomogeneity of the charge density of a real system.

2.2.3. GGA functional - PBE

An extension of the LDA functional, which only acts locally, is the addition of the charge density gradient. This type of exchange-correlation functionals belong to the class of generalized gradient approximation (GGA) functionals. By including the charge density gradient ∇n, the inhomogeneity of the charge density is taken into account. GGA functionals are also referred to as semilocal functionals. The general form of the exchange-correlation functional including the gradient and the electron spin is [42]

$$E_{\mathrm{XC}}^{\mathrm{GGA}}[n_\uparrow(\mathbf{r}), n_\downarrow(\mathbf{r})] = \int d^3r \; f(n_\uparrow(\mathbf{r}), n_\downarrow(\mathbf{r}), \nabla n_\uparrow(\mathbf{r}), \nabla n_\downarrow(\mathbf{r})) \tag{2.39}$$

with the combined charge density

$$n = n_\uparrow + n_\downarrow. \tag{2.40}$$

Note that there is some flexibility in generating a GGA functional. The function f can be constructed to obey specific constraints on the exact functional, or by fitting it to reproduce experimental results (empiric functionals). A discussion on the construction of f, or of XC-functionals in general, is beyond the scope of this thesis.
One specific derivation of a GGA functional, in which the parameters enter as universal constants, is the so-called PBE functional [21]. In principle, the function f in the case of PBE is constructed in such a way that it fulfils all energetically relevant constraints of the exact functional. Due to their additive nature, the exchange and correlation functional can be derived independently:

$$E_{\mathrm{XC}}^{\mathrm{GGA}}[n] = E_{\mathrm{X}}^{\mathrm{GGA}}[n] + E_{\mathrm{C}}^{\mathrm{GGA}}[n]. \tag{2.41}$$

The exchange functional is given as [21]:

$$E_{\mathrm{X}}^{\mathrm{GGA}}[n] = \int dr^3 \epsilon_{\mathrm{X}}^{\mathrm{unif}}(n(\mathbf{r}))n(\mathbf{r})F_{\mathrm{X}}(s) \tag{2.42}$$

with $\epsilon_{\mathrm{X}}^{\mathrm{unif}}$ being the homogeneous electron gas for the exchange energy per particle as in the derivation of LDA

$$\epsilon_{\mathrm{X}}^{\mathrm{unif}}(n) = -\frac{3e^2}{4\pi} k_{\mathrm{F}}(n) \tag{2.43}$$

and with the Fermi wavevector k_{F}

$$k_{\mathrm{F}}(n) = (3\pi^2 n)^{\frac{1}{3}}. \tag{2.44}$$

Furthermore, F_{X} is the spin-polarized enhancement factor, which is dependent on the dimensionless density gradient s

$$s(n) = \frac{1}{2k_{\mathrm{F}}(n)} \frac{|\nabla n|}{n}. \tag{2.45}$$

A specific form for F_{X}, in where the parameter κ and μ are included as universal constants, is

$$F_{\mathrm{X}}(s) = 1 + \kappa - \frac{\kappa}{1 + \frac{\mu s^2}{\kappa}} \tag{2.46}$$

with

$$\kappa = 0.804 \quad \text{and} \quad \mu = 0.21951. \tag{2.47}$$

Note that the difference in the exchange functional for GGA in equation (2.42) and for LDA in equation (2.33) is the gradient-dependent enhancement factor F_{X}.
The correlation functional is given by [21]:

$$E_{\mathrm{C}}^{\mathrm{GGA}}[n_\uparrow, n_\downarrow] = \int dr^3 n(\mathbf{r}) [\epsilon_{\mathrm{C}}^{\mathrm{unif}}(r_{\mathrm{s}}, \xi) + H(r_{\mathrm{s}}, \xi, t)] \tag{2.48}$$

where r_{s} is the local Seitz radius determined by

$$n = \frac{3}{4\pi r_{\mathrm{s}}^3} = \frac{k_{\mathrm{F}}^3}{3\pi^2}, \tag{2.49}$$

with ξ being the relative spin polarization

$$\xi = \frac{n_\uparrow - n_\downarrow}{n} \tag{2.50}$$

and t being the dimensionless density gradient in the case for the correlation

$$t = \frac{1}{2\phi k_s} \frac{|\nabla n|}{n}. \tag{2.51}$$

Here, the dimensionless density gradient t consists of the function ϕ, which is a spin-scaling factor

$$\phi(\xi) = \frac{[(1+\xi)^{\frac{2}{3}} + (1-\xi)^{\frac{2}{3}}]}{2}, \tag{2.52}$$

and the Thomas-Fermi screening wave number k_s

$$k_s = \sqrt{\frac{4k_F}{\pi a_0}}, \tag{2.53}$$

which includes the Bohr radius a_o

$$a_0 = \frac{\hbar^2}{me^2}. \tag{2.54}$$

The function H in (2.48) takes the gradient contribution into account and is structured in such a way that it fulfils *three specific conditions* that are beyond the scope of this thesis. H is given by

$$H = \left(\frac{e^2}{a_0}\right)\gamma\phi^3 \ln\left(1 + \frac{\beta}{\gamma}t^2\left(\frac{1 + At^2}{1 + At^2 + A^2t^4}\right)\right) \tag{2.55}$$

with A being

$$A = \frac{\beta}{\gamma}\left(\exp\left(-\epsilon_C^{\text{unif}}/(\gamma\phi^3 e^2/a_0)\right) - 1\right)^{-1} \tag{2.56}$$

and the parameter β and γ are included as universal constant with following values

$$\beta = 0.066725 \quad \text{and} \quad \gamma = 0.031091. \tag{2.57}$$

An advantageous property of the PBE functional is that it corresponds to the general form of a GGA functional, which can be retraced for some limiting cases of parameters. This allows, for example, PBE to go over to the local spin density approximation (LSD) or LSD functional for certain limiting cases.
Note that PBE does not include Van der Waals (VdW) interaction, which means it does not correctly describe long-range dispersion interaction. Furthermore, when testing the accuracy of PBE, DFT-PBE provides slightly more accurate band gaps than LDA [21, 43]. However, there are two more important points that serve for a generally good understanding of functionals. Firstly, the PBE correlation energy is only local, and this also applies to the hybrid functionals that are based on the PBE correlation energy. Secondly, PBE is a non-empirical functional.

2.2.4. Hybrid functional - HSE

Due to the fact that DFT-PBE leads to an underestimation and HF to an overestimation of the electronic band gap, it is intuitive to consider both theories in one functional. Mixing a fraction of Fock exchange or exact-exchange (EXX)[6] into an exchange-correlation functional forms the class of hybrid functionals. One simple example of a hybrid functional is the PBE0 functional [44], which is formed by mixing a

[6]Note that Fock exchange and exact-exchange are used synonymously.

constant fraction of 1/4 Fock exchange with the complementary fraction of 3/4 PBE exchange for the full exchange energy:

$$E_{\mathrm{X}}^{\mathrm{PBE0}} = \frac{1}{4}E_{\mathrm{X}}^{\mathrm{EXX}} + \frac{3}{4}E_{\mathrm{X}}^{\mathrm{PBE}}. \tag{2.58}$$

The correlation energy in PBE0 is not divided into different energy terms and consists only of the PBE correlation energy:

$$E_{\mathrm{XC}}^{\mathrm{PBE0}} = \frac{1}{4}E_{\mathrm{X}}^{\mathrm{EXX}} + \frac{3}{4}E_{\mathrm{X}}^{\mathrm{PBE}} + E_{\mathrm{C}}^{\mathrm{PBE}}. \tag{2.59}$$

Results from the literature show that electronic band gaps of common inorganic semiconductors calculated with the global hybrid functional PBE0 are overestimated [45]. As a hypothesis, it should be mentioned here, that the constant amount of Fock exchange in the long-range region of the so-called unscreened hybrid functional PBE0 could be responsible for the overestimation of the band gap. Note that the calculation of the full Fock exchange is computationally demanding.
In order to get rid of the Fock exchange in the long-range region, the class of screened hybrid functionals is introduced. The idea is to split the Coulomb potential into a short-range (SR) and a long-range (LR) region by using the error function (erf) [46, 47]. This results in the following identity:

$$\frac{1}{r} = \underbrace{\frac{1-\mathrm{erf}(\omega r)}{r}}_{\mathrm{SR}} + \underbrace{\frac{\mathrm{erf}(\omega r)}{r}}_{\mathrm{LR}}. \tag{2.60}$$

The parameter ω determines the division of SR and LR. Therefore ω is called the range-separation or screening parameter[7] and has the unit of the reciprocal length, e.g. Bohr^{-1} or $\mathrm{Å}^{-1}$. In the next step, each region will be treated with different amounts of the various exchange energies. The fraction of Fock exchange in the SR region is determined by the unitless parameter a, while the Fock exchange is not present in the LR region. This leads to following expression for the screened hybrid functional HSE that replaces the slowly decaying LR part of the Fock exchange with GGA exchange only:

$$E_{\mathrm{XC}}^{\mathrm{HSE}} = aE_{\mathrm{X}}^{\mathrm{EXX,SR}} + (1-a)E_{\mathrm{X}}^{\mathrm{PBE,SR}} + E_{\mathrm{X}}^{\mathrm{PBE,LR}} + E_{\mathrm{C}}^{\mathrm{PBE}}. \tag{2.61}$$

Note that the correlation energy is not screened and, as in the case of PBE0, contains only the PBE correlation energy. The specific parameters for the HSE functional are: $a = 0.25$ for the fraction of Fock exchange and $\omega = 0.2\,\mathrm{Å}^{-1}$ for the screening parameter [22, 23]. These parameters are chosen so that the electronic band gaps of standard semiconductors can be determined very accurately. The accuracy of the band gaps calculated with HSE has an average absolute error of $\sim 0.2\,\mathrm{eV}$ compared to band gaps from experiments [48]. Thus the assumption that mixing Fock exchange

[7] In connection with HSE, ω is often referred to as the screening parameter, while ω is referred to as the range-separation parameter in connection with SRSH.

and GGA exchange in one functional, as in the case of HSE, provides more accurate electronic band gaps compared to DFT-PBE or HF is indeed true [23, 49]. Note that the gained accuracy in band gaps calculated with HSE, requires more computational effort compared to the use of PBE, because of the non-locality in the Fock exchange.

However, on the one hand HSE is based on fixed parameters a and ω to precisely describe electronic properties, which means that HSE is non-empirical. On the other hand, the question arises whether these fixed parameters in screened hybrids provide accurate values for all properties of semiconducting systems [50].

2.2.5. Screened hybrid functional - SRSH

In order to describe the asymptotic decay correctly, since in an interacting electron system the electron density decays asymptotically, a fraction of the Fock exchange must be present in the LR region in comparison to the HSE functional [51]. The idea is as in conventional screened hybrid functionals to keep the mixing of Fock and semilocal exchange along the electron distance of the system, but with tunable fractions [52]. This can be achieved by a range-separation parameter, which is no longer a universal constant and is calculated from first principles for every system. Thereby, the calculation of the parameter obeys the ionization potential theorem, which states for the exact functional the assignment of the KS-VBM and KS-CBM to the opposite of the ionization potential and electron affinity, respectively [51]. This leads to the class of screened range-separated hybrid functionals (SRSH)[8] based on the generalized Kohn-Sham theory [51, 53, 52].
As in the case for conventional screened hybrid functionals, SRSH uses the splitting of the Coulomb potential into a SR and LR region with the help of the range-separation parameter. To control the amount of Fock exchange in the LR region, a tuning parameter β is introduced. The parameter β works in two ways: the fraction that β subtracts from the Fock exchange is added to the GGA exchange, and vice versa in principle. Note that β in [1] only has negative values and therefore subtracts from the Fock exchange. The Coulomb potential is split into the following form using the error function

$$\frac{1}{r} = \frac{\alpha + \beta\,\mathrm{erf}(\gamma r)}{r} + \frac{1 - [\alpha + \beta\,\mathrm{erf}(\gamma r)]}{r}. \tag{2.62}$$

Here, the Fock exchange is assigned to the first and the GGA exchange to the last term of the right-hand side. Table 2.1 shows an overview and description of the three SRSH parameters α, β and γ.
To easily recognize the effect of the tuning parameter β the split Coulomb potential can be rewritten as follows

$$\frac{1}{r} = \underbrace{\frac{\alpha + \beta\,\mathrm{erf}(\gamma r)}{r}}_{\text{EXX}} + \underbrace{\frac{(1-\alpha) - \beta\,\mathrm{erf}(\gamma r)}{r}}_{\text{GGA}}. \tag{2.63}$$

[8] In addition to the term SRSH for screened range-separated hybrid functionals, the term optimally tuned range-separated hybrid functionals (OTRSH) is also frequently used.

Table 2.1. List and description of the SRSH parameters. Note that α and β are unitless, whereas γ has the unit of $Å^{-1}$.

Parameter	Description
α	amount of exact-exchange
β	tuning parameter
γ	range-separation (screening) parameter

Using the split Coulomb potential, the SRSH functional including exchange and unscreened correlation energy can be written as follows

$$\begin{aligned} E_{\mathrm{XC}}^{\mathrm{SRSH}} = \alpha E_{\mathrm{X}}^{\mathrm{EXX,SR}} + (1-\alpha) E_{\mathrm{X}}^{\mathrm{GGA,SR}} \\ + (\alpha+\beta) E_{\mathrm{X}}^{\mathrm{EXX,LR}} + [(1-\alpha)-\beta] E_{\mathrm{X}}^{\mathrm{GGA,LR}} + E_{\mathrm{C}}^{\mathrm{GGA}}. \end{aligned} \tag{2.64}$$

The novel idea of the SRSH functional is that the dielectric constant ϵ should correctly describe the asymptotic decay of the screened exchange energy along the distance r of the electrons [52, 53]. For this reason, the parameters α and β are mapped to the dielectric constant ϵ using the following equation:

$$\alpha + \beta = \frac{1}{\epsilon}. \tag{2.65}$$

Consequently, α and β determine physically correct the LR exchange (see (2.64)). In particular for bulk materials, the tunable form of SRSH provides the correct asymptotic decay by screening the exchange interaction as:

$$\frac{1}{\epsilon\, r} \quad \text{for} \quad r \longrightarrow \infty. \tag{2.66}$$

Note that the numerical range of the tuning parameter β is limited to [52]:

$$-\alpha \leq \beta \leq 1-\alpha. \tag{2.67}$$

To illustrate the effect of the range separation parameter γ, which determines the transition between SR and LR and together with β the proportions of the EXX and GGA exchange, standard semiconductors are taken into account. For semiconductors, as analysed in [1], the tuning parameter β is always negative

$$\beta < 0. \tag{2.68}$$

Accordingly, the exchange of the SRSH functional can be written as follows:

$$E_{\mathrm{X}}^{\mathrm{SRSH}} = \begin{cases} \mathrm{SR}, r = 0: & \alpha E_{\mathrm{X}}^{\mathrm{EXX}} + (1-\alpha) E_{\mathrm{X}}^{\mathrm{GGA}}, \\ \mathrm{LR}, r \neq 0: & \frac{\left(\alpha - |\beta| \mathrm{erf}(\gamma r)\right)}{r} E_{\mathrm{X}}^{\mathrm{EXX}} + \frac{\left(1-\alpha+|\beta| \mathrm{erf}(\gamma r)\right)}{r} E_{\mathrm{X}}^{\mathrm{GGA}}. \end{cases} \tag{2.69}$$

Fig. 2.6 shows the effect of different values of γ and illustrates the portioning of EXX and GGA exchange along the distance. The area below the coloured lines shows the

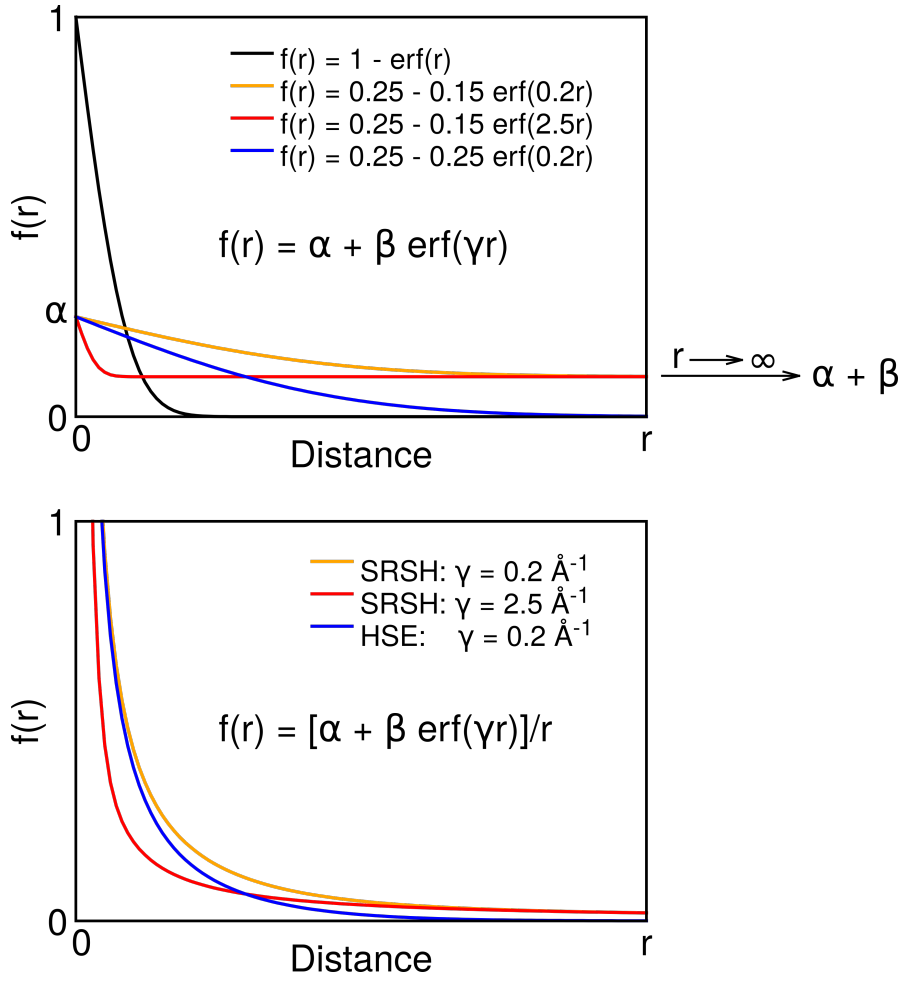

Figure 2.6. Schematic illustration of the drop in EXX exchange with increasing distance r for different values of the range-separation parameter γ. The other parameters are $\alpha = 0.25$ and $\beta = -0.15$ for the orange and red lines and $\alpha = -\beta = 0.25$ for the blue line to obtain HSE. The figure above shows the function $f(r) = \alpha + \beta \operatorname{erf}(r\,\gamma)$. For $r = 0$, the function tends to the EXX fraction of α, which is the same for all three cases, and for large distances r to the EXX fraction of $\alpha + \beta$. The figure below shows the same function, but multiplied by $\frac{1}{r}$. The following applies to both figures: the area below the colored lines indicates the fraction of EXX exchange, while the area above indicates the fraction of GGA. The blue line (HSE) shows that the fraction of EXX exchange decreases more rapidly with increasing distance r than the orange and red lines (SRSH), which retain a fraction of EXX exchange even at large distances.

amount of EXX exchange and the area above the coloured lines shows the amount of GGA exchange. If one compares the blue line (HSE) with the red line (SRSH), it is clear that SRSH retains a fraction of EXX in the LR range.
Furthermore, SRSH can be understood as a generalisation of functionals that can represent other functional types for a suitable choice of parameters. Table 2.2 shows some of the limit cases of parameters.

Table 2.2. Limit cases of the SRSH parameters that reproduce other types of functionals

Limiting case	Effect
$\beta = 0$	range-separation is turned off (SRSH becomes PBE0)
$\alpha + \beta = 1$	full EXX in LR, no GGA in LR
$\alpha = -\beta$	SRSH becomes HSE (if $\gamma = 0.2$ Å^{-1})
$\alpha = \beta = 0$	SRSH becomes PBE

In general, many physical quantities can be precisely determined by varying the SRSH parameters. The question that arises from tuning the parameters is whether the precise fixing of SRSH towards one quantity worsens the description of other quantities. In the case of Wing et al. [27], the parameter α is set constant to the α value of HSE, the parameter β is chosen to reproduce the dielectric constant ϵ according to equation (2.65) and γ is varied to fix the electronic band gap to the band gap value from GW calculations. Note that the GW theory can predict the electronic band gap very accurately, which, however, is associated with high computational costs. Since both parameters, β and γ, are tuned to theoretical results, i.e. both the theoretical dielectric constant ϵ and the band gap are calculated by the GW theory, SRSH can be understood as an experimental parameter-free functional. In addition to this way of tuning the SRSH functional, which makes SRSH a semi-empirical functional, there is also a non-empirical way of tuning using localized Wannier functions [54].
To summarize, the SRSH functional offers more flexibility by tuning compared to other rigid conventional hybrid functionals and, therefore, also includes Fock exchange in the LR region with variable proportion. In particular, the correct asymptotic decay $\frac{1}{\epsilon r}$ in the LR limit is guaranteed, which is an important difference to existing functionals relying on more than three parameters, such as (CAM-)B3LPY [55, 56]. Once SRSH is tuned, it can describe not only very accurate electronic properties such as the band gap, but also accurate optical absorption quantities such as spectra of standard semiconductors [27, 28]. This coexistence of accurate electronic and optical properties by using SRSH is the main advantage of it, which does not exist in conventional DFT.

2.2.6. Plane waves, energy cut-off and pseudo potentials

Since solids are usually approximated as periodic crystals modeled by repeating a unit-cell, translational symmetry plays an important role. In a periodic crystal, the potential also exhibits periodicity and can be expressed as a periodic potential:

$$V(\mathbf{r}) = V(\mathbf{r} + \mathbf{R}), \tag{2.70}$$

where $\mathbf{R}$ is an arbitrary translation vector. Therefore the periodic potential shows translational invariance. Furthermore, the foundation for the use of plane waves as a basis set for solids is provided by the Bloch theorem. The Bloch theorem states that the solution of the Schrödinger equation $\psi_{n\mathbf{k}}(\mathbf{r})$ in a periodic potential consists of periodic functions and plane waves [57]:

$$\psi_{n\mathbf{k}}(\mathbf{r}) = u_{n\mathbf{k}}(\mathbf{r}) e^{i\mathbf{kr}}, \tag{2.71}$$

with the periodic function

$$u_{n\mathbf{k}}(\mathbf{r} + \mathbf{R}) = u_{n\mathbf{k}}(\mathbf{r}). \tag{2.72}$$

Consequently, the solutions $\psi_{n\mathbf{k}}(\mathbf{r})$ are translationally invariant with the help of plane waves:

$$\psi_{n\mathbf{k}}(\mathbf{r} + \mathbf{R}) = \psi_{n\mathbf{k}}(\mathbf{r}) e^{i\mathbf{kR}}. \tag{2.73}$$

This justifies the choice of plane waves as a basis set for the expansion of the KS solutions. Note that the vector $\mathbf{k}$ is referred to as the Bloch vector, which is restricted to the first Brillouin zone, and the band index n refers to the number of electrons in the unit-cell. In conjunction with a Fourier transform, the periodic functions are expanded with the help of plane waves:

$$\psi_{n\mathbf{k}}(\mathbf{r}) = \frac{1}{\sqrt{\Omega}} \sum_{\mathbf{G}} C_{\mathbf{G}n\mathbf{k}} e^{i(\mathbf{G}+\mathbf{k})\mathbf{r}},$$

$$u_{n\mathbf{k}}(\mathbf{r}) = \frac{1}{\sqrt{\Omega}} \sum_{\mathbf{G}} C_{\mathbf{G}n\mathbf{k}} e^{i\mathbf{Gr}},$$

where $C_{\mathbf{G}n\mathbf{k}}$ are expansion coefficients. Note that $\mathbf{G}$ is a reciprocal lattice vector and Ω is the unit-cell volume. In addition, the Fourier transform guarantees efficient switching between real and reciprocal space by means of plane waves.
The number of plane waves, i.e. the number of basis functions, corresponding to a specific $\mathbf{k}$-point can be controlled by the kinetic energy relationship:

$$E_{\text{cut-off}} = \frac{\hbar^2}{2m} G^2_{\text{cut-off}} \quad \text{with} \quad |\mathbf{G} + \mathbf{k}| < G_{\text{cut-off}}. \tag{2.74}$$

On the one hand, the higher the energy value $E_{\text{cut-off}}$ for a specific $\mathbf{k}$-point, the more reciprocal $\mathbf{G}$-vectors are allowed, and consequently the number of plane waves in the basis set increases. On the other hand, specifying the value for $E_{\text{cut-off}}$, i.e. defining a cut-off energy $E_{\text{cut-off}}$, is equivalent to truncate the basis set. If the $\mathbf{k}$-point changes,

the number of suitable **G**-vectors changes accordingly to fulfil equation (2.74).
Note that with a larger number of **G**-vectors, which are equivalent to **G**-grid points spanning the fast Fourier transform (FFT) grid, a denser FFT grid can be achieved. In principle, the cut-off energy $E_{\text{cut-off}}$ is selected so that the FFT grid is fine enough to calculate converged quantities such as the total energy. Plane waves also offer other technical advantages, for example they are suitable for parallelizing the calculation in computer codes.
However, physical and chemical quantities are often determined by valence electrons and not by inner core electrons. For this reason, it would make sense to treat valence and core electrons differently in DFT. The grid potential $V_n(\mathbf{r})$ in the Kohn-Sham equation (2.31), which results from the ions, takes into account the nuclei and only the inner core electrons. This means, that the solutions of the Kohn-Sham equation (2.31) represent only the valence electrons as fictitious wave functions. As a consequence, the effective number of orbitals calculated by DFT is only the number of valence orbitals. In order to find an explicit expression for the ionic core potential $V_n(\mathbf{r})$, DFT uses the pseudo-potential approach, i.e. pseudo-potentials replace $V_n(\mathbf{r})$. In addition, pseudo-potentials are often based on the frozen-core approximation (FCA), where the core electrons and the nuclei are considered rigid [58].
In general, there are three variants of pseudo-potentials: norm-conserving, ultrasoft and projector-augmented wave (PAW) pseudo-potentials. To provide a simple insight into the functionality of pseudo-potentials, the first type is briefly explained. Norm-conserving pseudo-potentials are in principle an approach to correctly describe the charge density distribution of the ions and between them.
Following physical conditions for solids form the basis for the development of the norm-conserving pseudo-potential approach [58, 59, 60, 61]: first, the orbitals describing the inner core electrons are more localized than the orbitals describing the valence electrons and therefore exhibit less overlap with the orbitals of neighbouring atoms, and second, the part of the orbital close to the nucleus tends to oscillate strongly, while the part of the orbital away from the nucleus has a smooth structure (see Fig. 2.7). Consequently, outside the core region the choice for plane waves as a basis set is suitable. However, near the core region many plane waves would be needed to expand the oscillating part of the orbitals, which is technically laborious. This leads to the introduction of a so-called cut-off radius r_c, which divides the description of the real wave function into two parts, namely the strongly oscillating part near the core region ($r < r_c$) and the slowly varying part outside the core region ($r > r_c$). A division of the radial part of the wave function into two parts together with the corresponding potential is shown in Fig. 2.7. Outside r_c, the pseudo-potential follows the real Coulomb potential in order to reproduce a conformity of the wave functions ψ_{real} and ψ_{pseudo}. Inside r_c, the pseudo wave function is constructed to be smooth and nodeless unlike the real wave function. The smoothness of the pseudo wave function guarantees that fewer plane waves are needed in the expansion. Choosing the pseudo wave function to be nodeless allows to find the shape of the pseudo-potential by simply inverting the radial part of the Schrödinger equation.

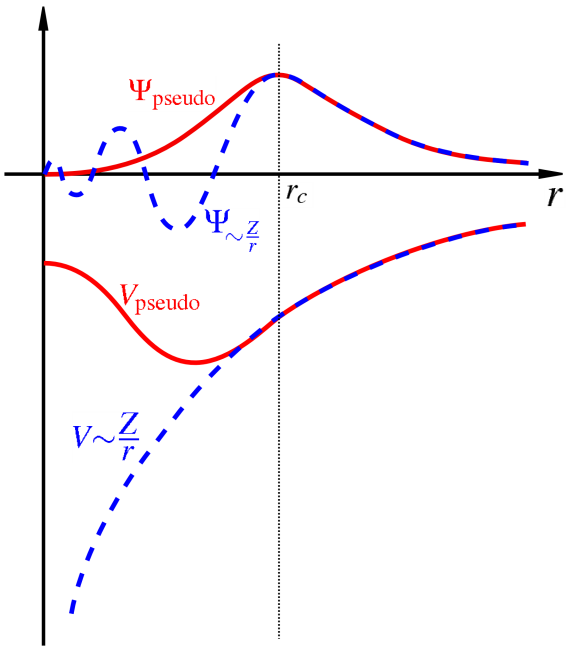

Figure 2.7. The blue dashed lines indicate the real all-electron wave function (upper line) in the external Coulomb potential of the core (bottom line). The red continuous lines indicate the pseudo wave function (upper line) in the pseudo potential (bottom line). Outside the core region r_c the real and pseudo wave function coincide with each other. Inside the core region r_c the real wave function shows strong oscillations, whereas the pseudo wave function shows smooth and nodeless character. Figure from [62].

However, replacing the potential by a pseudo-potential, i.e. modifying the potential inside r_c without affecting the shape of the wave function outside r_c, is only justified, if the pseudo-potential exhibits *transferability*, which is explained next. *Transferability* is defined by two criteria: first, the logarithmic derivatives and the first energy derivatives of the real and pseudo wave functions have to coincide outside r_c, i.e. for $r > r_c$, and second, the real and pseudo charge densities have to be the same [59]. Another characteristic of pseudo-potentials is *softness*, which refers to the smallest possible number of plane waves used to describe the pseudo wave function. Both characteristics, *transferability* and *softness*, are associated with the determination of the cut-off radius r_c. Note that an easily understandable upper limit for the cut-off radius r_c is therefore half the atomic distance to the neighbouring atom.
Consequently, norm-conserving pseudo-potentials guarantee that the charge density within r_c has to be the same for the real and the pseudo wave function:

$$\int_0^{r_c} |\psi_{\text{real}}(\mathbf{r})|^2 \, d^3r \stackrel{!}{=} \int_0^{r_c} |\psi_{\text{pseudo}}(\mathbf{r})|^2 \, d^3r. \tag{2.75}$$

Outside r_c, norm conservation is already given by the conformity of the two wave functions ψ_{real} and ψ_{pseudo}. This ensures an overall identical charge density between real and pseudo wave functions for the full wave function ($\psi = \psi_{<r_c} + \psi_{>r_c}$), which substantiates the replacement of the ionic grid potential $V_n(\mathbf{r})$ by a pseudo-potential.

To summarise, the pseudo-potential has two tasks: firstly, it describes the core

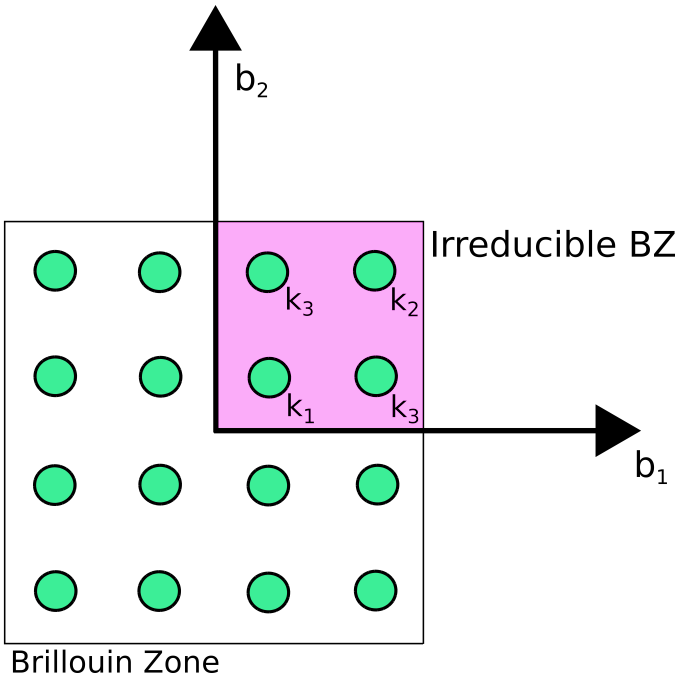

Figure 2.8. Schematic representation of a two-dimensional BZ in reciprocal space after the coordinate transformation of the corresponding two-dimensional unit-cell in real space. b_1 and b_2 are reciprocal lattice vectors. The BZ is sampled by k-points denoted as light green dots. The purple shaded area denote the irreducible BZ. Due to symmetry the total number of 16 k-points can be reduced to 3 k-points: k_1, k_2 and k_3.

electrons with the ionic core potential and secondly, it also describes the part of the valence electron wave function close to the nucleus.

2.2.7. K-point sampling

Following section is mainly based on [63]. The primitive unit-cell in reciprocal space is called the Brillouin zone (BZ). In order to calculate quantities such as the charge density, the density of states and others, an integration over the BZ is required. Since the analytical form is typically not known for those quantities one has to numerically solve the integral. For this purpose, a k-point mesh provides the finite sampling of the BZ and for a computational approach, the integrals are replaced by weighted sums over all k-points:

$$\frac{1}{\Omega_{\mathrm{BZ}}} \int_{\mathrm{BZ}} \longrightarrow \sum_{\mathbf{k}} \omega_{\mathbf{k}_i}. \tag{2.76}$$

Here, Ω_{BZ} is the volume of the BZ and $\omega_{\mathbf{k}_i}$ is the weight of the k-point $\mathbf{k}_i$. Fig. 2.8 shows the example of a two-dimensional cell in reciprocal space, which is sampled with a total of 16 k points. The total number of sample points can be reduced by symmetry, which means that k-points of the same symmetry only need to be calculated once and instead the weight of the equivalent k-points is multiplied accordingly. The symmetry-reduced k-point mesh therefore lies in the irreducible BZ[9]. In this

[9]The irreducible BZ is derived from the first BZ taking into account all symmetries of the lattice.

particular example of Fig. 2.8 the k-point $\mathbf{k}_1$ occurs 4 times and the corresponding weight is $\omega_1 = \frac{4}{16}$, which avoids multiple counting. The following applies to the other weights in this example:

$$\omega_1 = \frac{1}{4}, \quad \omega_2 = \frac{1}{4}, \quad \omega_3 = \frac{2}{4}. \tag{2.77}$$

Note that the sum of all weights is 1:

$$\sum_{\mathbf{k}_i} \omega_{\mathbf{k}_i} = 1. \tag{2.78}$$

The integral of any quantity F can therefore be written as:

$$\frac{1}{\Omega_{\mathrm{BZ}}} \int_{\mathrm{BZ}} F(\mathbf{k})\ d^3k \longrightarrow \sum_{\mathbf{k}_i} \omega_{\mathbf{k}_i} F(\mathbf{k}_i) = \frac{1}{4}F(\mathbf{k}_1) + \frac{1}{4}F(\mathbf{k}_2) + \frac{2}{4}F(\mathbf{k}_3). \tag{2.79}$$

As an example of a function F, consider the energy ϵ_i of the i-th Kohn-Sham state. The integration takes place over the continuous band-energy surface in the BZ and calculates the total energy of this specific state:

$$E_{\mathrm{total},i} = \frac{1}{\Omega_{\mathrm{BZ}}} \int_{\mathrm{BZ}} \epsilon_i(\mathbf{k})\ d^3k. \tag{2.80}$$

Note that doubling the unit-cell in real space, i.e. forming a supercell, halves the cell size in reciprocal space and therefore fewer k-points are required to sample the BZ. This goes hand in hand with the back folding of the zone boundary to the center of the BZ, which is the Γ-point.
In the previous chapter it was shown that the value of the energy cut-off controls the number of G-vectors based on the relation (2.74) and thus determines the number of plane waves available at each k-point. Consequently, the number of plane waves can vary for different k-points. As an analogy: the G-vectors form the G-grid and the k-points form the k-grid. In order to achieve convergence, e.g. a smoother volume energy surface, sufficiently dense k- and G-grids must be used.
In general, different quantities converge at different rates, for example energy differences converge faster than total energies with respect to the number of k-points. Furthermore, convergence does not necessarily have to be achieved monotonically. This means, that for some grids, for example, the integral in equation (2.80) is underestimated, i.e. the energy is too low, and for other grids the integral is overestimated, i.e. the energy is too high.

2.2.8. Van der Waals interaction

The Van der Waals (VdW) interaction describes a small contribution to the binding energy between atoms or molecules, caused by the motion of the electrons [57]. These instantaneous electron movements lead to the formation of temporal dipole moments. The interaction between dipole moments from different atoms is called

VdW interaction and can be described by a dispersion correction term. The corresponding interaction potential is weakly attractive with a R^6 dependence

$$V_{\text{Disp}}(\mathbf{R}) \approx -\frac{1}{R^6}. \tag{2.81}$$

Here, $\mathbf{R}$ denotes the connection vector between two atoms. Exchange-correlation functionals applied in DFT, such as semilocal or hybrid functionals, do not adequately account for the VdW interaction. Therefore, to achieve a more accurate description of the total energy, a dispersion correction energy E_{Disp} is added to the Kohn-Sham total energy:

$$E_{\text{tot}}^{\text{KS-DFT-Disp}} = E_{\text{tot}}^{\text{KS-DFT}} + E_{\text{Disp}}. \tag{2.82}$$

Note that there are several types of dispersion corrections and when added to the total energy, they inherently correct interatomic forces and stress tensors. In addition, dispersion corrections can also be included in calculations such as MD or vibrational calculations using finite displacements. An empirical ansatz for the dispersion correction energy can be written as follows [64, 65]:

$$E_{\text{Disp}}(\mathbf{R}) = -C_6 \frac{f_d(\mathbf{R}, R_A, R_B)}{R^6}, \tag{2.83}$$

which is a pairwise interatomic correction term. Here, $\mathbf{R}$ is the distance between two atoms, R_A and R_B are the VdW radii of atom A and B, f_d is the damping function and C_6 is the pair interaction coefficient determined by the atoms.
An extension of (2.83) is the parameter-free Tkatchenko-Scheffler (TS) method [66], which takes into account the spatially dependent charge density dependence of C_6 and f_d:

$$\alpha_i = \nu_i \, \alpha_i^{\text{free}},$$

$$C_{6ii} = \nu_i^2 \, C_{6ii}^{\text{free}},$$

$$R_{0i} = \left(\frac{\alpha_i}{\alpha_i^{\text{free}}} \right)^{\frac{1}{3}} R_{0i}^{\text{free}}.$$

Here, α is the frequency-dependent polarizability and the modified C_6 coefficient is also α-dependent, i.e. $C(\alpha)$. The index i runs over all atoms and the term "free" refers to the atom in vacuum. The effective atomic volume ν_i of atom i, which depends on the charge density $n(\mathbf{r})$, is given by

$$\nu_i(\mathbf{r}) = \frac{\int d^3r \; r^3 \, w_i(\mathbf{r}) \, n(\mathbf{r})}{\int d^3r \; r^3 \, n_i^{\text{free}}(\mathbf{r})}. \tag{2.84}$$

Here, $w_i(\mathbf{r})$ denotes the Hirshfeld weight

$$w_i(\mathbf{r}) = \frac{n_i^{\text{free}}(\mathbf{r})}{\sum_{j=1}^{N} n_j^{\text{free}}(\mathbf{r})}, \tag{2.85}$$

where N is the total number of atoms. Note that $w_i(\mathbf{r})$ can be interpreted as a relative charge density for atom i.
A further development of the TS method, which does not calculate the structure and energy of ionic solids with satisfactory accuracy, is the inclusion of the Hirshfeld partitioning. The method is therefore referred to as the Tkatchenko-Scheffler method with iterative Hirshfeld partitioning (TS-IH) [67, 68]. The concept behind this is to replace the conventional Hirshfeld weights by an iterative Hirshfeld partitioning. The partitioning is calculated self-consistently with fractional charges of the ions instead of neutral reference atoms compared to the TS method. The self-consistent procedure begins with updating the Hirshfeld weight. The updated Hirshfeld weight is then used to update the number of electrons per atom. After that the updated electron number is used to update the new charge density, which in turn is used to update the Hirshfeld weight. The algorithm starts with densities from neutral atoms, and the weight of the iteration step k is given by :

$$w_i^k(\mathbf{r}) = \frac{n_i^k(\mathbf{r})}{\sum_{j=1}^{N} n_j^k(\mathbf{r})}. \tag{2.86}$$

In general, the inclusion of the dispersion correction is important for the theoretical description of lead-halide organic-inorganic perovskites [69]. This holds in particular for structural properties such as relaxations based on energy-volume curves or direct optimizations via a stress tensor [70] (reference used TS method). For example, the inclusion of the dispersion correction in structure optimization affects the orientation of the methylammonium cation associated with distortions of the inorganic lead-halide framework in methylammonium lead iodide ($MAPbI_3$) in a specific direction [71]. However, the inclusion of VdW is also important for common inorganic semiconductors when it concerns structural properties such as lattice constants and bulk moduli or cohesive energies [72] (reference used TS method).
Note that in the result section 4, the TS method is used for the Monte-Carlo calculations, while the TS-IH method is used for MD calculations. On the one hand, the consideration of the VdW interaction influences the structural properties and, via these, also the electronic properties. On the other hand, the DFT band gap, for example, does not change when calculated with or without VdW for the same geometry, since the KS-eigenvalues are not VdW-corrected.

2.2.9. Hellmann-Feynman theorem

The Hellmann-Feynman theorem is a fundamental theorem from quantum mechanics that connects the derivative with respect to a parameter of a time-independent Hamilton operator with the corresponding ground state energy. In DFT, this theorem can be applied to the ground state energy of the Kohn-Sham Hamilton operator (2.31) to calculate the forces acting on the ions. In the Born-Oppenheimer approximation, the positions of the ions $\mathbf{R}_I$ are only included as parameters in the Kohn-Sham Hamilton operator, i.e. $\hat{H}^{\mathbf{R}_I}$. Note that the ground state energy $E_0^{\mathbf{R}_I}$ and the wave functions $\psi^{\mathbf{R}_I}$ also depend on $\mathbf{R}_I$ only as a parameter. Thus the force acting on an

ion I at position $\mathbf{R}_I$ can be written as (for reasons of clarity, the parameter $\mathbf{R}_I$ is in the following equation neglected) [73, 36]:

$$\begin{aligned} F_I &= -\nabla_I E_0 \\ &= -\frac{\partial}{\partial \mathbf{R}_I}\langle\psi_0|\hat{H}|\psi_0\rangle \\ &= -\big(\langle\nabla_I\psi_0|\hat{H}|\psi_0\rangle + \langle\psi_0|\nabla_I\hat{H}|\psi_0\rangle + \langle\psi_0|\hat{H}|\nabla_I\psi_0\rangle\big) \\ &= -\langle\psi_0|\nabla_I\hat{H}|\psi_0\rangle. \end{aligned} \tag{2.87}$$

The first and third terms of the third line vanish due to the variation principle applied to the ground state. As a result, the force acting on ion I is given by the expectation value of the ground state wave function and the derivative of the Kohn-Sham Hamilton operator with respect to the ion position $\mathbf{R}_I$. Furthermore, the acting force is only determined by the external potential V_{ext}, and for local potentials the expression is reduced to [74]:

$$\begin{aligned} F_I &= -\langle\psi_0|\frac{\partial}{\partial \mathbf{R}_I}V_{\text{ext}}|\psi_0\rangle \\ &= -\int dr^3\, n(\mathbf{r})\,\frac{\partial}{\partial \mathbf{R}_I}V_{\text{ext}}. \end{aligned} \tag{2.88}$$

Note that the first line also holds for non-local potentials, i.e. $V_{\text{ext}}(\mathbf{R}, \mathbf{R}')$. Specific examples of the application of the Hellmann-Feynman theorem are MD calculations using Newton's equation of motion, phonon frequency calculations by displacing the atoms from their equilibrium positions, relaxation calculations by moving the atoms according to the forces acting on the ions, and calculations of the stress tensor.

2.3. Spin-Orbit coupling

The relativistic extension of the Schrödinger equation is the Dirac equation, which can be derived from the relativistic classical energy relation for a free electron [75]:

$$E^2 = c^2\mathbf{p}^2 + m^2c^4. \tag{2.89}$$

This is achieved by the same correspondence rules for the substitution of classical quantities by differential operators as in the derivation of the Schrödinger equation. The relativistic classical energy relation guarantees the same power of space via p^2 with $p \longrightarrow \frac{\partial}{\partial x}$ and time via E^2 with $E \longrightarrow \frac{\partial}{\partial t}$, which is not the case in the Schrödinger equation, but is necessary for Lorentz invariance. In addition, the solutions of the Dirac equation are four-component spinors.
In the semi-classical model of angular momentum, i.e., the vectorial description of angular momentum, both the modulus and the z-component are discrete or quantized. This also holds for the orbit angular momentum $\mathbf{L}$ and the intrinsic spin $\mathbf{S}$ of the electron. It is known from the normal Zeeman-effect that an external magnetic field $\mathbf{B}_{ext}$ interacts with the orbital angular momentum $\mathbf{L}$ in the following way:

$$\hat{H}_{\text{Zeeman}} \propto \hat{\mathbf{L}} \cdot \hat{\mathbf{B}}_{\text{ext}}. \tag{2.90}$$

A similar relation can be derived for the electron spin **S** and the induced internal magnetic field B_{int} by the electron-nucleus motion:

$$\hat{H}_{\text{SOC}} \propto \hat{\mathbf{S}} \cdot \hat{\mathbf{B}}_{\text{int}}. \tag{2.91}$$

Regardless of which coordinate system is taken into account, that of the nucleus or the electron, moving charge generates a magnetic field $\mathbf{B}_{\text{int}}$. On the one hand, from the perspective of the electron, the nucleus is circling around and the moving charge of the nucleus generates a magnetic field at the position of the electron. On the other hand, this magnetic field $\mathbf{B}_{\text{int}}$ can be expressed in terms of the orbit angular momentum **L** of the electron and at the same time interacts with the spin **S** of the electron. That is why it is called spin-orbit coupling (SOC).
When considering the different inertial systems, it should be noted that the relative velocities v of the electrons become high for heavy atoms and so does the Lorentz factor:

$$\gamma = \frac{1}{\sqrt{1 - \left(\frac{v}{c}\right)^2}}. \tag{2.92}$$

As the Lorentz factor increases, the SOC contribution also becomes large.
However, this relativistic effect can be included in the Kohn-Sham equation (2.31) by adding the 2×2 SOC Hamilton operator. Note that the wave-functions then change to a two-component spinor with $\uparrow, \downarrow$ denoting the spin-up or spin-down orientation. The SOC Hamilton operator is proportional to

$$\hat{H}_{\text{SOC}} \propto \hat{\mathbf{S}} \cdot \hat{\mathbf{L}}. \tag{2.93}$$

Here, $\hat{\mathbf{S}}$ involves the Pauli matrices $\hat{\sigma}$. For the sake of clarity, it should be taken into account in a relativistic calculation that the motion of the electron is accelerated by the transition to the system of the nucleus (back transformation). Based on this idea, the magnetic field $\mathbf{B}_{\text{int}}$ or the angular momentum **L** in equation (2.93) in the rest frame of the electron can be expressed by the electric field ∇V and the electron momentum **p** [36]:

$$\hat{H}_{\text{SOC}} = \frac{e\hbar}{4m^2c^2}(\hat{\mathbf{p}} \times \nabla V) \cdot \hat{\sigma}. \tag{2.94}$$

For the general case that the spin orientation has no preferred direction such as the z-direction, a non-collinear spin description must be used. This can be achieved by using the spin density matrix to describe mixed spin states [36]:

$$\rho^{\alpha\beta}(\mathbf{r}) = \sum_{n,\mathbf{k}} f_{n\mathbf{k}}\, \tilde{\psi}^{\alpha *}_{n\mathbf{k}}(\mathbf{r}) \tilde{\psi}^{\beta}_{n\mathbf{k}}(\mathbf{r}). \tag{2.95}$$

In the case of solids, the dominant contribution of SOC comes from the core region of the atoms, where the gradient of the potential ∇V is large. Thus, the gradient can be reduced to the radial derivative $\hat{\mathbf{r}}\frac{\partial}{\partial \mathbf{r}}$, which is used, for example, for the SOC implementation in the Vienna Ab initio Simulation Package (VASP) [76].
The implementation uses the framework of the PAW method, which introduces a

basis set of projector functions $\tilde{p}_i$. In analogy to the cut-off radius r_c in chapter 2.2.6, the PAW sphere divides the core region into an inner and an outer region, in which the pseudo orbitals $\tilde{\psi}$ are projected onto the projector functions $\tilde{p}_i$ and are expressed with the all-electron partial waves ϕ_i (inside the PAW sphere). Assuming that the SOC contribution is large only in the core region and has negligible contribution outside the PAW sphere, the Hamilton operator expressed with the projector functions form the PAW Hamilton operator [76]:

$$\hat{\tilde{H}}_{\mathrm{SOC}} = \sum_{ij} |\tilde{p}_i\rangle\langle\phi_i|\hat{H}^{\alpha\beta}_{\mathrm{SOC}}|\phi_j\rangle\langle\tilde{p}_j|. \tag{2.96}$$

Note that the PAW Hamilton operator is reduced to the all-electron one-center contribution. Using the spin density matrix (2.95), the SOC energy contribution can be expressed as follows [76]:

$$E^{ij}_{\mathrm{SOC}} = \delta_{\mathbf{R}_i,\mathbf{R}_j}\delta_{l_i,l_j}\sum_{n,\mathbf{k}} w_{\mathbf{k}} f_{n\mathbf{k}} \sum_{\alpha,\beta}\langle\tilde{\psi}^{\alpha}_{n\mathbf{k}}|\tilde{p}_i\rangle\langle\phi_i|\hat{H}^{\alpha\beta}_{\mathrm{SOC}}|\phi_j\rangle\langle\tilde{p}_j|\tilde{\psi}^{\beta}_{n\mathbf{k}}\rangle, \tag{2.97}$$

where the all-electron partial waves $\phi_i(\mathbf{r}) = R_i(|\mathbf{r}-\mathbf{R}_i|)Y_{l_i m_i}(\theta,\phi)$ located at $\mathbf{R}_i$ include the radial function $R_i(|\mathbf{r}-\mathbf{R}_i|)$ and the spherical harmonics $Y_{l_i m_i}(\theta,\phi)$. The latter contains the corresponding quantum numbers l_i and m_i. This local basis set $\phi_i(\mathbf{r})$ disappears outside the PAW sphere, so that the pseudo-orbital $\tilde{\psi}^{\alpha}_{n\mathbf{k}}$ corresponds to the true one-electron orbital $\psi^{\alpha}_{n\mathbf{k}}$ (outside the PAW sphere). Furthermore, $\alpha = \uparrow$ or $\downarrow$ accounts for the spin-component of the two-component spinor, which is needed for the non-collinear description of the magnetism. The remaining variables are the band index n, the k-point weight $w_{\mathbf{k}}$ and the Fermi weight $f_{n\mathbf{k}}$. It is obvious that the first Kronecker symbol in (2.97) shows that the effect of SOC is limited within one nucleus, but for different orbitals. However, by adding H_{SOC} to the Kohn-Sham Hamilton operator, the Kohn-Sham equation is still a non-relativistic equation compared to the Dirac equation, but the equation becomes two-component $(\uparrow,\downarrow)$.

It is known that the SOC effect has a strong influence on the static band structure of materials such as perovskites, which is due to the large atomic number Z and, thus, due to the large mass of the constituting atoms. In general, the SOC effect can be understood as a kind of renormalization of the band gap, which minimizes the band gap. Note that perovskites crystallize in the typical perovskite structure ABX_3, where B is the metal atom such as lead or tin. This leads to a magnitude of the SOC effect of ≈1 eV for lead-based HaPs and of ≈0.3 eV for tin-based HaPs [77]. In addition, it is interesting to see whether there is an influence between the inclusion of temperature in the DFT theory and the SOC effect. This will be discussed in chapter 4. For example, a recent study showed for some III-V semiconductors and telluride semiconductors that first-principle calculations using the Allen-Heine-Cardona theory lead to a tiny reduction in the zero-point renormalization when SOC is included [78]. Note that the Allen-Heine-Cardona theory as well as the zero-point renormalization are explained in chapter 2.6.

In addition to the strong effect on the electronic structure for HaPs, the SOC effect is

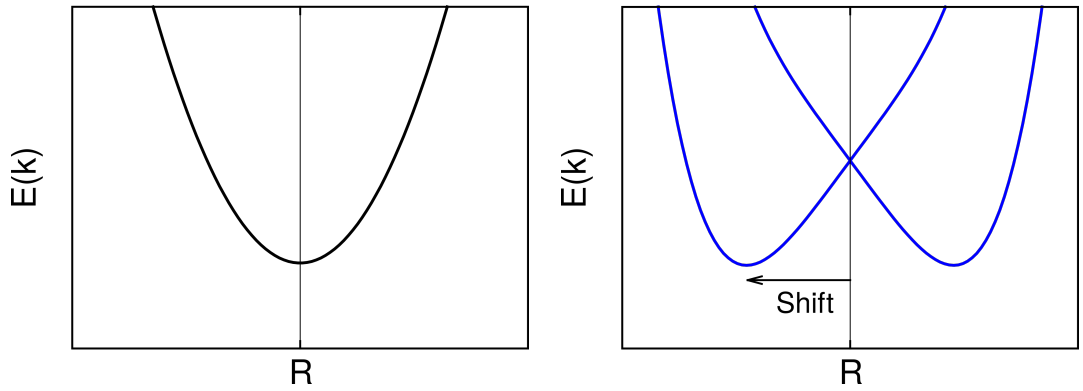

Figure 2.9. Left-hand side: a schematic representation of a degenerate non-splitted CBM (black line). Right-hand side: a schematic representation of a Rashba splitted CBM (blue lines). In this case, the initial band gap indicated at the R-point of the BZ is no longer well-defined. The label "shift" denotes the horizontal shift of the CBM.

also responsible for lifting the degeneracy of the electronic bands. For example, SOC involves the splitting of the CBM for HaPs on the one hand [79, 80] and the splitting of the VBM for standard semiconductors on the other hand [81]. Furthermore, the SOC effect is associated with the rarer Rashba effect of spin coupling [82]. Basically, the Rashba effect occurs in materials with a massive SOC contribution in combination with low inversion symmetry or symmetry breaking. As a result of these two effects, an intrinsic magnetic field occurs to which the spin states are exposed, leading to spin state splitting. In some cases, a slight horizontal shift of the CBM shifts the band gap away from the high symmetry point (see Fig. 2.9) [82].

2.4. Bulk properties

2.4.1. Lattice constant and bulk modulus

The equilibrium lattice constant of a material can be calculated using the energy-volume curve $E(V)$. To generate the energy-volume curve, the total energy E must be calculated for some test volumes V around the expected unit-cell volume given by the experimental lattice constant. For example, test volumes between 91% and 109% of the experimental volume at intervals of 3% are suitable. After calculating the total energies for the test volumes, the energy-volume curve $E(V)$ can be fitted using the Birch-Murnaghan equation of state [83, 84, 85]:

$$E(V) = E_0 + \frac{B_0 V}{B_0^{'}}\left(\frac{(V_0/V)^{B_0^{'}}}{B_0^{'}-1}+1\right) - \frac{V_0 B_0}{B_0^{'}-1}. \tag{2.98}$$

Here, E_0 is the total energy at the equilibrium volume V_0, B_0 is the bulk modulus and $B_0^{'}$ is the derivative of the bulk modulus with respect to the pressure. Note that the bulk modulus is a by-product of the Birch-Murnaghan equation, which is specified as a fitting parameter. Fig. 2.10 shows a schematic representation of an energy-volume curve for determining the theoretical equilibrium lattice constant.

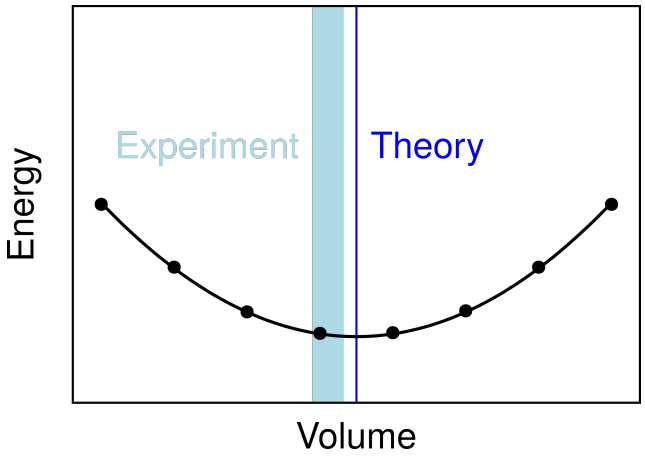

Figure 2.10. Schematic representation of a energy-volume curve $E(V)$. The black circles denote unit-cell volumes around the unit-cell volume given by the experimental lattice constant. The experimental volume is denoted by the light-blue area including the lower and higher limit of experimental values. The thin blue line denotes the minimum of the fitted Birch-Murnaghan equation of state. The minimum volume provides the theoretical lattice constant via $V_0 = \frac{1}{4}a_0^3$, which holds for materials crystallized in the face-centered cubic (fcc) structure, i.e. the rock-salt structure.

2.4.2. Atomization energy

The atomization energy (AE) or cohesive energy is the energy difference between a single atom in the vacuum and an atom bound in the crystal. Figuratively speaking, it is the energy that has to be used to break down the crystal into its individual atoms. The free atom or the atom in the vacuum can be simulated by just one atom in the supercell. Consequently, the AE can be expressed as follows:

$$E_{\mathrm{AE}}(M) = \frac{1}{N}\left[\sum_{\mathrm{atoms}} E_0(X) - E_0(M)\right]. \tag{2.99}$$

Here, M denotes the crystal, for example a semiconductor, and X the individual constituent atoms. Accordingly, $E_0(M)$ is the total energy of the crystal and $E_0(X)$ is the energy of the individual atom. The sum runs over all atoms N in the supercell. The AE is related to the Coulomb interaction of the atoms in the crystal, and its magnitude is a measure of the strength of the crystal. Note that materials with a high AE tend to crystallise in the fcc structure [81].

2.4.3. Phonon dispersion relations

In principle, there are several methods for calculating phonon properties such as phonon frequencies of solids. Two common approaches are density functional perturbation theory (DFPT) and the finite-difference method. The first method, DFPT, has the disadvantage that most implementations in electronic structure codes are only available for non-hybrid or GGA functionals. However, one advantage is that the linear response theory (DFPT) does not require the knowledge of the

size of the specific finite displacement, which is essential in the finite-difference method. In addition, the finite-difference method requires large supercells of the size of the phonon wavelength, whereas DFPT simply uses unit-cells. In any case, each method must determine the second order force constant matrix in order to calculate the phonon frequencies. Since the DFPT method is limited to non-hybrid functionals and in order to compare phonon frequencies from hybrid as well as GGA functionals, the focus here is on the finite-difference method.
As discussed in chapter 2.1.4, the interatomic force constant matrix is given by the second derivative of the potential with respect to the nuclear displacements and can be expressed with the same meaning of the indices as in chapter 2.1.4 as follows

$$C_{p\kappa\alpha,p'\kappa'\alpha'} = \frac{\partial^2 U}{\partial\tau_{p\kappa\alpha}\partial\tau_{p'\kappa'\alpha'}} = -\frac{\partial F_{p\kappa\alpha}}{\partial\tau_{p'\kappa'\alpha'}}. \tag{2.100}$$

The finite-difference method, as implemented in Phonopy [86], approximates the force constant matrix with the help of finite displacements $\Delta\tau$:

$$C_{p\kappa\alpha,p'\kappa'\alpha'} \approx \frac{F_{p\kappa\alpha}(\boldsymbol{\tau}^0_{p\kappa}, \boldsymbol{\tau}^0_{p'\kappa'} + \Delta\boldsymbol{\tau}_{p'\kappa'}) - F_{p\kappa\alpha}(\boldsymbol{\tau}^0_{p\kappa}, \boldsymbol{\tau}^0_{p'\kappa'})}{\Delta\boldsymbol{\tau}_{p'\kappa'}}. \tag{2.101}$$

Here, $F_{p\kappa\alpha}$ is the force acting on the κ-th nucleus in the p-th unit-cell at position $\boldsymbol{\tau}^0_{p\kappa}$ induced by a shifted nucleus at position $\boldsymbol{\tau}^0_{p'\kappa'} + \Delta\boldsymbol{\tau}_{p'\kappa'}$. Since phonon calculations require relaxed supercells, the last term in the equation above can be set to zero, i.e.

$$F_{p\kappa\alpha}(\boldsymbol{\tau}^0_{p\kappa}, \boldsymbol{\tau}^0_{p'\kappa'}) = 0. \tag{2.102}$$

The remaining expression for the force can be calculated using the Hellmann-Feynman theorem, as described in chapter 2.2.9. With this method, phonon frequencies $\omega_{\mathbf{q}\nu}$ are calculated by solving the following eigenvalue equation containing the dynamical matrix:

$$\sum_{p'\kappa'\alpha'} \frac{1}{\sqrt{M_\kappa M_{\kappa'}}} C_{0\kappa\alpha,p'\kappa'\alpha'} \exp(i\mathbf{q}\cdot\mathbf{R}_{p'})\; e_{\kappa'\alpha',\nu}(\mathbf{q}) = \omega^2_{\mathbf{q}\nu}\; e_{\kappa\alpha,\nu}(\mathbf{q}). \tag{2.103}$$

Note that the phonon frequencies are calculated in the harmonic approximation and without temperature effects.
In order to take into account the phonon branch splitting of the optical phonon frequencies, the non-analytical term correction (NAC) must be applied [87]. This leads to the splitting into longitudinal optical (LO) and transverse optical (TO) modes. However, the splitting only occurs in a narrow region close to the Γ-point at the BZ center and accounts for large wave vectors [88]. A direct consequence of the splitting is a partial cancellation of the degeneracy of the optical phonon frequencies. In general, the optical phonon branch splits into two energetically lower TO modes, which are still doubly degenerate, and one energetically higher LO mode.
LO/TO splitting only occurs in materials with a poly-atomic basis such as the semiconductor GaAs, while it does not occur in materials with a mono-atomic basis such

as silicon (Si) (see Fig. 2.11). The driving mechanism behind this is the symmetry breaking induced by the poly-atomic basis, which leads to the effect of distinguishable atoms in the unit-cell [32]. Consequently, in a unit-cell with a mono-atomic basis, the atoms are indistinguishable and the splitting is not relevant. Note that materials with unit-cells containing only one atom, which corresponds to a mono-atomic basis, exhibit only acoustic modes. In addition, one property of acoustic phonons is that they obey the acoustic sum rule[10]. This means that the acoustic phonons tend towards zero for long phonon wave vectors due to the charge neutrality or the associated "effective charge neutrality" of the system [87].
In the case of the X-point at the BZ boundary, the degeneracy of the phonons is different. For a mono-atomic basis such as in Si, the optical and acoustic frequencies are degenerate at the X-point (see upper panel of Fig. 2.11). In contrast, for a poly-atomic basis such as in GaAs, the optical and acoustic branches do not coincide and are therefore not degenerate at the X-point (see lower panel of Fig. 2.11).
However, the distinguishable atoms differ in their atomic mass as well as in their long-range Coulomb interaction. This results in different kinetic energies and different harmonic motions. Note that the atoms of a poly-atomic basis are exposed to the same interatomic potential. The difference in mass of the atoms causes symmetry breaking, which can be demonstrated by simulating oscillations with massless springs. For a poly-atomic linear chain consisting of a basis of two different atoms with masses M_1 and M_2, the solutions of the eigenvalue equation under the assumption of only nearest-neighbour interaction are as follows [32]:

$$\omega^2 = \frac{K}{M_1 M_2}\left(M_1 + M_2 \pm \sqrt{M_1^2 + M_2^2 + 2M_1 M_2 \cos(qa)}\right). \tag{2.104}$$

Here, K is the spring constant, a is the lattice constant and q is the q-vector. There are two special cases at the BZ boundary for $q = \frac{\pi}{a}$, which show the connection between degenerate phonon branches and different atom masses:

1. Case $M_1 = M_2$:

$$\begin{aligned} \omega^2 &= \frac{K}{M^2}\left(2M \pm \sqrt{2M^2 + 2M^2\cos(qa)}\right) \\ q \longrightarrow \frac{\pi}{a}: &\qquad \omega_\pm^2 = \frac{2K}{M} \end{aligned} \tag{2.105}$$

If the masses are equal, there is a degeneracy of optical and acoustic branches at the BZ boundary. This case corresponds to the case of Si with degeneracy at the X-point (see Fig. 2.11 upper panel, red rectangle on the right).

[10]Note that a uniform translation of the full crystal implies no forces on atoms.

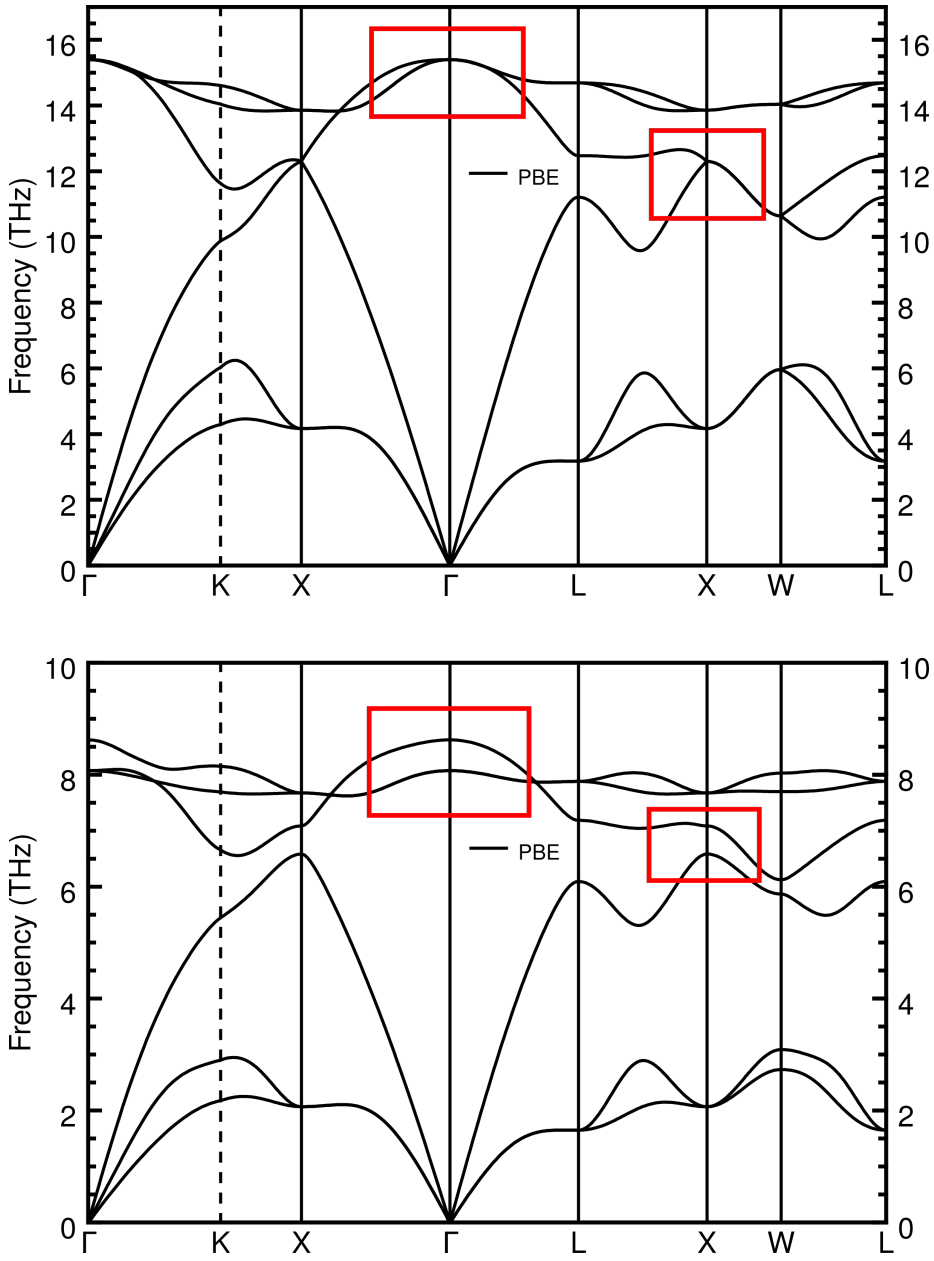

Figure 2.11. The upper panel shows the phonon dispersion relation for the semiconductor Si, which has a mono-atomic basis. The lower panel shows the phonon dispersion relation for the semiconductor GaAs, which has a poly-atomic basis. Both dispersion relations are calculated using the PBE functional. Each red rectangle on the left side enclosing the Γ-point emphasises that there is no LO/TO splitting for Si (upper panel), while LO/TO splitting is present for GaAs (lower panel). Each red rectangle on the right side enclosing the X-point at the BZ boundary shows degenerate acoustic and optical frequencies for Si (upper panel), while for GaAs (lower panel) the acoustic and optical frequencies are not degenerate.

2. Case $M_1 \neq M_2$:

$$q \longrightarrow \frac{\pi}{a}: \qquad \omega^2 = \frac{K}{M_1 M_2}\Big(M_1 + M_2 \pm (M_1 - M_2)\Big)$$
$$\omega_+^2 = \frac{2K}{M_2} \tag{2.106}$$
$$\omega_-^2 = \frac{2K}{M_1}$$

The different masses lift the degeneracy at the BZ boundary. This case corresponds to the case of GaAs without degeneracy at the X-point (see Fig. 2.11 lower panel, red rectangle on the right).

Dynamical matrix including NAC:

The aim of Pick et al. [87] was to derive an expression for the force constant matrix that also takes into account the long-range Coulomb forces. However, the conventional expression of the force constant matrix is restricted to a finite range, which means that such long-range effects are not considered. The conventional expression leads to an appropriate description for metals and non-ionic insulators. However, ionic crystals exhibit long-range Coulomb forces, which have to be included in the force constant matrix. Therefore, the long-range Coulomb forces are taken into account with the help of effective charges, also called Born effective charges, which are described by a charge tensor Z. In principle, the Born effective charges consider all effects of the charge polarization that act in the long-range. Additionally, the force constant matrix containing the Born effective charges leads to LO/TO splitting.
In order to obtain a microscopic expression for the force constant matrix, which provides an adequate description for ionic materials, the inverse of the dielectric function ϵ^{-1} of the electrons must be included in addition to the Born effective charges. Note that the derivation of the force constant matrix by Pick et al. is based only on the Born-Oppenheimer and harmonic approximation. The ϵ^{-1} dependence of the force constant matrix ensures a correct description of the disappearance of the acoustic frequencies for long phonon wavelengths. In this context, the static dielectric tensor ϵ describes the response of the nuclei in the static long-wavelength range. To take into account the Born effective charges, the NAC term has to be added to the dynamical matrix near the Γ-point [87, 89]:

$$D_{\alpha\beta}(jj', \mathbf{q} \to \mathbf{0}) = \underbrace{D_{\alpha\beta}(jj', \mathbf{q} = \mathbf{0})}_{\text{A term}} + \underbrace{\frac{1}{\sqrt{M_j M_{j'}}} \frac{4\pi}{\Omega_0} \frac{\left[\sum_\gamma q_\gamma Z_j^{\gamma\alpha}\right]\left[\sum_{\gamma'} q_{\gamma'} Z_{j'}^{\gamma'\beta}\right]}{\sum_{\alpha\beta} q_\alpha \epsilon_{\alpha\beta}^{\infty} q_\beta}}_{\text{NAC term}}. \tag{2.107}$$

Here, the Greek indices α, β, γ are running over the Cartesian coordinates x, y, z, while the index j is running over the different atoms in the unit-cell. In addition, Ω_0 is the unit-cell volume, M_j is the mass of the j-th atom in the unit-cell, q_α is the

α-th component of the phonon wave vector $\mathbf{q}$ and $Z_j^{\alpha\beta}$ is the effective charge tensor, i.e. the Born effective charges. The electronic dielectric function ϵ_0 is formed by a tensor $\epsilon_{\alpha\beta}^{\infty}$ and can be written as follows:

$$\epsilon_0(\mathbf{q}) = \sum_{\alpha,\beta} q_\alpha \epsilon_{\alpha\beta}^{\infty} q_\beta. \tag{2.108}$$

Note that the dielectric function ϵ_0 is valid at both macroscopic and microscopic levels. The main difference between the two terms on the right-hand side of the dynamical matrix in equation (2.107) is the analytical behavior with respect to the $\mathbf{q}$ wave vector at $\mathbf{q} = 0$. The A term in equation (2.107) is analytical in contrast to the NAC term, which includes the effective charges and is discontinuous for $\mathbf{q} = 0$. Moreover, the original dynamical matrix (A term) would be sufficient to describe metals and non-ionic insulators, whose interaction has a finite range. Additionally, the NAC term is needed to capture all long-range Coulomb interactions present in ionic crystals in conjunction with a poly-atomic basis.
In order to rationalize the NAC term, some important conditions for Z are illustrated. In analogy to the conventional charge neutrality of the system, which enables the Fourier transform of the Coulomb potential at zero [87]:

$$V_{\text{Coulomb}}(\mathbf{q}) = \begin{cases} \frac{4\pi Z e^2}{q^2} & \text{for} \quad q \neq 0, \\ 0 & \text{for} \quad q = 0, \end{cases}$$

the effective charge neutrality is defined as a well-defined tensor:

$$Z_j^{\alpha\beta} = \lim_{\mathbf{q}\to\mathbf{0}} Z_j^{\alpha\beta}(\mathbf{q}). \tag{2.109}$$

In particular, $Z_j^{\alpha\beta}$ shows the independence of the direction of $\mathbf{q}$. The corresponding necessary effective charge neutrality, which is a requirement of the system, can be written as follows:

$$\sum_j Z_j^{\alpha\beta} = 0. \tag{2.110}$$

Note that the effective charge neutrality is generally not identical to the conventional charge neutrality, but is implied by it here. Consequently, the effective charge neutrality ensures the acoustic sum rule when considering long phonon wavelengths, i.e. all frequencies of the acoustic modes disappear for $\mathbf{q} \to 0$.
Next, the Born effective charges can be linked to the macroscopic electric field $E_j^{\alpha\beta}$ using the microscopic expression for $Z_j^{\alpha\beta}$ [87]:

$$\lim_{\mathbf{q}\to 0} \epsilon_0^{-1}(\mathbf{q}) \sum_\alpha q_\alpha Z_j^{\alpha\beta} |e| = \frac{\Omega_0}{4\pi} \lim_{\mathbf{q}\to 0} \sum_\alpha q_\alpha E_j^{\alpha\beta}. \tag{2.111}$$

This means that the charge $Z_j^{\alpha\beta}|e|$ is screened in a macroscopic way and reveals the specific macroscopic electric field. Conversely, this is equivalent to keeping

the macroscopic electric field $E_j^{\alpha\beta}$ constant, which provides information about the intrinsic polarization caused by the system itself. With the help of the polarisation P_α per unit-cell, the Born effective charges are defined as follows [36]:

$$Z_j^{\alpha\beta}|e| = \left.\frac{\partial P_\alpha}{\partial \tau_{j\beta}}\right|_{E_{\text{macroscopic}}}. \tag{2.112}$$

Here, $\tau_{j\beta}$ is a displacement of the j-th nucleus. Note that the Born effective charges are non-zero for ionic crystals consisting of a poly-atomic basis, even in the absence of a macroscopic electric field [90].
To summarize, the intrinsic lattice polarization, as described by the Born effective charges Z, must be considered to account for long-range Coulomb forces. This leads to an additional term, the NAC term, which must be added to the interatomic force constant C when the phonon wave vectors become small, as is the case at the Γ-point (schematic representation of the formula):

$$C = C_{\text{analytical}} + C_{\text{non-analytical correction}}(Z). \tag{2.113}$$

The inclusion of the NAC term leads to the splitting of the optical branch into LO and TO branches at the BZ center for a material with a poly-atomic basis.

Imaginary phonon frequencies

If the eigenvalue equation of the dynamical matrix (2.21) provides also negative eigenvalues

$$\omega_{\mathbf{q}\nu}^2 = -|\lambda_{\mathbf{q}\nu}|, \tag{2.114}$$

the corresponding frequencies are referred to as imaginary frequencies

$$\omega_{\mathbf{q}\nu} = i\sqrt{|\lambda_{\mathbf{q}\nu}|}. \tag{2.115}$$

In general, imaginary frequencies provide indications of instabilities in the structure or geometry [14, 91]. They indicate that there is an ion configuration that corresponds to a negative potential, which is in contradiction to the assumption that the potential is in equilibrium or at its minimum [32]. Note that displacing the nuclei along a specific imaginary mode means that the structure becomes unstable or results in a structure of lower energy.
On the one hand for very harmonic materials such as Si (see chapter 3), theories like the finite-difference method provide an accurate phonon description that do not lead to imaginary frequencies. On the other hand, the finite-difference method also provides imaginary frequencies for anharmonic materials such as the HaP $CsPbBr_3$ (see Fig. 2.12). Phonon modes that belong to imaginary frequencies are also referred to as soft phonon modes. These soft phonon modes induced by anharmonicity are responsible for the octahedral tilting in materials such as HaPs [14, 92, 8]. Therefore, cubic HaP structures, which exhibit octahedral tilting, show a lower energy than

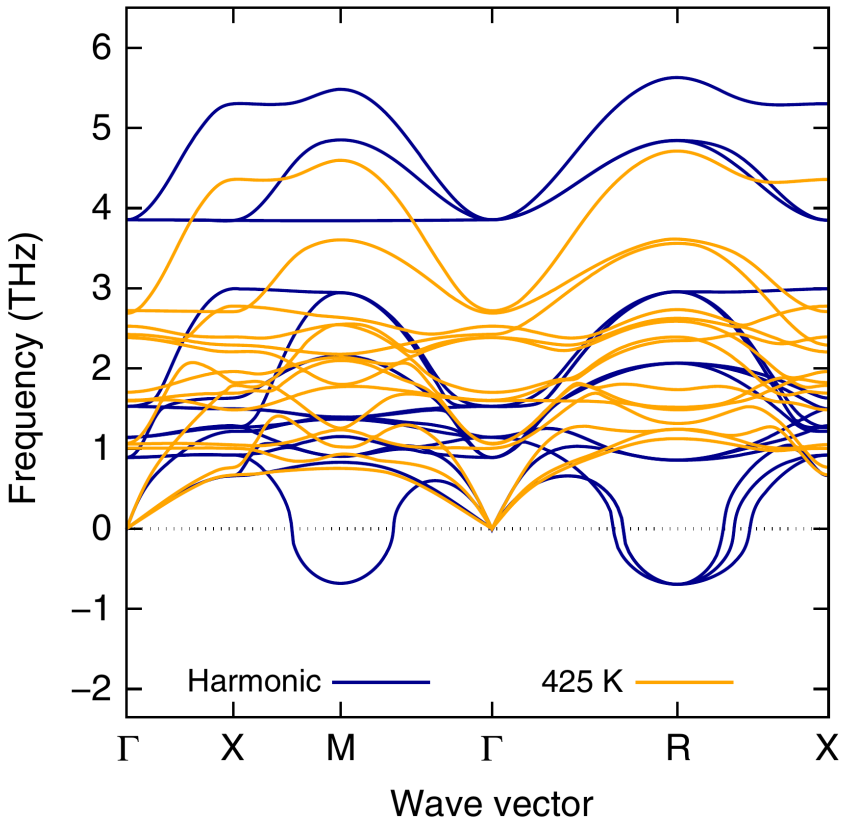

Figure 2.12. Phonon dispersion relation of cubic $CsPbBr_3$ calculated using the finite-difference method (blue line) without taking temperature into account and calculated with the help of MD (orange line) at finite-temperature $T = 425\,\mathrm{K}$. The finite-difference method works purely in the harmonic approximation and shows strong imaginary frequencies at the M- and R-point at the BZ boundary. The MD calculation also accounts for anharmonicity and therefore imaginary frequencies are not present. *Reprinted with permission from [93], published under a CC BY 4.0 license.*

the corresponding cubic high-symmetry structure, where the tilting is not present. However, in order to include soft phonon modes, the theory must take anharmonicity into account, as is the case in MD (see Fig. 2.12).
In addition to structural instabilities, numerical problems can also cause imaginary frequencies. These numerical issues can be circumvented by increasing the energy cut-off, but this cannot be regarded as a general solution for eliminating them.

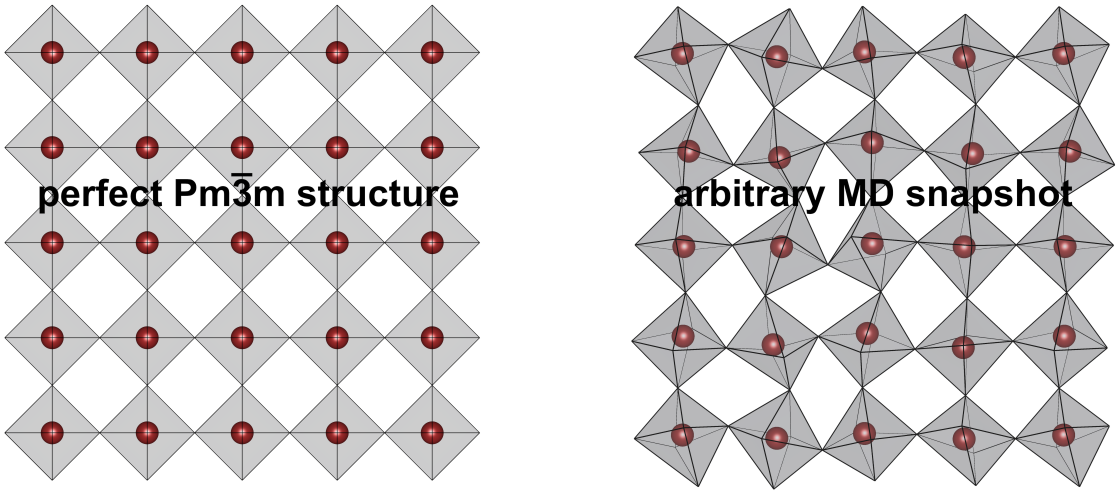

Figure 2.13. Left-hand side: cubic high-symmetry structure (Pm$\bar{3}$m) of $CsPbBr_3$, which can only be seen as an average. Right-hand side: arbitrary MD snapshot of the trajectory of $CsPbBr_3$. The thermal motion leads to disorder, which can be seen as tilting of the octahedra and displacements of the atoms (discussed in more detail in chapter 4).

2.5. Modeling of thermal and dynamical properties

2.5.1. Molecular dynamics

Molecular dynamics (MD) is based on the ergodic hypothesis, which states that the ensemble and time average of an observable A are equal:

$$\langle A \rangle = \underbrace{\int\int d\mathbf{q}\, d\mathbf{p}\; A(\mathbf{q},\mathbf{p})\rho(\mathbf{q},\mathbf{p})}_{\text{ensemble average}} = \underbrace{\lim_{t\to\infty} \frac{1}{t} \int_0^t dt' A(\mathbf{q}(t'),\mathbf{p}(t'))}_{\text{time average}} . \tag{2.116}$$

Here, ρ is the phase-space density and $\mathbf{q}, \mathbf{p}$ are the generalized coordinates and conjugate generalized momenta of an observable A. The expression on the right-hand side of the ergodic hypothesis (2.116) denotes the time average of the phase-space trajectory and is calculated with the help of the MD trajectory. In addition, the time evolution in MD simultaneously includes temperature and, therefore, leads to finite-temperature DFT. This is achieved by incorporating the thermal motion of a system, which leads to a change in structure due to displaced atoms. Over time, the thermal motion induces disorder in an initially ordered structure (see Fig. 2.13).
However, the inclusion of the thermal motion is based on a classical approach in which the motion of the nuclei is given by a macroscopic equation of motion, i.e. Newton's equations of motion. Note that tunneling effects or zero point vibrations are not considered in the classical equation of motion and, therefore, cannot be described by MD. If the motion of the nuclei is given by Newton's equation of

motion and the force acting on the nuclei can be expressed by a conservative force field V, the following can be written:

$$M_I \frac{d^2}{dt^2}\mathbf{R}_I(t) = -\nabla_I V(\{\mathbf{R}_I\}). \tag{2.117}$$

Here, M_I is the mass of the I-th nucleus and $\{\mathbf{R}_I\}$ denotes the set of nuclei positions. In general, there are two approaches to solve this equation: the first one is called force field MD, in which a complex parametrization of the potential force field $V^{FF}(\{\mathbf{R}_I\})$ is applied, and the second one is called ab-initio MD, in which the forces F_I acting on the nuclei are calculated using first-principles electronic structure methods, such as DFT. Note that the ab-initio MD is also referred to as first-principle MD and can be considered as parameter-free. The focus here is on ab-initio MD.
The ab-initio MD itself can be provided by either the Car-Parrinello MD or the Born-Oppenheimer MD. The main difference between these two approaches is the fact that Car-Parrinello MD [94] does not have to refer to the electronic ground state at every simulation step. However, the Born-Oppenheimer MD is implemented in VASP, and is therefore discussed in more detail here.
In order to be able to apply the Hellmann-Feynman theorem (see chapter 2.2.9), two requirements must be fulfilled: the first is given by the BO approximation, which states that the electrons remain in their ground state ψ_0 while the nuclei move, and the second is given by the fact that the positions of the nuclei R_I are only included as parameters in the Kohn-Sham Hamilton operator. Therefore, the forces acting on the nuclei can be expressed using the Hellmann-Feynman theorem as follows:

$$\mathbf{F}_I^t = -\nabla_I \min_{\{\psi_i\}} \langle \psi_i | H^{\mathrm{KS}} | \psi_i \rangle. \tag{2.118}$$

Furthermore, the Hellmann-Feynam theorem can only be applied to time-independent Hamilton operators, such as the Kohn-Sham Hamilton operator, and thus the time t only appears as a parameter, denoted by $\mathbf{F}_I^t$. Applying the variation principle to the ground state ψ_0 simplifies the above equation to

$$\mathbf{F}_I^t = -\langle \psi_0 | \nabla_I H^{\mathrm{KS}} | \psi_0 \rangle. \tag{2.119}$$

This equation is used by DFT to calculate the forces at a specific time t and a specific position R_I^t with respect to the ground state.
However, the Verlet algorithm is used to take into account the time evolution of the system, i.e. to update the positions of the nuclei over time [95]. Here, the trajectory develops in discrete time steps of the size Δt. The new position at time $t + \Delta t$ and the previous position at time $t - \Delta t$ can be expressed as follows:

$$\begin{aligned} \mathbf{R}_I^{t+\Delta t} &= \mathbf{R}_I^t + \Delta t\ \mathbf{v}_I^t + \frac{1}{2}\Delta t^2\ \mathbf{a}_I^t, \\ \mathbf{R}_I^{t-\Delta t} &= \mathbf{R}_I^t - \Delta t\ \mathbf{v}_I^t + \frac{1}{2}\Delta t^2\ \mathbf{a}_I^t. \end{aligned} \tag{2.120}$$

By summing up these equations, it is shown that only the information of the current position $\mathbf{R}_I^t$ at time t, the current acceleration $\mathbf{a}_I^t$ at time t and the information of the

previous position $\mathbf{R}_I^{t-\Delta t}$ at time $t - \Delta t$ is used to determine the new position $\mathbf{R}_I^{t+\Delta t}$ at time $t + \Delta t$:

$$\mathbf{R}_I^{t+\Delta t} = 2\mathbf{R}_I^t - \mathbf{R}_I^{t-\Delta t} + \Delta t^2 \, \mathbf{a}_I^t. \tag{2.121}$$

The acceleration can be expressed explicitly by the force:

$$\mathbf{R}_I^{t+\Delta t} = 2\mathbf{R}_I^t - \mathbf{R}_I^{t-\Delta t} + \Delta t^2 \, \frac{1}{M_I}\mathbf{F}_I^t. \tag{2.122}$$

This equation is used to calculate the new positions of the nuclei for each time step of the trajectory. Note that the investigated MD simulation time or the length of the trajectory consists of a sequence of discrete time steps.
This point raises two important questions: Firstly, how large must a time step Δt be, and secondly, how long must the simulation time be? In general, the time step is a very important parameter in an MD simulation and depends on the material itself and on the investigated observable. The upper limit is determined by the oscillation period of the atoms in the crystal, which means that one time step may only sample once per oscillation period. As a rule of thumb, the time step must be 10 to 100 times smaller than the oscillation period of vibrations in order to capture the dynamics correctly [96]. If the material consists of heavy and light atoms, the faster vibrating light atom determines the time step. However, the lower limit is given quantitatively by the available computer resources or by the fact that small time steps lead to long runtimes in MD simulations. This leads to the second question, namely the length of the trajectory or the simulation time.
In principle, the trajectory consists of an equilibration run and a production run. The former is completed when the initial velocities of the atoms are Maxwell-Boltzmann distributed, as in a classical particle system. Note that the Maxwell-Boltzmann distributed velocities are later a requirement for the definition of a constant temperature, which guarantees the validity of the equipartition theorem (2.123)). The production run must last until the investigated observable is statistically converged. For instance, the vibrational density of states (VDOS) of a material converges relatively fast when the phonon frequencies are high. But for a material with low phonon frequencies, long MD trajectories are required to achieve a converged VDOS. Thus, the length of the trajectory, as well as the size of the time step, are determined by both, the observable and the material.
Since MD describes the thermal motion at a specific temperature, a suitable definition of temperature must first be found. For this purpose, the equipartition theorem of energy is used to define the temperature. The equipartition theorem states that in thermal equilibrium the energy is equally distributed over all degrees of freedom. It follows that the average kinetic energy, distributed over all degrees of freedom, which occur quadratically in the Hamilton operator of the system, can be written as follows [97]:

$$\langle \frac{1}{2} M_I \mathbf{v}_I^2 \rangle = \frac{1}{2} k_\mathrm{B} T. \tag{2.123}$$

For a system consisting of N particles and N_f degrees of freedom, the total kinetic energy defines the macroscopic temperature at time t [97]:

$$T(t) = \frac{1}{N_\mathrm{f}} \frac{2}{k_\mathrm{B}} \sum_{i=I}^{N} \frac{1}{2} M_I \mathbf{v}_I(t)^2. \tag{2.124}$$

Since the velocities or the kinetic energy show a fluctuating behavior, there is consequently also a fluctuating temperature from time step to time step. Note that the temperature fluctuates along the trajectory around a predefined equilibrium temperature.
In addition, a requirement for the application of the Hellmann-Feynamic theorem in (2.118) is the time independence of the Hamilton operator, which leads to a vanishing total time derivative

$$\frac{dH}{dt} = 0 \quad \Leftrightarrow \quad E = \text{constant}. \tag{2.125}$$

This means that the total energy E of the system is conserved. Consequently, the system is in the microcanonical ensemble as an NVE ensemble, since so far the particle number and the cell parameters are not dynamic variables, i.e. N and V are also constant.
In order to control the temperature in (2.124), one possible approach would be to rescale the masses M_I or the velocities $\mathbf{v}_I$. However, this would lead to inaccuracies or unphysical behavior in the MD simulation with respect to the nuclear positions, which is a disadvantage. A more precise method to control the temperature is to use a thermostat, which avoids these inaccuracies caused by the rescaling approach. This leads to the canonical ensemble or NVT ensemble, in which the temperature T is kept constant instead of the total energy E. In the NVT ensemble, the system is embedded in a heat bath that allows for energy fluctuations, while the MD temperature fluctuates according to the kinetic energy of the ions. In principle, several variants of thermostats are available for the VASP-MD simulation, such as the Nosé-Hoover thermostat [98, 99].
The basic idea of isothermal-isochore MD using the Nosé-Hoover thermostat is to introduce an additional degree of freedom, denoted by s, which leads to additional terms in the Hamilton operator. The extension of the Hamilton operator[11] introduces artificial coordinates and momenta, so that a momentum p_s is assigned to the additional degree of freedom s. The connection between real and artificial variables is given by the following transformation, where real variables are denoted by a *prime* [97]:

$$\begin{aligned} \mathbf{R}'_I &= \mathbf{R}_I, \\ \mathbf{P}'_I &= \frac{1}{s} \mathbf{P}_I, \\ s' &= s, \\ \Delta t' &= \frac{1}{s} \Delta t. \end{aligned} \tag{2.126}$$

[11] Note that the original derivation of an extended Hamilton operator is based on an extended Lagrangian.

As this transformation also performs time scaling, there are variations in the time intervals. This leads to a time stretch of the artificial time interval, i.e. $\Delta t = s\Delta t'$. In order to avoid this undesirable effect in the MD simulation, a later transformation back to the real variables is necessary. However, with the help of the transformation, the Nosé-Hamilton operator for a system with N atoms can be written as follows:

$$H_{\text{Nosé}} = \sum_{I=1}^{N} \frac{\mathbf{p}_I^2}{2M_I s^2} + V(\{\mathbf{R}_I\}) + \frac{p_s^2}{2Q} + Lk_{\text{B}}T\ln(s) \tag{2.127}$$

Note that s is dimensionless and Q has the role of a hypothetical effective mass[12] corresponding to s. Furthermore, L is a factor that must be set to 3N for the real-variable description. The logarithmic term $\ln(s)$ ensures that the time is scaled correctly to obtain the NVT ensemble. The equations of motion can be derived from the Nosé-Hamilton operator using the Hamilton formalism:

$$\frac{d\mathbf{p}_I}{dt} = -\frac{\partial H_{\text{Nosé}}}{\partial \mathbf{R}_I}. \tag{2.128}$$

After transforming back to the real variables, the following equation is obtained for the momentum:

$$\frac{d}{dt}\mathbf{p}_I = -\nabla_I V(\{\mathbf{R}_I\}) - \frac{sp_s}{Q}\mathbf{P}_I. \tag{2.129}$$

Here, all variables are real, i.e. they are actually labeled with a *prime* sign, but for reasons of clarity all *prime* signs are neglected. With the exception of the last term on the right-hand side of the equation (2.129), this equation is identical to (2.117). The additional term ζ has the meaning of a thermodynamic friction or "viscosity" term

$$\zeta = \frac{sp_s}{Q}. \tag{2.130}$$

With the help of the complete friction term in (2.129), which is proportional to the velocity $\mathbf{v}_I$ via the momentum, the kinetic energy can be controlled and thus the temperature as defined in equation (2.124). In addition, the hypothetical mass Q is a measure of the coupling strength between the real system and the heat bath. Between the individual MD snapshots calculated for each time step, temperature fluctuations occur around the predetermined equilibrium temperature due to the instantaneous kinetic energies of the ions. Note that the ensemble is still an NVT ensemble, with energy fluctuations between the real system and the heat bath, while maintaining the energy of the combined system.

A similar derivation using an extension of the Hamilton operator can be applied to achieve an isothermal-isobaric MD simulation. In this MD simulation the system is an NPT ensemble with constant pressure P instead of constant volume V as in the NVT ensemble. In addition, a barostat is used to control the pressure. NPT MD is particularly essential for a correct description of phase transitions. However, computationally intensive optimisation processes of the dynamic lattice parameters

[12] Note that, mathematically speaking, Q is the partition function.

are unavoidable for each MD step in the NPT simulation.
Note that the MD method inherently takes into account anharmonicity, which is discussed in more detail in the chapter 2.5.3.

2.5.2. Monte-Carlo method

In addition to the MD method, the Monte-Carlo (MC) method is another first-principles approach to statistically access the thermal evolution of an observable, e.g. the band gap. In general, MC methods are used when no analytical solutions are possible and the information of the system can be predicted by repeating random executions using probability theory. However, the statistical prediction of an event is only justified on the basis of the law of large numbers. Here, the number to be maximised is the number of supercells, which is used to obtain converged results for the observable of interest.
A simple example to understand MC is to estimate the value of π by calculating a quarter of a circular area. The interesting question in this example is how to distribute or randomly generate the sampling points within the square surrounding the quarter circle. This task is transferred to the Markov chain, which cannot always be constructed trivially. In general, the mathematical phase space is often too large to perform the summation completely. However, the Markov chain specifies after which summand the summation over the states can be truncated. In addition, the Markov chain assigns different probability weights to the individual states in the summation. If a Markov chain can be found or constructed, one can speak of an *importance sampling*. It is particularly important that the Markov chain must cover the entire phase space and not just parts of it in order to take ergodicity into account. In the case of ergodicity, the expectation value of an observable A can simply be written as the arithmetic mean of the observable

$$\langle A \rangle = \frac{1}{n} \sum_{i=1}^{n} A(x_i), \tag{2.131}$$

where x_i denotes a probability-weighted state occurring in the Markov chain and n is the number of used samples.
The MC variant developed by Zacharias et al. [100], which is based on *importance sampling* MC [101], takes thermal motion into account and, therefore, incorporates temperature in DFT. These first-principles calculations involve lattice vibrations by sampling the displacements according to a temperature-dependent Markov chain. In particular, the atoms in the supercell are displaced by temperature-dependent displacements along the phonon eigenmodes, which generates thermally perturbed atomic configurations. For example, the MC method can calculate the temperature-renormalized band structure as a statistical average from the set of thermally perturbed supercells. Note that the MC method can also calculate the zero-point renormalization compared to MD, which is explained in chapter 2.6.
Here, the temperature-dependent electronic band gap A is investigated and can be

written as the arithmetic mean of band gaps calculated from the set of thermally perturbed structures x_i^{MC}:

$$\langle A(T)\rangle = \frac{1}{n}\sum_{i=1}^{n} A(x_i^{\mathrm{MC}}(T)). \tag{2.132}$$

Furthermore, the distorted structures generated from the *importance sampling* MC method are based on the quantum-harmonic oscillator, and therefore this specific MC approach uses the framework of the harmonic approximation [102]. The magnitude of the displacements is determined by a Gaussian probability distribution whose width is given by the mean square-displacement of the harmonic oscillator. The mean-square displacement can be written as follows:

$$\langle u_{\nu\kappa}^2\rangle = \frac{\hbar}{2M_\kappa\omega_\nu}\coth\frac{\hbar\omega_\nu}{2k_{\mathrm{B}}T}, \tag{2.133}$$

where M_κ is the mass of the κ-th atom in the supercell and ω_ν is the phonon eigenfrequency of the ν-th phonon mode. Using the temperature-dependent mean-square displacement, the Gaussian probability distribution can be formulated as follows:

$$dW_\nu(\kappa,T) = \frac{1}{2\pi\langle u_{\nu\kappa}^2\rangle}e^{-\frac{\kappa^2}{2\langle u_{\nu\kappa}^2\rangle}}d\kappa, \tag{2.134}$$

where κ is a multi-index that takes into account the Cartesian coordinates as well as the atom number in the supercell. Note that the probability distribution indicates the probability of an atom being located in the coordinate range $\kappa + d\kappa$.
Each sample of displacements or distorted structure is generated by adding temperature-dependent displacements $\Delta\tau_i^{\mathrm{MC}}$ to the equilibrium structure:

$$x_i^{\mathrm{MC}}(T) = x_{\mathrm{equilibrium}} + \Delta\tau_i^{\mathrm{MC}}(T), \tag{2.135}$$

where the specific form of the displacement is given by

$$\Delta\tau_i^{\mathrm{MC}}(T) = \sqrt{\frac{1}{M_\kappa}}\sum_{\nu}^{3(N-1)}\epsilon_{\kappa\nu}\,P(T). \tag{2.136}$$

The direction of the displacement is along the phonon eigenmode vector $\epsilon_{\kappa\nu}$ with a magnitude corresponding to a normal-distributed random variable $P(T)$ based on $dW_\nu(\kappa,T)$ of the equation (2.134). Furthermore, $P(T)$ also allows to select between the Bose-Einstein or the Maxwell-Boltzmann statistics when generating the random structures. Displacements according to acoustic modes are trivially excluded in the summation, i.e. translational modes are skipped. In the same way, phonon modes with negative or imaginary frequencies do not contribute to the set of displacements.

The MC method shows a correlation in the convergence behavior of the temperature-dependent band gap between the required number of samples n and the size of the supercells. The larger the size of the supercell, the fewer samples n are required

to achieve convergence. This fact led to the development of the One-Shot method (OS), in which the entire thermal information is contained in just one single distorted structure [103, 102]. The specific displacement in the OS method is given by:

$$\Delta\tau^{\mathrm{OS}} = \sqrt{\frac{1}{M_\kappa}} \sum_{\nu}^{3(N-1)} (-1)^{\nu-1} \epsilon_{\kappa\nu} \sigma_\nu(T), \tag{2.137}$$

where σ_ν determines the magnitude of the displacements:

$$\sigma_\nu(T) = \sqrt{\frac{\hbar}{2\omega_\nu}(2n_\nu(T)+1)}. \tag{2.138}$$

Here, the occupation number n_ν is given by the Bose-Einstein statistics of the equation (2.142) and the summation over ν runs from the lowest to the highest phonon eigenfrequency, i.e. in ascending order. Using the OS method, the arithmetic mean of the temperature-dependent band gap is given by a single calculation:

$$\langle A(T) \rangle = A(x^{\mathrm{OS}}(T)). \tag{2.139}$$

In principle, the results of the OS method and converged MC method tend to be equal, if the size of the supercell is increased towards infinity [103].
In addition, in statistical approaches based on distorted structures such as MD or MC, the temperature-dependent band gap is not only an average value over the number of supercells used, but also an average value of the contributing valence or conduction bands. For example, in diamond the VBM is threefold and the CBM is sixfold degenerate in the case of a unit-cell or non-displaced supercell. If the distorted structures are generated, as in MD or MC, the degeneracy of the VBM and CBM is lifted. Thus, in the case of diamond one would average over the three VBM and six CBM bands to obtain the actual VBM and CBM bands that contribute to the band gap. Note that the electronic bands remain degenerate in perturbative methods such as the Allen-Heine-Cardona theory, which is discussed in chapter 2.6.1.

2.5.3. Anharmonicity: The difference between molecular dynamics and Monte Carlo

Both first-principles methods, MD and MC, incorporate temperature by generating thermally distorted structures and thus go beyond static DFT calculations. However, the way in which MD and MC take thermal motions into account is completely different. The former, MD, calculates the positions of the atoms by solving Newton's classical equation of motion. The latter, MC, calculates phonons within the harmonic approximation and displaces atoms along the phonon modes using a Gaussian probability distribution based on the harmonic oscillator (HO). The principle of the harmonic approximation is the expansion of the nuclear potential around the equilibrium up to second order with respect to the nuclear displacements. This leads to a parabolic potential in which MC calculates the phonons. If the validity of

small phonon energies, which is the requirement for the harmonic approximation, is violated, a parabolic potential is no longer sufficient to sample thermal motions. Therefore, vibrational anharmonicity must be included in the description, which is achieved by considering all terms beyond the second order:

$$U = U_0 + \frac{1}{2!}\sum_{x\,x'} \frac{\partial^2 U}{\partial\tau_x \partial\tau_{x'}}\Delta\tau_x\Delta\tau_{x'} + \underbrace{\frac{1}{3!}\sum_{x\,x'\,x''} \frac{\partial^3 U}{\partial\tau_x \partial\tau_{x'}\partial\tau_{x''}}\Delta\tau_x\Delta\tau_{x'}\Delta\tau_{x''} + \ldots}_{\text{Anharmonicity}}, \tag{2.140}$$

where the notation is the same as in chapter 2.1.4, with x having the meaning of $x = (p\kappa\alpha)$. Therefore, MC cannot go beyond the independent phonon picture described by decoupled HO and neglects anharmonicity.
Especially for anharmonic materials such as HaPs, the anharmonicity strongly influences the description of phonons, as can be seen in Figure 2.12. Soft modes or imaginary phonon modes, which are a sign for an unstable structure, are an indication that a description in the harmonic approximation is insufficient and that the inclusion of anharmonicity is required.
In contrast to MC, MD takes into account all types of atomic motions, particularly anharmonic structural fluctuations. This is reflected in the fact that dynamics such as octahedral tilting or large atomic displacements, which are typical for anharmonicity [104, 105], occur in structures generated from MD but not from MC. A schematic diagram of the impact on the band gap resulting from different microscopic displacements, harmonically perturbed (MC) or including the anharmonic dynamics (MD), is shown in Fig. 1.1. For HaPs, however, there are different deviations from the static band gap, resulting from the average cubic high-symmetry structure, to the average band gap from samples generated by various dynamic [2, 7, 13] or quasistatic calculations [10].
In addition, these anharmonic dynamics are important, for example, to properly describe the temperature-dependent electronic band gap in comparison to the experiment [2]. Other examples where anharmonicity plays an important role for HaPs are the description of temperature-induced phase transitions [106], the calculation of short phonon lifetimes [93] and the calculation of Raman spectra [107, 108].

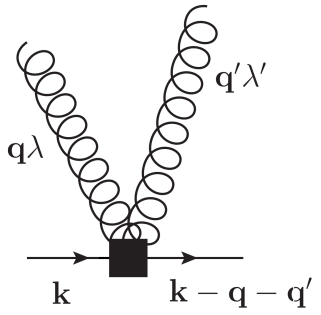

Figure 2.14. Diagrammatic representation of a second order interaction term or vertex from a Taylor expansion of the Hamilton operator with respect to nuclear displacements. The solid line denotes a electron with momentum **k** and the spiral line denotes a phonon with momentum **q** in the scattering event. λ is the phonon branch index and the quantities after the scattering event are labeled with a *prime*. Note that a single line denotes only a propagator in the diagrammatic approach. *Reprinted figure with permission from [110]. Copyright (2015) by the American Physical Society.*

2.6. Electron-phonon coupling

The standard DFT theory is often referred to as a ground state theory at zero Kelvin, which can be somewhat misleadingly interpreted as if the DFT describes physics at zero Kelvin. A more appropriate interpretation would be that DFT calculates the ground state density of a system without taking any temperature into account. The thermal evolution of electronic eigenvalues can be described within DFT using methods such as MD and MC or by calculating the electron-phonon coupling (EPC), taking into account the equivalence of phonons as lattice vibrations [109]. In the conventional Kohn-Sham DFT, the interaction between dynamic lattice vibrations and electrons is per se not present. Note that the term of the lattice potential V_{ext} in the Kohn-Sham equation (2.31) accounts for a static potential from the nuclei. In principle, the interaction of electrons and phonons can be described by a Hamilton operator as discussed in equation (2.13). From a perturbative ansatz, a Taylor expansion of the Hamilton operator with respect to the nuclear displacements leads to explicit expressions for higher-order interaction terms of electrons and phonons. For example, Fig. 2.14 shows a second order interaction vertex in the diagrammatic representation.

In general, two physical effects are responsible for the temperature dependence of the electronic band structure: the first is the thermal occupation of phonons, which can have a large influence, while the second, the thermal expansion of the lattice, makes a rather small contribution [111, 112]. Under the condition of constant pressure, the two effects causing the temperature dependence of the electronic eigenvalues can be written as follows [113]:

$$\left(\frac{\partial \epsilon_{i\mathbf{k}}}{\partial T}\right)_P = \underbrace{\left(\frac{\partial \epsilon_{i\mathbf{k}}}{\partial T}\right)_V}_{\text{Constant Volume}} + \underbrace{\left(\frac{\partial \epsilon_{i\mathbf{k}}}{\partial lnV}\right)_T}_{\text{Constant Temperature}} \underbrace{\left(\frac{\partial lnV}{\partial T}\right)_P}_{\text{Thermal Expansion}} . \tag{2.141}$$

The first term on the right-hand side of the equation takes into account the phonon population at constant volume, while the second term takes into account the thermal expansion at constant temperature.
The thermal occupation of the phonons follows the Bose-Einstein distribution

$$n_\nu(T) = \frac{1}{e^{\frac{\hbar\omega_\nu}{k_\mathrm{B}T}} - 1}, \tag{2.142}$$

where T is the temperature, k_B is the Boltzmann constant and ω_ν is the corresponding phonon frequency of branch ν. Assuming that the energy of the lattice vibration is small compared to the electronic excitation energy, the thermal contribution to the electronic eigenvalue can be written as follows [114]:

$$\epsilon_{i\mathbf{k}}(T) = \tilde{\epsilon}_{i\mathbf{k}}(0) + \frac{1}{N}\sum_\nu \frac{\partial\epsilon_{i\mathbf{k}}}{\partial n_\nu}\left(n_\nu(T) + \frac{1}{2}\right), \tag{2.143}$$

where $\tilde{\epsilon}_{i\mathbf{k}}(0)$ is the static electronic eigenvalue calculated with the equilibrium geometry, N is the total number of phonon vectors, $\frac{\partial\epsilon_{i\mathbf{k}}}{\partial n_\nu}$ is the EPC energy and n_ν is the phonon occupation number.
The EPC energy at zero temperature is understood as zero-point renormalization (ZPR), i.e. as a contribution to the electronic energy at temperature $T = 0\,\mathrm{K}$, while phonons are not occupied or present. Specifically, the ZPR is the band gap difference between the static DFT gap calculated without temperature and the band gap that includes the calculation of the EPC energy at $T = 0\,\mathrm{K}$. This can be illustrated by considering independent or decoupled harmonic oscillators (HO) in second-quantized form [111]:

$$H^{\mathrm{HO}}_{j\mathbf{q}} = \hbar\omega_{j\mathbf{q}}\left(a^\dagger_{j\mathbf{q}}a_{j\mathbf{q}} + \frac{1}{2}\right). \tag{2.144}$$

Here, $\mathbf{q}$ denotes the phonon wave vector and j the phonon branch index. Taking the ensemble average at finite-temperature T provides the electronic eigenenergies or averaged thermal energies:

$$E^{\mathrm{HO}}_{j\mathbf{q}} = \hbar\omega_{j\mathbf{q}}\left(n_j + \frac{1}{2}\right). \tag{2.145}$$

In the case that phonons are not occupied, the eigenenergy of each oscillator becomes a remaining energy contribution, i.e. the zero-point energy or zero-point oscillation:

$$E^{\mathrm{HO}}_{0\mathbf{q}} = \frac{1}{2}\hbar\omega_{0\mathbf{q}}. \tag{2.146}$$

Note that this energy contribution is purely quantum mechanical, because the ZPR disappears when the atomic mass becomes large, i.e. $m \longrightarrow \infty$, with $\omega \propto m^{-\frac{1}{2}}$ [111]. Furthermore, the ZPR is difficult to measure in experiments. However, for conventional semiconductors the contribution of the ZPR and the temperature dependence of the electronic band structure generally have the effect of reducing the

band gap, i.e. the energy contribution to the static band gap is negative. Conversely, the inclusion of temperature in HaPs leads to an opening of the band gap, while the effect of ZPR also reduces the band gap.
There are various methods such as statistical or perturbation-based approaches that can describe the thermal evolution of electronic eigenvalues. Each method has its advantages and disadvantages and provides results with varying accuracy compared to the experiment. In the following chapters, the Allen-Heine-Cardona theory and the frozen-phonon method are discussed.

2.6.1. Allen-Heine-Cardona theory

Another theory for calculating temperature effects with the help of DFT is the Allen-Heine-Cardona theory (AHC) [115, 116, 117], which is a purely perturbation-based many-body approach. In general, AHC calculates the electron-phonon self-energy, which is composed of two first-order and one second-order electron-phonon coupling vertices in the diagrammatic approach[13]. The two first order vertices provide the dynamical Fan self-energy and the second-order vertex provides the static Debye-Waller self-energy.
A general scheme of perturbation theory is as follows

$$H(\lambda) = H^{(0)} + \lambda H^{(1)} + \lambda^2 H^{(2)} + \lambda^3 H^{(3)} + \dots, \tag{2.147}$$

where H is the Hamilton operator and λ is a perturbation parameter. The AHC theory is based on 2nd order perturbation theory, which means that the expansion of the Hamilton operator with respect to the nuclear displacements is truncated after the second order. The terms $H^{(1)}$ and $H^{(2)}$ cannot be treated separately, but together they provide the second-order energy correction $\epsilon_n^{(2)}$ and form the Debye-Waller and the Fan terms [118]:

$$\epsilon_n^{(2)} = \underbrace{\langle \phi_n^{(0)} | H^{(2)} | \phi_n^{(0)} \rangle}_{\text{Debye-Waller}} + \underbrace{\frac{1}{2}\left(\langle \phi_n^{(0)} | H^{(1)} | \phi_n^{(1)} \rangle + \text{c.c.} \right)}_{\text{Fan}}. \tag{2.148}$$

Using the rigid-ion approximation, which states that the potential is rigidly shifted according to a shifted nucleus from its equilibrium position, the Debye-Waller term can be expressed in first order coupling terms. This means that the second-order change of the Hamilton operator $H^{(2)}$ due to nuclear displacements is approximated by first order derivatives. Consequently, the calculation of the remaining first order coupling terms is suitable for linear response, i.e. DFPT.
The EPC energy contribution resulting from the frequency-dependent Fan self-energy, which renormalizes the n-th eigenvalue at the Γ-point here, is proportional to [113, 119]:

$$\frac{\partial \epsilon_{\Gamma n}^{\text{Fan}}}{\partial n_{\mathbf{q}j}} \propto \frac{1}{\omega_{\mathbf{q}j}} \text{Re} \sum_{\tau\alpha\tau'\alpha'} \sum_{n'} \frac{\langle \phi_{\Gamma n} | \nabla_{\tau\alpha} H_\tau | \phi_{\mathbf{q}n'} \rangle \langle \phi_{\mathbf{q}n'} | \nabla_{\tau'\alpha'} H_{\tau'} | \phi_{\Gamma n} \rangle}{\epsilon_{\Gamma n} - \epsilon_{\mathbf{q}n'}}, \tag{2.149}$$

[13] For a detailed explanation of the diagrammatic approach, see Giustino [15].

where j is the phonon branch index, $\mathbf{q}$ is a specific q-point and $n_{\mathbf{q}j}$ is the phonon occupation number. Note that the eigenfrequencies $\omega_{\mathbf{q}j}$ and the eigenmodes, which are not listed in the equation (2.149), used for the Fan self-energy are calculated in the harmonic approximation. Therefore, the AHC method, like the MC method, refers to the harmonic approximation.
Figure 2.15 shows the EPC contributions to the Γ_{15c} and Γ'_{25v} states of the indirect gap of diamond resulting from a specific path in the BZ. The EPC contributions are calculated using both the AHC method and the frozen-phonon method, which is explained in the next chapter 2.6.2. Note that the AHC method relies on a fine q-point sampling of the BZ, which must be dense enough for converged EPC energies. An integration over all q-points or phonon wave vectors in the BZ gives the full EPC contribution to a specific electronic eigenvalue (see further details in the description of Fig. 2.15).
Since AHC works with small unit-cells, this first-principle perturbative method offers a quick starting point in the research of the temperature-dependent band gaps. However, it has been shown for HaPs, for example, that statistical methods such as MC can predict the temperature trend of the band gap better than perturbative methods such as AHC [16]. This is due to the fact that the AHC method truncates the Taylor expansion of the Hamilton operator with respect to the nuclear displacements after the second order, whereas the MC method retains the higher order terms. Note that the truncation of the full Hamilton operator after the second order can in principle also be seen in the equation (2.13) using the second quantization formalism. More precisely, the missing higher-order terms in AHC lead to an overestimation of the temperature-dependent band gap for HaPs, while MC can correctly predict the slope (see chapter 4.7). However, in the case of HaPs, both methods, AHC and MC, cannot predict absolute band gap values, which are close to the experimental band gap values. This also applies if the SOC effect and the DFT-PBE band gap problem are taken into account.

2.6.2. Frozen-phonon method

In principle, the frozen-phonon method (FP) is based on the displacement of atoms along phonon modes [120] and is therefore also known as the finite-difference or finite-displacement method. In addition, the FP method includes the temperature via the Bose-Einstein phonon occupation number $n_\nu(T)$.
The displacements are generated with the help of generic displacements, which are added to the equilibrium positions of the atoms [119, 113]. Here, $z\mathbf{u}$ denotes a generic displacement set with $z\mathbf{u} = \{z\mathbf{e}_{\kappa,\nu}\}$, where $\mathbf{e}_{\kappa,\nu}$ denotes the eigenvector of the phonon mode ν of the κ-th atom and z is the spatial displacement corresponding to the eigenvector. In the harmonic approximation with decoupled phonon modes, the temperature-dependent eigenenergy $\epsilon_{i\mathbf{k}}(T)$ can be expressed as the thermal average

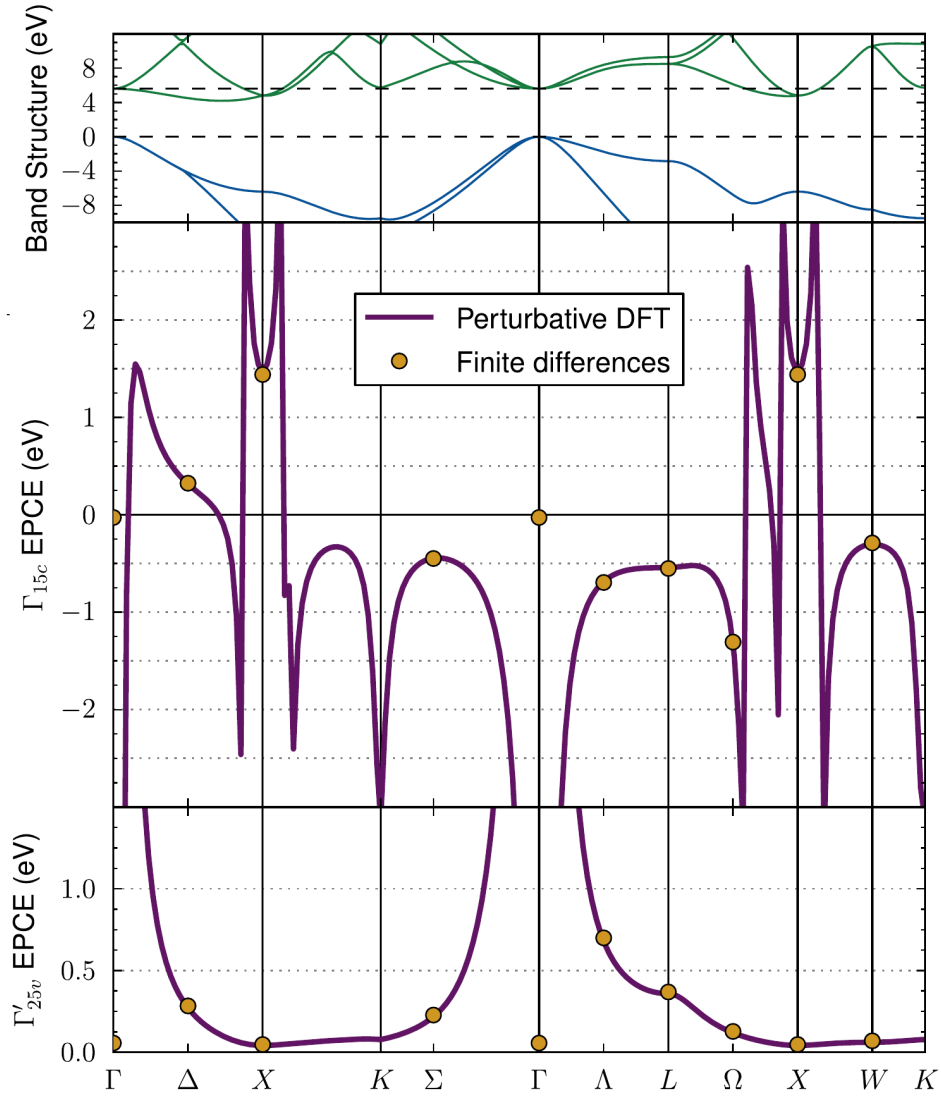

Figure 2.15. The electronic band structure of diamond is shown in the top panel, with the dashed lines indicating the energy levels of the conduction band minimum Γ_{15c} and the valence band maximum Γ'_{25v}. The notations Γ_{15c} and Γ'_{25v} denote the character table of the diamond wave functions at the Γ point, which belong to the symmetry operations of the five classes of the diamond point group (further information is provided in the Table 2.16 of [81]). The purple closed line indicates EPC energies to the Γ_{15c} state (middle panel) and Γ'_{25v} state (lower panel) from a specific path through the BZ, which are calculated with the AHC theory using DFPT. The yellow filled dots indicate the same meaning of EPC energies, but calculated with the frozen-phonon method, which is explained in the next chapter 2.6.2. Both approaches show good agreement with the exception of the Γ-point, where the AHC method shows strong divergences due to the denominator, as can be seen in the Fan self-energy in equation (2.149). Apart from the fact that most of the divergences cancel out after a full integration over the phonon wave vectors in the BZ, a small imaginary energy contribution is added to the denominator to resolve the divergence when the energies come close to the Γ-point energy (further details of smoothing the denominator are provided in [119]). *Reprinted figure with permission from [114]. Copyright (2014) by the American Physical Society.*

of the set of position-dependent eigenenergies $\tilde{\epsilon}_{i\mathbf{k}}(z\mathbf{u})$, which can be written as follows [119, 113]:

$$\begin{aligned}\epsilon_{i\mathbf{k}}(T) &\equiv \langle\tilde{\epsilon}_{i\mathbf{k}}(z\mathbf{u})\rangle(T)\\ &= \sum_{\nu}^{3N}\frac{1}{Z_\nu}\sum_{n_\nu}\exp\frac{-E_{n_\nu}}{k_\mathrm{B}T}\langle\chi_{\nu,n_\nu}|\epsilon_{i\mathbf{k}}(z\mathbf{u})|\chi_{\nu,n_\nu}\rangle.\end{aligned} \tag{2.150}$$

Here, $E_{n_\nu} = \hbar\omega_\nu(n_\nu + \frac{1}{2})$ and $|\chi_{\nu,n_\nu}\rangle$ are the eigenenergy and the eigenstate of the HO and $Z_\nu = \sum_{n_\nu}\exp\frac{-E_{n_\nu}}{k_\mathrm{B}T}$ is the mode-partition function. In addition, ν runs over all the phonon modes and n_ν is the integer phonon occupation number of the mode ν. The expansion of the eigenenergies $\tilde{\epsilon}_{i\mathbf{k}}(z\mathbf{u})$ in the harmonic approximation up to the second order in z can be written as follows:

$$\tilde{\epsilon}_{i\mathbf{k}}(z\mathbf{u}) = \tilde{\epsilon}_{i\mathbf{k}}(0) + \underbrace{\frac{\partial\tilde{\epsilon}_{i\mathbf{k}}(z\mathbf{u})}{\partial z}\bigg|_{z=0} z}_{=0} + \frac{1}{2}\frac{\partial^2\tilde{\epsilon}_{i\mathbf{k}}(z\mathbf{u})}{\partial^2 z}\bigg|_{z=0} z^2. \tag{2.151}$$

In principle, the thermal average of the terms in the expansion (2.151) are linked to the expectation values of the HO. Therefore, the first-order term vanishes, as it is an odd function:

$$\langle\chi_{\nu,n_\nu}|z|\chi_{\nu,n_\nu}\rangle = 0. \tag{2.152}$$

The expectation value of the mean square displacement of the HO can be calculated using the second quantization formalism as follows:

$$\langle\chi_{\nu,n_\nu}|z^2|\chi_{\nu,n_\nu}\rangle = \frac{\hbar}{m\omega_\nu}\left(n_\nu(T) + \frac{1}{2}\right). \tag{2.153}$$

If the expansion (2.151) is inserted into (2.150) and the results of the expectation values are used, the result is

$$\epsilon_{i\mathbf{k}}(T) = \tilde{\epsilon}_{i\mathbf{k}}(0) + \sum_{\nu}^{3N}\frac{1}{Z_\nu}\frac{\hbar}{2m\omega_\nu}\frac{\partial^2\tilde{\epsilon}_{i\mathbf{k}}(z\mathbf{u})}{\partial^2 z}\bigg|_{z=0}\sum_{n_\nu}\exp\frac{-E_{n_\nu}}{k_\mathrm{B}T}\left(n_\nu(T) + \frac{1}{2}\right). \tag{2.154}$$

Using the geometric series to calculate the sum over n_ν (see details in [119]), the above equation is simplified to

$$\Delta\epsilon_{i\mathbf{k}}(T) := \epsilon_{i\mathbf{k}}(T) - \tilde{\epsilon}_{i\mathbf{k}}(0) = \sum_{\nu}^{3N}\frac{\hbar}{2m\omega_\nu}\frac{\partial^2\tilde{\epsilon}_{i\mathbf{k}}(z\mathbf{u})}{\partial^2 z}\bigg|_{z=0}\left(n_\nu(T) + \frac{1}{2}\right). \tag{2.155}$$

If one takes the partial derivative with respect to the phonon occupation number

$$\frac{\partial\epsilon_{i\mathbf{k}}}{\partial n_\nu} := \frac{\partial\epsilon_{i\mathbf{k}}(T)}{\partial n_\nu(T)} = \frac{\hbar}{2m\omega_\nu}\frac{\partial^2\epsilon_{i,\mathbf{k}}(z\mathbf{u})}{\partial^2 z}\bigg|_{z=0}, \tag{2.156}$$

and since the phonon occupation number can be regarded as an independent variable, the equation of the temperature-dependent electronic eigenvalue can be written as follows:

$$\Delta\epsilon_{i\mathbf{k}}(T) = \sum_{\nu}^{3N} \frac{\partial\epsilon_{i\mathbf{k}}}{\partial n_\nu}\left(n_\nu(T) + \frac{1}{2}\right). \tag{2.157}$$

Taking into account the number of q-points N_q that sample the BZ for a discretization of the integral, the expression can be written as follows

$$\Delta\epsilon_{i\mathbf{k}}(T) = \frac{1}{N_q}\sum_{\mathbf{q}}\sum_{\nu}^{3N} \frac{\partial\epsilon_{i\mathbf{k}}}{\partial n_{\nu\mathbf{q}}}\left(n_{\nu\mathbf{q}}(T) + \frac{1}{2}\right). \tag{2.158}$$

This expression is the renormalization of the electronic band structure due to thermal motion in the FP method. However, the EPC energies only refer to the derivative $\frac{\partial\epsilon_{i\mathbf{k}}}{\partial n_{\nu\mathbf{q}}}$. Note that the renormalization in the FP method is only valid for small phonon energies compared to electronic excitation energies.
Figure 2.15 shows the EPC contributions to the Γ_{15c} and Γ'_{25v} states of diamond calculated with the FP method for some selected k-points in the BZ. The advantage of the FP method is that, compared to the AHC method, it does not rely on the rigid-ion approximation, but requires large supercells to capture the full phonon wavelength. In order to obtain the full EPC contribution to one state, the method is somewhat laborious, as the contribution can only be calculated point by point, i.e. without integration. In practice, the second-order derivatives in the FP or finite-displacement method are approximated, for example, by two- or five-point stencil formulas, where the displacements along the phonon modes provide the auxiliary points.

2.7. Further details on calculations

Structure relaxations

In order to perform phonon calculations, e.g. to obtain phonon dispersion relations or phonon frequencies, the initial geometry must be relaxed. In practice, this means that the forces acting on the atoms must be zero or at least below a certain threshold value. Structure relaxations can be carried out by using VASP [121] or the GADGET interface [122], for example.
However, for HaPs an instructive consistency check is to displace the atoms of the cubic high-symmetry structure by adding random, appropriately small displacements. A following structure relaxation with GADGET shows the tilting of the octahedron when the forces are minimised.

Phonon dispersion relations

The usual approach for calculating a phonon dispersion relation with Phonopy [86] is as follows: First, the atoms of the unit-cell are displaced within the supercell by

a default value of 0.1 Å for VASP. Symmetry is taken into account and reduces the number of displaced supercells required to obtain the phonon dispersion relation. Then, DFT calculations must be performed for each individual displaced supercell in order to determine the forces resulting from the displacements. Afterwards, Phonopy collects the forces to calculate the force constant matrix. After generating the dynamical matrix from the force constant matrix, Phonopy calculates the phonon frequencies and modes, i.e. the eigenvalues and eigenvectors for selected q-points. In the case of a full path through the BZ, the phonon dispersion relations are calculated by interpolation to finite q-points according to the method of Wang et al. [123, 124]. Due to numerical inaccuracies, the force constant matrix does not provide exact zero frequencies for the acoustic phonons at the Γ-point. To solve this problem, the plane wave energy cut-off in the DFT calculations can be increased, or the force threshold for the structure relaxation can be decreased. Note that these numerical issues would violate the acoustic sum rule and, therefore, need to be addressed.

3. Results and discussion: common inorganic semiconductors

3.1. Introduction to semiconductors

From the perspective of solid-state energy materials, there are three classes of materials distinguished by one of the most discussed quantity in condensed matter, namely the fundamental band gap. In the context of DFT, the fundamental band gap is given by the energy difference between the valence band (VB), i.e. the highest occupied band, and the conduction band (CB), i.e. the lowest unoccupied band. In the case of insulators, this energy barrier extends to infinity. If the fundamental band gap cannot be identified or does simply not exist, materials belong to the class of metals. The intermediate class of materials exhibit a fundamental band gap of several electron volts between 0 and 4 eV and form the class of semiconductors, which play an important role in photovoltaic or electronic devices, for example. Apart from the role of dividing the materials into classes, the fundamental band gap also characterizes the electronic response when the material is exposed to external effects, for example doping [125].
The most common inorganic semiconductors are composed from group IV of the periodic table or a combination of elements from groups III and V. This set of common inorganic semiconductors shows a distinction between direct and indirect semiconductors, which means that the fundamental band gap can be either direct as in gallium-arsenide (GaAs) or indirect as in silicon (Si). In the case of III-V compounds or group IV semiconductors the direct band gap is at the Γ-point of the BZ and the indirect band gap is at the Γ-point and along the Γ-X or the Γ-L direction [126].
Here, the specific set of investigated semiconductors is: AlAs, AlP, AlSb, GaAs, GaP, InP, and Si (the choice of this set is explained later). Si crystallizes in the cubic diamond structure belonging to the $Fd\bar{3}m$ space group (227), whereas all the remaining semiconductors crystallize in the zincblende structure belonging to the $F\bar{4}3m$ space group (216). Both structures rely on two nested face-centered cubic (fcc) Bravais lattices, which only differ in the packing density factor with a higher value for the zincblende than for the cubic diamond structure. The primitive vectors spanning up the fcc lattice are given by

$$\mathbf{a}_1 = \frac{a}{2}(0\ 1\ 1), \qquad \mathbf{a}_2 = \frac{a}{2}(1\ 0\ 1), \qquad \mathbf{a}_3 = \frac{a}{2}(1\ 1\ 0) \tag{3.1}$$

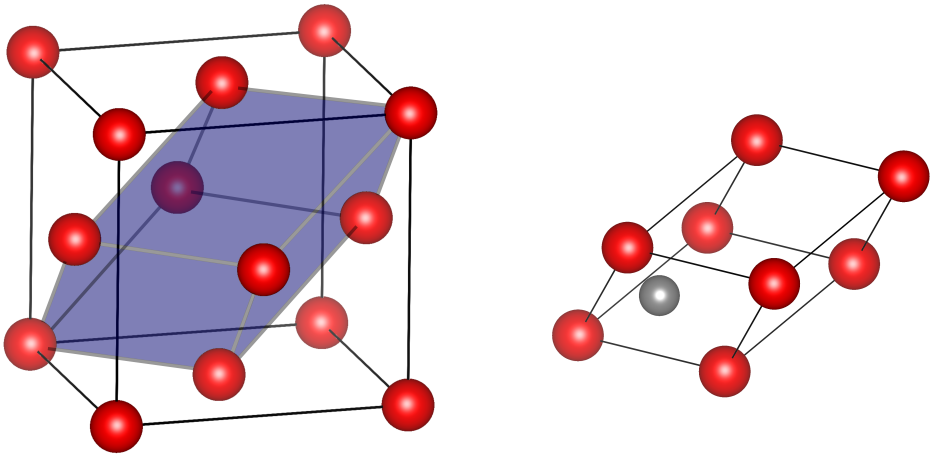

(a) Conventional Cell **(b)** Primitive Cell

Figure 3.1. (a) A conventional fcc cell containing one sort of atom and including the primitive cell, which contains only one atom (the primitive cell is shown in violet). (b) Primitive cell of a two-atomic basis resulting from two nested fcc lattices, i.e. including two different atoms as in the case of GaAs with Ga (red) and As (grey). Note that the number of atoms in the primitive cell of GaAs is calculated as 8 times 1/8 Ga atoms and 1 As atom. The crystal structure of the semiconductors considered here consist of two nested fcc lattices featuring the diamond cubic or zincblende structure.

and enclose an angle of 60°. Fig. 3.1 shows a conventional fcc cell on the left-hand side including a primitive cell containing one type of atom and on the right-hand side a primitive cell with a two-atomic basis. In this chapter, all investigated semiconductors contain two different atoms in the primitive cell, except for Si.
In the field of solar cell applications, Si reaches an energy conversion efficiency of up to 36% in recently investigated silicon-based multi-junction solar cells [5] or 26% in conventional crystalline Si solar cells [4]. Most likely Si is the best understood common inorganic semiconductor, which is certainly also due to the fact that Si is one of the pioneering materials in applying the concept of electronic band structure [127].
The standard workhorse nowadays to calculate static as well as dynamic electronic band structures is DFT (see chapter 2.2), which inherently applies exchange-correlation functionals (see chapter 2.2.2). The (semi-)local class of functionals such as LDA [40] or PBE [21] are very successful in the overall description of semiconductors, but generally suffer from an underestimation of the electronic band gap, which is often referred to as the DFT band gap problem [41]. This issue has been addressed by using hybrid functionals, which include a fraction of exact exchange. One of the most important examples from the screened hybrid functionals is HSE [22, 23], which showed well-founded results not only for electronic [128, 129] but also for other bulk properties [26, 130, 131, 132]. Especially in comparison to PBE, HSE provides more precise electronic band structures and, thus, also more accurate band gaps at the expense of computation time [23, 133]. The electronic

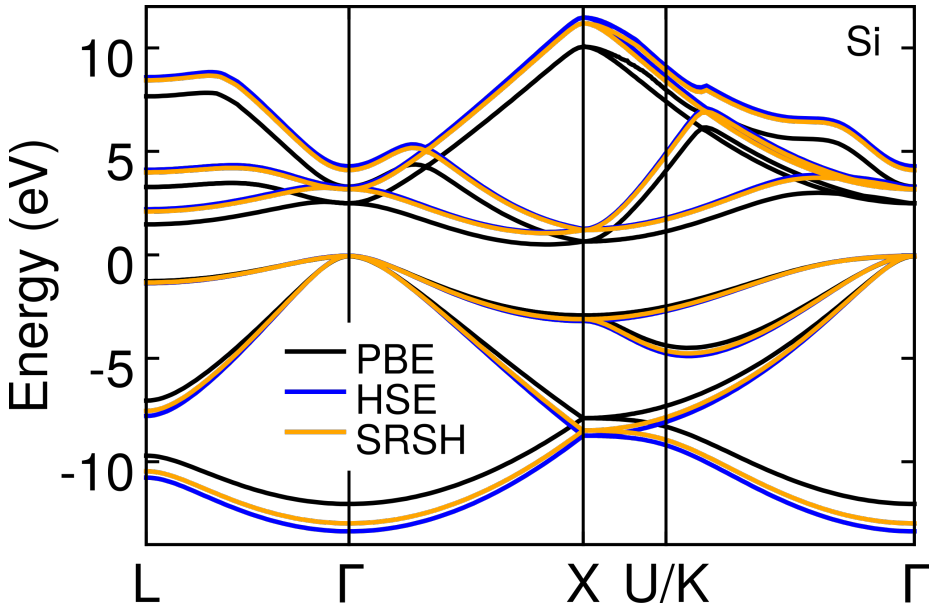

Figure 3.2. Electronic band structure of Si, which crystallizes in the diamond cubic structure, calculated with DFT using three different functionals: the GGA-type PBE functional (black line), the screened hybrid functional HSE (blue line) and the screened range-separated hybrid functional SRSH (orange line). The DFT calculation does not include SOC. The indirect band gap is given by the VBM located at the Γ-point and the CBM detected along the Γ-X direction.

band structure of Si is shown in Fig. 3.2, for example. Here the CB calculated with HSE (blue line) is higher in energy than the band calculated with PBE (black line)[1]. This shift in energy changes the band gap values accordingly. Specifically, as listed in Table 3.1, the Si PBE indirect band gap is 0.57 eV, the HSE indirect gap is 1.15 eV and the experimental optical gap is 1.12 eV. Thus, the calculation of the band gap using HSE is more than half an electron volt closer to experiment than using PBE. As a side note, SOC has only a minor influence on the Si band structure. For example, the difference between the PBE direct gap without SOC and with SOC is only 0.04 eV. This fact of small SOC contribution also holds for all III-V and IV semiconductors.
Moreover, the entire mean absolute deviation (MAD) for the band gaps of the set of seven semiconductors (see Table 3.1) is 35% for PBE and 5% for HSE compared to experiment, reinforcing the higher accuracy of screened hybrid functionals due to the incorporation of exact exchange. This seems overwhelming at first glance, but on the second view it is less surprising, since the two parameters, which dictate the HSE functional, namely α and γ, have been chosen to provide accurate electronic band structures [22, 23].
In summary, an accurate description of the electronic band structure is only possible by the inclusion of exact exchange. A relatively recently developed class of functionals, so-called SRSH functionals were introduced, which still keep a portion of exact

[1]Note that the Fermi-level corresponds to the highest occupied state in VASP. Consequently, all VBs calculated with the three functionals coincide at the Γ-point.

Table 3.1. Direct and - where available - indirect fundamental band gaps of the set of standard semiconductors. In order to avoid error propagation, stemming from different structures provided by different functionals, impacting the band gaps and to guarantee a consistent comparison, the experimental lattice constant was used throughout for each material. The calculation of the band gaps used the PBE, HSE and SRSH functional. The MAD is calculated as the mean absolute deviation from experimental optical gaps, which were taken from [134] and [135] for the Si direct gap only. The specific MAD values for the direct band gaps of all semiconductors are 0.76 eV for PBE, 0.14 eV for HSE and 0.22 eV for SRSH. *Reprinted table with permission from [1]. Copyright (2021) by the American Physical Society.*

	Direct fund. gap						Direct opt. gap
	PBE		HSE		SRSH		Expt.
Name	E_g (eV)	Deviation (%)	E_g (eV)	Deviation (%)	E_g (eV)	Deviation (%)	E_g (eV)
AlAs	2.06	-32.0	2.93	-3.3	2.80	-7.6	3.03
AlP	3.30	-9.1	4.23	+16.5	4.26	+17.4	3.63
AlSb	1.60	-30.4	2.39	+3.9	2.30	+0.0	2.30
GaAs	0.53	-62.7	1.43	+0.7	1.09	-23.2	1.42
GaP	1.83	-34.4	2.80	+0.4	2.58	-7.5	2.79
InP	0.68	-49.3	1.47	+9.7	1.29	-3.7	1.34
Si	2.56	-23.6	3.33	-0.6	3.23	-3.6	3.35
MAD(%)		34.5		5.0		9.0	
	Indirect fund. gap						Indirect opt. gap
AlAs	1.43	-33.5	2.10	-2.3	2.07	-3.7	2.15
AlP	1.58	-35.5	2.29	-6.5	2.40	-2.0	2.45
AlSb	1.19	-26.5	1.80	+11.1	1.78	+9.9	1.62
GaP	1.59	-30.0	2.27	+0.0	2.20	-3.1	2.27
Si	0.57	-49.1	1.15	+2.7	1.10	-1.8	1.12
MAD(%)		34.9		4.5		4.1	

exchange also in the long-range region compared to HSE. This class of functionals was initially designed for molecules with reasonable results [51] and later extended to semiconductors. In the latter case, two ideas determine the form of the SRSH functional: first, the HSE parameter α is used for the SR, and second, the dielectric constant ϵ dictates the long range behavior by introducing another parameter β. Note that the dielectric constant ϵ is material-dependent and therefore SRSH does not offer a universal set of parameters.

Since SRSH provides more flexibility in splitting EXX and GGA over SR and LR, it also describes the asymptotic decay of $\frac{1}{\epsilon r}$ correctly in comparison to HSE. Because of its tuning nature, the parameters α, β and γ can be adjusted in a way to fix the SRSH band gap value to the band gap value calculated with the higher-level GW theory. In this work, the values for the parameters α, β and γ reported by Wing et al. [27] were used. In their work, Wing et al. set $\alpha = 0.25$ and $\alpha + \beta = \frac{1}{\epsilon_{\infty}^{\text{theory}}}$, while tuning γ to reproduce the GW band gap [136] for each of the seven semiconductors. Hence, the focus is on properties of these seven semiconductors in this work. Note that the choice for the value of $\alpha = 0.25$ in SRSH is the same as in HSE. An explicit list of the tuned parameters is shown in Table 3.2. Therefore, it makes sense that the MAD of the band gaps calculated with SRSH is similarly low as the MAD of HSE for the set of selected semiconductors. Specifically, as shown in Table 3.1, the

Table 3.2. The SRSH parameters α, β and γ as well as the theoretical dielectric constant $\epsilon_\infty^{\text{theory}}$ are listed here for the investigated prototypical set of semiconductors. *Reprinted table with permission from [1]. Copyright (2021) by the American Physical Society.*

Name	$\epsilon_\infty^{\text{theory}}$	α	β	γ (Å^{-1})
AlAs	8.2	0.25	-0.13	1.25
AlP	7.3	0.25	-0.11	0.80
AlSb	9.8	0.25	-0.15	0.63
GaAs	10.5	0.25	-0.15	2.50
GaP	8.9	0.25	-0.14	1.15
InP	8.9	0.25	-0.14	1.30
Si	11.3	0.25	-0.16	0.62

MAD of SRSH for the indirect band gaps is 4.1% in comparison with the MAD of HSE, which is 4.5%. This behavior of equal accuracy between SRSH and HSE can also be seen in the band structure of Si depicted in Fig. 3.2, where the orange line (SRSH) is almost congruent with the blue line (HSE).
In summary, SRSH as well as HSE perform equally well in band structure calculations for semiconductors, with the SRSH parameters being tuned compared to the universal HSE parameters. Both functionals are superior in comparison to PBE. Also for other bulk properties, such as lattice dynamics, the class of hybrid functionals like HSE provided reasonable results [137, 138]. Especially for phonon dispersion relations of group IV semiconductors such as Si, it is known that HSE provides also more accurate dispersion relations in comparison to the semilocal PBE functional, which showed an underestimation of phonon frequencies compared to experiment [137]. But on the other hand, the power of having a constant fraction of exact exchange as in popular hybrid functionals, does not lead to accurate results in all variants of semiconductors [50]. In view of all the above findings on the performance of semilocal and hybrid functionals, it would be useful to test the performance of the SRSH functional developed later. The flexibility of varying GGA and EXX as well as the general tuning ability of SRSH already showed proper results for semiconductors not only in electronic structure, but also in optical-absorption properties [28]. Simultaneous accuracy in electronic structure and phonon frequencies is required, when calculating electron-phonon coupling energies, which are a fundamental quantity in understanding thermal activity, such as the temperature-dependent band gap of semiconductors. Therefore, it is interesting to investigate whether or not the accurate results of SRSH in the electronic band structure come at the expense of lower accuracy in the calculation of other bulk properties. This is the purpose of this research conducted here. Specifically, results for lattice constants, bulk moduli, atomization energies and phonon dispersion relations of the set of semiconductors using the SRSH functional are benchmarked against results from the well-established PBE and HSE functionals.

3.2. Computational parameters

DFT calculations to assess the accuracy of the SRSH functional were performed with the VASP code, which includes an implementation of SRSH. The pseudo potentials were provided via the projector-augmented wave (PAW) method with extra semicore d states for Ga and In, in order to be consistent with existing results from literature. The overall convergence criterion for the total energy is 2 meV per atom and was initially tested with the PBE functional. This leads to energy cutoffs (E_{cut}) listed in Table 3.3 for the calculation of lattice constants, bulk moduli and atomization energies. In order to handle some numerical instabilities in phonon band structure calculations at the Γ-point, a slight higher energy cutoff has to be chosen for some materials. The energy cutoff (E_{cut}^{ph}) for phonons is also listed in Table 3.3. To achieve converged k-point grids, a Γ-centered Monkhorst-Pack grid with $8 \times 8 \times 8$ k-points for AlAs, AlP, AlSb, InP and $9 \times 9 \times 9$ k-points for GaAs, GaP, Si is used. In the case of phonon calculations, the unit-cell size is increased to a $4 \times 4 \times 4$ supercell size and the k-point grid is reduced accordingly to a $2 \times 2 \times 2$ k-point grid.

Table 3.3. In order to calculate equilibrium lattice constants, bulk moduli and atomization energies a plane-wave energy cutoff E_{cut} is used (middle column). In some cases, a higher energy cutoff E_{cut}^{ph} has to be used for phonon dispersions (right column). *Reprinted table with permission from [1]. Copyright (2021) by the American Physical Society.*

Name	E_{cut} (eV)	E_{cut}^{ph} (eV)
AlAs	220	220
AlP	245	245
AlSb	190	240
GaAs	280	380
GaP	300	350
InP	255	355
Si	270	270

3.3. Lattice constant and bulk modulus

Table 3.4 lists in detail the results of the respective lattice constants for the seven semiconductors calculated with the PBE, HSE and SRSH functionals (see chapter 2.4.1). In addition, the experimental values of the lattice constants are listed as well. The MAD, given in %, for each functional results from the average of the deviations between the theoretical and experimental lattice constants of all seven semiconductors. Despite the fact that the theoretical lattice constants are calculated without temperature effects and that the experimental lattice constants are measured at finite temperatures (e.g., room temperature), there is an overall good agreement between both. This can be clearly seen in Fig. 3.3, as no outliers can be detected and the PBE functional yields a maximum MAD value of 1.3%. In general, all

Table 3.4. Theoretical lattice constants a(Å) computed with the PBE, HSE and SRSH functionals in comparison to experimental lattice constants measured at room temperature. The deviation is given with respect to experimental data, which is taken for all semiconductors from [126]. The MAD is the mean absolute deviation from experiment. *Reprinted table with permission from [1]. Copyright (2021) by the American Physical Society.*

	PBE		HSE		SRSH		Expt.
Name	a (Å)	Deviation (%)	a (Å)	Deviation (%)	a (Å)	Deviation (%)	a (Å)
AlAs	5.74	1.4	5.68	0.4	5.70	0.7	5.66
AlP	5.51	0.9	5.47	0.2	5.48	0.4	5.46
AlSb	6.24	1.6	6.15	0.2	6.18	0.7	6.14
GaAs	5.75	1.8	5.68	0.5	5.72	1.2	5.65
GaP	5.51	1.1	5.46	0.2	5.48	0.6	5.45
InP	5.96	1.5	5.90	0.5	5.93	1.0	5.87
Si	5.47	0.7	5.44	0.2	5.45	0.4	5.43
MAD(%)		1.3		0.3		0.7	

three functionals tend to slightly overestimate the experimental lattice constants in a consistent way, as indicated by values above the red line (line through origin with a gradient of one) in Fig. 3.3. Thereby, the theoretical lattice constants are arranged in such a way that the x-coordinate corresponds to the experimental value. Furthermore, the MAD of HSE is 0.3% and the one of SRSH 0.7%.
The absolute values of the MAD for the three functionals are 0.07 Å for PBE, 0.02 Å for HSE, 0.04 Å for SRSH and the maximum deviation (MD) to experiment are 0.10 Å for PBE, 0.03 Å for HSE and 0.07 Å for SRSH. The overall trend towards shorter lattice constants by HSE in comparison to PBE is consistent with previous literature [139, 140, 141]. Furthermore, one can conclude that lattice constants provided by SRSH are more accurate than lattice constants by PBE, but slightly less accurate than lattice constants by HSE. Finally, based on the fact that the maximum deviation is only 0.04 Å (in the case of GaAs) between SRSH and HSE for the set of semiconductors, SRSH is of equal accuracy in providing lattice constants for semiconductors.
Note that the theoretical lattice constants are calculated here without temperature effects and experimental lattice constants are measured at room temperature. However, the validity of the high consensus between theoretical and experimental lattice constants is justified since thermal expansion of the lattice is a rather small effect. In the case of Si, for example, there is a small positive thermal expansion above 200 K [142]. So, on the one hand, if one interprets DFT at 0 K, i.e., the theoretical lattice constants are provided at 0 K, together with the overestimation of the lattice constants throughout all functionals, the MAD is expected to grow slightly, if one includes thermal expansion. On the other hand, this would ensure a more objective comparison of the theoretical and experimentally measured lattice constants at the same temperatures.
Furthermore, the effect of dispersion corrections, such as van der Waals interactions, were not taken into account here. Apart from the additional computational cost of

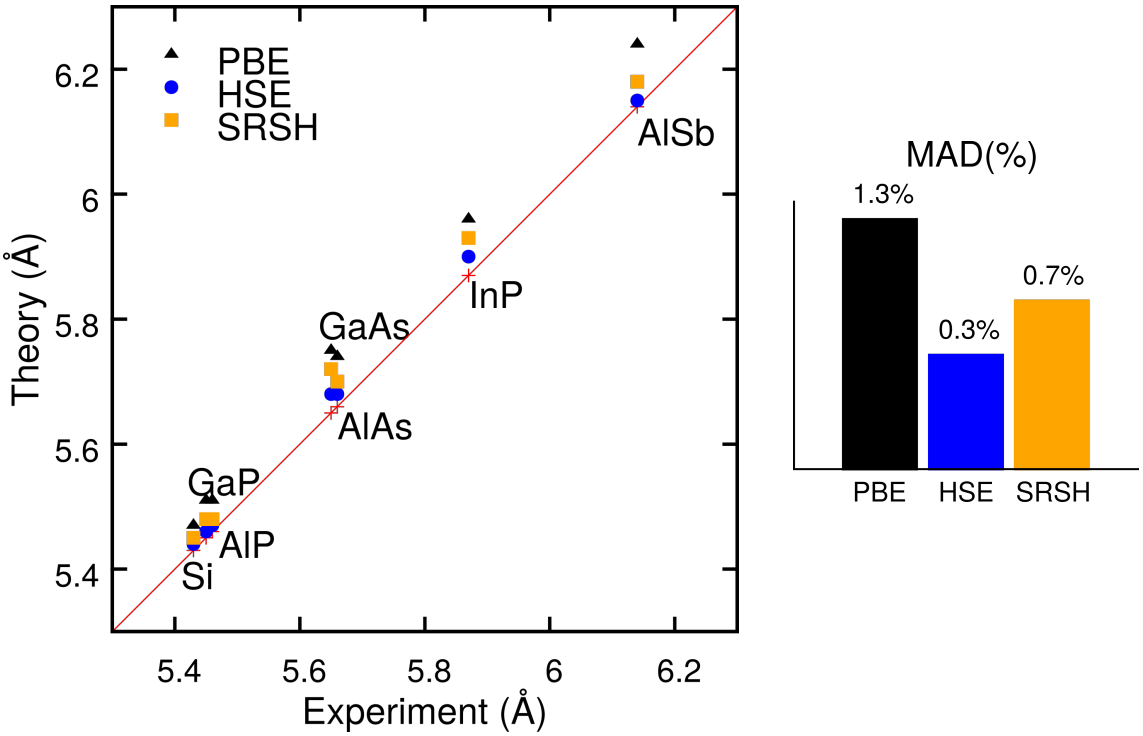

Figure 3.3. Left-hand side: theoretical lattice constants calculated with the PBE, HSE and SRSH functionals. The experimental values are indicated on the line (red crosses). Right-hand side: the corresponding MAD in %.

including van der Waals interactions, the main motivation for their exclusion in this study was the fact, that DFT dispersion contributions seem to be dependent on the choice of the exchange-correlation functional [72]. Thus, to guarantee a proper comparison between each functional, van der Waals interactions were neglected. However, considering that the three functionals generally overestimate the lattice constants, there are indications that the inclusion of van der Waals would lead to lower theoretical lattice constants on the one hand and to higher atomization energies for semiconductors on the other hand [72].

Table 3.5. Theoretical bulk moduli B(GPa) computed with the PBE, HSE and SRSH functionals in comparison to experimental bulk moduli. *Reprinted table with permission from [1]. Copyright (2021) by the American Physical Society.*

	PBE		HSE		SRSH		Expt.
Name	B	Dev. (%)	B	Dev. (%)	B	Dev. (%)	B
AlAs	67	-11	76	+1	72	-5	74-77 [143, 134]
AlP	81	-7	89	+2	90	+3	86-88 [144, 145]
AlSb	49	-13	58	+3	55	-3	55-58 [145, 146, 147]
GaAs	60	-21	72	-5	66	-13	75-76 [148, 149]
GaP	78	-11	88	+1	84	-4	87-88 [150, 134]
InP	62	-14	71	-1	67	-7	71-73 [151, 134]
Si	89	-10	98	-1	95	-4	98-99 [148, 134]
MAD(%)		12		2		5	

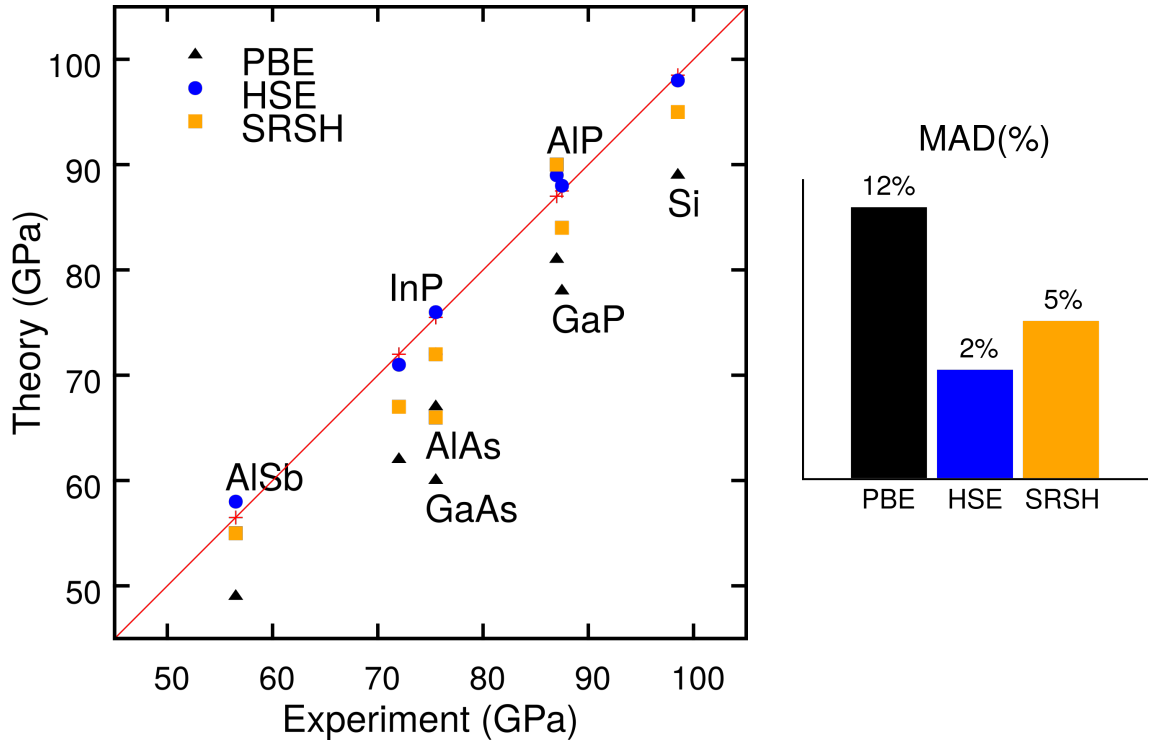

Figure 3.4. Left-hand side: theoretical bulk moduli calculated with the PBE, HSE and SRSH functionals. The experimental values are indicated on the line (red crosses). Right-hand side: the corresponding MAD in %.

Whereas the theoretical lattice constants are overestimated by the three functionals, the theoretical bulk moduli tend to be somewhat underestimated. Table 3.5 lists the bulk moduli calculated with PBE, HSE and SRSH functionals for the set of the seven semiconductors. Experimental values for the bulk moduli are provided using an experimental range reported in literature. The MAD as well as the MD values refer to the theoretical bulk moduli and to the arithmetic mean of the experimental range. For clarity, the results of the bulk moduli are visualized like the results of the lattice constants in Fig. 3.4 where the experimental values are the ones on the red line. A clear trend of underestimation of the bulk moduli is given by the PBE functional and thus, together with the overestimation in lattice constants, is consistent to previous studies [130]. The trend of highly accurate lattice constants from HSE continues here as well and provides the most accurate bulk moduli of the three functionals with a MAD of 2%. The SRSH functional provides slightly underestimated bulk moduli throughout all semiconductors with one outlier for AlP. But in general, bulk moduli from SRSH are more accurate than bulk moduli from PBE, which is clearly demonstrated by the MAD of 5% for SRSH and 12% for PBE. The absolute values of the MAD in GPa for the three functionals are 10 GPa for PBE, 1 GPa for HSE and 4 GPa for SRSH. Furthermore, the MDs are given by 16 GPa for PBE, 4 GPa for HSE and 10 GPa for SRSH.
In summary, the accuracy provided by the three functionals for the theoretical bulk moduli follows the trend of the theoretical lattice constants, with an underestimation for the former and an overestimation for the latter. Note that the bulk modulus is the

reciprocal of the compressibility and the results therefore show the relation between increasing volume and decreasing pressure. However, the trend of high accuracy applies in particular to the HSE lattice constants and HSE bulk moduli with deviations that are well below the experimental range for most of the seven semiconductors. Finally, compared to HSE, SRSH can maintain the accurate results for the lattice constants as well as the bulk moduli, while PBE is slightly worse.

3.4. Atomization energies

Table 3.6 shows the atomization energies for the set of prototypical semiconductors calculated with the PBE, HSE and SRSH functionals (see chapter 2.4.2). In general, all functionals perform reasonably accurate, which is reflected in deviations less than 10%. To be more precise, the comparison of the theoretical and the experimental values reveals that all functionals tend to underestimate the atomization energies. In order to better visualize the performance of the functionals, the results are also shown in Fig. 3.5. There, the underestimation of the atomization energies by the functionals is easy to see, since all values are below the red line. In this context, PBE shows the best agreement to experiment with a MAD of 2.7% followed by HSE with 3.1% and finally SRSH with 3.8%. The MAD in absolute values is 0.10 eV for PBE, 0.11 eV for HSE and 0.14 eV for SRSH, which confirms the overall good performance. Note that the theoretical results of the atomization energies strongly depend on the material, which can be seen by the wide range of the relative deviations. This range lies between −0.4% for Si PBE and −9.0% for InP SRSH. It is worth noting that zero-point corrections are not included in the DFT calculations. But there is evidence that their inclusion would further lower the theoretical atomization energies [130].

Table 3.6. Theoretical atomization energies E_{AE} (eV/atom) computed with the PBE, HSE and SRSH functionals in comparison to experimental atomization energies. *Reprinted table with permission from [1]. Copyright (2021) by the American Physical Society.*

	PBE		HSE		SRSH		Expt.
Name	E_{AE}	Dev. (%)	E_{AE}	Dev. (%)	E_{AE}	Dev. (%)	E_{AE}
AlAs	3.73	-1.3	3.70	-2.1	3.68	-2.6	3.78 [152]
AlP	4.13	-3.1	4.10	-3.8	4.08	-4.2	4.26 [152]
AlSb	3.28	-0.9	3.28	-0.9	3.27	-1.2	3.31 [153]
GaAs	3.18	-3.9	3.16	-4.5	3.13	-5.4	3.31 [26]
GaP	3.52	-1.1	3.51	-1.4	3.47	-2.5	3.56 [152]
InP	3.16	-7.9	3.15	-8.2	3.12	-9.0	3.43 [154]
Si	4.60	-0.4	4.58	-0.9	4.56	-1.3	4.62 [155]
MAD(%)		2.7		3.1		3.8	

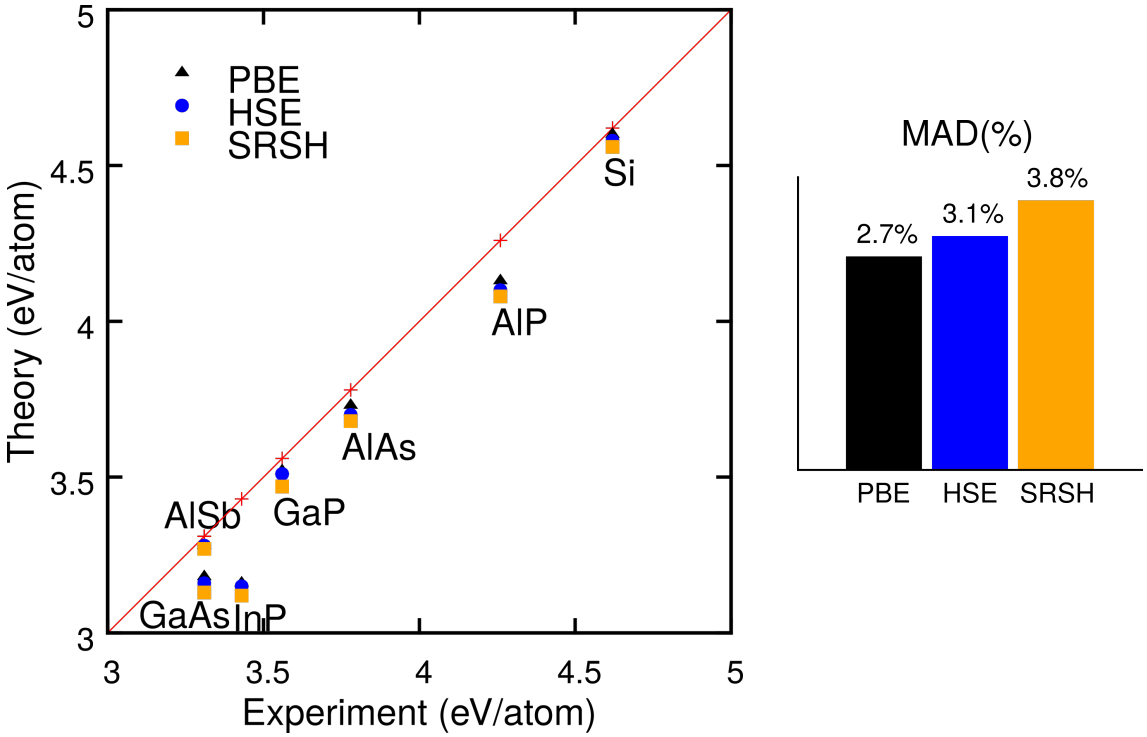

Figure 3.5. Left-hand side: theoretical atomization energies calculated with the PBE, HSE and SRSH functionals. The experimental values are indicated on the line (red crosses). Right-hand side: the corresponding MAD in %.

3.5. Phonon dispersion relations

In order to compare the phonon band structures, calculated with the three functionals (see chapter 2.4.3), a specific path through the BZ was chosen for all semiconductors. The path $\Gamma - K - X - \Gamma - L - X - W - L$ is depicted and explained in more detail in Fig. 3.6. Note that the Γ-point occurring in the middle of the entire path is the end point of the path $\Gamma - K - X - \Gamma$, i.e. the Γ-point from the neighbored BZ (see figure on top in Fig. 3.6), and the starting point of the path $\Gamma - L - X - W - L$ in only one BZ. The choice of this path allows comparison to existing results from theory and experiment found in the literature.
Furthermore, the phonon dispersion relations are calculated in two ways for each semiconductor. First, the calculation for each functional uses the theoretical equilibrium lattice constant calculated with the corresponding functional. The used lattice constants are the ones listed in Table 3.4. Second, the same experimental lattice constant for each material was used for all of the three functionals. The latter approach is a standard procedure as reported in [158] and prevents error propagation of the functionals by using the respective lattice constants, which would include the error of the lattice constant caused by the functional.
The phonon dispersion relations of GaAs and Si are shown in Fig. 3.8 and Fig. 3.9. All other phonon dispersion relations for the remaining five semiconductors are shown in the appendix A.2 for reasons explained later. Furthermore, a list of explicit phonon frequencies calculated with the three functionals for GaAs and Si are

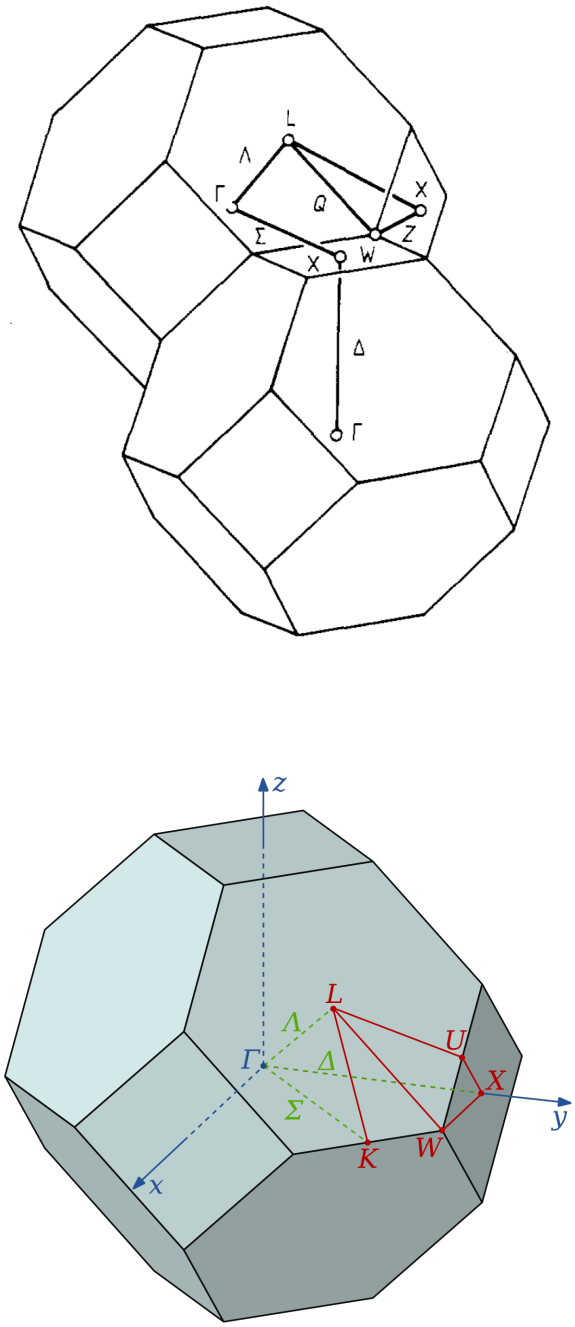

Figure 3.6. Both figures show the first BZ of a fcc lattice with high symmetry points and wave vector directions labeled with capital letters. The figure on top shows two neighboured BZs showing following path through both zones: $\Gamma-(\Delta)-\mathrm{X}-(\Sigma)-\Gamma-(\Lambda)-\mathrm{L}-\mathrm{X}-(\mathrm{Z})-\mathrm{W}-(\mathrm{Q})-\mathrm{L}$. This path, including six wave vector directions, consists of two parts, namely of $\Gamma-(\Delta)-\mathrm{X}-(\Sigma)-\Gamma$ across two BZs and of $\Gamma-(\Lambda)-\mathrm{L}-\mathrm{X}-(\mathrm{Z})-\mathrm{W}-(\mathrm{Q})-\mathrm{L}$ in only one BZ. The figure on the bottom shows only one BZ with also labeling the K-point at the intersection to the neighboured BZ. Here, the same path is used for the phonon dispersion relations calculated with the three functionals. Neglecting the labeling of the wave vector directions the path is denoted as $\Gamma-K-\mathrm{X}-\Gamma-\mathrm{L}-\mathrm{X}-\mathrm{W}-\mathrm{L}$. Top figure: *Used with permission of IOP Publishing, Ltd, from [156]; permission conveyed through Copyright Clearance Center, Inc.*; Bottom figure: *Reprinted with permission from [157], released into the public domain.*

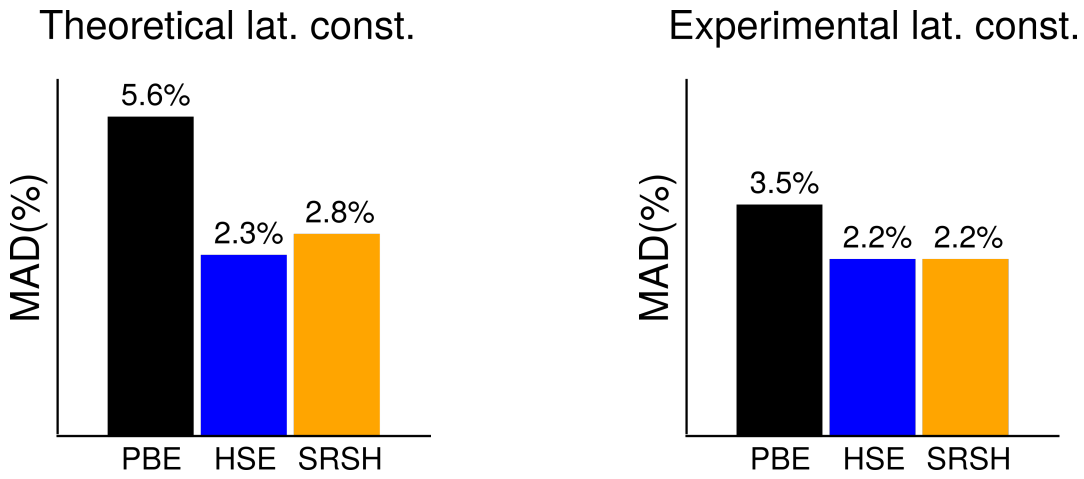

Figure 3.7. The MAD (in %) calculated for selected high symmetry points, where experimental data is available, for all semiconductors. On the left, there is the MAD resulting from PBE, HSE and SRSH using the respective theoretical lattice constant. On the right, there is the corresponding MAD using the experimental lattice constant for all three functionals.

shown in Table 3.7 and 3.8. The frequencies are shown together with experimental frequencies for selected high symmetry points, where data is available. Explicit frequencies for the remaining five semiconductors can be found in the appendix A.3. The overall MAD of the phonon dispersion relations, which is calculated by collecting the single MADs of the seven semiconductors and taking the average, is shown in Fig. 3.7. Comparing the overall MADs in Fig. 3.7 for phonon dispersions by using the theoretical lattice constants (left-hand side) and experimental lattice constants (right-hand side), reveals that the accuracy of the phonon calculations using the three functionals strongly depends on the accuracy of the respective equilibrium lattice constant.

Specifically, the MADs using the theoretical lattice constants for the frequencies are 5.6% for PBE, 2.3% for HSE and 2.8% for SRHS. This is consistent with the findings for the equilibrium lattice constants in Fig. 3.3, namely that the largest deviation in the lattice constants results in the largest deviation in the phonon frequencies. Thus, the trend in this scenario is given by PBE, SRSH and HSE with ascending accuracy. In general, PBE tends to underestimate the phonon frequencies, regardless of the choice of the lattice constants. Furthermore, the frequencies obtained by PBE are always lower than the frequencies produced by HSE and SRSH. There is no overall trend that using overestimated lattice constants results in an underestimation of phonon band structures. This can be seen in the dispersion relations of GaAs (Fig. 3.8) and Si (Fig. 3.9), where the former are underestimated and the latter overestimated in the scenario of hybrid functionals using overestimated lattice constants. In summary, a consistent underestimation of phonon frequencies is only given by the PBE functional and no clear trend is seen in the case of HSE and SRSH.

The MADs using the experimental lattice constants (see right-hand side of Fig. 3.3) are 3.5% for PBE, 2.2% for HSE, and 2.2% for SRHS. Basically, all three functionals provide similarly accurate phonon band structures, when using the same experimen-

tal lattice constant for each semiconductor. Especially the two hybrid functionals, HSE and SRSH, perform at the same level of accuracy, followed by the less accurate PBE functional.
In the expectation that the largest deviation of the theoretical lattice constant from the experiment also results in the largest deviation of the phonon frequencies and vice versa, the materials GaAs and Si are selected for further detailed discussion. Note that the theoretical lattice constant of GaAs has the largest and the theoretical lattice constant of Si the smallest deviation compared to the respective experimental lattice constant (see Table 3.4). In the following detailed discussion, GaAs is described first, then Si, using first the theoretical and then the experimental lattice constant for each material.

GaAs phonon frequencies using theoretical lattice constants:

Indeed, for the GaAs phonon band structure using the respective theoretical lattice constant, a clear trend between overestimation in the lattice constant and an underestimation in the frequencies can be seen (see upper panel of Fig. 3.8). The closer the theoretical lattice constant, obtained from a specific functional, is to the experimental one, the closer are the phonon frequencies to the experimental frequencies. Since all theoretical lattice constants are overestimated, all phonon frequencies are underestimated in the case of GaAs. In this observation, the order in providing the most accurate results in both quantities has not changed, i.e. HSE is followed by SRSH and PBE with decreasing accuracy. Note that a distinction in the accuracy between acoustic and optical phonons is not required because all functionals yield a similar behavior for acoustic and optical phonons.

GaAs phonon frequencies using experimental lattice constants:

The overall observation, when using the same GaAs experimental lattice constant for the calculation of the phonon band structure, is the reduction of the deviation between the results obtained with the three functionals (see lower panel of Fig. 3.8). Taking into account the LO phonon energy at the Γ-point (Γ_{LO}), one sees from Table 3.7 that the spread is almost halved from 0.7 THz for the theoretical to 0.4 THz for the experimental lattice constant. Thus, in the case of GaAs, all three functionals provide proper phonon frequencies and are in the same level of accuracy. For a more detailed discussion it is helpful to distinguish between optical and acoustic phonons. The accuracy depends on the choice of the phonon branch. For acoustic phonons, especially far away from the Γ-point, HSE provides frequencies closest to experiment, followed by frequencies from SRSH and from PBE. In the case of the optical phonons, far away from the Γ-point all three functionals provide very accurate description. However, in the area around the Γ-point SRSH is most accurate, whereas HSE provides slightly overestimated and PBE slightly underestimated phonon frequencies.

Si phonon frequencies using theoretical lattice constants:

For Si, already in the case of the theoretical lattice constants, a reduction of the fre-

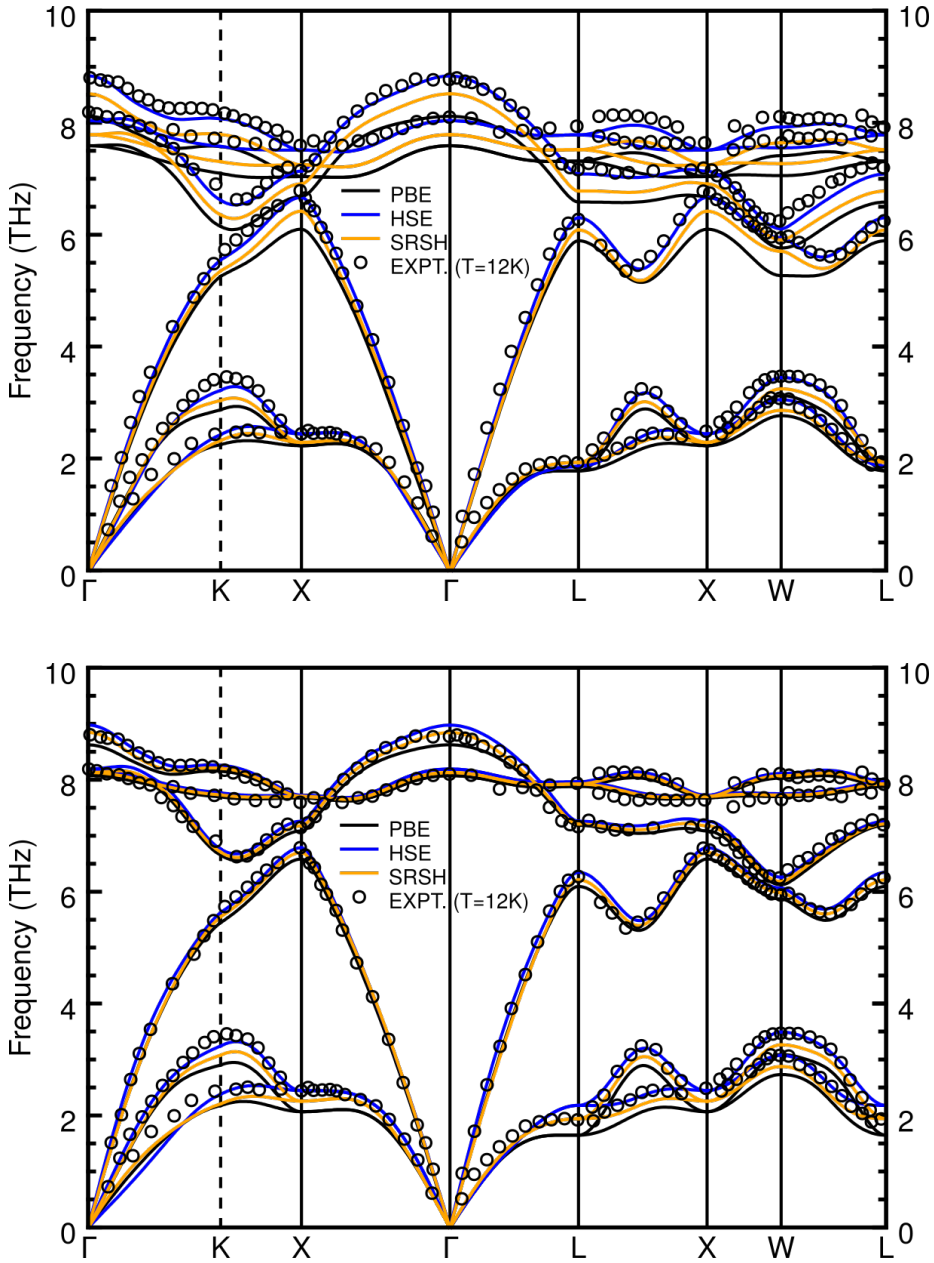

Figure 3.8. The upper panel shows the phonon dispersion relation of fcc-structured GaAs using the theoretical lattice constants calculated with the PBE, HSE and SRSH functionals (solid colored lines) as well as experimental data (open black circles), which was extracted from [156]. Note that experimental data was measured at 12 K. The lower panel shows the phonon dispersion relation for only using the experimental lattice constant throughout the three functionals. *Reprinted figure with permission from [1]. Copyright (2021) by the American Physical Society.*

Table 3.7. Phonon frequencies calculated with PBE, HSE and SRSH functionals for GaAs. Each left sub-column denotes frequencies resulting from the theoretical lattice constant, a_{theo}, and each right sub-column from the experimental lattice constant, a_{exp}. The deviation Δ refers to experimental values at specific high-symmetry points, where available. Classification of phonons and experimental values are from [156]. *Reprinted table with permission from [1]. Copyright (2021) by the American Physical Society.*

	PBE				HSE				SRSH				Expt.
	a_{theo}		a_{exp}		a_{theo}		a_{exp}		a_{theo}		a_{exp}		
(THz)	ω	Δ (%)	ω	Δ (%)	ω	Δ (%)	ω	Δ (%)	ω	Δ (%)	ω	Δ (%)	ω
L_{TA}	1.8	-5.3	1.6	-15.8	1.9	0.0	2.2	15.8	1.9	0.0	1.9	0.0	1.9
X_{TA}	2.2	-12.0	2.1	-16.0	2.4	-4.0	2.4	-4.0	2.3	-8.0	2.3	-8.0	2.5
L_{LA}	5.9	-6.3	6.1	-3.2	6.3	0.0	6.3	0.0	6.1	-3.2	6.2	-1.6	6.3
X_{LA}	6.1	-10.3	6.6	-2.9	6.7	-1.5	6.8	0.0	6.4	-5.9	6.7	-1.5	6.8
L_{LO}	6.6	-8.3	7.2	0.0	7.1	-1.4	7.3	1.4	6.8	-5.6	7.2	0.0	7.2
X_{LO}	6.7	-6.9	7.1	-1.4	7.1	-1.4	7.3	1.4	6.9	-4.2	7.2	0.0	7.2
X_{TO}	7.0	-9.1	7.7	0.0	7.5	-2.6	7.7	0.0	7.2	-6.5	7.7	0.0	7.7
L_{TO}	7.3	-7.6	7.9	0.0	7.8	-1.3	8.0	1.3	7.5	-5.1	7.9	0.0	7.9
Γ_{TO}	7.6	-7.3	8.1	-1.2	8.0	-2.4	8.2	0.0	7.8	-4.9	8.1	-1.2	8.2
Γ_{LO}	8.1	-8.0	8.6	-2.3	8.8	0.0	9.0	2.3	8.5	-3.4	8.8	0.0	8.8
MAD(%)		8.1		4.3		1.5		2.6		4.7		1.2	

quency spread by the three functionals is expected, as the theoretical lattice constants hardly deviate from each other (see again Table 3.4). However, this is not the case. The frequency spread is 0.7 THz for optical phonons at the Γ-point (see Table 3.8). Going into more detail, using the slight different theoretical lattice constants (see upper panel in Fig. 3.9), the acoustic phonons are equally accurate described by all three functionals. For the optical phonons around the Γ-point (see the inset of the upper panel in Fig. 3.9) a clear trend can be observed: the PBE-calculated frequencies are slightly underestimated in comparison to experimental frequencies, HSE-calculated ones are slightly overestimated and SRSH-calculated ones are the most accurate. This trend also applies to a lesser extent to the optical phonons away from the Γ-point. Note that in the case of GaAs the most accurate theoretical lattice constant provides the most accurate phonon dispersion relation. This does not hold for the case of Si due to a smaller variation among the theoretical lattice constants of Si.

Si phonon frequencies using experimental lattice constants:

The Si phonon band structure calculated with the same experimental lattice constant for the three functionals (see lower panel in Fig. 3.9) provides a frequency spread of 0.5 THz for the optical phonons at the Γ-point (see Table 3.8). Thus, the reduction of the frequency spread is slightly less than in the case of GaAs, when going from the theoretical to the experimental lattice constant. Overall, both hybrid functionals, HSE and SRSH, slightly overestimate the phonon frequencies for optical as well as acoustic frequencies. Furthermore, the difference between frequencies from HSE and SRSH is negligible. PBE, in general, slightly underestimates the frequencies in this scenario. In comparison to frequencies from HSE and SRSH the observation is as follows: the optical phonons are described most accurately by PBE compared

to the experiment, but the acoustic phonons are better described by the two hybrid functionals. However, in the case of the experimental lattice constant of Si, all three functionals provide very accurate phonon frequencies, so that the differences between them are minor.

Experimental phonon frequencies measured at different temperatures:

Note that the experimental data of GaAs was measured at a temperature of 12 K, whereas the data of Si at 300 K. All the experimental lattice constants were measured at room temperature. Since, for the phonon dispersion relations obtained using experimental lattice constants, somehow all results from DFT are close to experimental data regardless of the functional, it is expected that the temperature difference of 288 K in measuring experimental frequencies plays a minor role.

Table 3.8. Phonon frequencies calculated with PBE, HSE and SRSH functionals for Si. Each left sub-column denotes frequencies resulting from the theoretical lattice constant, a_{theo}, and each right sub-column from the experimental lattice constant, a_{exp}. The deviation Δ refers to experimental values at specific high-symmetry points, where available. Classification of phonons and experimental values are from [159] and [160]. *Reprinted table with permission from [1]. Copyright (2021) by the American Physical Society.*

	PBE				HSE				SRSH				Expt.
	a_{theo}		a_{exp}		a_{theo}		a_{exp}		a_{theo}		a_{exp}		
(THz)	ω	Δ (%)	ω	Δ (%)	ω	Δ (%)	ω	Δ (%)	ω	Δ (%)	ω	Δ (%)	ω
L_{TA}	3.3	-5.7	3.2	-8.6	3.6	2.9	3.5	0.0	3.8	8.6	3.4	-2.9	3.5
X_{TA}	4.4	-2.2	4.2	-6.7	4.3	-4.4	4.7	4.4	4.4	-2.2	4.6	2.2	4.5
L_{LA}	11.1	-1.8	11.2	-0.9	11.7	3.5	11.7	3.5	11.5	1.8	11.5	1.8	11.3
$X_{\text{LA/LO}}$	12.0	-1.6	12.3	0.8	12.6	3.3	12.7	4.1	12.4	1.6	12.6	3.3	12.2
L_{LO}	12.1	-4.0	12.5	-0.8	12.5	-0.8	12.7	0.8	12.4	-1.6	12.6	0.0	12.6
L_{TO}	14.3	-2.7	14.7	0.0	15.0	2.0	15.1	2.7	14.8	0.7	15.0	2.0	14.7
$\Gamma_{\text{LO/TO}}$	15.1	-2.6	15.4	-0.6	15.8	1.9	15.9	2.6	15.6	0.6	15.8	1.9	15.5
MAD(%)		2.9		2.6		2.7		2.6		2.4		2.0	

3.6. Discussion of bulk properties

The overarching task of this chapter is to benchmark the performance of the SRSH functional for static as well as dynamic bulk properties. It is known that SRSH is accurate in predicting electronic and optical properties of semiconductors due to its tuning nature. Therefore, it is interesting to see if the tuning procedures reduce the accuracy in predicting other bulk properties. The information used to tune the parameters, e.g. the band gap calculated by GW, makes SRSH an empirical functional, while PBE and also HSE with a universal screening parameter can be understood as non-empirical functionals. The most important finding is that SRSH can compete with well-established functionals such as PBE and HSE. Especially, for the related quantities of lattice constants and bulk moduli, SRSH is more accurate than PBE and maintains the accuracy of HSE as seen in Fig. 3.3 and Fig. 3.4. This also holds when computing phonon dispersion relations as demonstrated with the MADs seen in Fig. 3.7. In the calculation of atomization energies (see Fig. 3.5), the PBE func-

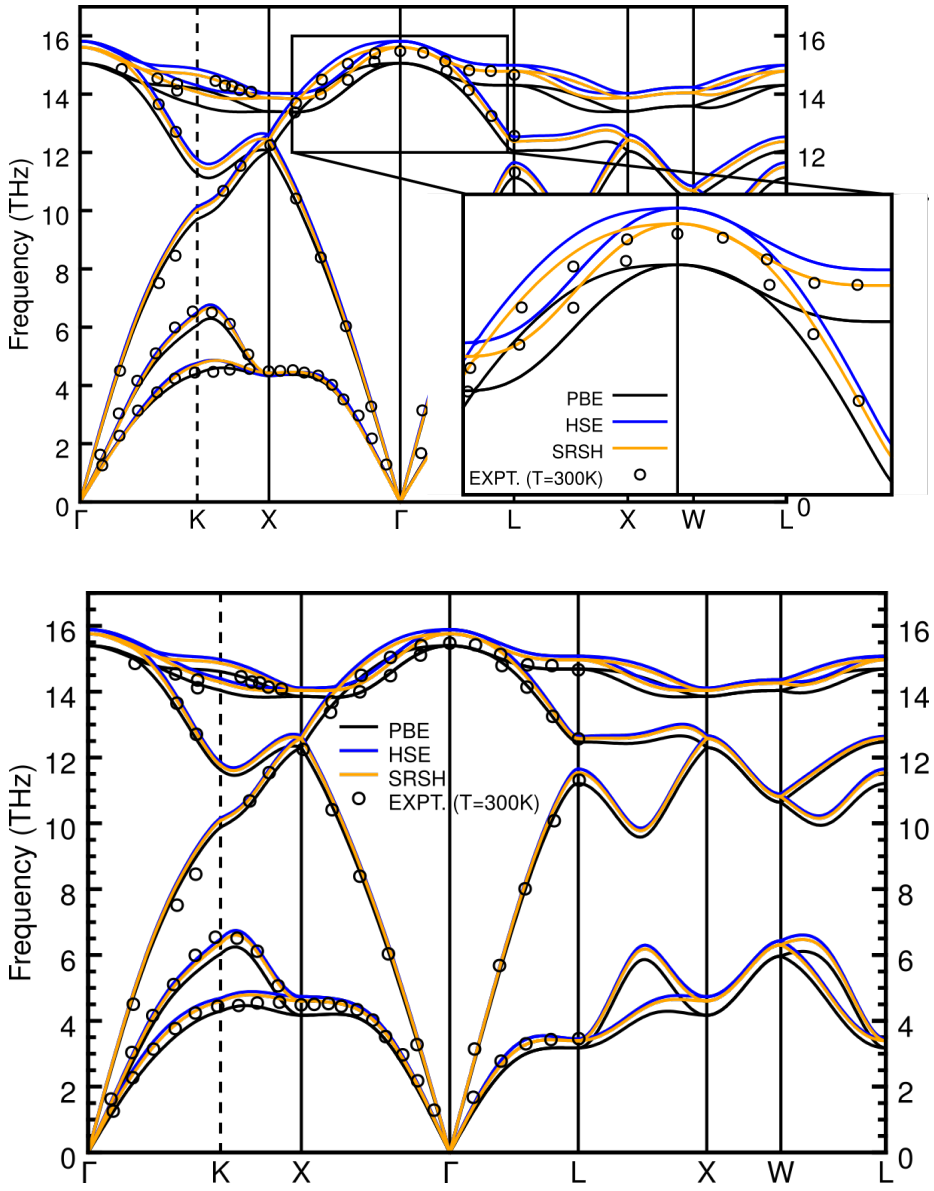

Figure 3.9. The upper panel shows the phonon dispersion relation of cubic diamond structured Si using the theoretical lattice constants calculated with the PBE, HSE and SRSH functionals (solid colored lines) as well as experimental data (open black circles), which was extracted from [159] and [160]. Note that experimental data was measured at 300 K. The lower panel shows the phonon dispersion relation for only using the experimental lattice constant throughout the three functionals. *Reprinted figure with permission from [1]. Copyright (2021) by the American Physical Society.*

tional is superior compared to the two hybrid functionals, which contain not only GGA but also EXX exchange with variable fractions along the interaction distance r.
Based on the performance of the functionals there are two ways of a general explanation: the first argument aims at the total amount of the GGA exchange in a functional, for instance 100% as in PBE or only 75% as in HSE, and the second argument aims at the construction of the GGA exchange itself, as there are adjustable parameters. The latter is directly linked to the reduced density gradient inherent in GGA functionals. In principle, the amount of the reduced density gradient determines whether structural properties like lattice constants or atomization energies are accurately described. Recalling the specific from of the spin-unpolarized exchange energy in equation 2.42, the enhancement factor $F_x(s)$ depends on the density gradient s, which reads

$$s(n) = \frac{1}{2k_F(n)} \frac{|\nabla n|}{n}. \tag{3.2}$$

The gradient expansion of the enhancement factor guarantees the uniform gas limit for small s [161]:

$$F_x(s) = 1 + \mu s^2 + \ldots \qquad (s \to 0). \tag{3.3}$$

The amount of the density gradient s is dictated by the parameter μ, which was motivated for PBE for other, non-empirical, reasons than generating accurate exchange energies for neutral atoms. In a similar expansion procedure for the correlation energy, the parameter ν dictates the amount of s (in the correlation energy).
The impact of the density gradients μs and νs can be seen by comparing results from the PBE and PBEsol functional [161]. Both functionals belong to the type of GGA functionals, but with different amount of the reduced density gradients. PBEsol can simply be derived from PBE by changing the amounts of the parameters μ and ν. In order to gain proper exchange energies of atoms, which is especially important for atomization energies in solids, the GGA functional has to reject the gradient expansion in the case of almost constant densities by increasing the parameter μ [162]. Note that the PBE and PBEsol functionals differ, for example, in the parameter μ by a factor of 2, i.e. $\mu_{\mathrm{PBE}} = 2\mu_{\mathrm{PBEsol}}$. As a consequence, the nonlocality given by the s dependence of the GGA functional is reduced from PBE to PBEsol by tweaking μ and ν. Whereas PBEsol is more accurate in describing lattice constants, it worsens the atomization energies in comparison to PBE due to being less dependent on the density gradient than PBE [139].
As with the reduction of the impact of the density gradient via a parameter, one can state that hybrid functionals further extenuate the influence of the density gradient by replacing a fraction of GGA by EXX. Specifically, SRSH and HSE use only a fraction of 75% of GGA exchange in the short range. Thus, on the one hand, hybrid functionals worsen the description of atomization energies and, on the other hand, simultaneously increase the accuracy of the lattice constant. In view of the attenuation of the density gradient, it is not surprising that SRSH provides the lowest accuracy for atomization energies in comparison to PBE and HSE as seen in Table 3.6, because of the still existing EXX in the long range. In other words,

HSE has full influence of the density gradient in the long range and, thus, is slightly superior in the atomization energies to SRSH. This is supported by Fig. 2.6, which illustrates the range-separation parameter and the variation of the GGA fraction by γ along the interaction distance r. In principle, it would be also possible for solids or isolated molecules to tune the SRSH parameter γ towards proper atomization energies. Needless to say, a comparison of total energies stemming from different γ parameters is somehow nonsensical and therefore a calculation of atomization in this way is unreasonable [163].
The calculation of phonon dispersion relations showed that all three functionals provide accurate results compared to experiment. When the frequencies are calculated for each functional with the respective theoretical geometry, an error propagation exists due to the deviation of the theoretical lattice constants. Thus, the differences in the phonon frequencies of the various functionals are somewhat larger in this scenario. But when using the same experimental lattice constant throughout testing each functional, these differences become smaller (see Fig. 3.7). In particular, results from SRSH and HSE become more equal and both are slightly more accurate than results from PBE. In principle, the calculation of phonon frequencies can be traced back to the calculation of forces obtained from displaced atoms. It seems that the portioning between the Hartree-Fock exchange and the generalized gradient approximation using a density gradient does not impact the calculation of forces in the short range much.
Note that when testing SRHS the range-separation parameter γ varies from 0.62 for Si up to 2.50 for GaAs, which is roughly a variation by a factor of four. In principle, there is no correlation between the magnitude of γ and the error of bulk properties calculated with SRSH. In Fig. 3.10, the deviation of the theoretical lattice constant compared to experiment is shown as a function of γ. Since PBE is not range-separated and HSE has a universal γ, the error behavior of these two functionals demonstrate the absence of a correlation between γ and the accuracy of SRSH. This means that a slight change of the γ parameter will change the band gap a little, but will not fully destroy the accuracy of SRSH in the description of bulk properties.

Note that the accuracy of the two hybrid functionals with respect to band gaps and, where applicable, bulk properties is accompanied by an increase in computational cost in comparison to the PBE functional. A list of computation times as well as a ratio factor can be seen in Table A.1 of the appendix. Furthermore, additional effects such as zero-point corrections, which require an enormous computational effort, and the already mentioned dispersion corrections such as the van der Waals corrections were not taken into account.
In addition to the previous research about SRSH [27, 28], benchmarking of bulk properties calculated with SRHS [1] complements the idea of tuning the band gap towards a GW band gap and letting the dielectric constant describe the long-range behavior. It was demonstrated that the accuracy of SRSH for electronic and optical properties of common inorganic semiconductors does not deteriorate the calculation of bulk quantities. Furthermore, SRSH can reproduce accurate results from the established PBE and HSE functionals.

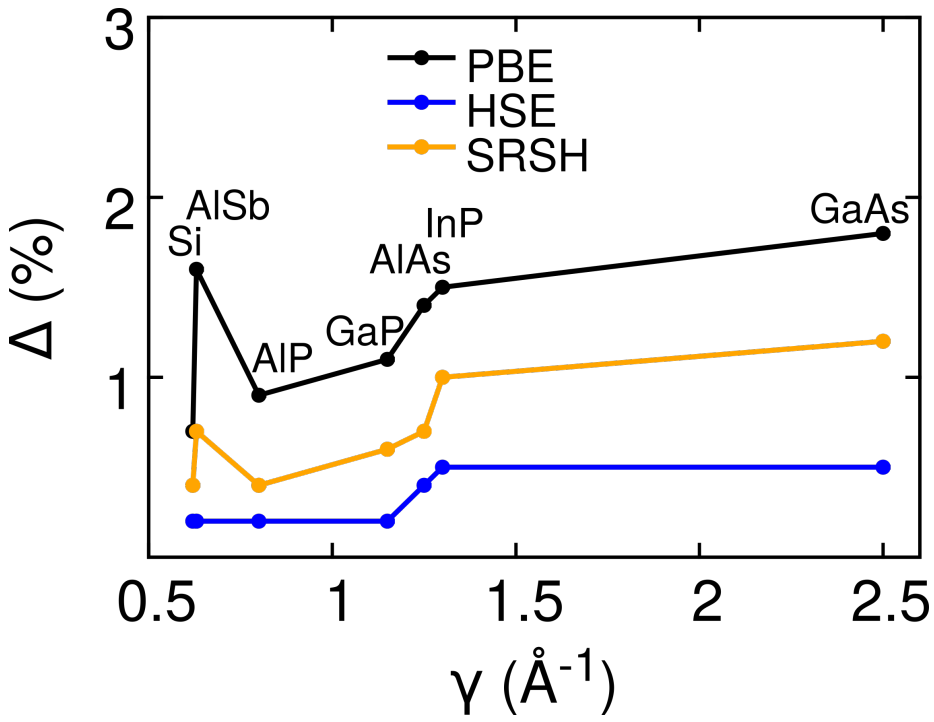

Figure 3.10. Deviation Δ (in %) of the theoretical from the experimental lattice constant as a function of the range-separation parameter $\gamma(\text{Å}^{-1})$. Only the SRSH functional depends on γ, which is different for each material. The materials are labeled as insets and the explicit γ values can be seen in Table 3.2. Note that the HSE functional has a constant range-separation parameter $\gamma = 0.2\,\text{Å}^{-1}$ and the PBE functional is not range-separated.

3.7. Impact of the EXX amount on the temperature-dependent band gap

The temperature-dependent band gap of diamond and Si is calculated for further investigations regarding the influence of the proportions of EXX and GGA in the short range. In order to access the temperature dependency of the aforementioned materials the Monte-Carlo or One-Shot methods, as introduced in the section 2.5.2, were applied. These methods rely on phonon-distorted structures in calculating the electron-phonon coupling energies responsible for the temperature dependence. For testing the influence of the EXX amount, the EXX amount of the HSE functional is varied. This is achieved by variations of the parameter α, dictating the amount of EXX in the SR, and the range-separation parameter γ, dictating the separation between short and long range, by reasonable amounts. Fig. 2.6 illustrates the effect of α and γ. The specific variations of α and γ are listed in Table 3.9 and for each calculation only one parameter is varied. In the case of diamond the temperature-dependent band gap is calculated using the LDA, PBE, HSE and variations of the HSE functional, in order to test whether there is a difference between conventional and hybrid functionals. The overall observation for diamond is that the change of the band gap with temperature seems to be insensitive regarding to the choice of the functional. A similar trend can also be observed for Si.

Table 3.9. The left-hand multi-column shows the HSE parameters with varied values for α, which determine the fraction of EXX in the SR. The right-hand multi-column shows the HSE parameters with varied values for γ, which specify the range separation in SR and LR. Note that the original HSE is determined by $\alpha = 0.25$ and $\gamma = 0.2$.

HSE(α)		HSE(γ)	
α	γ(Å^{-1})	α	γ(Å^{-1})
0.05	0.2	0.25	0.1
0.25	0.2	0.25	0.2
0.45	0.2	0.25	0.3

All calculations applied a $4 \times 4 \times 4$ supercell with 128 atoms using the experimental lattice constant for each material. The energy cutoff and number of k-points are converged separately. Note that in order to calculate the band gap for diamond or Si, the stated gap values are averaged over degenerate bands, i.e. averaged over the sixfold degeneration of the CBM close to the X-point and the threefold degeneration of the VBM at the Γ-point. The temperature dependence is calculated beginning from 0 K up to 700 K in steps of 100 K, where results from literature are available.

Temperature-dependent band gap of diamond:

Starting with diamond, first, the zero-point renormalization is calculated using the PBE and HSE functional (see Table 3.10). No significant difference can be observed

Table 3.10. Calculated zero-point renormalization energies for the diamond indirect band gap applying the PBE and HSE functionals. The calculation used a $4 \times 4 \times 4$ supercell containing 128 atoms and applied the full MC method. Note that the ZPR energy is negative and its inclusion to the static band gap value lowers or closes the band gap. The experimental ZPR is taken from [111] via extrapolation of the temperature dependence towards 0 K. In addition, ZPR energies resulting from selected phonon modes were calculated with the help of the AHC method as implemented in ABINIT, verifying results from [114].

	PBE	HSE	Exp
ZPR (eV)	0.368	0.375	0.370

in the ZPR values resulting from a pure GGA or hybrid functional. Overall, there is good agreement of ZPR to experiment. Next, the change of the temperature-dependent band gap is calculated using the PBE and HSE functional, as well as two variations of HSE by varying α (0.05 and 0.45), as seen in Fig. 3.11. The already known fact that the MC method can correctly predict the temperature trend for semiconductors is also demonstrated. One observes that there is no significant difference between the results from the different functionals, even when the amount of EXX is varied. Furthermore, the LDA functional is also tested with no visible difference to the other functionals. Therefore, LDA is not depicted in Fig. 3.11. In order to demonstrate the similarity between the accuracy of the MC and OS method, one value is calculated at 600 K using the full MC method with the PBE functional.

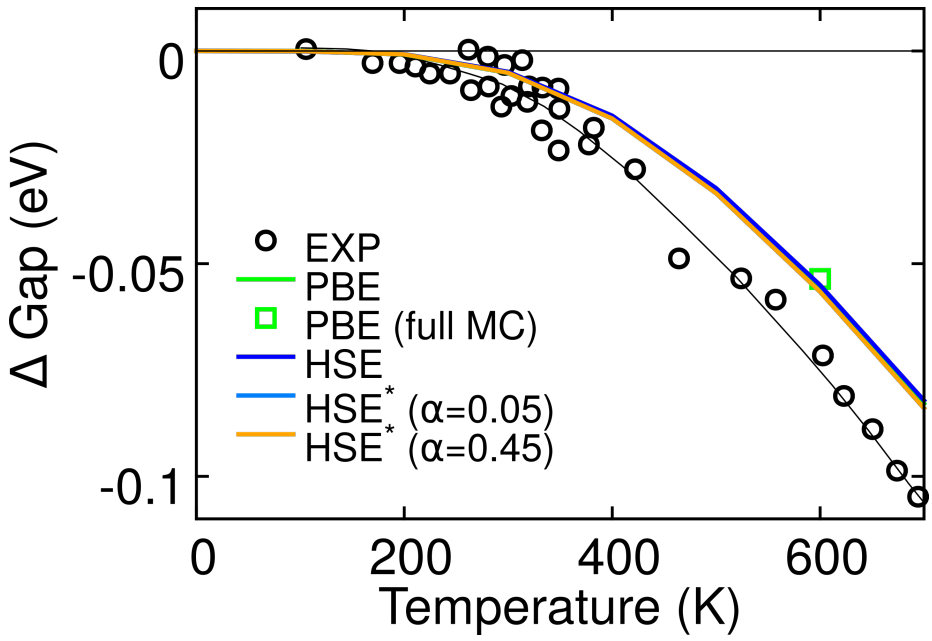

Figure 3.11. Change of the temperature-dependent band gap of diamond from 0 K up to 700 K. The plot shows the indirect band gap change including the effect of ZPR. All calculations applied the OS method and only one single calculation at 600 K applied the full MC method. All deviations Δ have been calculated with respect to the the static band gap resulting from the respective functional. Note that all four functionals provide very similar results so that the four lines coincide. The functional variants with $\alpha = 0.05$ and $\alpha = 0.45$ are functionals of the type HSE with accordingly varied α. Experimental data (open black circles) were extracted from [164] and the experimental fit is denoted as a thin black line.

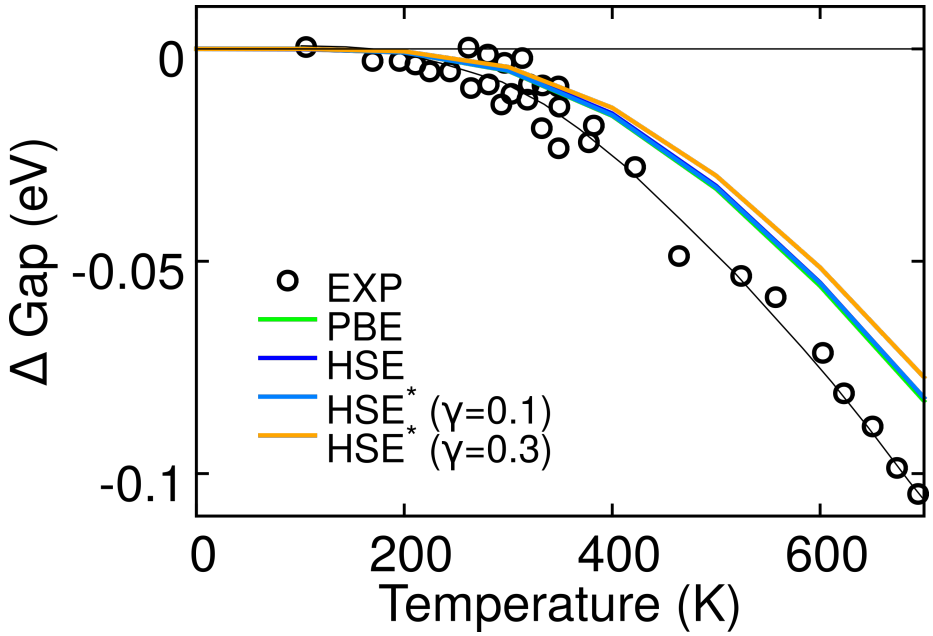

Figure 3.12. Description of the figure is the same as in Fig. 3.11, except that the functional variants of HSE have varied range-separation parameter to $\gamma = 0.1\,\text{Å}^{-1}$ and $\gamma = 0.3\,\text{Å}^{-1}$, instead of varied amount of exact-exchange via α.

Next, the portioning of EXX and GGA is investigated along the interaction distance r by varying the range-separation parameter γ of the HSE functional. Fig. 3.12 shows the variation of γ together with results from PBE and HSE. Also in this scenario, the temperature dependent changes of the indirect band gap are very similar for the different functionals. It can be assumed that the similarity of the results from all functionals also applies to other energy differences in the BZ. Note that in diamond the band gap change of the direct gap increases faster with temperature than the band gap change of the indirect gap [165, 166]. Overall, the results calculated here agree with results from literature, i.e. the band gap closing of approximately 80 meV for the diamond indirect band gap across the temperature range is consistent with the band gap closing of approximately 80 meV from [102]. Also, the results of the ZPR at the indirect gap of 368 meV for PBE and 375 meV for HSE coincide with the ZPR of 363 meV for PBE from [102]. Note that [114] stated approximately 90 meV gap closing for the direct gap using DFPT. Furthermore, [167] stated somewhat larger values for the direct gap closing of approximately 190 meV as well as for the ZPR of 600 meV, both values calculated with GW applying a scissor operator correction[2]. Furthermore, the inclusion of thermal expansion in the calculation of the temperature-dependent band gap remedies the difference between theory and experiment (see Fig. 3.13). In principle, including volume effects can be achieved by increasing the lattice constant with reasonable values from experimental thermal expansion. Here, the volume effects are incorporated via quasi-harmonic (QH) calculations [102].

[2]The authors of [102] mention that these large values are probably a misunderstanding resulting from the unique case of the direct band gap of diamond and the 200 meV larger results for the ZPR from G_0W_0 than from DFT.

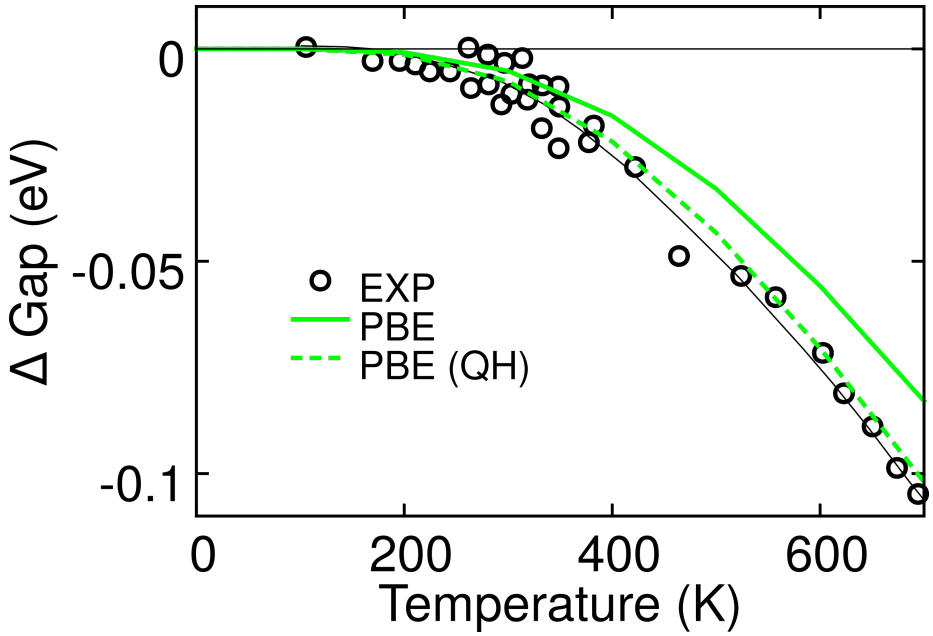

Figure 3.13. Description of the figure is the same as in Fig. 3.11, except that only the PBE functional was tested using the constant experimental lattice constant (closed green line) and the experimental lattice constant including thermal expansion (dashed green line). The thermal expansion or volume effects is achieved via quasi-harmonic calculations of the temperature-dependent lattice constants.

Temperature-dependent band gap of Si:

First, the ZPR for Si was calculated as listed in Table 3.11. The ZPR value of

Table 3.11. Zero-point renormalization energies for the Si indirect band gap appling the PBE, PBE0 and HSE functionals. The calculation used a $4 \times 4 \times 4$ supercell containing 128 atoms and applied the full MC method. Note that the ZPR energy is negative and its inclusion to the static band gap value lowers or even closes the band gap. The value of the ZPR calculated with PBE0 is taken from [102] and the experimental ZPR is taken from [111] via extrapolation from the temperature dependence up to 0 K.

	PBE	PBE0	HSE	Exp
ZPR (eV)	0.057	0.064	0.062	0.064

57 meV for PBE and 62 meV for HSE coincide with the 64 meV for PBE0 reported in literature [102]. Furthermore there is a good agreement to the experimental ZPR of 64 meV [111]. However, the difference between values from PBE and HSE are of a single-digit order of magnitude (5 meV) and thus not significant. Next, the temperature-dependent change of the indirect band gap of Si was calculated as seen in Fig. 3.14. Only the functionals PBE and HSE are tested to find out whether there is a difference between GGA and hybrid functionals. The largest deviation between the two results is roughly 10 meV at 700 K. The overall magnitude of the band gap closing is approximately 100 meV on a temperature range of 700 K, which is slightly less than the band gap change of 100 meV already reached at 500 K in [103]. This

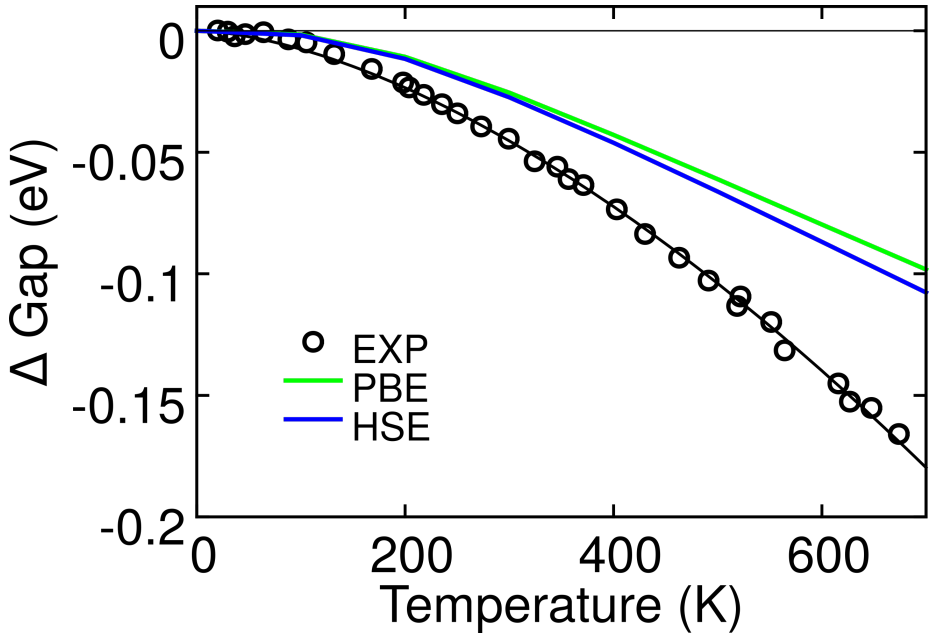

Figure 3.14. Change of the temperature-dependent band gap of Si from 0 K up to 700 K. The plot shows the indirect band gap change including the effect of zero-point renormalization. All deviations Δ have been calculated with respect to the the static band gap resulting from the respective functional. Experimental data (open black circles) were extracted from [168] and the experimental fit is denoted as a thin black line.

difference can be attributed to the different supercell sizes. The calculations in [103] used a $8 \times 8 \times 8$ supercell, whereas this study used a $4 \times 4 \times 4$ supercell.

Conclusion:

On the one hand, the ZPR for diamond is large (a few hundred meV) and the change in the temperature-dependent band gap is small in comparison (only one hundred meV) over a temperature range from 0 K to 700 K. For Si, on the other hand, the ZPR (60 meV) is smaller than the temperature-dependent change (100 meV) in the band gap. However, both materials demonstrate that the ZPR as well as the band gap change according to temperature do not strongly depend on the choice of functional, if at all.
Additionally, it can be assumed that the AHC method can also describe the temperature curve of the band gap for semiconductors with the correct gradient. It seems that a quadratic theory in the EPC terms is sufficient for harmonic materials where the effect of anharmonicity is not pronounced.
Initially, it was assumed that the choice of functional influences the magnitude of the EPC energy and thus also the temperature dependence of the band gap. Particularly, the formulation of the EPC energy in the frozen-phonon method (see equation 2.156) motivated this assumption. The EPC energy given by this approach depends explicitly on electronic eigenvalues and phonon frequencies. Thus, it is reasonable to assume that more precise values, as provided by hybrid functionals, could lead to more precise EPC values. However, since the EPC energy seems to be almost

insensitive of the choice of functional, whether GGA or hybrid, the strategy of exploiting the accuracy provided by SRSH, i.e. being accurate in both, electronic and frequency eigenvalues, has become somewhat obsolete. When going deeper into detail, taking into account the electron-phonon coupling matrix elements, regardless of first or second order, the matrix elements are mainly dictated by the wave functions. In the framework of perturbative methods in DFT, a general definition of the electron-phonon matrix element can be written as follows [15]:

$$g_{mn\mathbf{k},\nu\mathbf{q}} = \langle \psi_{m\mathbf{k}+\mathbf{q}} | \partial_{\nu\mathbf{q}} \hat{H} | \psi_{n\mathbf{k}} \rangle. \tag{3.4}$$

Therefore, if the calculation of the wave function is independent of the amount of EXX, it is obvious that the electron-phonon coupling matrix elements are insensitive to the choice of the functional, be it the generalized gradient approximation or the hybrid functional.

4. Results and discussion: halide perovskites

Note that the results discussed in chapter 4 are based on [2] and are the outcome of the collaboration with Xiangzhou Zhu (equal contributions).

4.1. Introduction to halide perovskites

A new class of energy materials, known as HaPs, has attracted great interest in semiconductor research, as the energy conversion efficiency of HaP-based solar cells is increasing rapidly. In particular, the rapidly increasing efficiency compared to conventional inorganic semiconductors is outstanding. For Si, for example, it took several decades to reach an efficiency of 26.1% for crystalline Si cells (non-concentrator, single crystal) [4]. In contrast, emerging photovoltaics (PV) including perovskite cells have already achieved an efficiency of 26.1% in only the last decade [4]. In addition, emerging PV using perovskite-silicon tandem (monolithic) solar cells have achieved an outstanding efficiency of 33.9% since its introduction in 2017 [4].
However, the bottleneck of the new energy material HaPs is that the material is unstable, or exhibits only short-term stability. This structural instability must be overcome, if HaPs are to be considered for solar cell applications. The typical perovskite structure has the form ABX_3, whereby in the case of halide perovskites the X-site anion is a halide of group VII. Typical halides in HaPs are the elements chlorine (Cl), bromine (Br) and iodine (I). In the case of all-inorganic HaPs, the A-site cation can be an alkali metal, such as the caesium atom (Cs) from group I. In another case of organic-inorganic HaPs, the A-site cation can be an organic molecule, such as the methylammonium (MA) or the slightly larger formamidinium (FA), where MA=CH_3NH_3 and FA=CH-$(NH_2)_2^+$. In general, if A is an organic molecule, it is a rather small molecule, and if A is an inorganic atom, it is a rather large atom[1]. In addition, the B-site cation in lead halide perovskites is formed by the metallic element lead (Pb). Two paradigmatic examples in the research of HaPs are the all-inorganic $CsPbBr_3$ and the hybrid organic-inorganic $MAPbI_3$.
Furthermore, the characteristic structure in HaPs is given by the B and X atoms, which form the inorganic lead-halide structure of a BX_6 octahedra, with the metallic atom B in the center and surrounded by the six halide atoms X. An A-site cation is located between eight corner and halide-sharing octahedra. An example of a cubic

[1] Note that for the mentioned cations following size relation holds: Cs < MA < FA.

ABX_3 perovskite structure is shown in Fig. 4.1.

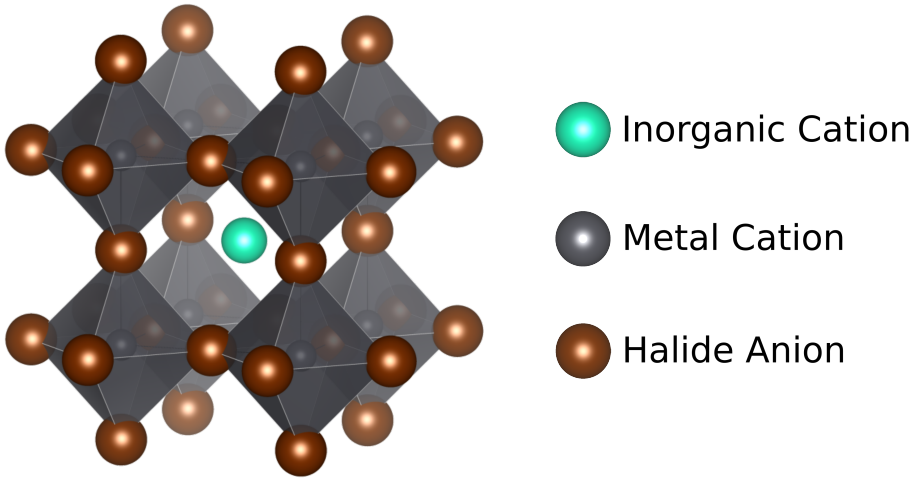

Figure 4.1. Schematic structural representation of the typical ABX_3 structure for cubic HaPs. Together with six halide anions X, the metal cation B forms the BX_6 octahedra, which is shown as gray shaded area. The eight shown octahedra enclose the inorganic cation A. In $CsPbBr_3$, for example, the cubic unit-cell consists of only 5 atoms. In organic-inorganic HaPs, the inorganic cation (cyan) is replaced by an organic molecule, such as in $MAPbI_3$. Note that the atoms shown on the right-hand side are not drawn to scale.

In contrast to common inorganic semiconductors, which can have a direct or indirect band gap (see chapter 3), the band gap of HaPs is always direct [169], when disregarding the Rashba effect in the inclusion of SOC. For cubic HaPs, for example, the direct band gap is located at the R-point, i.e. the edge of the BZ. This can be seen by means of the static band structure without SOC for cubic $CsPbBr_3$, as shown in Fig. 4.2. Since solar materials are used approximately at room temperature, it is of utmost importance to go beyond the static description and to understand the influence of thermal effects on the band gap. While the band gap of inorganic semiconductors decreases with increasing temperature, which is known as the "Varshni effect" [15]

$$E_{\mathrm{Gap}}(T) = E_{\mathrm{Gap}}^{\mathrm{Static}} - |\Delta E_{\mathrm{Gap}}^{\mathrm{ZPR}}| \left(1 + 2n\left(\frac{\hbar\omega_o}{k_{\mathrm{B}}T}\right)\right), \tag{4.1}$$

the band gap of HaPs increases with increasing temperature [170, 16]. The opening of the band gap due to thermal effects is schematically shown in Fig. 4.2 by the thick light-blue lines.
However, the dominant contribution that leads to the opening of the band gap of HaPs due to thermal effects remains to be discussed. Remarkably, the band-gap value calculated from the static cubic high-symmetry structure, which is considered only as an average crystal structure, can differ enormously from a band-gap value averaged over structural samples from HaPs. This holds for samples from quasistatic calculations [8, 10, 171] as well as for samples from fully dynamic calculations [7, 13]. In general, the thermal effects in HaPs that affect the band gap are the lattice expansion [92] and phononic vibrations [172, 8]. Both together are reflected in

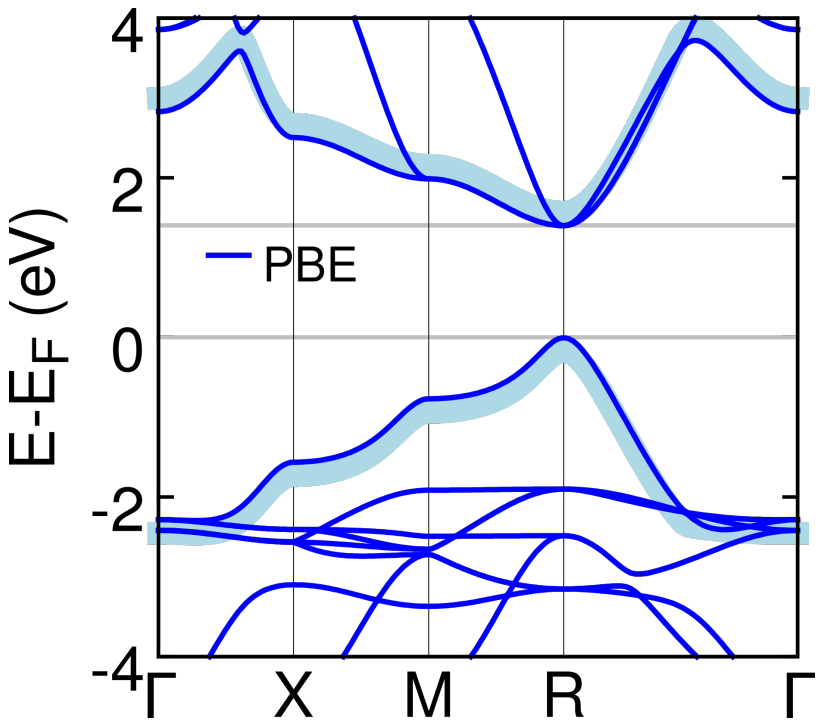

Figure 4.2. Static DFT band structure for cubic $CsPbBr_3$ calculated with PBE and without SOC (shown as thin blue line). The direct band gap is located at the *R*-point at the BZ boundary. A schematic representation of the opening of the band gap due to the inclusion of thermal effects is shown by the thick light-blue lines.

structural fluctuations associated with the unusual anharmonic motions that dominate HaPs. Indications of anharmonicity in HaPs are octahedral tilting (see Fig. 2.13) and atomic displacements with a large amplitude [8, 173, 174, 175, 105, 176].
For optoelectronic properties of HaPs, it is of particular interest to rationalize these structural fluctuations induced by vibrational anharmonicity, since they inherently determine the HaP atomic structure. In order to capture the full anharmonic picture, it is not adequate to remain in the harmonic approximation, when considering structural fluctuations at finite temperature. In particular, the interaction of the thermal phonon coupling is not taken into account in the harmonic approximation, in which the phonon modes are completely decoupled. In principle, the thermal atomic displacements calculated in harmonic approximation strictly follow a quadratic potential-energy surface (see also Fig. 4.10). But in HaPs, the atomic displacements due to anharmonic thermal vibrations go beyond a quadratic shape.

Typical for HaPs is a potential-energy surface that enables dynamic symmetry breaking, as offered by the double-well potential, schematically shown in Fig. 4.3. Such a double-well potential can be verified by using a Boltzmann inversion, as explained in chapter 4.5, of specific atomic displacements in HaPs. In $CsPbBr_3$, for example, atomic displacements, which reveal reminiscently a double-well potential, are Br displacements in a plane perpendicular to the Pb-Br-Pb bonding axis [105]. Such a potential-energy surface is considered dynamic because, for a given temperature, all phonon modes contribute to the vibrational anharmonicity, not just selected modes.

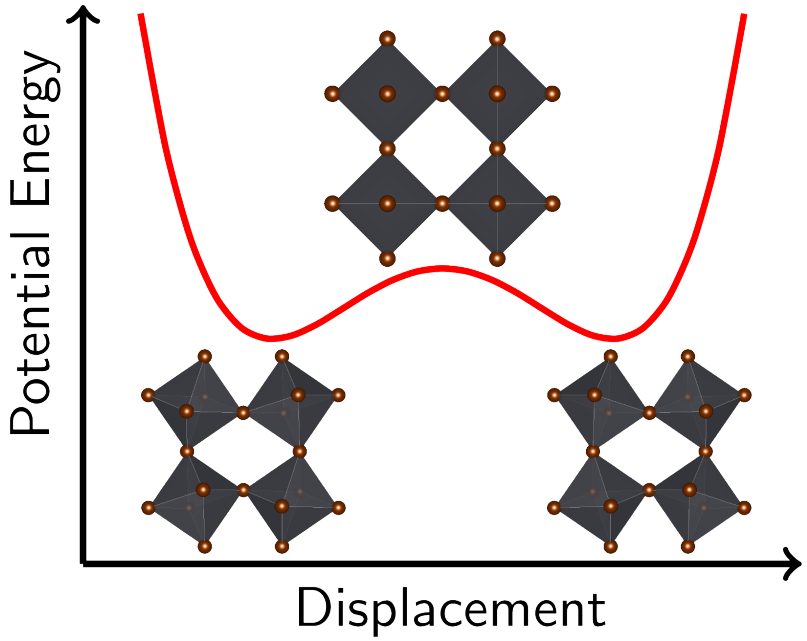

Figure 4.3. Schematic double-well potential characterizing the potential-energy surface of HaPs. Note that the local maximum corresponds to the cubic high-symmetry structure. At sufficiently high temperatures, the atoms can overcome the potential barrier of the local maximum, i.e. the double-well is smeared out so that the atoms have access to the entire potential-energy surface.

Also the large atomic displacements of Br perpendicular to Pb–Br–Pb bonding axis inherently show vibrational anharmonicity, which is accompanied by a rapid increase in the joint density of states [177]. Furthermore, non-Gaussian distributed Cs and Br displacements with respect to the highly symmetric cubic structure prove anharmonicity in the instantaneous perovskite structure [105]. In addition, both types of HaPs, hybrid organic-inorganic such as $MAPbI_3$ and all-inorganic such as $CsPbBr_3$, show unusual anharmonic behavior [174]. Note that in hybrid HaPs, rotations of the organic molecules occur [11], which are also responsible for anharmonicity [174]. In this research, however, the focus is on combining the unusual structural dynamics with the temperature-dependent band gap, which enables a microscopic understanding of vibrational anharmonicity in HaPs.
Additionally, anharmonicity is also linked to some extent to the calculation of electron-phonon interaction. This can be recognized in the calculation of the thermal band gap for HaPs and common inorganic semiconductors with and without higher-order EPC terms. For the harmonic semiconductor Si, for example, the inclusion or neglect of higher-order EPC terms shows no significant difference in the calculation of the temperature-dependent band gap (see chapter 4.2). In contrast to harmonic Si, anharmonic HaPs require the inclusion of higher-order EPC terms to correctly predict the slope of the temperature-dependent band gap, while neglecting higher-order EPC terms strongly overestimates the slope [16, 178]. Therefore, for harmonic materials, higher order EPC terms are not relevant, whereas for anharmonic materials, higher order EPC terms must be considered when investigating the

thermal band gap (see chapter 4.7).
HaPs in general occur in three phases, namely the orthorhombic, tetragonal and cubic phase. The prototypical HaP $CsPbBr_3$, for example, experiences two phase transitions at the temperature 361 K for the orthorhombic-to-tetragonal phase and at 403 K for the tetragonal-to-cubic phase [179, 180]. Fig. 4.4 shows structures of the orthorhombic and cubic phase of $CsPbBr_3$, since only these two phases are the subject of this investigation. The mere fact that the static band gaps of the

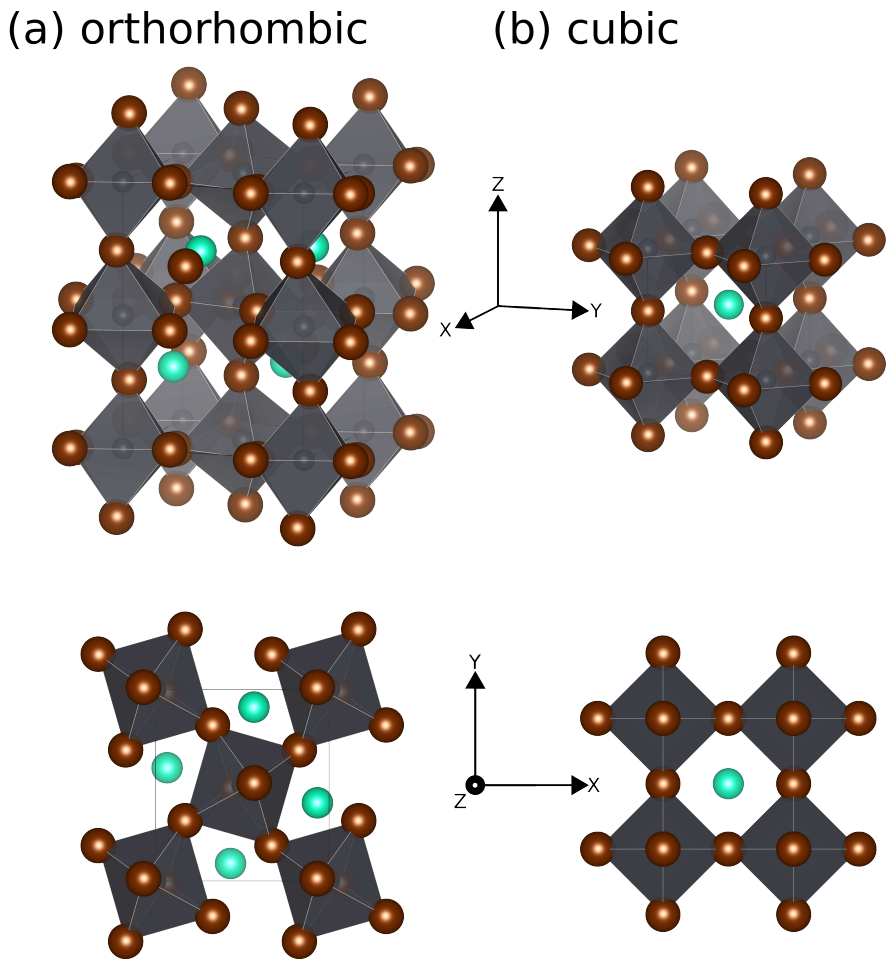

Figure 4.4. Schematic representation of the structures of the orthorhombic (a) and cubic (b) phase of $CsPbBr_3$. The panels on the bottom show the bird's eye view of the structures. Note that the phase transitions occur at following temperatures: orthorhombic-tetragonal at 361 K and tetragonal-cubic at 403 K.

orthorhombic and cubic structures differ greatly from each other raises the need for further investigations. Specifically, the static PBE-DFT band gap including SOC is 0.6 eV for the cubic phase [80] and 1.3 eV for the orthorhombic phase of $CsPbBr_3$ [181], a difference of 0.7 eV. A further task of this research is, therefore, to find out how the inclusion of thermal effects can overcome the jump in the band gap caused by two different phases. Note that the temperature range of the intermediate tetragonal phase is only 40 K and from experiments is known that the band gap is continuous across phase transitions [17].

Next, some additional features of HaPs are listed below. Apart from the fact that Pb is toxic, which is unfavorable for use as a solar material, the Pb atom is also very heavy due to its high nuclear charge. In the case of $CsPbBr_3$, the atomic masses are 133 u for Cs, 207 u for Pb and 80 u for Br. Due to the large mass of the Pb atom, the SOC contribution is generally dominant in lead-based HaPs and must therefore be taken into account. Note that the SOC contribution in $CsPbBr_3$ and $MAPbI_3$ lowers the static DFT band gap by hundreds of meV (see chapter 4.6). Another contribution that has an indirect effect on the band gap via a changed structure are dispersive corrections such as the long-range VdW interaction (see chapter 2.2.8). Compared to conventional inorganic semiconductors, where the inclusion of VdW interaction only slightly influences the structure[2] [72], the inclusion of VdW in HaPs leads to more precise structures. For $MAPbI_3$, for example, the inclusion of the pair-wise VdW interaction showed a reduction of the unit-cell volume and thus a lowering of the theoretical lattice parameters[3], which leads to a better agreement with the experiment [70]. In general, both the SOC effect and the VdW interaction do not influence each other, but must be taken into account in an appropriate description of HaPs [70].
However, the connection between anharmonic structural fluctuations and their effect on the band gap of HaPs has not yet been sufficiently discussed. Apart from the effect on the band gap, it is known that quantities like charge-carrier mobilities [182, 183], defect energetics [184], Urbach energies [93, 177] and exciton properties [185] are also influenced by the anharmonic lattice vibration present in HaPs. A profound understanding of vibrational anharmonicity, achieved by comparing theories excluding (MC) and including anharmonicity (MD), helps to further explain the impact on optoelectronic properties such as the electronic band gap. It will be demonstrated, how the inclusion of anharmonic fluctuations closes the band-gap difference from the static structures at the different phases of $CsPbBr_3$. This leads to an appropriate comparison to a continuous thermal band gap from the experiment. In addition, this research also aims to provide further insight into the unusual structural properties of HaPs caused by vibrational anharmonicity. In particular, the study determines band gap values averaged from structural samples of the statistical MC and MD methods and compares the results with each other and to experimental data. It will be agreed that anharmonicity can be understood as the difference that results from subtracting the results from MC and MD.

[2] In the case of Si, the difference between the PBE and PBE+VdW lattice parameters is 0.03 Å [72].
[3] In the case of $MAPbI_3$, the difference between the PBE and PBE+VdW lattice parameter is 0.13 Å [70].

4.2. Temperature-dependent band gap for harmonic materials

Computational details for Si:

In principle, the calculation of the temperature-dependent band gap with MD and MC consists of two parts. First, distorted structures are generated as samples, either from an MD trajectory or an MC calculation. Then the band-gap value is calculated as an average of the individual band gaps from the samples.
The following computational parameters are the same for the MD and MC method: All calculations are performed with VASP and use the PBE functional. A $4 \times 4 \times 4$ supercell built out of the Si fcc unit-cell containing 2 atoms is used, which results in a total of 128 atoms. The lattice parameter is the experimental Si lattice constant of 5.43 Å. Converged results are achieved with an energy cutoff of 270 eV and a k-point grid of one single k-point at the Γ-point. The explicit temperature-dependent band-gap values are calculated as an average out of 500 band gaps from MD snapshots or distorted MC structures for selected temperatures of 100 K, 300 K and 700 K. The individual band-gap calculations to determine the average value use an energy convergence threshold of 10^{-4} eV. Note that the indirect gap shown here refers to the band gap of the supercell at the Γ-point, which is not rigorously the indirect band gap of Si after the back-folding of the bands. However, this fact is insignificant if only the temperature evolution is studied. In addition, the band-gap values are calculated without the SOC contribution, which is negligible for common inorganic semiconductors. Moreover, the band-gap values from MD and MC are not only averaged over the sample structures, but also over the originally degenerate bands. Since the distorted structures lift the degeneracy, the individual band-gap values are averaged over the originally sixfold degenerate CBM and the originally threefold degenerate VBM. In contrast, the band-gap value calculated from AHC is not averaged over bands as the bands are still degenerate.
The distinct computational parameters referring to the first part of the calculation are: The MC calculations use an energy convergence threshold of 10^{-4} eV, which is sufficient to achieve converged phonon frequencies and modes for Si. Additionally, the MC method uses the Bose-Einstein statistics to create random structures. The MD calculations use a slightly more stringent energy convergence threshold of 10^{-5} eV, a total runtime of 18 ps and a time step of 2 fs.

Results for Si:

In order to rationalize the influence of anharmonicity on the temperature-dependent band gap, a comparison of the results from MC and MD is informative when anharmonicity initially plays a minor role. Using harmonic materials, it can be shown that the results calculated with MD, which inherently takes anharmonicity into account, and the MC method do not differ significantly from each other. This is illustrated in Fig. 4.5 by the band-gap distributions for Si calculated with MD and MC, together with the result from the AHC method (see chapter 2.6 for explanations

of all three methods). The averaged band-gap values at the temperature of 700 K are 549 meV for MD, 537 meV for MC and 520 meV for AHC. This leads to a band-gap difference of 12 meV between the averaged band gaps from MD and MC, and to a band-gap difference of 17 meV between the band gaps from AHC and MC. Consequently, the band-gap values calculated with all three methods hardly differ from each other.

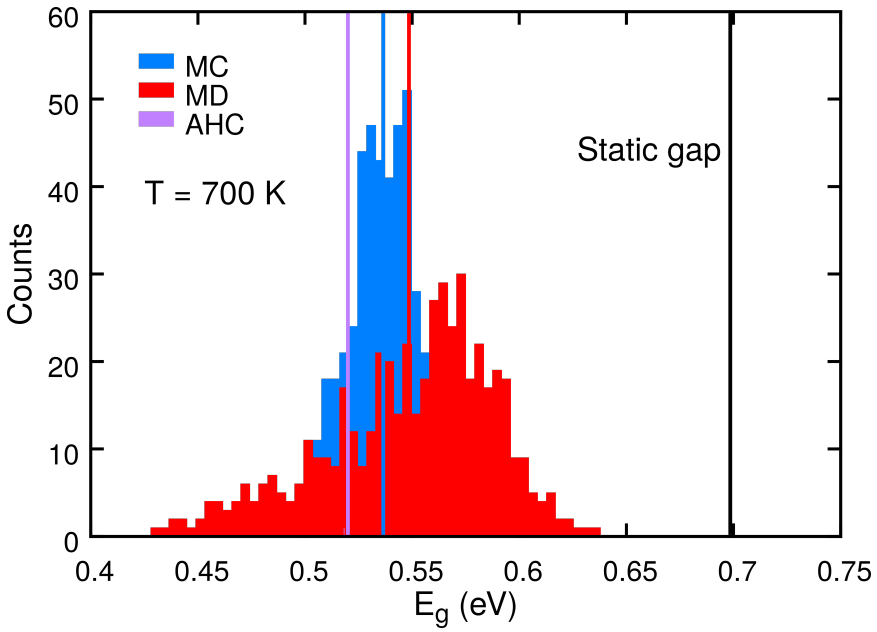

Figure 4.5. Temperature-dependent indirect band gap for Si calculated at 700 K. The averaged band-gap values are 536.5 meV for MC (blue vertical line) and 548.5 meV for MD (red vertical line) and differ by only 12 meV. The band-gap value determined with the AHC method is 520 meV (violet vertical line) and differs by only 16.5 meV to the band-gap value from MC. Note that the AHC band-gap change is calculated within the non-adiabatic AHC method and is taken from Ponce et al. [119]. The AHC band-gap change is 178.5 meV for the temperature range of 700 K and is subtracted from the static band-gap value of 698.5 meV. The temperature-dependent band-gap values are calculated with the LDA functional in the case of AHC and with the PBE functional in the case of MC and MD. Note that the choice of functional has negligible effects on the calculation of the temperature-dependent band gap (see chapter 3.7).

In particular, the statistically calculated band-gap values show that MD and MC provide almost equivalent results for the temperature-dependent band gap when anharmonic effects are negligible. In addition, the statistical approaches provide also similar results, in the case of harmonic Si, to the result from the perturbative AHC method applying the DFPT framework. This implies that higher-order EPC terms, as considered in MC and neglected in AHC, do not contribute much for harmonic materials, such as Si, while they are required for anharmonic materials (see chapter 4.7). Therefore, higher order EPC terms are connected to anharmonicity in the sense that they are relevant for anharmonic materials but play a less important role for harmonic materials. Note that the corresponding static band gap in Fig. 4.5 is 699 meV, which shows that the inclusion of temperature leads to a reduction in the band gap as expected for common inorganic semiconductors.
Furthermore, Fig. 4.6 shows the Si temperature-dependent band gap calculated with MD and MC for the temperatures 100 K, 300 K and 700 K. The corresponding band-gap distributions are depicted in the appendix A.4. In general, the band-gap distributions from MC are Gaussian distributed, since the probability distribution for the generation of the displacements is also Gaussian distributed (see details in chapter 2.5.2). In addition, the effect of a temperature-induced broadening of the distribution can be observed in both band-gap distributions from MD and MC[4]. To summarize, the example of harmonic Si shows that the results from MD and MC above room temperature are very similar, if anharmonicity is a small effect.

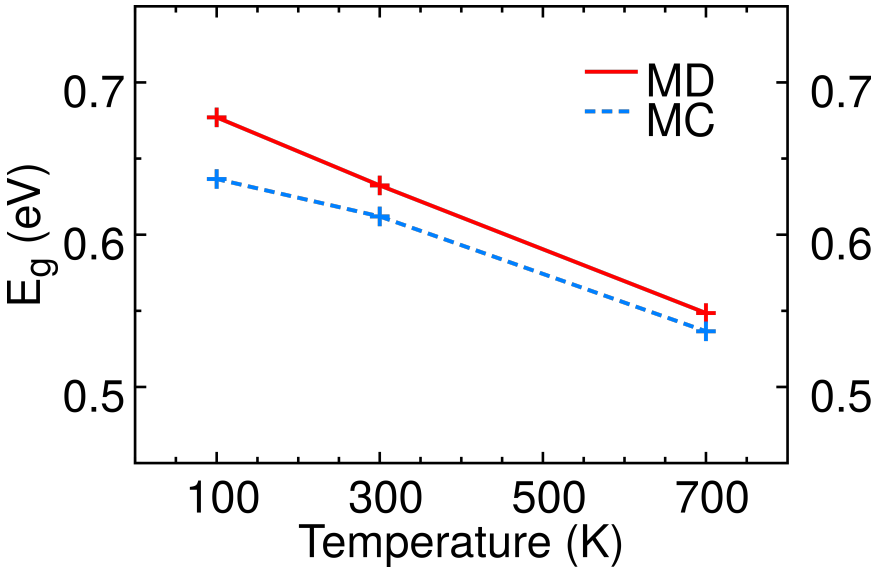

Figure 4.6. Temperature-dependent indirect band gap for Si calculated with the MC method (blue-dashed line) and MD (red line) for 100 K, 300 K and 700 K. Note that the band-gap values are calculated as an average over structures from MC and MD. *Reprinted figure with permission from [2]. Copyright (2023) by the American Physical Society.*

[4]It would be interesting to compare the shapes of the MD band-gap distributions for common inorganic semiconductors, where the band-gap decreases with increasing temperature, with the shapes of the MD band-gap distributions for HaPs, where the band-gap increases with increasing temperature.

4.3. Temperature-dependent reflectance measurements of $CsPbBr_3$

To classify the results from MD and MC for $CsPbBr_3$, it is important to refer to experimental data as a benchmark. Therefore, not only the absolute values of the experimental band gap for some selected finite temperatures are essential, but also the temperature evolution of the band gap over a larger temperature range including the phase transitions.

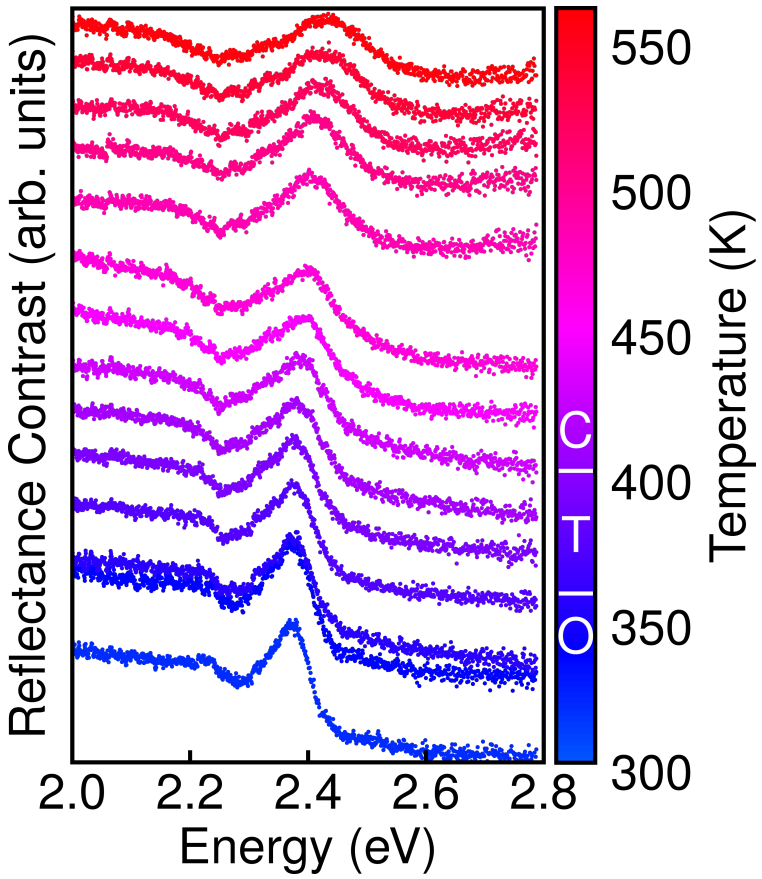

Figure 4.7. Reflectance measurements of single crystal $CsPbBr_3$ in a temperature range from 300 K to 560 K measured in intervals of 20 K. The color bar (right side) indicates the specific temperature for each measured spectra and the horizontal white lines in the inset denote the temperatures of the phase-transitions. *Reprinted figure with permission from [2]. Copyright (2023) by the American Physical Society.*

Therefore, reflectance measurements of single crystal $CsPbBr_3$ [2] are shown in Fig. 4.7[5]. The measured spectra extend over a temperature range from 300 K to 560 K including the orthorhombic-to-tetragonal phase transition at 361 K and the tetragonal-to-cubic phase transition at 403 K [179, 180]. The spectra are measured in steps of 20 K. The reflectance measurements show a pronounced peak at ≈2.4 eV, which corresponds to the excitonic absorption [186]. Due to a small exciton binding energy for $CsPbBr_3$ of ≈26 meV [187], the slight right shift of the pronounced peak

[5]The experimental data were measured by Guy Reuveni, Sigalit Aharon and Omer Yaffe.

(see Fig. 4.7) with increasing temperature can be rationalized as the temperature dependency of the band gap. Note that the exciton binding energy of $CsPbBr_3$ at room temperature is in the order of magnitude of the thermal energy given by $k_B T$ and can therefore be considered small [187].
A Tauc plot[6] is used to estimate the temperature-dependent band gap as the intersection point from the linear fit with the x-axis of the corresponding absorption spectra. The estimated temperature-dependent band-gap values of $CsPbBr_3$ are shown in Fig. 4.8. Increasing the temperature leaves the band gap almost unchanged, which can be seen by only mild changes in the gap across the investigated temperature range. The experimental data also show no strong fluctuations in the band gap at the phase transition temperatures. Notably, no discontinuity is observed in comparison to the band gap difference of 0.7 eV from the orthorhombic and cubic static gap. Thus phase transitions have minor impact on the band gap of $CsPbBr_3$. In addition, the experimental results presented in Fig. 4.7 are consistent with the experimental data available in the literature [17]. For further explanations of the experimental measurements, the reader is referred to appendix B: "Experimental methods" in Seidl et al. [2].

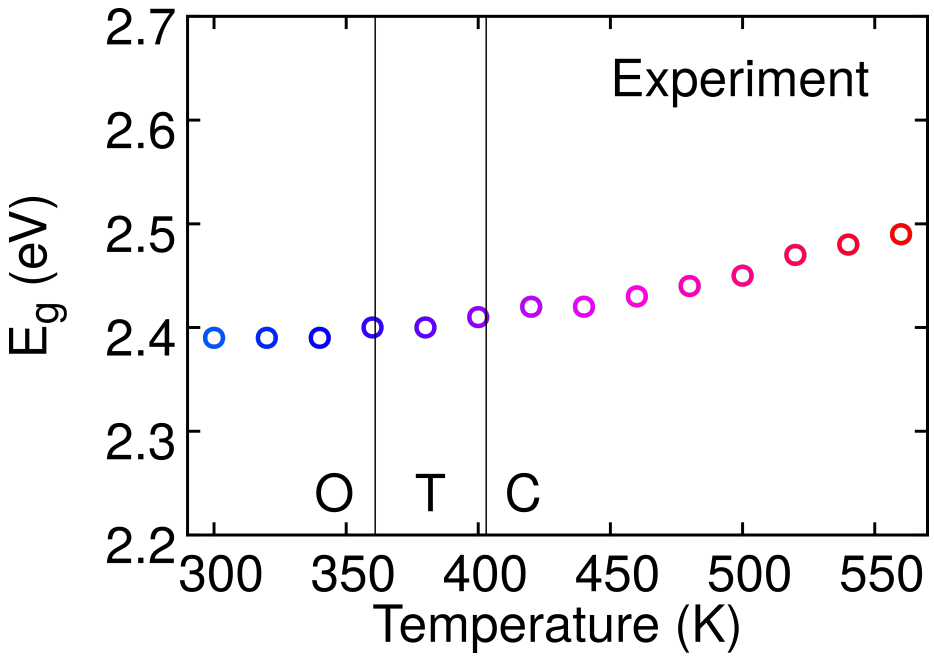

Figure 4.8. Temperature-dependent band gap for $CsPbBr_3$ corresponding to the reflectance measurement of Fig. 4.7. The color scheme of the band gaps corresponds to the color bar of Fig. 4.7. The band gap is given as an estimate by the intersection point of the linear fit using a Tauc plot and the x-axis of the absorption spectra. The thin vertical lines indicate the three phases of $CsPbBr_3$: orthorhombic (O), tetragonal (T) and cubic (C) [179].

[6] A detailed explanation of a Tauc plot can be found in Ref. [188].

4.4. Temperature-dependent fundamental band gap of $CsPbBr_3$

Computational details for $CsPbBr_3$:

All DFT calculations for the MD and MC method, as well as the standard band-gap calculations are performed with VASP in conjunction with the PBE functional. A PAW pseudo-potential is applied for the core-valence interactions including semi-core Pb-6s, Cs-5p and Cs-6s states as valence electrons. The orthorhombic structure of $CsPbBr_3$ is used for the temperatures 275 K, 325 K and 375 K and the cubic for 425 K, 475 K and 525 K (see chapter 4.1 for details of the corresponding structure). For both phases, supercells with 160 atoms are used, which are formed for the orthorhombic phase by a $2 \times 2 \times 2$ supercell and for the cubic phase by a $4 \times 4 \times 2$ supercell. The corresponding unit-cells are first relaxed before the supercells are created. Therefore, relaxation calculations are performed with following parameters: an energy cutoff of 400 eV, an energy convergence threshold of 10^{-6}, a $8 \times 8 \times 8$ Γ-centered k-grid for the cubic structure, a $6 \times 4 \times 6$ Γ-centered k-grid for the orthorhombic structure and a convergence threshold of 5×10^{-3} eV / Å for the maximum residual forces on the atoms. Note that the unit-cell relaxations are executed with the dispersive corrections of the Tkatchenko-Scheffler method with and without the iterative Hirshfeld partitioning (see chapter 2.2.8).
A Nosé hoover thermostat is used for the MD calculations to define the temperature in the canonical NVT ensemble (see chapter 2.5.1). Note that thermal expansion is not included in the NVT ensemble. The Tkatchenko-Scheffler method with iterative Hirshfeld partitioning (TS-IH) is used for the dispersive corrections in the MD (see chapter 2.2.8). The $CsPbBr_3$ supercells for MD are created out of the orthorhombic *Pbnm* unit-cell with the lattice parameters of 8.61 Å, 11.76 Å and 7.94 Å and out of the cubic $Pm\bar{3}m$ unit-cell with the lattice parameter of 5.94 Å for each direction (both relaxed with TS-IH). The orthorhombic supercell is sampled with one single k-point at the Γ-point and the cubic supercell with a $1 \times 1 \times 2$ Γ-centered k-grid according to the size of the supercell. In addition, a kinetic-energy cutoff of 300 eV and a energy convergence threshold of 10^{-6} eV are used for both phases. The MD time step to capture the oscillation period of the atoms is set to 8 fs. The equilibration run for each phase is 8 ps, followed by a 42-ps long production run. Snapshots to calculate separately the average band-gap values for each temperature are taken from the first 16 ps of the production run in equidistant time intervals. The averaged band-gap values are converged with only 100 gaps from different snapshots. Note that tests of using different time intervals for the snapshot selection from the 42-ps long trajectory do not show any difference in the convergence behavior of the averaged band-gap value.
MC calculations require a slightly more stringent parameter setting to accurately calculate the phonon frequencies and modes at the Γ-point (see chapter 2.5.2). Therefore, an energy cutoff of 400 eV and an energy convergence threshold of 10^{-8} eV are used for both phases. The Tkatchenko-Scheffler method (TS) is used for the dispersive corrections in MC (see chapter 2.2.8). The $CsPbBr_3$ supercells for MC

are created out of the orthorhombic *Pbnm* unit-cell with the lattice parameters of 8.43 Å, 11.85 Å and 7.65 Å and out of the cubic $Pm\bar{3}m$ unit-cell with the lattice parameter of 5.81 Å for each direction (both relaxed with TS). The orthorhombic supercell is sampled with a $3 \times 2 \times 3$ k-grid and the cubic with a $2 \times 2 \times 4$ k-grid, which are both Γ-centered. Note that in the MD and MC calculations the applied dispersive corrections using the Tkatchenko-Scheffler method differ by the iterative Hirshfeld partitioning, because the corresponding dispersive correction improved the numerical stability for the respective method.
In all statistical calculations of the band-gap average for each temperature, 100 MD snapshots or distorted MC structures are used for convergence. The standard band-gap calculations use an energy cutoff of 300 eV and an energy convergence threshold of 10^{-4} eV throughout the different phases. A Γ-centered $2 \times 2 \times 4$ k-grid is used for the cubic phase and a Γ-centered $3 \times 2 \times 3$ k-grid for the orthorhombic phase. In the orthorhombic phase of $CsPbBr_3$ the direct gap is located at the Γ-point. In contrast, the cubic phase of $CsPbBr_3$ has the direct gap located at the *R*-point. Due to the back-folding of the bands in the calculation for the cubic supercell, the band gap is also specified at the Γ-point. In addition, the SOC effect is included in the average band-gap values for each temperature.

Results for $CsPbBr_3$:

The research of the thermal evolution of the $CsPbBr_3$ band gap is interesting not only due to the lack of complete understanding of the anharmonic fluctuations, but also due to the strong differences between experiment and theory. From experimental data of $CsPbBr_3$, as easily recognizable in Fig. 4.8, a continuous temperature-dependent band gap across phase transitions is observed. Interestingly, the experimental band-gap values range from absolute values of ≈2.4 to ≈2.5 eV and show a slight opening of the band gap of ≈100 meV in the temperature range from 300 K to 560 K. These observations from experiment are in contradiction to theoretical static DFT calculations. For example, the band-gap value calculated using the static orthorhombic structure with PBE and including SOC, shows a difference of about 1 eV compared to experiment. This discrepancy is even more pronounced when considering the static cubic structure with a band-gap value of 0.6 eV (PBE+SOC). Although weakening the underestimation of the band gap by PBE when using HSE, which leads to a band gap-value of 1.2 eV (HSE+SOC) for the static cubic structure, a large difference to the experiment remains. These experiment-theory differences require a more detailed discussion, whereby the description of thermal effects from MD and MC give insight. It is also important to clarify how the difference between the static orthorhombic and cubic band gap of 0.7 eV is affected when temperature is taken into account.
Therefore, the temperature-dependent fundamental band gap is calculated for temperatures of the orthorhombic and cubic phase of $CsPbBr_3$ using the MD and MC methods. The statistical band-gap values include the SOC effect and are presented in Fig. 4.9. Note that the detailed computational parameters are described below.

The corresponding PBE band-gap values, as well as the values without SOC, are presented in Table 4.1. The intermediate tetragonal phase is neglected in the investigations, as it only occurs in a narrow temperature range.

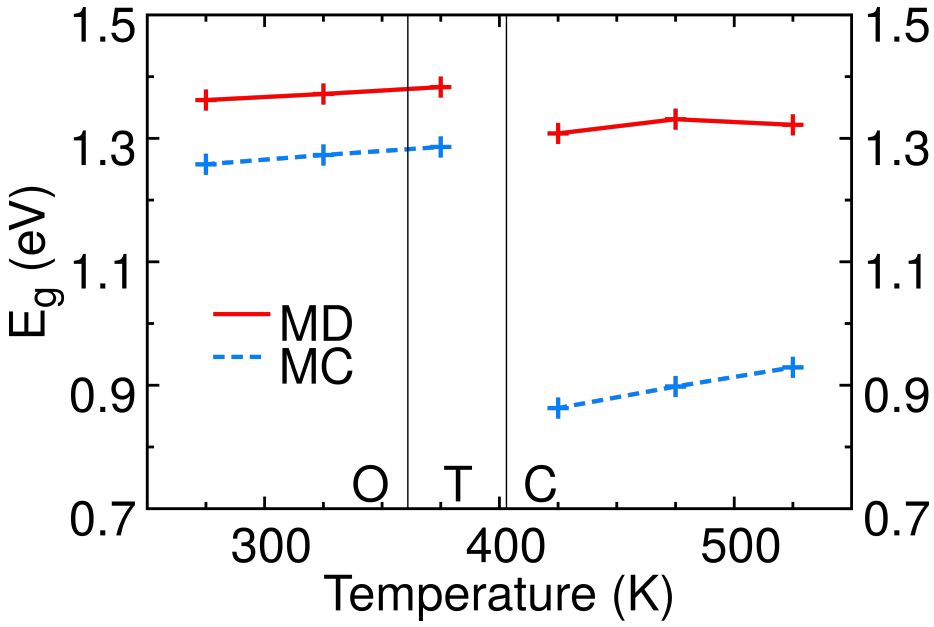

Figure 4.9. DFT-based calculations show the fundamental band of $CsPbBr_3$ calculated for following selected temperatures: 275 K, 325 K and 375 K for the orthorhombic phase and 425 K, 475 K and 525 K for the cubic phase. All bang-gap values are calculated as the average of 100 gaps from MD snapshots (red lines) or distorted MC structures (blue dashed lines). Note that the bang-gap values include the SOC effect and are calculated with the PBE functional. The thin vertical lines indicate the three phases of $CsPbBr_3$: orthorhombic (O), tetragonal (T) and cubic (C) [179]. *Reprinted figure with permission from [2]. Copyright (2023) by the American Physical Society.*

Table 4.1. Temperature-dependent band-gap values calculated without (upper row) and with (lower row) SOC for the orthorhombic and cubic phase of $CsPbBr_3$. Further details can be found in the description of Fig. 4.9. *Reprinted table with permission from [2]. Copyright (2023) by the American Physical Society.*

		Orthorhombic			Cubic		
	Temperature (K)	275	325	375	425	475	525
without SOC	E_g^{MD} (eV)	2.187	2.186	2.189	2.149	2.150	2.130
	E_g^{MC} (eV)	2.094	2.098	2.100	1.775	1.791	1.804
SOC	E_g^{MD} (eV)	1.362	1.372	1.383	1.308	1.331	1.322
	E_g^{MC} (eV)	1.258	1.273	1.286	0.863	0.898	0.929

At first glance, the results from MC show that a continuous description of the band gap across the phase transitions, as observed in the experiment, is not possible (see Fig. 4.9). The corresponding band-gap values of 1.27 eV at 325 K and 0.86 eV at

425 K show a decrease of 0.41 eV between the orthorhombic and cubic phase. This means that the phonon-induced gap renormalization by MC can attenuate the band gap difference between the static cubic and orthorhombic structures by 0.3 eV, but still leaves a significant jump. Even if the band-gap underestimation by PBE is taken into account, the MC method relying on the average crystal structure cannot provide band-gap values, which are approximately comparable with the values from experiment (≈2.4 to ≈2.5 eV). In the orthorhombic phase the MC method shows a band-gap opening of 28 meV and in the cubic phase of 66 meV (see Table 4.1), which together results in a band gap opening of ≈100 meV in a temperature range of 200 K. This is a slight overestimation compared to the experimentally observed band-gap opening of ≈100 meV in a temperature range of 260 K (see Fig. 4.8). Thus, the thermal samples of MC, generated by phonon-displaced atoms in the harmonic approximation, can predict the temperature trend correctly, which is remarkable, but fail when comparing the absolute values with the experiment. Also, they cannot explain a phase transition and therefore leave a significant jump in the thermal evolution of the band gap.
In the case of results from MD, one can see that the band-gap values are consistently above 1.3 eV (see Fig. 4.9). In addition, the discrepancy of ≈0.7 eV between the static orthorhombic and cubic structure is almost resolved by MD. This is confirmed by the corresponding band-gap values of 1.372 eV at 325 K and 1.308 eV at 425 K, resulting in a band-gap difference of only ≈60 meV. However, an entire continuous thermal evolution of the band gap, as observed in the reflection spectrum (see Fig. 4.8), cannot be determined with NVT MD. Next, results from MD show a mild band-gap opening of 21 meV in the orthorhombic phase and 14 meV in the cubic phase (see Table 4.1). This leads to a band-gap opening of ≈40 meV in a temperature range of 200 K, which is lower than the band-gap opening of ≈100 meV in a temperature range of 260 K in the experiment.
The most significant difference between results from MD and MC is the large jump at the phase transition by MC. The discontinuity from MC (≈0.4 eV) is almost seven times larger than the discontinuity from MD (≈0.06 eV). Consequently, MD resolves with more success the band-gap difference from the static orthorhombic and cubic structures of $CsPbBr_3$. The overall largest band-gap difference is observed in the cubic phase at 425 K, where the band-gap values from MD and MC differ by 445 meV. This difference decreases with increasing temperature in the cubic phase. In the case of the orthorhombic phase the band-gap difference from MD and MC remains somehow equidistant and is ≈100 meV for the selected temperatures.
In chapter 4.2 it was demonstrated that for harmonic bulk Si, results between MC, which is a phonon-based method in the harmonic approximation, and MD, which includes vibrational anharmonicity to full extent, are very similar. For anharmonic materials, such as $CsPbBr_3$, MD captures also dynamic structure fluctuations beyond harmonic motions and therefore provides results, which are closer to experiment than results from MC. This is particularly apparent by the large difference of ≈0.4 eV between band gaps from MD and MC throughout the entire cubic phase. This difference can be attributed to a contribution from anharmonicity, which is described by the

semiclassical description of structure fluctuations in MD. To summarize, the specific band-gap values from experiment and theory at the temperature of 425 K are: ≈2.4 eV from experiment, ≈1.3 eV from MD and ≈0.9 eV from MC. Since all theoretical band-gap values are generally too small due to the band-gap underestimation by PBE, the use of hybrid functionals, such as the HSE functional, can increase the band gap of $CsPbBr_3$ by ≈0.7 eV (see chapter 4.6). Consequently, the results from MD in the cubic phase are twice as close to the experimental range as those from MC, when considering the improvement due to HSE. This emphasizes the importance of anharmonic effects for the electronic structure, which are not included in pure-phonon contributions based in the harmonic approximation.
In addition, the SOC contribution calculated by using MD structures is ≈0.8 eV throughout the two phases, whereas the SOC contribution from distorted MC structures is ≈0.8 eV for the orthorhombic and ≈0.9 eV for the cubic phase. A further discussion of the influence of the SOC effect on the temperature-dependent band gap of $CsPbBr_3$ is provided in chapter 4.6.
Here, it is only qualitatively mentioned that changes in the lattice constants result in changes of the band gap. In $CsPbBr_3$, for example, a cubic lattice constant of 5.81 Å exhibits a smaller static band gap than a lattice constant of 5.94 Å. However, with regard to the various dispersive corrections, the relaxed cubic lattice constant of 5.81 Å must be used for MC calculations and 5.94 Å for MD calculations. The same applies to the orthorhombic lattice constant.

4.5. Role of Br dynamics

Several studies have reported a strong influence of octahedral-tilting motions associated with Br or other halide displacements on the HaP electronic structure [8, 7, 13, 11, 189]. Therefore, the atomic motions are analyzed in more detail. Specifically, transversal Br motions perpendicular to the Pb-Br-Pb bond axis are connected to octahedral-tilting motions [105, 177]. In order to investigate the connection between the thermal Br dynamics and the temperature-dependent band gap, the free energy is examined as a function of the transverse Br displacements. Therefore, a Boltzmann inversion of histograms of transversal Br displacements from MD trajectories and MC-distorted structures yields changes in the free energy (see Fig. 4.10 (a) for the results and see next paragraph for the description of the Boltzmann inversion). As a result, relatively small thermal Br displacements from MD are observed in the orthorhombic phase at 325 K and the free energy behaves almost harmonically. Moreover, the change of the free energy from MC-distorted structures at 425 K is intrinsically harmonic and the thermal Br displacements are larger than from MD in the orthorhombic phase at 325 K. In contrast, the free energy from MD in the cubic phase at 425 K is anharmonic with the largest Br displacements and a flat potential shape, which is far from harmonic.
Note that after applying the Boltzmann inversion, the change in free energy is determined by

$$E(\delta r_1, \delta r_2, \delta r_3) \propto -\ln[n(\delta r_1, \delta r_2, \delta r_3)] \cdot k_\mathrm{b}T \tag{4.2}$$

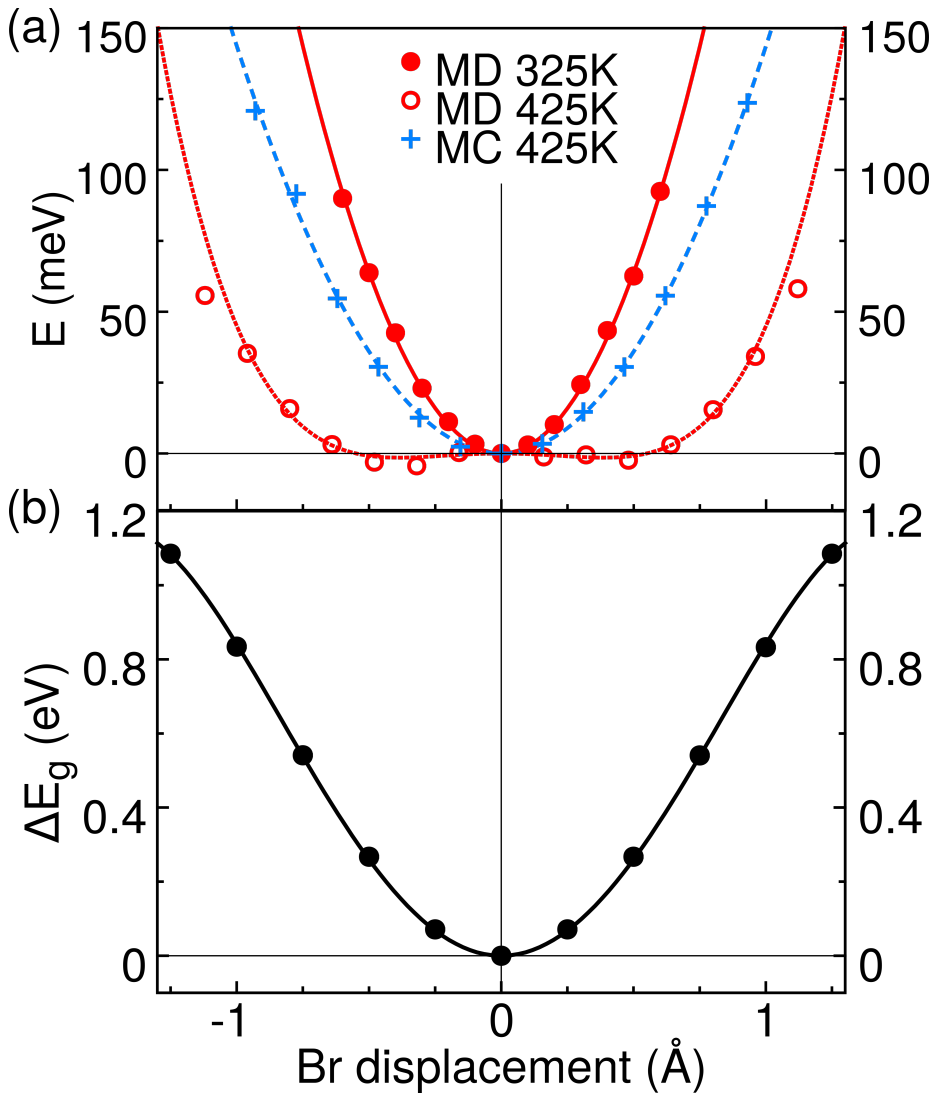

Figure 4.10. (a) Changes of the free energy according to transversal Br dynamics in the plane perpendicular to the Pb-Br-Pb bond axis in $CsPbBr_3$. The changes are calculated with a Boltzmann inversion using structures from the orthorhombic MD trajectory at 325 K (red disks), from the cubic MD trajectory at 425 K (red circles) and from cubic MC-distorted structures at 425 K (blue crosses). Data from orthorhombic MD at 325 K and cubic MC at 425 K are fitted to a quadratic function (red closed and blue dashed line). Data from cubic MD at 425 K is fitted to a double-well similar function, i.e. $ax^4 + bx^2$ (red short-dashed line). The origin of the graph, i.e. zero displaced Br atoms, indicates that the Br atoms are at the position of the cubic-high symmetry or static orthorhombic structure. Note that the selected transversal Br displacements are not equally spaced, i.e. they are selected to best represent the potential shape. (b) Band-gap change ΔE_g induced by specific transversal Br displacements according to a octahedral-tilting mode, i.e. imaginary phonon mode. The change is calculated using a sufficient large number of structures, where the Br atoms are displaced along the projection of the imaginary phonon mode on the plane perpendicular to the Pb-Br-Pb bond axis. The specific imaginary phonon mode is located at the M-point (see appendix A.7). *Reprinted figure with permission from [2]. Copyright (2023) by the American Physical Society.*

with the displacement histogram $n(\delta r_1, \delta r_2, \delta r_3)$ and the displacements δr_i with $i = x, y, z$, which are only considered as transversal displacements. The potential shape is presented as a one dimensional graph, which is determined by averaging over the two directions spanning the x-z-plane perpendicular to the Pb-Br-Pb bond axis, i.e. $E(r) = E(\delta r, 0, 0) + E(0, 0, \delta r))/2$. The broadening of the potential shape is determined solely by the different transversal Br motions, i.e. harmonic or anharmonic motions, while the temperature or $k_\mathrm{b}T$ can be interpreted as a tiny scaling factor. For example, the order of magnitude of the scaling factor $k_\mathrm{b}T$ for 100 K is ≈10 meV and can lead to overcoming the potential barrier induced by the double-well potential. This scenario is also mentioned in the description of Fig. 4.3 or can be seen in Fig. A.8 in the appendix, where the potential shape is calculated for cubic structures from MD at different temperatures. In contrast, almost congruent potential shapes occur for orthorhombic structures from MD at different temperatures, as can be seen in Fig. A.8 of the appendix. This means, that the difference of $k_\mathrm{b}T$ for different temperatures is compensated by different displacement histograms in the orthorhombic phase, but not in the cubic phase. However, the similarity of the potential shapes in the orthorhombic phase of $CsPbBr_3$ can be associated with the mild changing thermal band gap in the orthorhombic phase (see Fig. 4.8). Additionally, potential shapes from MC-distorted structures of the cubic and orthorhombic phase are shown together in one figure (see Fig. A.7 in the appendix), which shows the expected harmonic shape in both phases and that larger temperatures result in larger transversal Br displacements.
Notably, comparing the free-energy changes from MD and MC in the orthorhombic phase at the temperature of 325 K, as presented in Fig. 4.11, substantiates the similarity of the slopes of the thermal band gaps from MD and MC in the orthorhombic phase (see Fig. 4.9). It is expected that the free-energy changes from MD and MC for the other temperatures at 275 K and 375 K are also similarly close as for the temperature at 325 K presented in Fig. 4.11.
The most significant result of Fig. 4.10 (a) is that the changes in the free energy from transversal Br motions in MD structures in the orthorhombic and cubic phase of $CsPbBr_3$ are very different. This is in contrast to a band gap that hardly changes across the various phases in the experiment. There is evidence that the instantaneous structures from MD in the cubic phase are of lower symmetry and differ strongly from the cubic high-symmetry structure [7, 8, 13, 189]. In addition, the instantaneous structures also temporarily exhibit dynamic octahedral tiltings similar to the average structure of the orthorhombic phase (see Fig. A.11 in the appendix). This substantiates the barely changing band gap of $CsPbBr_3$ across the investigated temperature range including the phase transitions, since the instantaneous lower-symmetry structures emerge on timescales of thermal effects in the HaP band structure.
To relate the vibrational anharmonicity, which affects the temperature-dependent band gap especially in the cubic phase of $CsPbBr_3$, to octahedral tiltings, it is instructive to investigate the structural distortions due to one single phonon mode. This artificially distorted structure can be used to estimate the contribution of this specific phonon mode to the band gap. On the first view, this deliberately simplistic model is

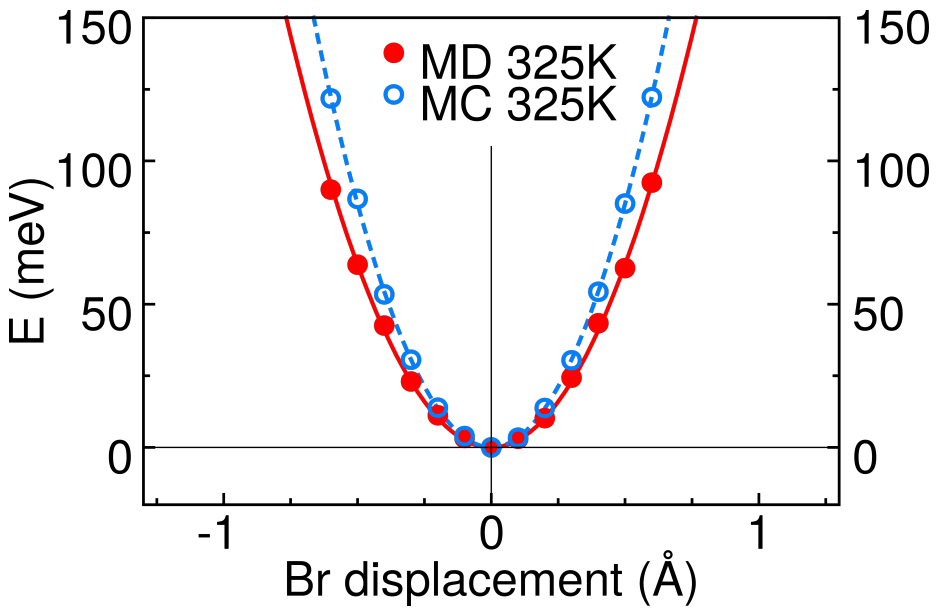

Figure 4.11. Changes of the free energy associated with structures in the orthorhombic phase at 325 K from MD (red disks) and from MC (blue circles). Further description of the figure as in Fig. 4.10 (a). Note that the transversal Br displacements are chosen to be equidistant.

reminiscent to the picture of decoupled oscillators in the harmonic approximation. However, the focus here lies on specific octahedral-tilting modes responsible for anharmonicity. These modes are known as soft modes or imaginary modes in the cubic phase, which appear in lattice dynamics calculations based on the harmonic approximation. In addition, imaginary modes are responsible for lowering the crystal symmetry [8] when considered in dynamic structure calculations such as MD. In contrast, pure harmonic modes, as used in MC, do not capture anharmonicity, but only the tilting modes. Note that the MC method explicitly excludes imaginary modes.

However, MD is able to account for all types of modes, but it is in general not a trivial task to link thermal band-gap changes to specific modes. In addition, the simplistic one-phonon model does not take into account the interactions between the phonon modes, i.e. the interactions of the selected tilting mode with other vibrational modes. In order to calculate the band-gap change from only one specific tilting mode of cubic $CsPbBr_3$, the PHONOPY interface is used to extract the imaginary phonon mode at the M-point (see Fig. A.10 in the appendix). Next, a set of structures is generated, where Br atoms are displaced along this specific mode in the plane perpendicular to the Pb-Br-Pb bond axis. With the help of DFT, the band-gap change $\Delta E_g(x)$ is calculated as a function of these transversal Br displacements, x, and presented in Fig. 4.10 (b). The corresponding band-gap change can be classically integrated by using a thermal integration with a free-energy potential shape according to MC or

MD structures, such as shown in Fig. 4.10 (a). The integration is determined as follows

$$\Delta E_{\mathrm{g}}^{\text{tot-transvesal}}(T) = \frac{1}{Z}\int dx\ \Delta E_{\mathrm{g}}(x)\ \exp\left[\frac{-V_i(x)}{k_{\mathrm{b}}T}\right], \tag{4.3}$$

with the partition function, $Z = \int dx\ \exp[-V_i(x)/k_{\mathrm{b}}T]$, and the index i referring to the MD or MC free-energy potential shape at 425 K. Note that the integration assumes that all transversal Br displacements along this specific tilting mode follow the same free-energy potential shape, i.e. optionally the one from MD or MC, where the latter is calculated from structures not considering tilting modes. The simplistic one-phonon model results in a transversal band-gap change of 0.17 eV for the MC-shape and 0.28 eV for the MD-shape of the potential energy surface. This substantiates that a harmonic free-energy potential shape cannot induce large changes in the temperature-dependent band gap due to the lack of anharmonic structure fluctuations, which in contrast are covered in anharmonic potential shapes from MD. Consequently, MD takes into account not only large anharmonic displacements but also vibrational interactions of phonon modes. Both effects are reflected in slow octahedral-tilting motions, which are mainly responsible for anharmonic contributions to the band gap.

4.6. Discussion

Differences between room-temperature experiments and static theory calculations prompt to rationalize the thermal effects in the finite-temperature electronic structure for HaPs. Therefore, investigations of thermal lattice vibrations provide a deeper insight of the thermal evolution of the electronic band gap using a prototypical HaP semiconductors, such as $CsPbBr_3$. To analyze the effects of different lattice vibrations, i.e. harmonic or anharmonic vibrations, the averaged band gaps calculated with MD and MC are compared. Consequently, in the cubic phase of $CsPbBr_3$ at 425 K the largest difference between the band gaps calculated with distorted structures from purely harmonic phonons (MC) and from anharmonic phonons (MD) is ≈450 meV. Note that both methods provide band-gap contributions that lead to an increase of the band gap, but the increase from MD is ≈450 meV higher.
In order to classify the contribution of anharmonicity (≈0.5 eV), other contributions to the band gap, such as SOC (≈0.8 eV) or the band-gap correction by hybrid exchange-correlation (≈0.7 eV), can be considered. The comparison of these magnitudes supports the importance of vibrational anharmonicity. Furthermore, the inclusion of thermal anharmonic fluctuations as in MD can almost compensate the discrepancy of 0.7 eV between the static band gaps of the orthorhombic and cubic structure, leading to a more consistent description of the phase transition than in MC. This can be explained by the instantaneously cubic structure leaving the cubic high-symmetry structure and adopting structures of lower symmetry and of lower total energy [190], which results in an increase in the band gap. This underlines the fact that the band gap of the average structure does not correspond to the average band gap of transient structures. In conjunction with the instantaneously lower-symmetry

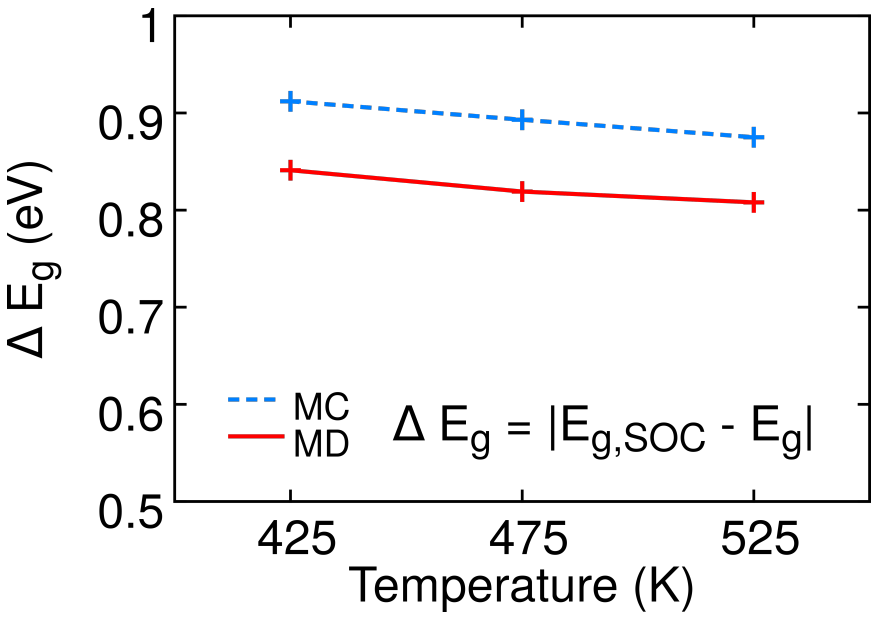

Figure 4.12. Influence of SOC on the temperature-dependent band gap for cubic $CsPbBr_3$ shown as the difference between the band gaps with and without SOC. The corresponding band-gap values are listed in Table 4.1. The difference between the band-gap values from MC (blue-dashed line) and MD (red line) is almost constant at ≈70 meV across the temperatures.

structures, the anharmonic atomic displacements, as considered in MD, are characterized by octahedral tilting (see Fig. A.11 in the appendix). Consequently, distorted cubic structures from MD show temporally octahedral tiltings, which are reminiscent to the orthorhombic average structure, and therefore lead to an insignificant change in the band gap when it comes to phase transitions as reported from experiment.
In addition, non-quadratic potential wells for transversal Br displacements in the cubic phase from MD, are key to understand the lower-symmetry structures containing the octahedral tiltings. In contrast, MC does not consider soft modes, which are responsible for octahedral tilting, and transversal Br displacements in MC-structures show harmonic potential wells that do not account for vibrationl anharmonicity. The impact of vibrational anharmonicity on the thermal band gap can be further evidenced by the simplistic one-phonon model when using the potential shape from MD or MC. Since anharmonic fluctuations are not as pronounced in the orthorhombic phase than in the cubic phase, also transversal Br displacements from MD result in quadratic potential shapes, which are nearly congruent for different temperatures. This explains the almost constant evolution of the temperature-dependent band gap in the orthorhombic phase of $CsPbBr_3$.
Next, the SOC effect is investigated, whereby a slightly temperature-dependent SOC contribution is observed in addition to the known reduction in the band gap. Specifically, the SOC contribution leads to a band-gap opening with increasing temperature, which holds for the orthorhombic as well as for the cubic phase of $CsPbBr_3$. The corresponding band-gap opening in the cubic phase is presented in Fig. 4.12, which can be recognized by the decreasing difference $\Delta E_g(\mathrm{eV})$. Note that the difference $\Delta E_g(\mathrm{eV})$ is calculated as the modulus from the difference between the band gap with

and without SOC. The influence of SOC on the temperature-dependent band gap is on the order of some tens of meV for the cubic phase, i.e. ≈35 meV for band gaps from MC as well as MD. Interestingly, the difference between the SOC contributions in Fig. 4.12 from MC (blue-dashed line) and MD (red line) is ≈70 meV for the selected temperatures and remains constant through the temperatures. This means that the SOC contribution has larger effects on structures from MC in the cubic phase that do not contain octahedral tiltings. In contrast, the difference between the SOC contributions from MC and MD in the orthorhombic phase is less pronounced and has a constant value of only ≈10 meV for the selected temperatures (see Fig. A.9 in the appendix). In addition, the SOC-induced temperature-dependent band gap opening in the orthorhombic phase is similar to the one in the cubic phase. For clarity, the differences of the SOC contributions between MC and MD as well as the magnitudes of the band-gap opening due to SOC are shown in Table 4.2 for both phases.

Table 4.2. Comparison of the SOC contributions calculated with structures from MC and MD in the orthorhombic and cubic phase of $CsPbBr_3$. Δ_T^{SOC}: Band-gap opening due to SOC as the difference between the band gap at the lowest and highest temperature of one phase. Note that the temperature-dependent band-gap opening due to SOC, i.e. Δ_T^{SOC}, is approximately the same for MC and MD. $\Delta_{MC\text{-}MD}^{SOC}$: Almost constant difference between the SOC contributions from MC and MD across the temperatures of one phase.

	Orthorhombic	Cubic
Δ_T^{SOC} (meV)	20	35
$\Delta_{MC\text{-}MD}^{SOC}$ (meV)	10	70

Thus, there is evidence that vibrational anharmonicity associated with octahedral tilting has influence on the SOC contribution. Existing results from Amat et al. [190] show that the SOC contribution is dependent on the octahedral tilting angle. This explains the negligible SOC difference $\Delta_{MC\text{-}MD}^{SOC}$ of ≈10 meV between MD and MC in the orthorhombic phase, since octahedral tiltings already characterize the static orthorhombic structure. Explaining the SOC difference, $\Delta_{MC\text{-}MD}^{SOC}$, between MC and MD in the cubic phase, one could argue that slightly different lattice constants, as used in MC and MD, influence the SOC contribution[7]. This is disproved because the SOC difference $\Delta_{MC\text{-}MD}^{SOC}$ is negligible in the orthorhombic phase, where the lattice parameters are also slightly different in MC and MD calculations. It seems, that MC-distorted structures, which are based on the cubic-high symmetry structure and with thermal displacements according to a Gaussian probability distribution, are more sensitive to the SOC effect. Note that when calculating the average band-gap values including SOC, as shown in section 4.4, the Rashba effect (see section 2.3) occurred together with the splitting of the CBM.
Furthermore, the influence of hybrid exchange-correlation functionals on the temperature-dependent band gap of $CsPbBr_3$ is investigated using the example of HSE.

[7] The lattice constants are slightly different due to different dispersive corrections in the relaxation as mentioned in section 4.4.

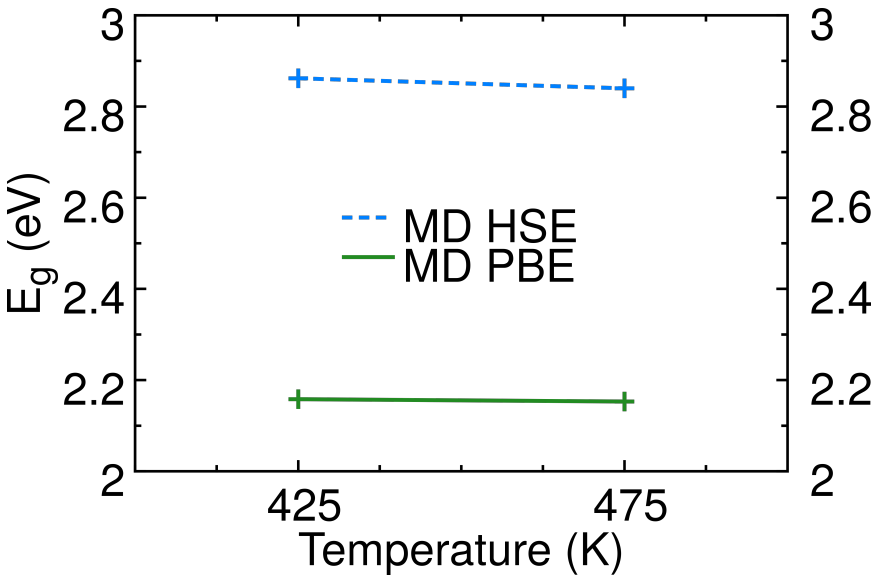

Figure 4.13. DFT-based calculations show the fundamental band for cubic $CsPbBr_3$ calculated as an average using the same 100 structures from MD at 425 K and 475 K as in Fig. 4.9. The temperature-dependent band gap is calculated without SOC for the PBE (green line) and HSE (blue-dashed line) functional. The difference between the band gaps is 704 meV at 425 K and 687 meV at 475 K. Note that the computational parameters differ in the Γ-centered $1 \times 1 \times 3$ k-point grid and in the energy cutoff of 240 eV to the parameters in Fig. 4.9. *Reprinted figure with permission from [2]. Copyright (2023) by the American Physical Society.*

Fig. 4.13 shows the fundamental band gap of cubic $CsPbBr_3$ calculated with MD structures at 425 K and 475 K using the PBE and HSE functional. The HSE functional increases the fundamental band gap by ≈0.7 eV and therefore reduces the DFT band-gap problem caused by PBE, as expected. However, there is no strong influence of the exact-exchange, as a part of the HSE functional, on the slope of the temperature-dependent band gap. The difference of ≈20 meV between the band gaps from HSE at 425 K and 475 K can be attributed to statistical fluctuation, which is caused by averaging the band gap over randomly selected structures. As tested in chapter 3.7 for common inorganic semiconductors, the influence of hybrid functionals on the temperature-dependent band gap is negligible.
Thinking outside the box, the above findings are also relevant for other types of HaPs that follow the same order of phase transitions in conjunction with structures going from lower-to-higher symmetry at the phase transition. Remaining in the class of Br-halide HaPs and replacing the inorganic Cs cation with the organic MA molecule, one obtains $MAPbBr_3$ as a prototypical organic-inorganic HaPs, which shows its phase transition from the orthorhombic-to-tetragonal phase at ≈150 K and from the tetragonal-to-cubic at ≈240 K [191]. As far as the thermal evolution of the band gap at the phase transitions is concerned, a small decrease of the optical transition energy by about 10 meV at the lower transition and a continuous behavior at the upper transition is observed in the experiment [17]. From a theoretical point of view, the band gaps calculated with DFT show a strong decrease of 0.6 eV between the tetrag-

onal and cubic static structure of $MAPbBr_3$ [192]. The principle that anharmonic fluctuations play an important role in the thermal evolution of the electronic band structure of $CsPbBr_3$, such as a mild change of the band gap across the phase transition, can therefore also apply to $MAPbBr_3$. Anharmonic fluctuations are expected to be responsible for the continuous band gap across the tetragonal-to-cubic phase transition for $MAPbBr_3$, which would be consistent with the continuous band gap for the related $MAPbI_3$ HaP found in existing theoretical [7] and experimental [108] results. Corresponding to the transition from the orthorhombic-to-tetragonal phase, the anharmonic fluctuations are not as dominant, and probably a tiny jump in the band gap remains when the average structure transitions to the picture of the instantaneous structures, analogous to the effect reported in previous research by templating cations [190, 193].
To conclude, the investigation of the different phases, in which the structures change from a lower to a higher symmetry with increasing temperature, shows that the average crystal symmetry cannot describe the thermal characteristics of the band gap of $CsPbBr_3$. Consequently, the inclusion of vibrational anharmonicity is necessary for an in-depth understanding of the electronic band structure at finite temperature. The present results show that anharmonic fluctuations in the cubic phase of $CsPbBr_3$ have the largest influence, as shown in the chapter 4.4 and chapter 4.5, while the orthorhombic phase exhibits octahedral tiltings in its average structure and therefore the vibrational anharmonicity is less pronounced. Specifically, the values for the thermal band gap calculated from MD are overall larger than 1.3 eV and, taking into account the increase in the band-gap values by $\approx$0.7 eV due to HSE, they are close to values from experimental reflectance measurement of $CsPbBr_3$. In contrast, band-gap values from MC remain far from the experimental range and therefore MD, which inherently accounts for vibrational anharmonicity, significantly outperforms MC. Finally, the mechanism of vibrational anharmonicity, showing HaP-characteristic unusual displacements, can be relevant for anharmonic semiconductors in general.

4.7. AHC applied to $CsPbBr_3$

To demonstrate the effect of higher order EPC terms on the slope of the thermal band gap, the temperature-dependent band gap is calculated using the AHC and MC method, as described in chapter 2.6.1 and in chapter 2.5.2 respectively. It is known that the AHC method is a perturbative method, which terminates the expansion of the nuclear displacements after the second order and thus does not consider higher-order EPC terms. In addition, the temperature-dependent band gap of $MAPbI_3$ calculated with AHC strongly overestimates the slope [16]. In contrast, the MC method also considers higher-order EPC terms and therefore correctly describes the increase of the temperature-dependent band gap for $MAPbI_3$ [16] compared to the experiment. However, both the MC and AHC methods do not provide absolute band-gap values that are close to the experimental range of $MAPbI_3$. Up to now, the AHC and MC methods have not yet been applied to $CsPbBr_3$ and compared with each other. Furthermore, these investigations contribute to the understanding of the thermal

band gap of $CsPbBr_3$, also with regard to the results from MD.
Therefore, the temperature-dependent band gap of cubic $CsPbBr_3$ is calculated using the AHC method as implemented in ABINIT [194]. The results are shown together with the averaged band gaps calculated with MC in Fig. 4.14. The AHC method

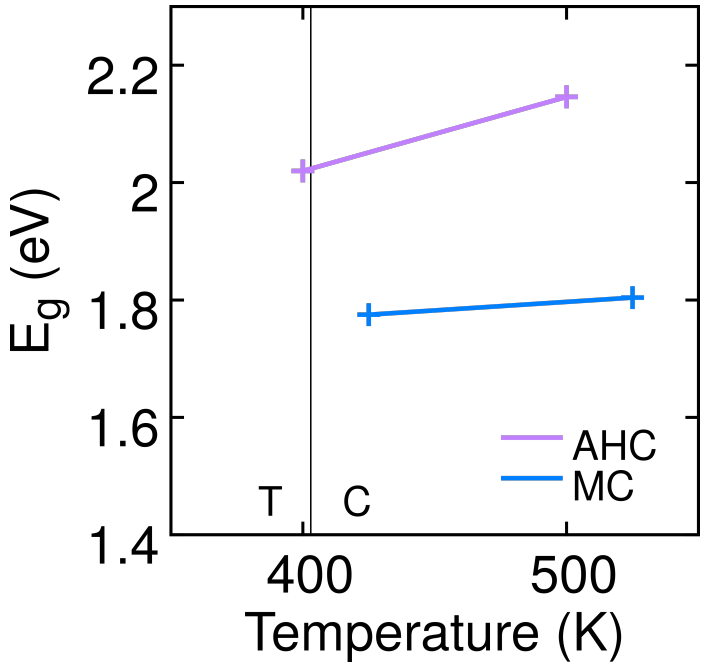

Figure 4.14. Temperature-dependent fundamental band gap for $CsPbBr_3$, calculated with the AHC method (purple line) for 400 K and 500 K, and with the MC method (blue line) for 425 K and 525 K. The band-gap values are calculated with the PBE functional and without SOC. The vertical line indicates the phase transition from the tetragonal-to-cubic phase. Note that the AHC calculations are not converged with respect to the q-point grid, but this does not affect the significance of the figure.

calculates an increase of the band gap of ≈140 meV per 100 K. In contrast, the increase of the band gap calculated with MC is ≈30 meV between the temperature range of 425 K and 525 K. In comparison, the experimental increase of the thermal band gap (see Fig. 4.8) between 420 K and 520 K is ≈50 meV. If only the slopes of the thermal band gaps are compared, the MC method can closely reproduce the experimental slope, while the AHC completely overestimates the slope. Note that the band gaps from AHC and MC are calculated without SOC and using the PBE functional. Due to cancelation of errors, the AHC method yields band-gap values that are quite close to the experimental range of ≈2.3 eV for $CsPbBr_3$. This also applies if the SOC effect, which reduces the band gap by ≈0.8 eV, and the hybrid functional HSE, which increases the band gap by ≈0.7 eV, are taken into account. The reason for this agreement is that the AHC method increases the band gap linearly, which leads to an increase of the band gap by ≈140 meV per 100 K, starting from a static band-gap value of ≈1.4 eV. Note that the static band gaps of structures used for the AHC or MC method differ by 15 meV, which is due to the separately relaxed structures with ABINIT and VASP, respectively. To summarize, it is also shown for

$CsPbBr_3$ that missing higher-order EPC terms lead to an overestimated increase of the temperature-dependent band gap.

5. Conclusions and Outlook

Probably the most discussed quantity of an energy material is its fundamental band gap, which is often compared with the optical band gap from the experiment. The DFT theory accesses the fundamental band gap as an eigenvalue difference, using exchange-correlation functionals. It is known that semilocal or exact exchange of a functional influences the band-gap value strongly, as well as the mixing of both exchange energy terms. The development of functionals is an ongoing challenge, especially when the functional is designed in such a way that it accurately predicts electronic and optical properties at the same time. The recently developed SRSH functional offers this advantage. However, the question of whether this simultaneous accuracy is accompanied by a deterioration in the prediction of bulk properties of common inorganic semiconductors has not yet been answered. This task was discussed in chapter 3.
Furthermore, a novel class of energy materials are HaPs, which attract increasing attention in semiconductor research due to the rapidly increasing energy conversion efficiency of HaP-based solar cells. HaPs are characterized by their unusual structural dynamics, such as octahedral tilting, in conjunction with vibrational anharmonicity, which can explain their remarkable optoelectronic properties. Here, various first-principles methods, such as MD and MC, were applied to determine the thermal evolution of the band gap for the prototypical HaP $CsPbBr_3$. A comparison of the calculated band-gap values at finite temperature with the experimental range of the band gap quantified the anharmonic contribution to the band gap. Specifically, thermal samples from both theories allowed to rationalize the limitations of a harmonically perturbed average crystal structure compared to structures containing all types of atomic motions, in particular anharmonic motions. This task was discussed in chapter 4.

The recently developed functional, SRSH, which belongs to the class of screened range-separated hybrid functionals, incorporates the feature of optimally tuning. This means that the individual parameters of the functional can be adjusted to accurately calculate a specific quantity. For instance, when SRSH is tuned to reproduce accurate band-gap values calculated using the GW theory for a set of common inorganic semiconductors, the electronic and optical properties can also be calculated accurately. [52, 27]. However, the accuracy of bulk properties has not yet been tested for the tuned SRSH parameters. In chapter 3, bulk properties, such as lattice constants, bulk moduli, atomization energies and phonon dispersion relations, are calculated for common inorganic semiconductors with the help of the tuned SRSH functional. These results are compared with the results of other well-established

functionals, such as PBE and HSE, as well as with experimental results.
The lattice constants calculated with SRSH for a set of common inorganic semiconductors are more accurate than the lattice constants of PBE and slightly less accurate than the lattice constants of HSE compared to the experiment. Consequently, the associated bulk moduli follow the trend of the lattice constants. While all three functionals overestimate the lattice constants, almost all bulk moduli are underestimated. In terms of atomization energies, the results of SRSH are the least accurate, followed by the results of HSE and then PBE. The high accuracy offered by PBE can be attributed to the greater density gradient dependence of the functional than in HSE and SRSH. However, the atomization energies calculated with all three functionals show underbinding. With regard to phonon dispersion relations, a general distinction must be made between two cases: Phonon dispersion relations that are calculated with the theoretical or the experimental lattice constant. Using the theoretical lattice constant implies the error propagation from the theoretical lattice constant. This leads to the most accurate phonon dispersion relations for HSE, followed by phonon dispersion relations from SRSH and then from PBE. Using the experimental lattice constant for all three functionals shows that the phonon dispersion relations calculated with SRSH and HSE are equally accurate, and both are more accurate than PBE. In general, independent of the use of the experimental or the theoretical lattice constants, phonon dispersion relations from all functionals provide respectable accuracy.
To summarize, the results for the bulk properties of the set of common inorganic semiconductors calculated with SRSH show that SRSH can compete with the accuracy of PBE and HSE. This demonstrates that SRSH cannot only accurately calculate the electronic-structure and optical properties of common inorganic semiconductors, but also their bulk properties. In particular, the inclusion of EXX also in the long-range region of SRSH, while it is absent in HSE, ensures the correct asymptotic decay given by the dielectric constant. In addition, a universal choice of the screening parameter, such as for HSE, may not apply to all types of materials. The empirical tuning of SRSH, in order to implement the theoretical dielectric constant and, for example, the direct band gap at the Γ-point calculated by the GW theory, determine the three parameters α, β and γ. Hence, the flexibility of SRSH represents a major advance in the development of functionals and the search for the perfect universal functional. This is probably achieved without the aspect of overfitting a functional. However, the continuous improvement of exchange-correlation functionals in the last decades, thereby gaining more and more accuracy, comes along with an increasing amount of empiricism. Therefore, a further level of sophistication of SRSH was developed by Wing et al. [54] that provides a non-empirical way to tune SRSH [1]. However, evaluating this approach for the bulk properties of conventional semiconductors is out of the scope of this work.

In order to incorporate temperature into the investigation of common inorganic semi-

[1] In principle, this approach captures the tendency of delocalized orbitals for solids by involving an orbital-localization procedure that provides chemical bonds, which are comparable to those of molecules.

conductors, the MC method was used with the aim to investigate the influence of different functionals on the temperature-dependent band gap. Therefore, the parameters of the HSE functional were varied to recognize the impact of EXX on the thermal band gap. While the choice of functional or variations of the functional parameters strongly influenced the static band gap, the thermal band-gap change remained unaffected. This result is not easily recognizable in the MC method. However, when considering the electron-phonon coupling matrix elements as expressed in DFPT, one can argue that the matrix elements depend only on the wave functions of the system, which are independent of the choice of the functional.

While thermal effects or lattice dynamics for common inorganic semiconductors can be adequately described with the harmonic approximation, as can be seen from quantities such as phonon dispersion relations or thermal band gaps, this approximation is insufficient for anharmonic materials. HaPs are promising energy materials and exhibit strong anharmonicity, which can be seen, for example, in large atomic displacements or unusual atomic movements. A characteristic of HaPs is that they occur in three different phases with corresponding phase transitions over a short temperature range. Interestingly, the static band gaps of $CsPbBr_3$, a prototypical full-inorganic HaP, differ strongly for the reference structures of the different phases, while the experimental band gap shows smoothness across the corresponding temperature range. In chapter 4, first-principles MD simulations are applied to $CsPbBr_3$ in order to investigate vibrational anharmonicity. The advantage of MD is that all types of atomic motions, i.e. harmonic and anharmonic motions, are taken into account, since MD does not rely on truncating the Taylor expansion of the nuclear potential energy in the displacements after the second order. To elaborate the impact of anharmonicity, the temperature-dependent band gap is calculated using MD and MC, where the latter does not consider anharmonic fluctuations and is based on the harmonic approximation. This is valid because the equality of MD and MC has been shown for harmonic materials.
From an experimental point of view, reflectance measurements performed by collaborators showed a continuous and slightly increasing temperature-dependent band gap of $CsPbBr_3$ across the phase transitions. Disregarding the intermediate tetragonal phase, which only occurs in a narrow temperature range, the thermal band gap investigated with MD and MC shows a discontinuity between the orthorhombic and cubic phase. While the discontinuity in the case of MD is much smaller than 0.1 eV, the discontinuity in the case of MC is greater than 0.4 eV. Consequently, the average high-symmetry structure as the initial structure for the MC theory thermally perturbed by harmonic phonons cannot explain the band-gap value from experiment. In contrast, using the same structure as starting point for MD leads to a trajectory of instantaneous structures with lower symmetry that contain anharmonic fluctuations and can explain the smoothness of the experimental band gap. Overall, MD can fairly account for the experimental band gap, both in the orthorhombic and cubic phase, when considering the band gap underestimation by DFT. However, the largest band-gap difference between MD and MC, as located at the cubic phase transition,

can be assigned to anharmonic fluctuations. A schematic contribution of the impact of anharmonicity is presented in Fig. 5.1.

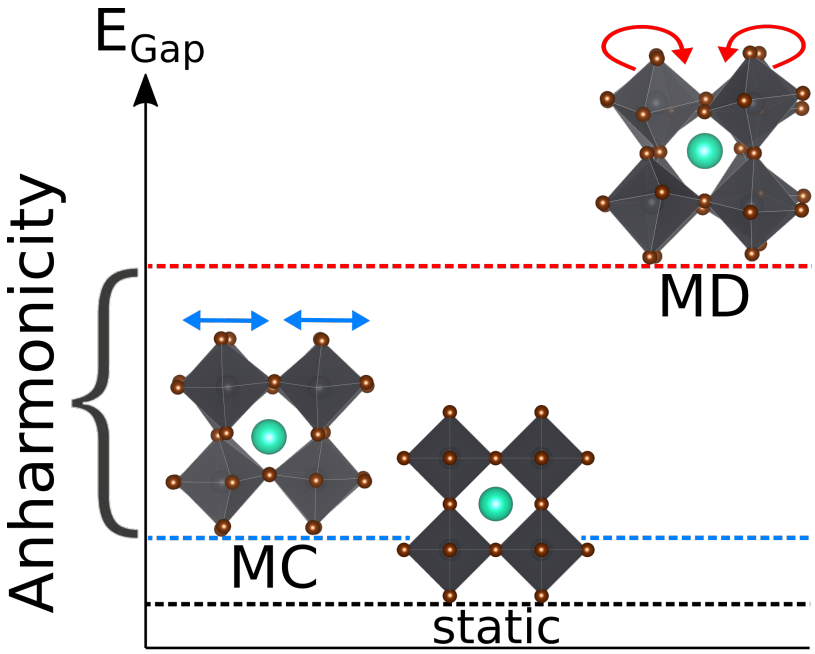

Figure 5.1. Schematic diagram of the magnitude of the band gaps from the static cubic high-symmetry structure (middle), distorted MC structure (left) and distorted MD structure (right). Note that the atomic motions described by MD lead to a tilting of the octahedra (red arrows), while the atomic motions of MC do not (blue arrows). The magnitude of the band gaps is denoted on the y-axis. The difference between the MC and MD band gap is contributed to anharmonicity.

In Pb-based HaPs, due to the heaviness of the lead element, the inclusion of SOC is essential. Apart from the known decrease of the band gap for HaPs, the SOC contribution for $CsPbBr_3$ leads to a slight opening of the band gap with increasing temperature. Thereby, the mere band gap opening across the temperature range is similar for structures from MC and MD. However, the SOC contributions calculated from MC and MD structures differ between the orthorhombic and cubic phase. While the difference in the orthorhombic phase is negligible, the difference in the cubic phase is more pronounced and amounts to some tens of meV. Thus, the role of octahedral tilting, which is present in structures from MD and absent in structures from MC, affects the amount of SOC and requires further discussion. It appears that instantaneous structures of lower symmetry from MD, which inherently contain anharmonic disorder, account for some magnitude of the SOC contribution compared to structures from MC [190].
Thermal expansion tests were performed for cubic $CsPbBr_3$ by increasing and decreasing the equilibrium lattice constant for higher and lower temperatures, respectively, to investigate the effect on the thermal band gap as well as to control the external pressure. Suppression of volume expansion, as in NVT MD, leads to the hypothesis that MD averages with higher temperature more and more towards the picture of non-tilted octahedra in the cubic phase. This could be recognized with

the help of the potential energy surfaces, which change from a double-well shape to a parabolic shape in conjunction with lowering the band gap. Consequently, the averaged band gap of the instantaneous structures of lower symmetry for higher temperatures tend to the smaller band gap value of the cubic-high symmetry structure. Note that the band gap of the average structure is not necessarily the average value of the band gaps of the instantaneous structures. While for harmonic Si, for example, the reference structures denotes a minimum, the cubic-high symmetry structure, as it exists as an average structure for HaPs, denotes a saddle point or a local maximum of the potential energy surface. In the MC method, which neglects imaginary phonon modes responsible for octahedral tilting, the magnitude of harmonic thermal displacements increases with increasing temperature, so that the cubic-high symmetry structure is increasingly abandoned. Since the imaginary phonon modes characterize the shape of the double-well potential, the potential shape for MC-distorted structures is parabolic. Therefore, it would be interesting to include phonons in the MC theory, which are calculated beyond the harmonic approximation, and to investigate the influence on the thermal band gap. This model would also account for imaginary phonon modes as they occur in harmonic phonon calculations, while the phonon-phonon interactions are probably difficult to consider.
Neither MC nor MD in the NVT ensemble is expected to provide continuity in the thermal band gap across phase transitions, as the instantaneous structures cannot transform from the initial orthorhombic reference structure into a cubic-like structure when the temperature is increased. The same applies to the initial cubic reference structure when the temperature is lowered in one of the theories.
The halide motions in HaPs, for example in $CsPbBr_3$, whether transversal to the Pb-Br-Pb or Cs-Br-Cs axis, are considered to be of particular importance. There is evidence that transversal Br displacements of the Pb-Br-Pb bond axis contribute significantly to octahedral rotations [105]. Non-symmetric pair distribution functions of Pb-Br or Cs-Br distances are also characteristic for HaPs. These observations of vibrational anharmonicity in conjunction with tilting modes are absent in structures perturbed in a harmonic phonon picture based on decoupled phonon modes. Note that a revealing consistency check would be to examine pair distribution functions or 2D displacement histograms of Br atoms from MC structures to identify Gaussian behavior. Furthermore, to quantify the impact of anharmonic effects a simplistic one-phonon model is constructed, which creates a set of distorted structures with Br atoms displaced along one specific tilting mode. A subsequent classical thermal integration, using either the harmonic energy surface from MC or the double-well-like energy surface from MD, shows that the contribution from transversal Br displacements to the band gap is much lager for the energy surface from MD than from MC.
The transferability of the findings obtained here to other variants of HaPs is highly probable if the phase transitions are in conjunction with changes from lower-symmetry structures to higher-symmetry structures. Experiments show orthorhombic-to-tetragonal and tetragonal-to-cubic phase transitions with a similar continuous thermal band gap for hybrid organic-inorganic HaPs, such as $MAPbX_3$, where X denotes the halide ion [17, 195, 196]. In contrast, static band-gap values from DFT

show a pronounced decrease at the phase transition, when the reference structure changes from lower symmetry to higher symmetry [192]. Consequently, anharmonic structure fluctuations can also help to explain the thermal evolution of the band gap in hybrid HaPs, which exhibit only minor changes in the band gap during phase transitions. Here, the effect of vibrational anharmonicity is less dominant in the low temperature phases.
The replacement of toxic lead can be achieved by considering elements such as tin or germanium, which are simply listed above lead in the periodic table, or bismuth. The question of why tin is not used straight away is answered by the fact that only lead-based perovskite cells could achieve high energy conversion efficiencies comparable to or even higher than those of Si. Tin, on the other hand, shows a rapid decrease of the efficiency in conjunction with oxidation. Thus, the substitution of lead offers plenty of future research, also with regard how the substitution affects the halide motion transversal to the atom-halogen-atom bond axis. A recent study has shown that the choice of the metallic cation, such as in $CsPbBr_3$ or $CsSnBr_3$, which differ in the octahedral cation electron configuration, has no influence on the pronounced anharmonicity or low-frequency lattice dynamics for HaPs [107]. The new tailoring of the chemical composition of perovskites also investigates the embedding of organic groups, such as phenethylammonium-chloride molecules, to screen tin for oxidation, which leads to 2D perovskites. In addition, the doping of solar materials, as in conventional semiconductors, can also be important for HaPs. Also vacancies, such as halide vacancies in $CsPbBr_3$, influence the structural dynamics of neighbouring metallic cations, resulting in energy level fluctuations, which cannot be explained in a static picture [184]. All these considerations support the future design of perovskites.
Despite the drastic underestimation of the band gap by PBE-DFT, the interesting physics shows up in the trend rather than in absolute values, which is why DFT calculations are often very useful. The development of hybrids, such as SRSH, represents a major advancement in the direction of a universal functional. The inclusion of lattice dynamics for solar materials is essential and can be achieved by methods such as MC and MD. Remaining in the harmonic approximation is sufficient for common inorganic semiconductors where MC and MD are fairly equal. However, new energy materials, such as HaPs, need the inclusion of vibrational anharmonicity as captured in MD, since anharmonic atomic motions govern the electronic band gap.

A. Appendix

A.1. Computing time for the standard semiconductor Si

Table A.1. DFT computation time of Si for a unit-cell (2 atoms) and a 4×4×4 supercell (128 atoms). The time is given as averaged real time for one DFT self-consistency step of each functional. In order to estimate the run time differences among the three functionals, the factor F provides the ratio of computation time of hybrid functionals over the computation time of the PBE functional. *Reprinted table with permission from [1]. Copyright (2021) by the American Physical Society.*

	unit-cell		supercell	
	time (s)	F	time (s)	F
PBE	0.015	1	10.840	1
HSE	3.690	246	995.158	92
SRSH	3.339	223	976.650	90

A.2. Phonon dispersion relations for AlAs, AlP, AlSb, GaP and InP

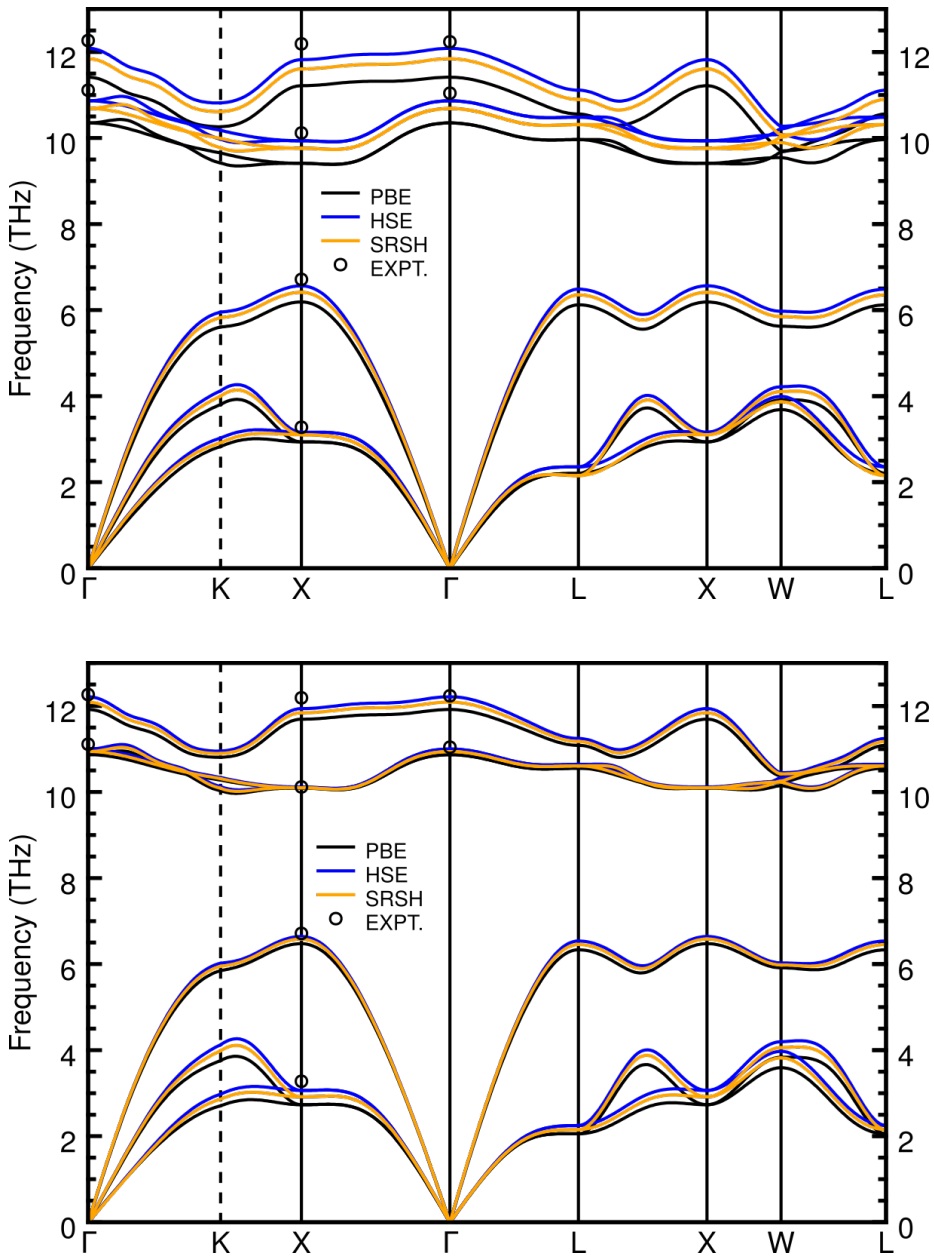

Figure A.1. The upper panel shows the phonon dispersion relation of fcc-structured AlAs using the theoretical lattice constant calculated using the PBE, HSE and SRSH functionals (solid colored lines) as well as experimental data (open black circles), which was extracted from reference [197] and [198]. The lower panel shows respectively the phonon dispersion relation for only using the experimental lattice constant throughout the three functionals. *Reprinted figure with permission from [1]. Copyright (2021) by the American Physical Society.*

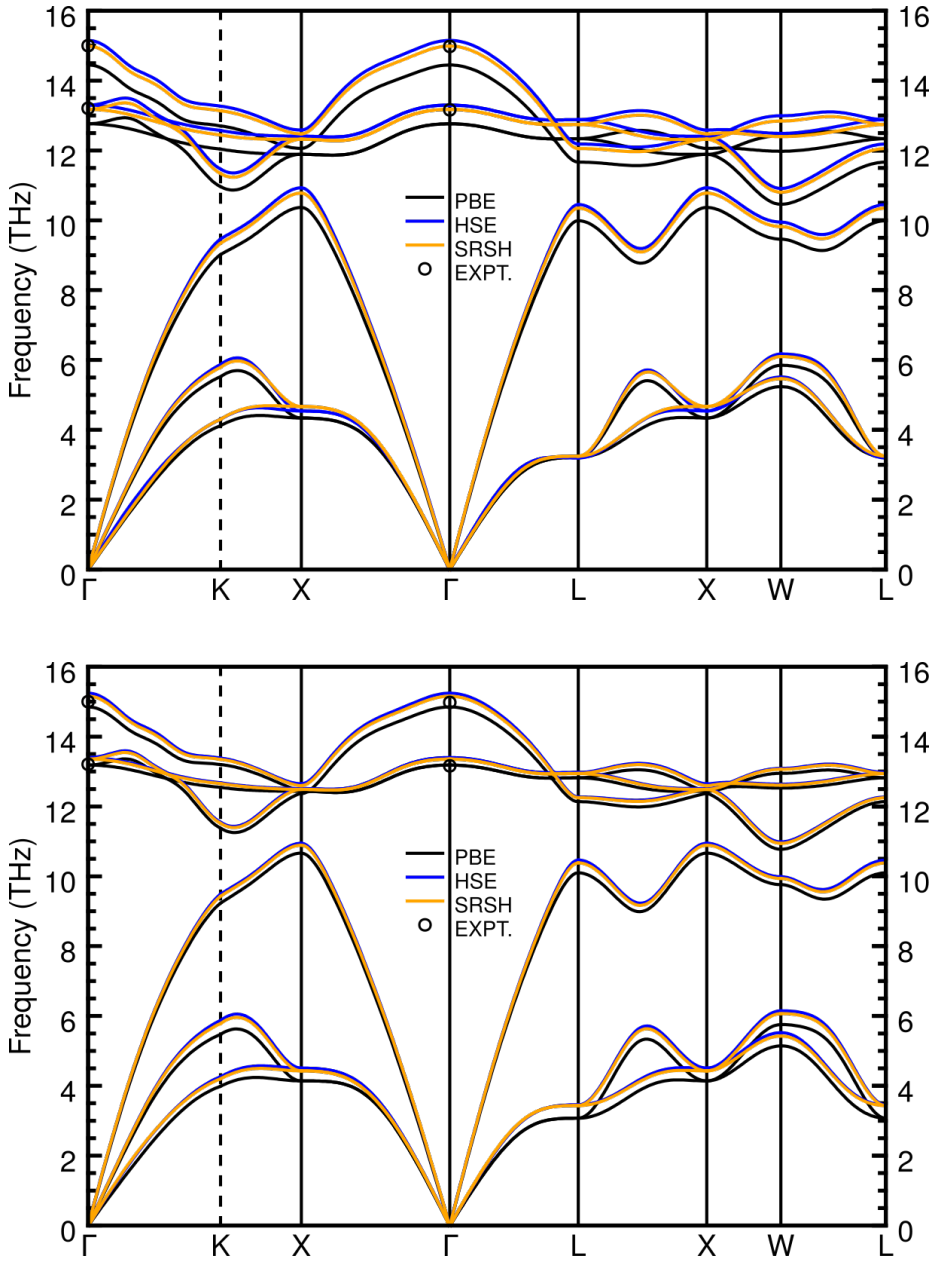

Figure A.2. The upper panel shows the phonon dispersion relation of fcc-structured AlP using the theoretical lattice constant calculated using the PBE, HSE and SRSH functionals (solid colored lines) as well as experimental data (open black circles), which was extracted from reference [197]. The lower panel shows respectively the phonon dispersion relation for only using the experimental lattice constant throughout the three functionals. *Reprinted figure with permission from [1]. Copyright (2021) by the American Physical Society.*

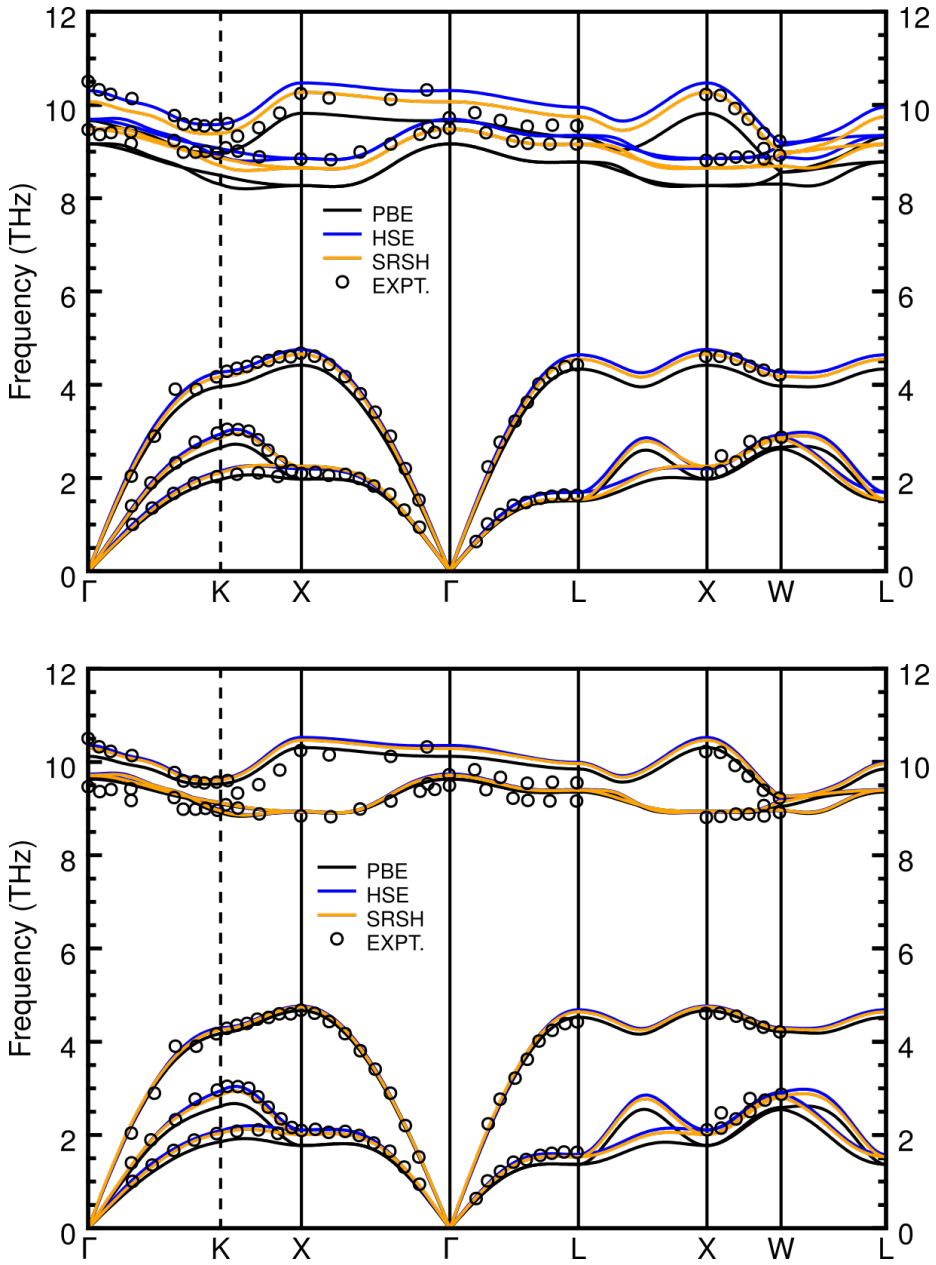

Figure A.3. The upper panel shows the phonon dispersion relation of fcc-structured AlSb using the theoretical lattice constant calculated using the PBE, HSE and SRSH functionals (solid colored lines) as well as experimental data (open black circles), which was extracted from reference [199]. The lower panel shows respectively the phonon dispersion relation for only using the experimental lattice constant throughout the three functionals. *Reprinted figure with permission from [1]. Copyright (2021) by the American Physical Society.*

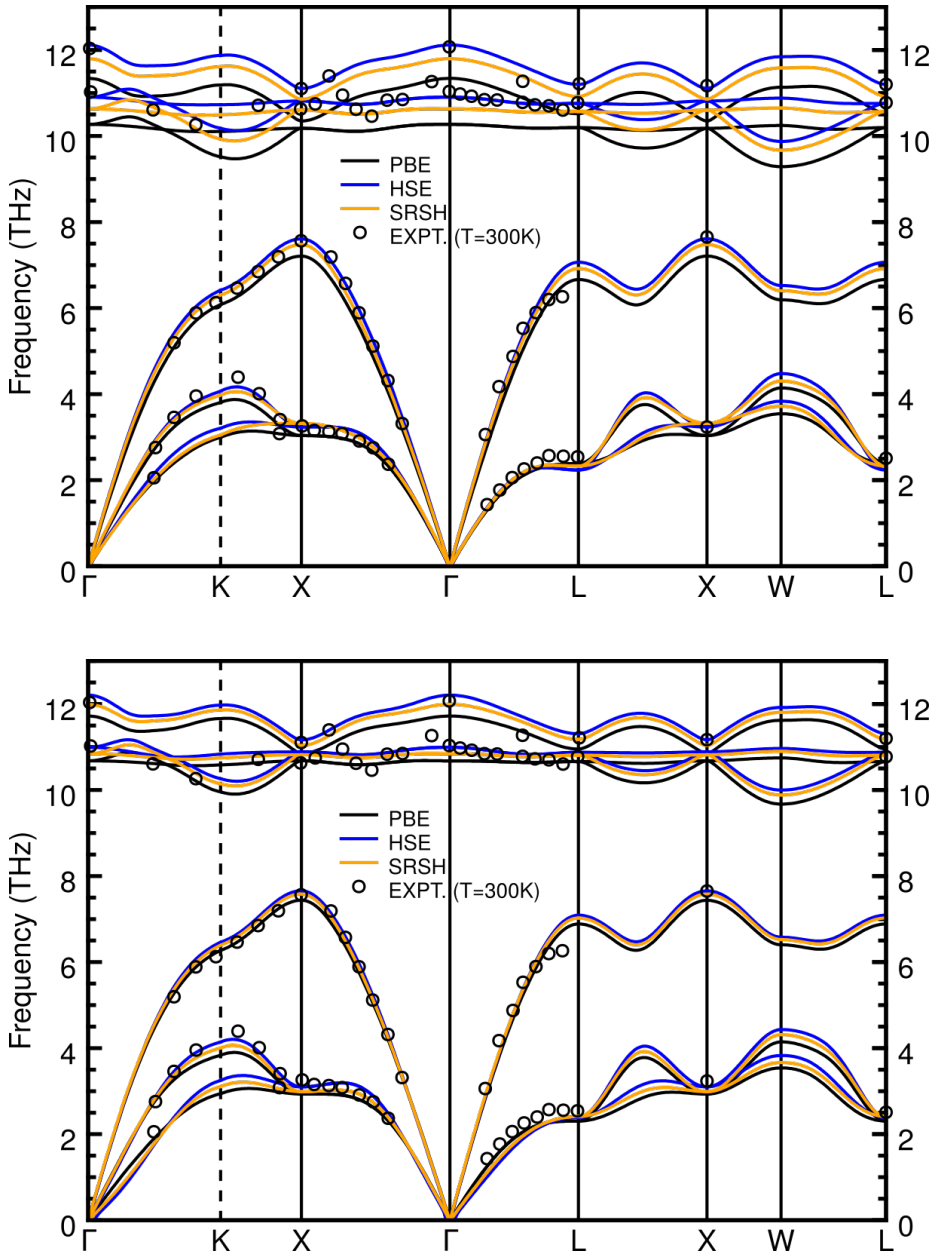

Figure A.4. The upper panel shows the phonon dispersion relation of fcc-structured GaP using the theoretical lattice constant calculated using the PBE, HSE and SRSH functionals (solid colored lines) as well as experimental data (open black circles), which was extracted from reference [200]. The lower panel shows respectively the phonon dispersion relation for only using the experimental lattice constant throughout the three functionals. *Reprinted figure with permission from [1]. Copyright (2021) by the American Physical Society.*

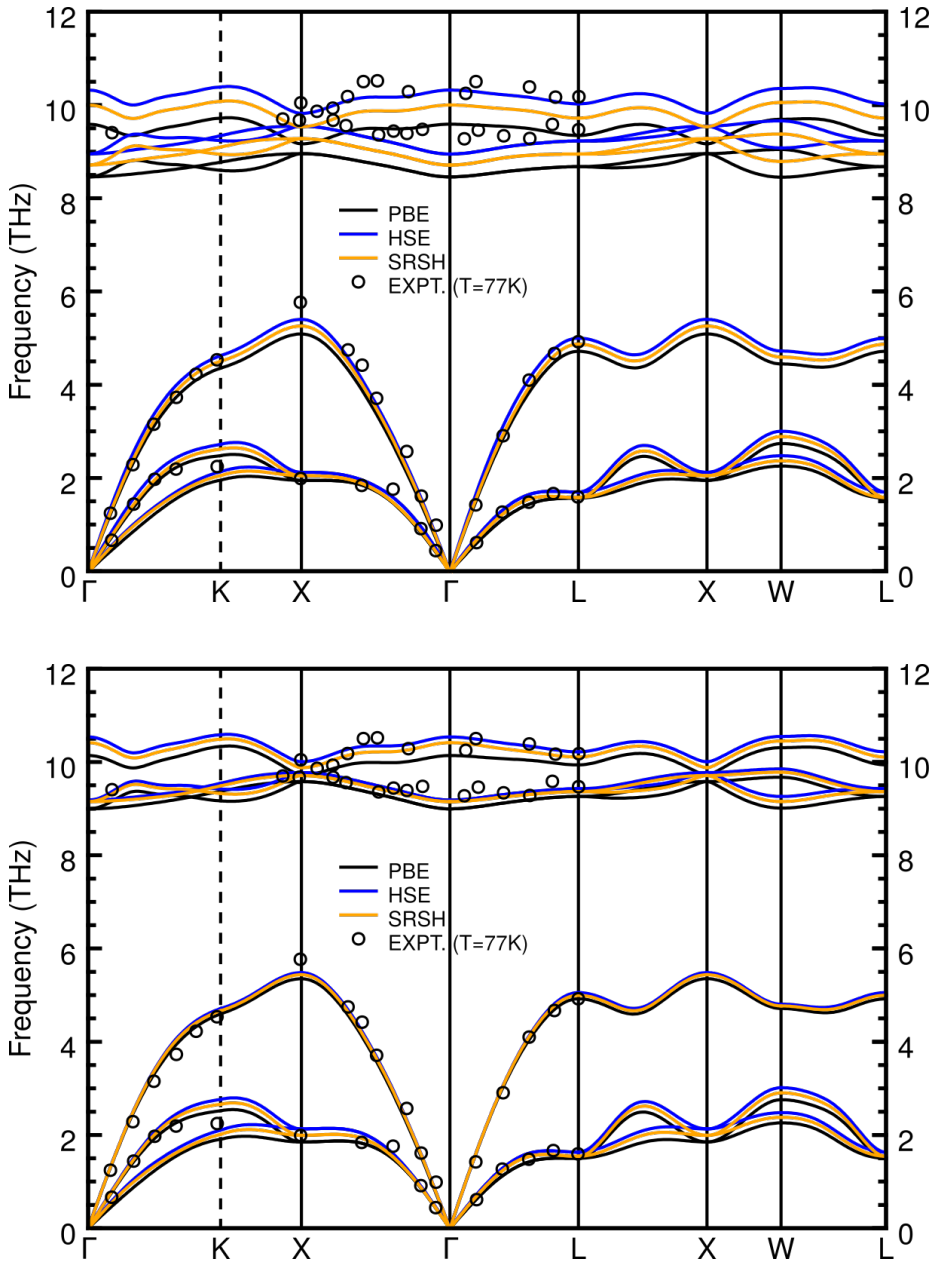

Figure A.5. The upper panel shows the phonon dispersion relation of fcc-structured InP using the theoretical lattice constant calculated using the PBE, HSE and SRSH functionals (solid colored lines) as well as experimental data (open black circles), which was extracted from reference [201]. The lower panel shows respectively the phonon dispersion relation for only using the experimental lattice constant throughout the three functionals. *Reprinted figure with permission from [1]. Copyright (2021) by the American Physical Society.*

A.3. Phonon frequencies at high-symmetry points for common standard semiconductors

Table A.2. Phonon frequencies calculated with PBE, HSE and SRSH for AlAs. Each left sub-column denotes frequencies resulting from the theoretical lattice constant, a_{theo}, and each right sub-column from the experimental lattice constant, a_{exp}. The deviation Δ refers to experimental values at specific high-symmetry points, where available. Classification of phonons and experimental values are from reference [197] and [198]. *Reprinted table with permission from [1]. Copyright (2021) by the American Physical Society.*

	PBE				HSE				SRSH				Expt.
	a_{theo}		a_{exp}		a_{theo}		a_{exp}		a_{theo}		a_{exp}		
(THz)	ω	Δ (%)	ω	Δ (%)	ω	Δ (%)	ω	Δ (%)	ω	Δ (%)	ω	Δ (%)	ω
X_{TA}	2.9	-12.0	2.7	-18.2	3.2	-3.0	3.1	-6.1	3.1	-6.1	2.9	-12.1	3.3
X_{LA}	6.2	-7.5	6.5	-3.0	6.6	-1.5	6.6	-1.5	6.4	-4.5	6.6	-1.5	6.7
X_{TO}	9.4	-6.9	10.1	0.0	9.9	-2.0	10.1	0.0	9.8	-3.0	10.1	0.0	10.1
Γ_{TO}	10.4	-5.5	10.9	-0.9	10.9	-0.9	11.0	0.0	10.7	-2.7	10.9	-0.9	11.0
X_{LO}	11.2	-8.2	11.7	-4.1	11.8	-3.3	11.9	-2.5	11.6	-4.9	11.8	-3.3	12.2
Γ_{LO}	11.4	-6.6	11.9	-2.5	12.1	-0.8	12.2	0.0	11.8	-3.3	12.1	-0.8	12.2
MAD(%)		7.8		4.8		1.9		1.7		4.1		3.1	

Table A.3. Phonon frequencies of AlP with description of the table like in Table A.2. Classification of phonons and experimental values are from reference [197]. *Reprinted table with permission from [1]. Copyright (2021) by the American Physical Society.*

	PBE				HSE				SRSH				Expt.
	a_{theo}		a_{exp}		a_{theo}		a_{exp}		a_{theo}		a_{exp}		
(THz)	ω	Δ (%)	ω	Δ (%)	ω	Δ (%)	ω	Δ (%)	ω	Δ (%)	ω	Δ (%)	ω
Γ_{TO}	12.8	-3.0	13.2	0.0	13.3	0.8	13.4	1.5	13.2	0.0	13.4	1.5	13.2
Γ_{LO}	14.4	-4.0	14.8	-1.3	15.2	1.3	15.2	1.3	15.0	0.0	15.2	1.3	15.0
MAD(%)		3.5		0.7		1.0		1.4		0.0		1.4	

Table A.4. Phonon frequencies of AlSb with description of the table like in Table A.2. Classification of phonons and experimental values are from reference [199]. *Reprinted table with permission from [1]. Copyright (2021) by the American Physical Society.*

	PBE				HSE				SRSH				Expt.
	a_{theo}		a_{exp}		a_{theo}		a_{exp}		a_{theo}		a_{exp}		
(THz)	ω	Δ (%)	ω	Δ (%)	ω	Δ (%)	ω	Δ (%)	ω	Δ (%)	ω	Δ (%)	ω
L_{TA}	1.5	-6.3	1.4	-12.5	1.7	6.3	1.6	0.0	1.5	-6.3	1.5	-6.3	1.6
X_{TA}	2.0	-4.8	1.8	-14.3	2.2	4.8	2.1	0.0	2.2	4.8	2.0	-4.8	2.1
L_{LA}	4.3	-2.3	4.5	2.3	4.6	4.5	4.7	6.8	4.6	4.5	4.6	4.5	4.4
X_{LA}	4.4	-6.4	4.7	0.0	4.8	2.1	4.8	2.1	4.7	0.0	4.7	0.0	4.7
X_{LO}	8.3	-5.7	8.9	1.1	8.9	1.1	8.9	1.1	8.7	-1.1	8.9	1.1	8.8
L_{LO}	8.8	-4.3	9.4	2.2	9.3	1.1	9.4	2.2	9.2	0.0	9.4	2.2	9.2
Γ_{TO}	9.2	-3.2	9.6	1.1	9.7	2.1	9.7	2.1	9.5	0.0	9.7	2.1	9.5
L_{TO}	9.3	-3.1	9.9	3.1	10.0	4.2	10.0	4.2	9.7	1.0	10.0	4.2	9.6
Γ_{LO}	9.7	0.0	10.1	4.1	10.3	6.2	10.4	7.2	10.1	4.1	10.3	6.2	9.7
X_{TO}	9.8	-4.9	10.3	0.0	10.5	1.9	10.5	1.9	10.3	0.0	10.5	1.9	10.3
MAD(%)		4.1		4.1		3.4		2.8		2.2		3.3	

Table A.5. Phonon frequencies of GaP with description of the table like in Table A.2. Classification of phonons and experimental values are from reference [200]. *Reprinted table with permission from [1]. Copyright (2021) by the American Physical Society.*

	PBE				HSE				SRSH				Expt.
	a_{theo}		a_{exp}		a_{theo}		a_{exp}		a_{theo}		a_{exp}		
(THz)	ω	Δ (%)	ω	Δ (%)	ω	Δ (%)	ω	Δ (%)	ω	Δ (%)	ω	Δ (%)	ω
L_{TA}	2.4	-4.0	2.3	-8.0	2.2	-12.0	2.3	-8.0	2.3	-8.0	2.4	-4.0	2.5
X_{TA}	3.0	-9.1	2.9	-12.1	3.2	-3.0	3.1	-6.1	3.3	0.0	3.0	-9.1	3.3
X_{LA}	7.2	-5.3	7.4	-2.6	7.6	0.0	7.7	1.3	7.5	-1.3	7.6	0.0	7.6
X_{TO}	10.2	-3.8	10.7	0.9	10.8	1.9	10.9	2.8	10.6	0.0	10.8	1.9	10.6
L_{TO}	10.2	-5.6	10.7	-0.9	10.8	0.0	10.9	0.9	10.6	-1.9	10.8	0.0	10.8
Γ_{TO}	10.3	-7.2	10.7	-3.6	10.9	-1.8	11.0	-0.9	10.6	-4.5	10.8	-2.7	11.1
X_{LO}	10.3	-7.2	10.8	-2.7	11.1	0.0	11.2	0.9	10.9	-1.8	11.0	-0.9	11.1
L_{LO}	10.5	-6.3	11.0	-1.8	11.2	0.0	11.3	0.9	10.9	-2.7	11.2	0.0	11.2
Γ_{LO}	11.3	-6.6	11.7	-3.3	12.1	0.0	12.2	0.8	11.8	-2.5	12.0	-0.8	12.1
MAD(%)		6.1		4.0		2.1		2.5		2.5		2.2	

Table A.6. Phonon frequencies of InP with description of the table like in Table A.2. Classification of phonons and experimental values are from reference [201]. *Reprinted table with permission from [1]. Copyright (2021) by the American Physical Society.*

	PBE				HSE				SRSH				Expt.
	a_{theo}		a_{exp}		a_{theo}		a_{exp}		a_{theo}		a_{exp}		
(THz)	ω	Δ (%)	ω	Δ (%)	ω	Δ (%)	ω	Δ (%)	ω	Δ (%)	ω	Δ (%)	ω
L_{TA}	1.6	0.0	1.5	-6.3	1.7	6.3	1.6	0.0	1.6	0.0	1.5	-6.3	1.6
X_{TA}	1.9	-5.0	1.8	-10.0	2.1	5.0	2.1	5.0	2.0	0.0	2.0	0.0	2.0
L_{LA}	4.7	-4.1	4.9	0.0	5.0	2.0	5.1	4.1	4.9	0.0	5.0	2.0	4.9
X_{LA}	5.1	-12.1	5.4	-6.9	5.4	-6.9	5.5	-5.2	5.3	-8.6	5.4	-6.9	5.8
L_{TO}	8.7	-8.4	9.3	-2.1	9.2	-3.2	9.4	-1.1	8.9	-6.3	9.4	-1.1	9.5
X_{TO}	9.0	-7.2	9.6	-1.0	9.5	-2.1	9.8	1.0	9.3	-4.1	9.7	0.0	9.7
X_{LO}	9.2	-8.0	9.7	-3.0	9.8	-2.0	10.0	0.0	9.5	-5.0	9.9	-1.0	10.0
L_{LO}	9.3	-8.8	9.9	-2.9	10.0	-2.0	10.2	0.0	9.7	-4.9	10.1	-1.0	10.2
MAD(%)		6.7		4.0		3.7		2.0		3.6		2.3	

A.4. Temperature-dependent band gap for Si

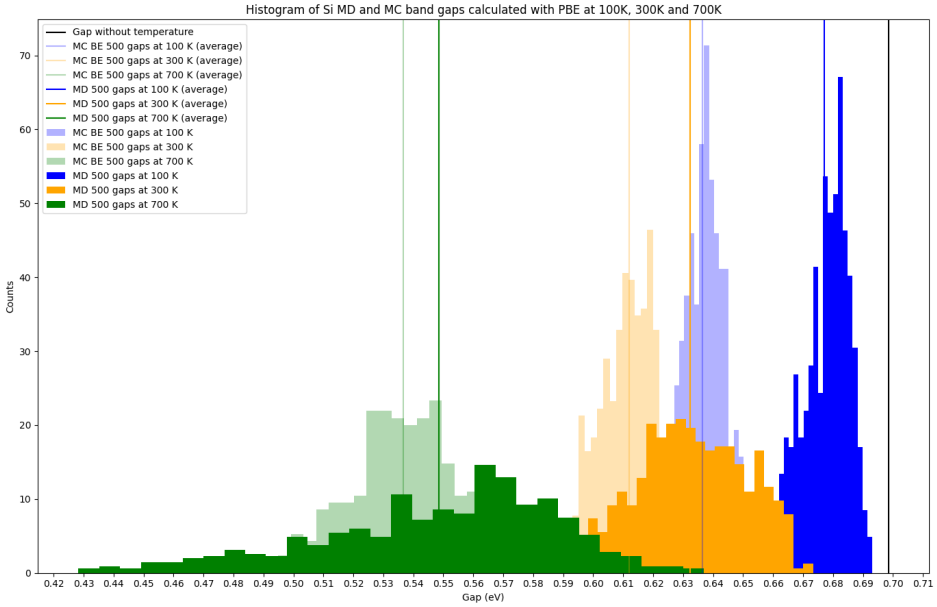

Figure A.6. Temperature-dependent indirect band gap distributions of Si calculated with the MC method and MD for 100 K, 300 K and 700 K. The average band-gap values are depicted as vertical thin lines. The thin black line depicts the static band-gap value.

A.5. Changes of the free energy for $CsPbBr_3$

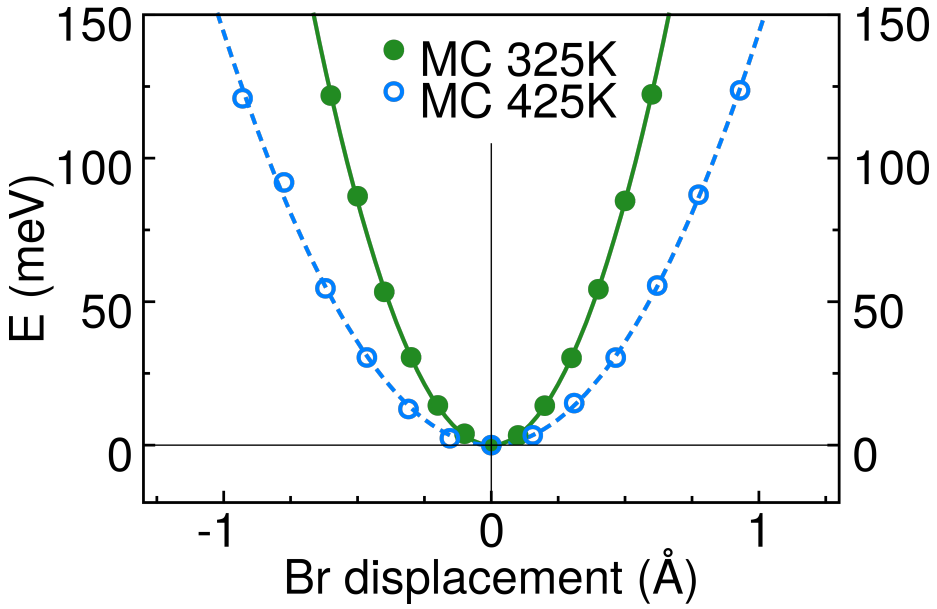

Figure A.7. Changes of the free energy according to transversal Br dynamics in the plane perpendicular to the Pb-Br-Pb bond axis in $CsPbBr_3$. The changes are calculated using a Boltzmann inversion of the orthorhombic MC-distorted structures at 325 K (green disks) and of cubic MC-distorted structures at 425 K (blue circles). Data from the Boltzmann inversion are fitted to a quadratic function (closed and dashed lines). Note that the origin (zero displaced Br atom) denotes the Br atom at the cubic-high symmetry or static orthorhombic structure.

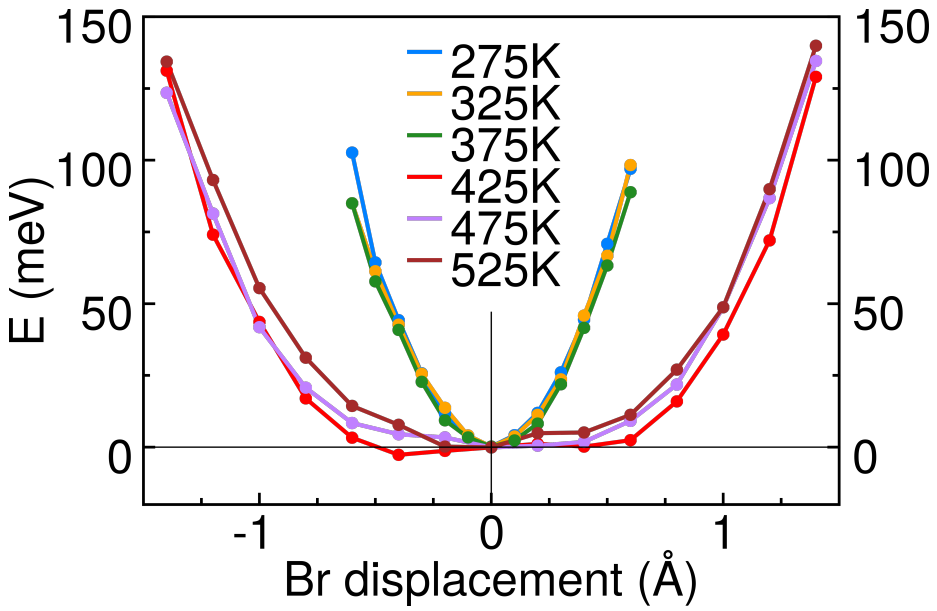

Figure A.8. The description of the figure is the same as in Fig. A.7, apart from the fact that the structures are all from the MD. The temperatures 275 K, 325 K and 375 K correspond to the orthorhombic phase of $CsPbBr_3$ and the temperatures 425 K, 475 K and 525 K correspond to the cubic phase. Note that the results from the Boltzmann inversion of the Br displacements are not converged with respect to the length of the MD trajectory.

A.6. Influence of SOC for orthorhombic $CsPbBr_3$

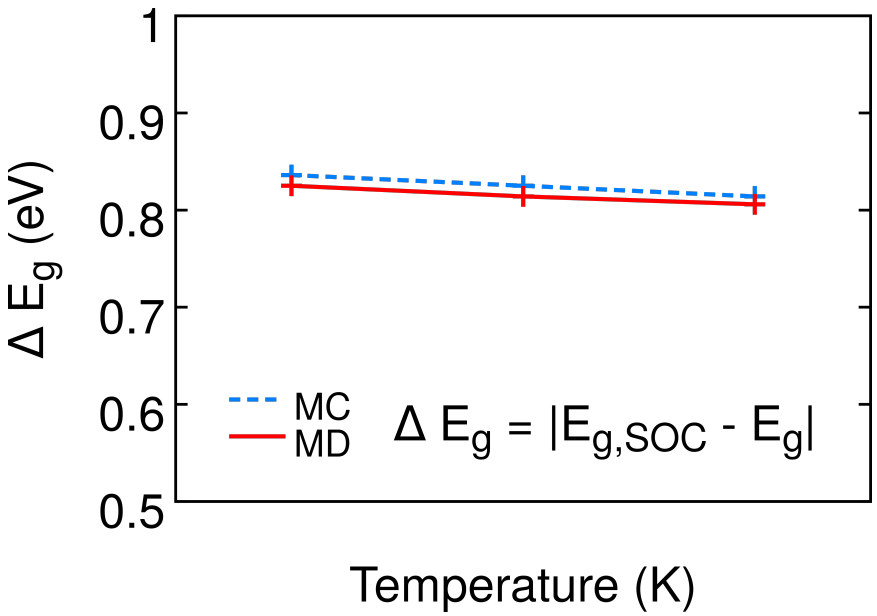

Figure A.9. Influence of SOC on the temperature-dependent band gap of orthorhombic $CsPbBr_3$ depicted as the difference between the band gap with and without SOC. The corresponding band-gap values are listed in Table 4.1. The difference between data points from MC (blue-dashed line) and MD (red line) is almost constant of ≈10 meV throughout the temperatures.

A.7. Phonon dispersion relation for cubic $CsPbBr_3$

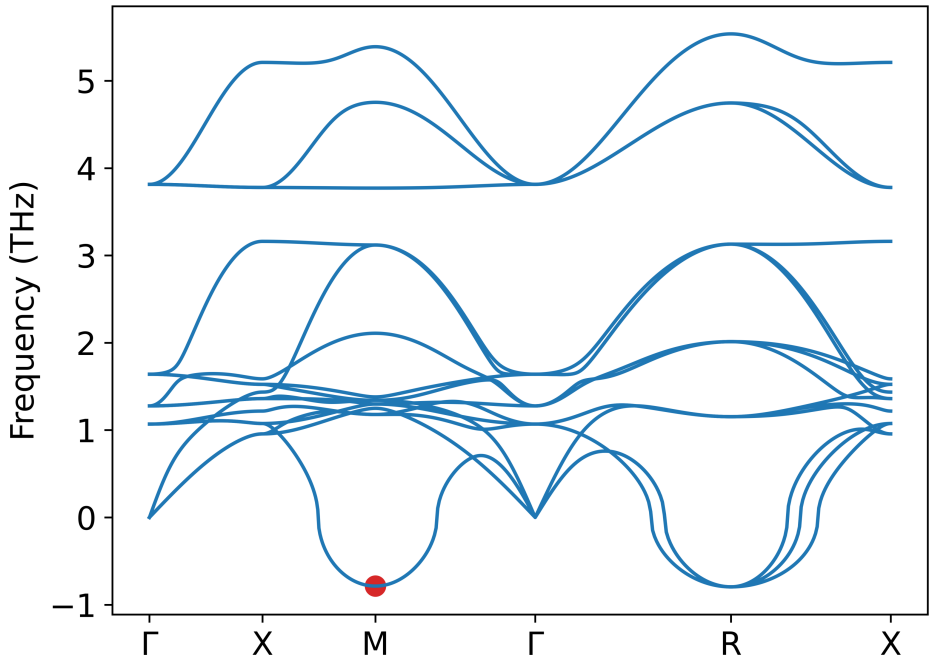

Figure A.10. Phonon dispersion relation for cubic $CsPbBr_3$ calculated with Phonopy using DFT. The red disk indicates the imaginary mode at the M-point. This mode is used to generate transversely displaced Br structures in order to investigate changes in the band gap (see chapter 4.5). Note that the imaginary modes correspond to the octahedral-tilting modes, which are included in MD and excluded in MC. *Reprinted figure with permission from [2]. Copyright (2023) by the American Physical Society.*

A.8. Orthorhombic and cubic schematic structures as average from MD snapshots for $CsPbBr_3$

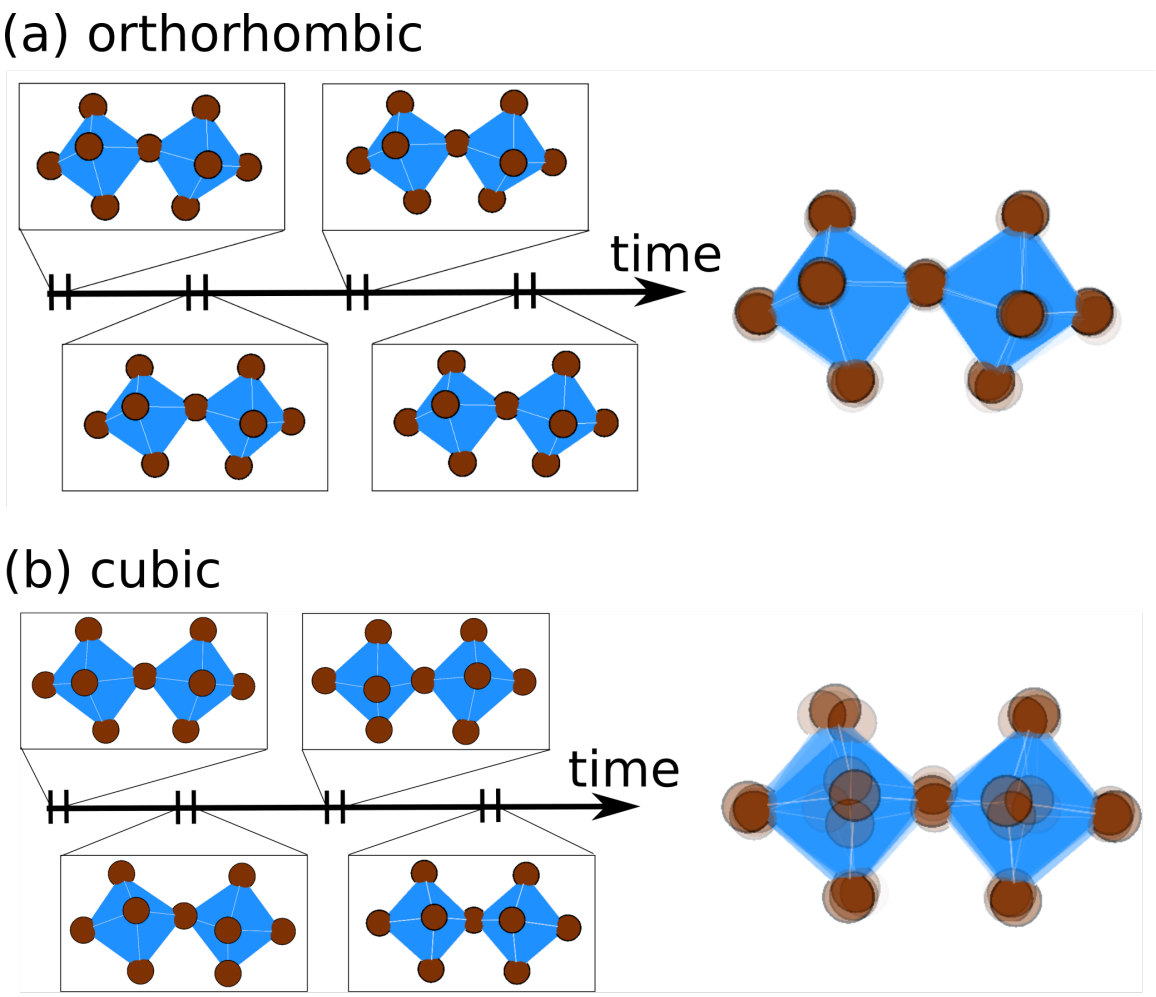

Figure A.11. (a) The black arrow indicates the MD trajectory at 375 K for orthorhombic $CsPbBr_3$, from which time intervals of 1 ps are considered, shown as rectangles. The structures within the rectangles denote the corresponding time-averaged structures. An overlay of the individual time-averaged structures is shown on the right. (b) Similar description as in (a), but for the MD trajectory at 425 K for cubic $CsPbBr_3$. Note that the thermal atomic motions are smaller in the orthorhombic than in the cubic phase of $CsPbBr_3$ with respect to the static structures and that instantaneous octahedral tiltings occur in the individual cubic structures as in the static orthorhombic structure.

Bibliography

[1] S. A. Seidl, B. Kretz, C. Gehrmann, and D. A. Egger, "Assessing the accuracy of screened range-separated hybrids for bulk properties of semiconductors," *Physical Review Materials*, vol. 5, p. 034602, 2021.

[2] S. A. Seidl, X. Zhu, G. Reuveni, S. Aharon, C. Gehrmann, S. Caicedo-Dávila, O. Yaffe, and D. A. Egger, "Anharmonic fluctuations govern the band gap of halide perovskites," *Physical Review Materials*, vol. 7, p. L092401, 2023.

[3] "International Renewable Energy Agency (IRENA)," https://www.irena.org/News/pressreleases/2024/Mar/Record-Growth-in-Renewables-but-Progress-Needs-to-be-Equitable-DE, Acessed: 2024-06-09.

[4] "National Renewable Energy Laboratory (NREL)," https://www.nrel.gov/pv/assets/pdfs/best-research-cell-efficiencies.pdf, Accessed: 2024-02-10.

[5] "Fraunhofer Institute for Solar Energy Systems (ISE)," https://www.ise.fraunhofer.de/en/press-media/news/2023/silicon-based-multijunction-solar-cell-reaches-record-efficiency-of361-percent.html, Accessed: 2023-09-19.

[6] E. L. da Silva, J. M. Skelton, S. C. Parker, and A. Walsh, "Phase stability and transformations in the halide perovskite $CsSnI_3$," *Physical Review B*, vol. 91, no. 14, p. 144107, 2015.

[7] C. Quarti, E. Mosconi, J. M. Ball, V. D'Innocenzo, C. Tao, S. Pathak, H. J. Snaith, A. Petrozza, and F. D. Angelis, "Structural and optical properties of methylammonium lead iodide across the tetragonal to cubic phase transition: Implications for perovskite solar cells," *Energy & Environmental Science*, vol. 9, no. 1, pp. 155–163, 2016.

[8] R. X. Yang, J. M. Skelton, E. L. da Silva, J. M. Frost, and A. Walsh, "Spontaneous octahedral tilting in the cubic inorganic cesium halide perovskites $CsSnX_3$ and $CsPbX_3$ (X = F, Cl, Br, I)," *The Journal of Physical Chemistry Letters*, vol. 8, pp. 4720–4726, 2017.

[9] C. C. Stoumpos and M. G. Kanatzidis, "The renaissance of halide perovskites and their evolution as emerging semiconductors," *Accounts of Chemical Research*, vol. 48, no. 10, pp. 2791–2802, 2015.

[10] X.-G. Zhao, G. M. Dalpian, Z. Wang, and A. Zunger, "Polymorphous nature of cubic halide perovskites," *Physical Review B*, vol. 101, no. 15, p. 155137, 2020.

[11] M. A. Carignano, A. Kachmar, and J. Hutter, "Thermal Effects on $CH_3NH_3PbI_3$ Perovskite from Ab Initio Molecular Dynamics Simulations," *The Journal of Physical Chemistry C*, vol. 119, no. 17, pp. 8991–8997, 2015.

[12] M. A. Carignano, S. A. Aravindh, I. S. Roqan, J. Even, and C. Katan, "Critical Fluctuations and Anharmonicity in Lead Iodide Perovskitesfrom Molecular Dynamics Supercell Simulations," *The Journal of Physical Chemistry C*, vol. 121, no. 38, pp. 20 729–20 738, 2017.

[13] J. Wiktor, U. Rothlisberger, and A. Pasquarello, "Predictive Determination of Band Gaps of Inorganic HalidePerovskites," *The Journal of Physical Chemistry Letters*, vol. 8, no. 22, pp. 5507–5512, 2017.

[14] A. Marronnier, H. Lee, B. Geffroy, J. Even, Y. Bonnassieux, and G. Roma, "Structural Instabilities Related to Highly Anharmonic Phonons in Halide Perovskites," *The Journal of Physical Chemistry Letters*, vol. 8, no. 12, pp. 2659–2665, 2017.

[15] F. Giustino, "Electron-phonon interactions from first principles," *Reviews of Modern Physics*, vol. 89, no. 1, p. 015003, 2017.

[16] W. A. Saidi, S. Poncé, and B. Monserrat, "Temperature Dependence of the Energy Levels of Methylammonium Lead Iodide Perovskite from First-Principles," *The Journal of Physical Chemistry Letters*, vol. 7, no. 24, pp. 5247–5252, 2016.

[17] G. Mannino, I. Deretzis, E. Smecca, A. La Magna, A. Alberti, D. Ceratti, and D. Cahen, "Temperature-Dependent Optical Band Gap in $CsPbBr_3$, $MAPbBr_3$, and $FAPbBr_3$ single crystals," *The Journal of Physical Chemistry Letters*, vol. 11, no. 7, pp. 2490–2496, 2020.

[18] Q. Meng, Y. Chen, Y. Y. Xiao, J. Sun, X. Zhang, C. B. Han, H. Gao, Y. Zhang, and H. Yan, "Effect of temperature on the performance of perovskite solar cells," *Journal of Materials Science: Materials in Electronics*, vol. 32, no. 10, pp. 12 784–12 792, 2021.

[19] J. A. Nelson, *The Physics Of Solar Cells*, 1st ed. London: World Scientific Publishing Company, 2003.

[20] M. Songvilay, N. Giles-Donovan, M. Bari, Z.-G. Ye, J. L. Minns, M. A. Green, G. Xu, P. M. Gehring, K. Schmalzl, W. D. Ratcliff, C. M. Brown, D. Chernyshov, W. van Beek, S. Cochran, and C. Stock, "Common acoustic phonon lifetimes in inorganic and hybrid lead halide perovskites," *Physical Review Materials*, vol. 3, no. 9, p. 093602, 2019.

[21] J. P. Perdew, K. Burke, and M. Ernzerhof, "Generalized Gradient Approximation Made Simple," *Physical Review Letters*, vol. 77, no. 18, p. 4, 1996.

[22] J. Heyd, G. E. Scuseria, and M. Ernzerhof, "Hybrid functionals based on a screened Coulomb potential," *The Journal of Chemical Physics*, vol. 118, no. 18, pp. 8207–8215, 2003.

[23] A. V. Krukau, O. A. Vydrov, A. F. Izmaylov, and G. E. Scuseria, "Influence of the exchange screening parameter on the performance of screened hybrid functionals," *The Journal of Chemical Physics*, vol. 125, no. 22, p. 224106, 2006.

[24] A. D. Becke, "Density-functional exchange-energy approximation with correct asymptotic behavior," *Physical Review A*, vol. 38, no. 6, pp. 3098–3100, 1988.

[25] C. Lee, W. Yang, and R. G. Parr, "Development of the Colle-Salvetti correlation-energy formula into a functional of the electron density," *Physical Review B*, vol. 37, no. 2, pp. 785–789, 1988.

[26] J. Paier, M. Marsman, and G. Kresse, "Why does the B3LYP hybrid functional fail for metals?" *The Journal of Chemical Physics*, vol. 127, no. 2, p. 024103, 2007.

[27] D. Wing, J. B. Haber, R. Noff, B. Barker, D. A. Egger, A. Ramasubramaniam, S. G. Louie, J. B. Neaton, and L. Kronik, "Comparing time-dependent density functional theory with many-body perturbation theory for semiconductors: Screened range-separated hybrids and the G W plus Bethe-Salpeter approach," *Physical Review Materials*, vol. 3, no. 6, p. 064603, 2019.

[28] S. Refaely-Abramson, M. Jain, S. Sharifzadeh, J. B. Neaton, and L. Kronik, "Solid-state optical absorption from optimally tuned time-dependent range-separated hybrid density functional theory," *Physical Review B*, vol. 92, no. 8, p. 081204, 2015.

[29] G. Czycholl, *Theoretische Festkörperphysik Band 1*, 4th ed. Berlin Heidelberg: Springer-Verlag, 2016.

[30] E. Pavarini, E. Koch, and U. Schollwöck, *Lecture Notes of the Autumn School Correlated Electrons 2013: Emergent Phenomena in Correlated Matter*, Forschungszentrum Jülich, Institute for Advanced Simulation, 2013.

[31] K. Baumann, "On the Temperature Dependence of the Band-Gap in Semiconductors," *Physica Status Solidi (b)*, vol. 63, no. 1, pp. K71–K74, 1974.

[32] N. W. Ashcroft and N. D. Mermin, *Solid State Physics*, 1st ed. New York: Holt, Rinehart and Winston, 1976.

[33] H. Sormann and E. Sachinger, *Vorlesung: Theoretische Festkörperphysik, Bandstrukturmethoden*, TU Graz, 2012.

[34] P. Hohenberg and W. Kohn, "Inhomogeneous Electron Gas," *Physical Review*, vol. 136, no. 3B, pp. B864–B871, 1964.

[35] W. Kohn and L. J. Sham, "Self-Consistent Equations Including Exchange and Correlation Effects," *Physical Review*, vol. 140, no. 4A, pp. A1133–A1138, 1965.

[36] R. M. Martin, *Electronic Structure: Basic Theory and Practical Methods*, 2nd ed. Cambridge: Cambridge University Press, 2020.

[37] E. Kraisler and L. Kronik, "Fundamental gaps with approximate density functionals: The derivative discontinuity revealed from ensemble considerations," *The Journal of Chemical Physics*, vol. 140, no. 18, p. 18A540, 2014.

[38] R. M. Dreizler and E. K. U. Gross, *Density Functional Theory: An Approach to the Quantum Many-Body Problem*, 1st ed. Heidelberg: Springer Science & Business Media, 2012.

[39] A. Seidl, A. Görling, P. Vogl, J. A. Majewski, and M. Levy, "Generalized Kohn-Sham schemes and the band-gap problem," *Physical Review B*, vol. 53, no. 7, pp. 3764–3774, 1996.

[40] J. P. Perdew and A. Zunger, "Self-interaction correction to density-functional approximations for many-electron systems," *Physical Review B*, vol. 23, no. 10, pp. 5048–5079, 1981.

[41] J. P. Perdew, "Density functional theory and the band gap problem," *International Journal of Quantum Chemistry*, vol. 28, no. S19, pp. 497–523, 1985.

[42] D. C. Langreth and M. J. Mehl, "Beyond the local-density approximation in calculations of ground-state electronic properties," *Physical Review B*, vol. 28, no. 4, pp. 1809–1834, 1983.

[43] J. P. Perdew and A. Ruzsinszky, "Density-functional energy gaps of solids demystified," *The European Physical Journal B*, vol. 91, no. 6, p. 108, 2018.

[44] J. P. Perdew, M. Ernzerhof, and K. Burke, "Rationale for mixing exact exchange with density functional approximations," *The Journal of Chemical Physics*, vol. 105, no. 22, pp. 9982–9985, 1996.

[45] A. J. Garza and G. E. Scuseria, "Predicting Band Gaps with Hybrid Density Functionals," *The Journal of Physical Chemistry Letters*, vol. 7, no. 20, pp. 4165–4170, 2016.

[46] T. Leininger, H. Stoll, H.-J. Werner, and A. Savin, "Combining long-range configuration interaction with short-range density functionals," *Chemical Physics Letters*, vol. 275, no. 3-4, pp. 151–160, 1997.

[47] D. Pines, *Elementary Excitations In Solids*, 4th ed. Boca Raton: CRC Press, 2019.

[48] M. J. Lucero, T. M. Henderson, and G. E. Scuseria, "Improved semiconductor lattice parameters and band gaps from a middle-range screened hybrid exchange functional," *Journal of Physics: Condensed Matter*, vol. 24, no. 14, p. 145504, 2012.

[49] J. Heyd, J. E. Peralta, G. E. Scuseria, and R. L. Martin, "Energy band gaps and lattice parameters evaluated with the Heyd-Scuseria-Ernzerhof screened hybrid functional," *The Journal of Chemical Physics*, vol. 123, no. 17, p. 174101, 2005.

[50] M. Jain, J. R. Chelikowsky, and S. G. Louie, "Reliability of Hybrid Functionals in Predicting Band Gaps," *Physical Review Letters*, vol. 107, no. 21, p. 216806, 2011.

[51] L. Kronik, T. Stein, S. Refaely-Abramson, and R. Baer, "Excitation Gaps of Finite-Sized Systems from Optimally Tuned Range-Separated Hybrid Functionals," *Journal of Chemical Theory and Computation*, vol. 8, no. 5, pp. 1515–1531, 2012.

[52] S. Refaely-Abramson, S. Sharifzadeh, M. Jain, R. Baer, J. B. Neaton, and L. Kronik, "Gap renormalization of molecular crystals from density-functional theory," *Physical Review B*, vol. 88, no. 8, p. 081204, 2013.

[53] L. Kronik and S. Kümmel, "Dielectric Screening Meets Optimally Tuned Density Functionals," *Advanced Materials*, vol. 30, no. 41, p. 1706560, 2018.

[54] D. Wing, G. Ohad, J. B. Haber, M. R. Filip, S. E. Gant, J. B. Neaton, and L. Kronik, "Band gaps of crystalline solids from Wannier-localization–based optimal tuning of a screened range-separated hybrid functional," *Proceedings of the National Academy of Sciences*, vol. 118, no. 34, p. e2104556118, 2021.

[55] A. D. Becke, "Density-functional thermochemistry. I. The effect of the exchange-only gradient correction," *The Journal of Chemical Physics*, vol. 96, no. 3, pp. 2155–2160, 1992.

[56] T. Yanai, D. P. Tew, and N. C. Handy, "A new hybrid exchange–correlation functional using the Coulomb-attenuating method (CAM-B3LYP)," *Chemical Physics Letters*, vol. 393, no. 1, pp. 51–57, 2004.

[57] R. Gross and A. Marx, *Festkörperphysik*, 1st ed. Oldenbourg: De Gruyter, 2014.

[58] B. Meyer, Ed., *The Pseudopotential Plane Wave Approach*, 1st ed. Jülich: John von Neumann-Institut für Computing, 2006.

[59] D. R. Hamann, M. Schlüter, and C. Chiang, "Norm-Conserving Pseudopotentials," *Physical Review Letters*, vol. 43, no. 20, pp. 1494–1497, 1979.

[60] G. Kresse, "Pseudopotentials (Part I)," https://www.vasp.at/vasp-workshop/pseudopp1.pdf, Accessed: 2023-08-25.

[61] D. S. Sholl and J. A. Steckel, *Density Functional Theory - A Practical Introduction*, 1st ed. Hoboken: Wiley, 2009.

[62] W. Quester, "Sketch Pseudopotentials," https://de.wikipedia.org/wiki/Pseudopotential#/media/Datei:Sketch_Pseudopotentials.png, Accessed: 2023-08-15.

[63] A. Eichler, "Sampling The Brillouin-zone," https://www.vasp.at/vasp-workshop/k-points.pdf, Accessed 2023-09-01.

[64] Q. Wu and W. Yang, "Empirical correction to density functional theory for van der Waals interactions," *The Journal of Chemical Physics*, vol. 116, no. 2, pp. 515–524, 2002.

[65] S. Grimme, "Semiempirical GGA-type density functional constructed with a long-range dispersion correction," *Journal of Computational Chemistry*, vol. 27, no. 15, pp. 1787–1799, 2006.

[66] A. Tkatchenko and M. Scheffler, "Accurate Molecular Van Der Waals Interactions from Ground-State Electron Density and Free-Atom Reference Data," *Physical Review Letters*, vol. 102, no. 7, p. 073005, 2009.

[67] T. Bučko, S. Lebègue, J. Hafner, and J. G. Ángyán, "Improved Density Dependent Correction for the Description of London Dispersion Forces," *Journal of Chemical Theory and Computation*, vol. 9, no. 10, pp. 4293–4299, 2013.

[68] T. Bučko, S. Lebègue, J. G. Ángyán, and J. Hafner, "Extending the applicability of the Tkatchenko-Scheffler dispersion correction via iterative Hirshfeld partitioning," *The Journal of Chemical Physics*, vol. 141, no. 3, p. 034114, 2014.

[69] Y. Wang, T. Gould, J. F. Dobson, H. Zhang, H. Yang, X. Yao, and H. Zhao, "Density functional theory analysis of structural and electronic properties of orthorhombic perovskite $CH_3NH_3PbI_3$," *Physical Chemistry Chemical Physics*, vol. 16, no. 4, pp. 1424–1429, 2014.

[70] D. A. Egger and L. Kronik, "Role of Dispersive Interactions in Determining Structural Properties of Organic–Inorganic Halide Perovskites: Insights from First-Principles Calculations," *The Journal of Physical Chemistry Letters*, vol. 5, no. 15, pp. 2728–2733, 2014.

[71] N. Pandech, T. Kongnok, N. Palakawong, S. Limpijumnong, W. R. L. Lambrecht, and S. Jungthawan, "Effects of the van der Waals Interactions on Structural and Electronic Properties of CH_3NH_3(Pb,Sn)(I,Br,Cl)$_3$ Halide Perovskites," *ACS Omega*, vol. 5, no. 40, pp. 25 723–25 732, 2020.

[72] G.-X. Zhang, A. Tkatchenko, J. Paier, H. Appel, and M. Scheffler, "Van der Waals Interactions in Ionic and Semiconductor Solids," *Physical Review Letters*, vol. 107, no. 24, p. 245501, 2011.

[73] J. Hafner, "Foundations of density functional theory," https://www.vasp.at/vasp-workshop/dft_introd.pdf, Accessed 2023-09-07.

[74] P. Giannozzi, "Forces, stresses and structural optimization," http://qe2019.ijs.si/talks/Giannozzi_Day2-1.pdf, Accessed 2023-09-07.

[75] M. Planck, "Das Prinzip der Relativität und die Grundgleichungen der Mechanik," *Verhandlungen der Deutschen Physikalischen Gesellschaft*, vol. 8, no. 7, p. 136–141, 1906.

[76] S. Steiner, S. Khmelevskyi, M. Marsmann, and G. Kresse, "Calculation of the magnetic anisotropy with projected-augmented-wave methodology and the case study of disordered Fe_{1-X} Co_x alloys," *Physical Review B*, vol. 93, no. 22, p. 224425, 2016.

[77] P. Umari, E. Mosconi, and F. De Angelis, "Relativistic GW calculations on $CH_3NH_3PbI_3$ and $CH_3NH_3SnI_3$ Perovskites for Solar Cell Applications," *Scientific Reports*, vol. 4, no. 1, p. 4467, 2014.

[78] V. Brousseau-Couture, X. Gonze, and M. Côté, "Effect of spin-orbit coupling on the zero-point renormalization of the electronic band gap in cubic materials: First-principles calculations and generalized Fröhlich model," *Physical Review B*, vol. 107, no. 11, p. 115173, 2023.

[79] J. Even, L. Pedesseau, M.-A. Dupertuis, J.-M. Jancu, and C. Katan, "Electronic model for self-assembled hybrid organic/perovskite semiconductors: Reverse band edge electronic states ordering and spin-orbit coupling," *Physical Review B*, vol. 86, no. 20, p. 205301, 2012.

[80] J. Even, L. Pedesseau, J.-M. Jancu, and C. Katan, "Importance of Spin–Orbit Coupling in Hybrid Organic/Inorganic Perovskites for Photovoltaic Applications," *The Journal of Physical Chemistry Letters*, vol. 4, no. 17, pp. 2999–3005, 2013.

[81] P. Y. Yu and M. Cardona, *Fundamentals of Semiconductors: Physics and Materials Properties*, 4th ed. Berlin, Heidelberg: Springer Berlin Heidelberg, 2010.

[82] M. Kepenekian and J. Even, "Rashba and Dresselhaus Couplings in Halide Perovskites: Accomplishments and Opportunities for Spintronics and Spin–Orbitronics," *The Journal of Physical Chemistry Letters*, vol. 8, no. 14, pp. 3362–3370, 2017.

[83] F. Birch, "Finite Elastic Strain of Cubic Crystals," *Physical Review*, vol. 71, no. 11, pp. 809–824, 1947.

[84] F. D. Murnaghan, "The Compressibility of Media under Extreme Pressures," *Proceedings of the National Academy of Sciences of the United States of America*, vol. 30, no. 9, pp. 244–247, 1944.

[85] C. L. Fu and K. M. Ho, "First-principles calculation of the equilibrium ground-state properties of transition metals: Applications to Nb and Mo," *Physical Review B*, vol. 28, no. 10, pp. 5480–5486, 1983.

[86] A. Togo and I. Tanaka, "First principles phonon calculations in materials science," *Scripta Materialia*, vol. 108, pp. 1–5, 2015.

[87] R. M. Pick, M. H. Cohen, and R. M. Martin, "Microscopic Theory of Force Constants in the Adiabatic Approximation," *Physical Review B*, vol. 1, no. 2, p. 910, 1970.

[88] C. H. Henry and J. J. Hopfield, "Raman Scattering by Polaritons," *Physical Review Letters*, vol. 15, no. 25, pp. 964–966, 1965.

[89] W. Cochran and R. A. Cowley, "Dielectric constants and lattice vibrations," *Journal of Physics and Chemistry of Solids*, vol. 23, no. 5, pp. 447–450, 1962.

[90] R. Zallen, "Symmetry and Reststrahlen in Elemental Crystals," *Physical Review*, vol. 173, no. 3, pp. 824–832, 1968.

[91] I. Pallikara, P. Kayastha, J. M. Skelton, and L. D. Whalley, "The physical significance of imaginary phonon modes in crystals," *Electronic Structure*, vol. 4, no. 3, p. 033002, 2022.

[92] L. Y. Huang and W. R. L. Lambrecht, "Lattice dynamics in perovskite halides $CsSnX_3$ with X = I,Br,Cl," *Physical Review B*, vol. 90, no. 19, p. 195201, 2014.

[93] C. Gehrmann and D. A. Egger, "Dynamic shortening of disorder potentials in anharmonic halide perovskites," *Nature Communications*, vol. 10, no. 1, p. 3141, 2019.

[94] R. Car and M. Parrinello, "Unified Approach for Molecular Dynamics and Density-Functional Theory," *Physical Review Letters*, vol. 55, no. 22, pp. 2471–2474, 1985.

[95] L. Verlet, “Computer "Experiments" on Classical Fluids. I. Thermodynamical Properties of Lennard-Jones Molecules,” *Physical Review*, vol. 159, no. 1, pp. 98–103, 1967.

[96] T. Bucko, “Introduction to molecular dynamics (VASP online lecture),” https://www.youtube.com/watch?v=8txbZcgm6pQ, Accessed 2023-10-30.

[97] D. Frenkel and B. Smit, *Understanding Molecular Simulation*, 1st ed. London: Academic Press, 1996.

[98] S. Nosé, “A unified formulation of the constant temperature molecular dynamics methods,” *The Journal of Chemical Physics*, vol. 81, no. 1, pp. 511–519, 1984.

[99] W. G. Hoover, “Canonical dynamics: Equilibrium phase-space distributions,” *Physical Review A*, vol. 31, no. 3, pp. 1695–1697, 1985.

[100] M. Zacharias, C. E. Patrick, and F. Giustino, “Stochastic Approach to Phonon-Assisted Optical Absorption,” *Physical Review Letters*, vol. 115, no. 17, p. 177401, 2015.

[101] C. E. Patrick and F. Giustino, “Quantum nuclear dynamics in the photophysics of diamondoids,” *Nature Communications*, vol. 4, no. 1, p. 2006, 2013.

[102] F. Karsai, M. Engel, E. Flage-Larsen, and G. Kresse, “Electron–phonon coupling in semiconductors within the GW approximation,” *New Journal of Physics*, vol. 20, no. 12, p. 123008, 2018.

[103] M. Zacharias and F. Giustino, “One-shot calculation of temperature-dependent optical spectra and phonon-induced band-gap renormalization,” *Physical Review B*, vol. 94, no. 7, p. 075125, 2016.

[104] O. Yaffe, Y. Guo, L. Z. Tan, D. A. Egger, T. Hull, C. C. Stoumpos, F. Zheng, T. F. Heinz, L. Kronik, M. G. Kanatzidis, J. S. Owen, A. M. Rappe, M. A. Pimenta, and L. E. Brus, “Local Polar Fluctuations in Lead Halide Perovskite Crystals,” *Physical Review Letters*, vol. 118, no. 13, p. 136001, 2017.

[105] X. Zhu, S. Caicedo-Dávila, C. Gehrmann, and D. A. Egger, “Probing the Disorder Inside the Cubic Unit Cell of Halide Perovskites from First-Principles,” *ACS Applied Materials & Interfaces*, vol. 14, no. 20, pp. 22 973–22 981, 2022.

[106] L. Zhi-Gang, M. Zacharias, Y. Zhang, F. Wei, Y. Qin, Y.-Q. Yang, L.-C. An, F.-F. Gao, W. Li, J. Even, and X.-H. Bu, “Origin of Phase Transitions in Inorganic Lead Halide Perovskites: Interplay between Harmonic and Anharmonic Vibrations,” *ACS Energy Letters*, vol. 8, no. 7, pp. 3016–3024, 2023.

[107] S. Caicedo-Dávila, A. Cohen, S. G. Motti, M. Isobe, K. M. McCall, M. Grumet, M. V. Kovalenko, O. Yaffe, L. M. Herz, D. H. Fabini, and D. A. Egger, “Disentangling the Effects of Structure and Lone-Pair Electrons in the

Lattice Dynamics of Halide Perovskites," *Nature Communications*, vol. 15, no. 4184, 2024.

[108] R. Sharma, Z. Dai, L. Gao, T. M. Brenner, L. Yadgarov, J. Zhang, Y. Rakita, R. Korobko, A. M. Rappe, and O. Yaffe, "Elucidating the atomistic origin of anharmonicity in tetragonal $CH_3NH_3PbI_3$ with Raman scattering," *Physical Review Materials*, vol. 4, no. 9, p. 092401, 2020.

[109] J. S. Reid, "Phonon gas," *Physics Education*, vol. 11, no. 5, p. 348, 1976.

[110] A. Marini, S. Poncé, and X. Gonze, "Many-body perturbation theory approach to the electron-phonon interaction with density-functional theory as a starting point," *Physical Review B*, vol. 91, no. 22, p. 224310, 2015.

[111] M. Cardona and M. L. W. Thewalt, "Isotope effects on the optical spectra of semiconductors," *Reviews of Modern Physics*, vol. 77, no. 4, pp. 1173–1224, 2005.

[112] D. Olguín, A. Cantarero, and M. Cardona, "Temperature and Isotopic Mass Dependence of the Direct Band Gap in Semiconductors: LCAO Calculations," *Physica Status Solidi (b)*, vol. 220, no. 1, pp. 33–39, 2000.

[113] X. Gonze, "Electron-Phonon Physics from First Principles (ICTP,Psi-k,CECAM School)," https://docs.epw-code.org/_downloads/7ef8918fae724daea39f71f638a99600/Thu.2.Gonze.pdf, Accessed 2023-10-05, 20,3,2018.

[114] G. Antonius, S. Poncé, P. Boulanger, M. Côté, and X. Gonze, "Many-Body Effects on the Zero-Point Renormalization of the Band Structure," *Physical Review Letters*, vol. 112, no. 21, p. 215501, 2014.

[115] P. B. Allen and V. Heine, "Theory of the temperature dependence of electronic band structures," *Journal of Physics C: Solid State Physics*, vol. 2305, no. 9, 1976.

[116] P. B. Allen and M. Cardona, "Theory of the temperature dependence of the direct gap of germanium," *Physical Review B*, vol. 23, no. 4, pp. 1495–1505, 1981.

[117] P. Allen and M. Cardona, "Temperature dependence of the direct gap of Si and Ge," *Physical Review B*, vol. 27, no. 8, pp. 4760–4769, 1983.

[118] X. Gonze, "Temperature and zero-point motion effects on the electronic band structure (ICTP,Psi-k,CECAM School), Lausanne," 2012.

[119] S. Poncé, Y. Gillet, J. Laflamme Janssen, A. Marini, M. Verstraete, and X. Gonze, "Temperature dependence of the electronic structure of semiconductors and insulators," *The Journal of Chemical Physics*, vol. 143, no. 10, p. 102813, 2015.

[120] K. Kunc and R. M. Martin, "Ab Initio Force Constants of GaAs: A New Approach to Calculation of Phonons and Dielectric Properties," *Physical Review Letters*, vol. 48, no. 6, pp. 406–409, 1982.

[121] G. Kresse and J. Furthmüller, "Efficient iterative schemes for ab initio total-energy calculations using a plane-wave basis set," *Physical Review B*, vol. 54, no. 16, pp. 11 169–11 186, 1996.

[122] T. Bučko, J. Hafner, and J. G. Ángyán, "Geometry optimization of periodic systems using internal coordinates," *The Journal of Chemical Physics*, vol. 122, no. 12, p. 124508, 2005.

[123] Y. Wang, J. J. Wang, W. Y. Wang, Z. G. Mei, S. L. Shang, L. Q. Chen, and Z. K. Liu, "A mixed-space approach to first-principles calculations of phonon frequencies for polar materials," *Journal of Physics: Condensed Matter*, vol. 22, no. 20, p. 202201, 2010.

[124] A. Togo, L. Chaput, and I. Tanaka, "Distributions of phonon lifetimes in Brillouin zones," *Physical Review B*, vol. 91, no. 9, p. 094306, 2015.

[125] G. E. Scuseria, "Advancing solid-state band gap predictions," *PNAS*, vol. 118, no. 35, p. e2113648118, 2021.

[126] W. Martienssen and H. Warlimont, Eds., *Springer Handbook of Condensed Matter and Materials Data*, 1st ed. Berlin Heidelberg: Springer-Verlag, 2005.

[127] F. Herman, "The Electronic Energy Band Structure of Silicon and Germanium," *Proceedings of the IRE*, vol. 43, no. 12, pp. 1703–1732, 1955.

[128] B. G. Janesko, T. M. Henderson, and G. E. Scuseria, "Screened hybrid density functionals for solid-state chemistry and physics," *Phys. Chem. Chem. Phys.*, vol. 11, no. 3, pp. 443–454, 2009.

[129] E. N. Brothers, A. F. Izmaylov, J. O. Normand, V. Barone, and G. E. Scuseria, "Accurate solid-state band gaps via screened hybrid electronic structure calculations," *The Journal of Chemical Physics*, vol. 129, no. 1, p. 011102, 2008.

[130] J. Paier, M. Marsman, K. Hummer, G. Kresse, I. C. Gerber, and J. G. Ángyán, "Screened hybrid density functionals applied to solids," *The Journal of Chemical Physics*, vol. 124, no. 15, p. 154709, 2006.

[131] M. Marsman, J. Paier, A. Stroppa, and G. Kresse, "Hybrid functionals applied to extended systems," *Journal of Physics: Condensed Matter*, vol. 20, no. 6, p. 064201, 2008.

[132] Y. Hinuma, A. Grüneis, G. Kresse, and F. Oba, "Band alignment of semiconductors from density-functional theory and many-body perturbation theory," *Physical Review B*, vol. 90, no. 15, p. 155405, 2014.

[133] J. Heyd, J. E. Peralta, G. E. Scuseria, and R. L. Martin, "Energy band gaps and lattice parameters evaluated with the Heyd-Scuseria-Ernzerhof screened hybrid functional," *The Journal of Chemical Physics*, vol. 123, no. 17, p. 174101, 2005.

[134] O. Madelung, *Semiconductors: Data Handbook*, 3rd ed. Berlin Heidelberg: Springer-Verlag, 2004.

[135] M. Welkowsky and R. Braunstein, "Interband Transitions and Exciton Effects in Semiconductors," *Physical Review B*, vol. 5, no. 2, pp. 497–509, 1972.

[136] B. D. Malone and M. L. Cohen, "Quasiparticle semiconductor band structures including spin–orbit interactions," *Journal of Physics: Condensed Matter*, vol. 25, no. 10, p. 105503, Mar. 2013.

[137] K. Hummer, J. Harl, and G. Kresse, "Heyd-Scuseria-Ernzerhof hybrid functional for calculating the lattice dynamics of semiconductors," *Physical Review B*, vol. 80, no. 11, p. 115205, Sep. 2009.

[138] Q. Cai, D. Scullion, A. Falin, K. Watanabe, T. Taniguchi, Y. Chen, E. J. G. Santos, and L. Hua Li, "Raman signature and phonon dispersion of atomically thin boron nitride," *Nanoscale*, vol. 9, no. 9, pp. 3059–3067, 2017.

[139] L. Schimka, J. Harl, and G. Kresse, "Improved hybrid functional for solids: The HSEsol functional," *The Journal of Chemical Physics*, vol. 134, no. 2, p. 024116, 2011.

[140] Y.-S. Kim, K. Hummer, and G. Kresse, "Accurate band structures and effective masses for InP, InAs, and InSb using hybrid functionals," *Physical Review B*, vol. 80, no. 3, p. 035203, 2009.

[141] M. Schlipf, M. Betzinger, C. Friedrich, M. Ležaić, and S. Blügel, "HSE hybrid functional within the FLAPW method and its application to GdN," *Physical Review B*, vol. 84, no. 12, p. 125142, 2011.

[142] Y. Okada and Y. Tokumaru, "Precise determination of lattice parameter and thermal expansion coefficient of silicon between 300 and 1500 K," *Journal of Applied Physics*, vol. 56, no. 2, pp. 314–320, 1984.

[143] *Landolt-Börnstein Semiconductors, Edited by O. Madelung, U. Rössler, and M. Schulz (Springer-Verlag, Berlin, 2002), Vols. 41A1b and 41A1a.*

[144] P. Rodriguez-Hernandez and A. Munoz, "Ab initio calculations of electronic structure and elastic constants in AlP," *Semiconductor Science and Technology*, vol. 7, no. 12, pp. 1437–1440, 1992.

[145] S. B. Zhang and M. L. Cohen, "High-pressure phases of III-V zinc-blende semiconductors," *Physical Review B*, vol. 35, no. 14, pp. 7604–7610, 1987.

[146] H. Hirano, S. Uehara, A. Mori, A. Onodera, K. Takemura, O. Shimomura, Y. Akahama, and H. Kawamura, "High-pressure phase transitions in AlSb," *Journal of Physics and Chemistry of Solids*, vol. 62, no. 5, pp. 941–949, 2001.

[147] S. Ves, K. Strössner, and M. Cardona, "Pressure dependence of the optical phonon frequencies and the transverse effective charge in AlSb," *Solid State Communications*, vol. 57, no. 7, pp. 483–486, 1986.

[148] V. N. Staroverov, G. E. Scuseria, J. Tao, and J. P. Perdew, "Tests of a ladder of density functionals for bulk solids and surfaces," *Physical Review B*, vol. 69, no. 7, p. 075102, 2004.

[149] H. J. McSkimin, A. Jayaraman, and P. Andreatch, "Elastic Moduli of GaAs at Moderate Pressures and the Evaluation of Compression to 250 kbar," *Journal of Applied Physics*, vol. 38, no. 5, pp. 2362–2364, 1967.

[150] S. Ves, K. Strössner, C. K. Kim, and M. Cardona, "Dependence of the direct energy gap of GaP on hydrostatic pressure," *Solid State Communications*, vol. 55, no. 4, pp. 327–331, 1985.

[151] R. Trommer, H. Müller, M. Cardona, and P. Vogl, "Dependence of the phonon spectrum of InP on hydrostatic pressure," *Physical Review B*, vol. 21, no. 10, pp. 4869–4878, 1980.

[152] W. A. Harrison, *Electronic Structure and the Properties of Solids*. New York: Dover Publications, Inc., 1980.

[153] B. Paulus, P. Fulde, and H. Stoll, "Cohesive energies of cubic III-V semiconductors," *Physical Review B*, vol. 54, no. 4, pp. 2556–2560, 1996.

[154] T. Soma, "The electronic theory of III-V and II-VI tetrahedral compounds. I. Crystal energy and bulk modulus," *Journal of Physics C: Solid State Physics*, vol. 11, no. 13, pp. 2669–2679, 1978.

[155] M. W. Chase, *NIST-JANAF Thermochemical Tables*. Washington, D.C.; Woodbury, N.Y.: American Institute of Physics for the National Institute of Standards and Technology, 1998.

[156] D. Strauch and B. Dorner, "Phonon dispersion in GaAs," *Journal of Physics: Condensed Matter*, vol. 2, p. 1457, 1990.

[157] "Brillouin Zone (1st,FCC)," https://de.wikipedia.org/wiki/Brillouin-Zone#/media/Datei:Brillouin_Zone_(1st,_FCC).svg, Accessed 2023-11-09.

[158] F. Favot and A. Dal Corso, "Phonon dispersions: Performance of the generalized gradient approximation," *Physical Review B*, vol. 60, no. 16, pp. 11 427–11 431, 1999.

[159] G. Dolling, "Inelastic scattering of neutrons in solids and liquids," *International Atomic Energy Agency, Vienna*, vol. 11, p. 37, 1963.

[160] G. Nilsson and G. Nelin, "Study of the homology between silicon and germanium by thermal-neutron spectrometry," *Physical Review B*, vol. 6, p. 3777, 1972.

[161] J. P. Perdew, A. Ruzsinszky, G. I. Csonka, O. A. Vydrov, G. E. Scuseria, L. A. Constantin, X. Zhou, and K. Burke, "Restoring the Density-Gradient Expansion for Exchange in Solids and Surfaces," *Physical Review Letters*, vol. 100, no. 13, p. 136406, 2008.

[162] J. P. Perdew, L. A. Constantin, E. Sagvolden, and K. Burke, "Relevance of the Slowly Varying Electron Gas to Atoms, Molecules, and Solids," *Physical Review Letters*, vol. 97, no. 22, p. 223002, 2006.

[163] A. Karolewski, L. Kronik, and S. Kümmel, "Using optimally tuned range separated hybrid functionals in ground-state calculations: Consequences and caveats," *The Journal of Chemical Physics*, vol. 138, no. 20, p. 204115, 2013.

[164] K. P. O'Donnell and X. Chen, "Temperature dependence of semiconductor band gaps," *Applied Physics Letters*, vol. 58, no. 25, pp. 2924–2926, 1991.

[165] C. D. Clark, P. J. Dean, P. V. Harris, and W. C. Price, "Intrinsic edge absorption in diamond," *Proceedings of the Royal Society of London. Series A. Mathematical and Physical Sciences*, vol. 277, no. 1370, pp. 312–329, 1997.

[166] V. S. Vavilov and E. A. Konorova, "Semiconducting diamonds," *Soviet Physics Uspekhi*, vol. 19, no. 4, p. 301, 1976.

[167] F. Giustino, S. G. Louie, and M. L. Cohen, "Electron-Phonon Renormalization of the Direct Band Gap of Diamond," *Physical Review Letters*, vol. 105, no. 26, p. 265501, 2010.

[168] V. Alex, S. Finkbeiner, and J. Weber, "Temperature dependence of the indirect energy gap in crystalline silicon," *Journal of Applied Physics*, vol. 79, no. 9, pp. 6943–6946, 1996.

[169] T. Das, G. Di Liberto, and G. Pacchioni, "Density Functional Theory Estimate of Halide Perovskite Band Gap: When Spin Orbit Coupling Helps," *The Journal of Physical Chemistry C*, vol. 126, no. 4, pp. 2184–2198, 2022.

[170] B. J. Foley, D. L. Marlowe, K. Sun, W. A. Saidi, L. Scudiero, M. C. Gupta, and J. J. Choi, "Temperature dependent energy levels of methylammonium lead iodide perovskite," *Applied Physics Letters*, vol. 106, no. 24, p. 243904, 2015.

[171] M. Zacharias, G. Volonakis, F. Giustino, and J. Even, "Anharmonic electron-phonon coupling in ultrasoft and locally disordered perovskites," *npj Computational Materials*, vol. 9, no. 1, pp. 1–13, 2023.

[172] L. D. Whalley, J. M. Skelton, J. M. Frost, and A. Walsh, "Phonon anharmonicity, lifetimes, and thermal transport in $CH_3NH_3PbI_3$ from many-body perturbation theory," *Physical Review B*, vol. 94, no. 22, p. 220301, 2016.

[173] A. N. Beecher, O. E. Semonin, J. M. Skelton, J. M. Frost, M. W. Terban, H. Zhai, A. Alatas, J. S. Owen, A. Walsh, and S. J. L. Billinge, "Direct Observation of Dynamic Symmetry Breaking above Room Temperature in Methylammonium Lead Iodide Perovskite," *ACS Energy Letters*, vol. 1, no. 4, pp. 880–887, 2016.

[174] O. Yaffe, Y. Guo, L. Z. Tan, D. A. Egger, T. Hull, C. C. Stoumpos, F. Zheng, T. F. Heinz, L. Kronik, M. G. Kanatzidis, J. S. Owen, A. M. Rappe, M. A. Pimenta, and L. E. Brus, "Local Polar Fluctuations in Lead Halide Perovskite Crystals," *Physical Review Letters*, vol. 118, no. 13, p. 136001, 2017.

[175] X. Wu, L. Z. Tan, X. Shen, T. Hu, K. Miyata, M. T. Trinh, R. Li, R. Coffee, S. Liu, D. A. Egger, I. Makasyuk, Q. Zheng, A. Fry, J. S. Robinson, M. D. Smith, B. Guzelturk, H. I. Karunadasa, X. Wang, X. Zhu, L. Kronik, A. M. Rappe, and A. M. Lindenberg, "Light-induced picosecond rotational disordering of the inorganic sublattice in hybrid perovskites," *Science Advances*, vol. 3, no. 7, p. e1602388, 2017.

[176] N. J. Weadock, T. C. Sterling, J. A. Vigil, A. Gold-Parker, I. C. Smith, B. Ahammed, M. J. Krogstad, F. Ye, D. Voneshen, P. M. Gehring, A. M. Rappe, H.-G. Steinrück, E. Ertekin, H. I. Karunadasa, D. Reznik, and M. F. Toney, "The nature of dynamic local order in $CH_3NH_3PbI_3$ and $CH_3NH_3PbBr_3$," *Joule*, vol. 7, no. 5, pp. 1051–1066, 2023.

[177] C. Gehrmann, S. Caicedo-Dávila, X. Zhu, and D. A. Egger, "Transversal Halide Motion Intensifies Band-To-Band Transitions in Halide Perovskites," *Advanced Science*, vol. 9, no. 16, p. 2200706, 2022.

[178] W. A. Saidi and A. Kachmar, "Effects of Electron–Phonon Coupling on Electronic Properties of Methylammonium Lead Iodide Perovskites," *The Journal of Physical Chemistry Letters*, vol. 9, no. 24, pp. 7090–7097, 2018.

[179] S. Hirotsu, J. Harada, M. Iizumi, and K. Gesi, "Structural Phase Transitions in $CsPbBr_3$," *Journal of the Physical Society of Japan*, vol. 37, no. 5, pp. 1393–1398, 1974.

[180] C. C. Stoumpos, C. D. Malliakas, J. A. Peters, Z. Liu, M. Sebastian, J. Im, T. C. Chasapis, A. C. Wibowo, D. Y. Chung, A. J. Freeman, B. W. Wessels, and M. G. Kanatzidis, "Crystal Growth of the Perovskite Semiconductor $CsPbBr_3$: A New Material for High-Energy Radiation Detection," *Crystal Growth & Design*, vol. 13, no. 7, pp. 2722–2727, 2013.

[181] B. Kang and K. Biswas, "Exploring Polaronic, Excitonic Structures and Luminescence in Cs_4PbBr_6 / $CsPbBr_3$," *The Journal of Physical Chemistry Letters*, vol. 9, no. 4, pp. 830–836, 2018.

[182] M. Z. Mayers, L. Z. Tan, D. A. Egger, A. M. Rappe, and D. R. Reichman, "How Lattice and Charge Fluctuations Control Carrier Dynamics in Halide Perovskites," *Nano Letters*, vol. 18, no. 12, pp. 8041–8046, 2018.

[183] M. J. Schilcher, P. J. Robinson, D. J. Abramovitch, L. Z. Tan, A. M. Rappe, D. R. Reichman, and D. A. Egger, "The Significance of Polarons and Dynamic Disorder in Halide Perovskites," *ACS Energy Letters*, vol. 6, no. 6, pp. 2162–2173, 2021.

[184] A. V. Cohen, D. A. Egger, A. M. Rappe, and L. Kronik, "Breakdown of the Static Picture of Defect Energetics in HalidePerovskites: The Case of the Br Vacancy in $CsPbBr_3$," *The Journal of Physical Chemistry Letters*, vol. 10, no. 16, pp. 4490–4498, 2019.

[185] O. Yaffe, A. Chernikov, Z. M. Norman, Y. Zhong, A. Velauthapillai, A. Van Der Zande, J. S. Owen, and T. F. Heinz, "Excitons in ultrathin organic-inorganic perovskite crystals," *Physical Review B*, vol. 92, no. 4, p. 045414, 2015.

[186] M. Fox, *Optical Properties of Solids*, 2nd ed. Oxford: Oxford University Press, 2010.

[187] G. R. Yettapu, D. Talukdar, S. Sarkar, A. Swarnkar, A. Nag, P. Ghosh, and P. Mandal, "Terahertz Conductivity within Colloidal $CsPbBr_3$ Perovskite Nanocrystals: Remarkably High Carrier Mobilities and Large Diffusion Lengths," *Nano Letters*, vol. 16, no. 8, pp. 4838–4848, 2016.

[188] P. Makuła, M. Pacia, and W. Macyk, "How To Correctly Determine the Band Gap Energy of Modified Semiconductor Photocatalysts Based on UV–Vis Spectra," *The Journal of Physical Chemistry Letters*, vol. 9, no. 23, pp. 6814–6817, 2018.

[189] T. Lanigan-Atkins, X. He, M. J. Krogstad, D. M. Pajerowski, D. L. Abernathy, G. N. M. N. Xu, Z. Xu, D.-Y. Chung, M. G. Kanatzidis, S. Rosenkranz, R. Osborn, and O. Delaire, "Two-dimensional overdamped fluctuations of the soft perovskite lattice in $CsPbBr_3$," *Nature Materials*, vol. 20, no. 7, pp. 977–983, 2021.

[190] A. Amat, E. Mosconi, E. Ronca, C. Quarti, P. Umari, Md. K. Nazeeruddin, M. Grätzel, and F. D. Angelis, "Cation-Induced Band-Gap Tuning in Organohalide Perovskites: Interplay of Spin–Orbit Coupling and Octahedra Tilting," *Nano Letters*, vol. 14, no. 6, pp. 3608–3616, 2014.

[191] A. Poglitsch and D. Weber, "Dynamic disorder in methylammoniumtrihalogenoplumbates (II) observed by millimeter-wave spectroscopy," *The Journal of Chemical Physics*, vol. 87, no. 11, pp. 6373–6378, 1987.

[192] E. Mosconi, P. Umari, and F. D. Angelis, "Electronic and optical properties of $MAPbX_3$ perovskites (X = I, Br, Cl): A unified DFT and GW theoretical analysis," *Physical Chemistry Chemical Physics*, vol. 18, no. 39, pp. 27 158–27 164, 2016.

[193] J. L. Knutson, J. D. Martin, and D. B. Mitzi, "Tuning the Band Gap in Hybrid Tin Iodide Perovskite Semiconductors Using Structural Templating," *Inorganic Chemistry*, vol. 44, no. 13, pp. 4699–4705, 2005.

[194] X. Gonze, "The Abinit project: Impact, environment and recent developments," *Computer Physics Communications*, vol. 248, p. 107042, 2020.

[195] A. D. Wright, C. Verdi, R. L. Milot, G. E. Eperon, M. A. Pérez-Osorio, H. J. Snaith, F. Giustino, M. B. Johnston, and L. M. Herz, "Electron–phonon coupling in hybrid lead halide perovskites," *Nature Communications*, vol. 7, no. 1, p. 11755, 2016.

[196] J. Tilchin, D. N. Dirin, G. I. Maikov, A. Sashchiuk, M. V. Kovalenko, and E. Lifshitz, "Hydrogen-like Wannier–Mott Excitons in Single Crystal of Methylammonium Lead Bromide Perovskite," *ACS Nano*, vol. 10, no. 6, pp. 6363–6371, 2016.

[197] A. Onton, "Proceedings of the 10th international conference on the physics of semiconductors," *International Conference on the Physics of Semiconductors, Cambridge: (USAEC, Oak Ridge)*, vol. 107, 1970.

[198] B. Monemar, "Fundamental energy gaps of AlAs and Alp from photoluminescence excitation spectra," *Physical Review B*, vol. 8, p. 5711, 1973.

[199] D. Strauch, B. Dorner, and K. Karch, "Phonons 89, ed. by S. Hunklinger, W. Ludwig, G. Weiss," *World Scientific, Singapore*, vol. 89, p. 82, 1990.

[200] J. L. Yarnell, J. L. Warren, R. G. Wenzel, and P. J. Dean, "Lattice dynamics of gallium phosphide," *Neutron Inelastic Scattering Vol. I. Proceedings of a Symposium on Neutron Inelastic Scattering*, 1968.

[201] P. H. Borcherds, G. F. Alfrey, A. D. B. Woods, and D. H. Saunderson, "Phonon dispersion curves in indium phosphide," *Journal of Physics C: Solid State Physics*, vol. 8, p. 2022, 1975.